Title
(Dumpster) Diving from the Land into the Sea with Seismology

Author
Shaddox, Heather

Publication Date
2021

UNIVERSITY OF CALIFORNIA
SANTA CRUZ

(DUMPSTER) DIVING FROM THE LAND INTO THE SEA WITH SEISMOLOGY

A dissertation submitted in partial satisfaction
of the requirements for the degree of

DOCTOR OF PHILOSOPHY

in

EARTH SCIENCES

by

Heather R. Shaddox

September 2021

The Dissertation of Heather R. Shaddox is approved:

Professor Susan Y. Schwartz, Chair

Professor Emily E. Brodsky

Professor Thorne Lay

Professor Kristen A. Davis

Peter Biehl
Vice Provost and Dean of Graduate Studies

Table of Contents

List of Figures vi

List of Tables x

Abstract xi

Dedication xvi

Acknowledgements xvii

Chapter 1 - Subducted Seamount Diverts Shallow Slow Slip to the Forearc of the Northern Hikurangi Subduction Margin, New Zealand 1

- **1.1 Introduction** 1
- **1.2 Hikurangi Subduction Margin** 3
- **1.3 Data and methods** 6
- **1.4 Results** 7
- **1.5 Discussion** 10
- **1.6 Conclusions** 13
- **1.7 Brief follow-up study during the 2019 slow slip event** 14
  - 1.7.1. Purpose, data, and methods 14
  - 1.7.2. Results 17
  - 1.7.3. Discussion and conclusions 20

Chapter 2 - Afterslip and Spontaneous Aseismic Slip on the Anza Segment of the San Jacinto Fault Zone, Southern California 22

- **2.1 Introduction** 22
- **2.2 Anza Segment of the San Jacinto Fault Zone** 29

2.3 Detecting and locating transient aseismic slip 32

2.3.1 Near-repeating earthquakes and general seismicity 32

2.3.2 Borehole strainmeter data 35

2.3.3 Afterslip distribution 35

2.4 Results 39

2.4.1 Previously identified afterslip/triggered aseismic slip transients 39

2.4.2 Newly detected afterslip 45

2.4.3 Newly detected spontaneous aseismic slip transient 49

2.5 Discussion 51

2.5.1 Afterslip of the 2010, 2013, and 2016 earthquakes 51

2.5.2 Near-repeating earthquakes as a proxy for transient aseismic slip 55

2.5.3 Deep slip in the trifurcation area 58

2.5.4 Afterslip of moderate-sized earthquakes 59

2.5.5 April 2020 earthquake and triggered aseismic slip 61

2.6 Conclusions 66

Chapter 3 - Seismic Detection of Oceanic Internal Gravity Waves from Subaerial Seismometers 68

3.1 Internal waves and expected seismic signals 68

3.2 Dongsha Atoll and the South China Sea 75

3.3 Data and methods 76

3.3.1 Satellite and oceanographic data 76

3.3.2 Seismic data 78

3.4 Observations **81**
3.4.1 Transient seismic tilt signals 81
3.4.2 Comparison of seismic and satellite observations 84
3.4.3 Comparison of seismic and oceanographic observations 87
3.4.4 Signal across seismic stations 90
3.4.5 Seismic amplitude 92
3.5 Summary of observations and potential mechanisms **94**
3.5.1 Passing of internal waves 95
3.5.2 Collision of internal waves 96
3.6 Caveats and conundrums **97**
3.6.1 North-south dominant tilt 97
3.6.2 Detection of only one type of wave 98
3.6.3 Seismic performance compared to existing methods 100
3.6.4 Mechanism 102
3.7 Conclusion **102**
3.8 Brief follow-up study from ocean-bottom seismic observations **103**
3.8.1 Purpose and introduction 103
3.8.2 Data and methods 103
3.8.3 Observations 106
3.8.4 Discussion and conclusions 116
Appendices **118**
References **165**

List of Figures

Figure 1-1. Map of Hikurangi Ocean Bottom Investigation of Tremor and Slow Slip (HOBITSS) array. 5

Figure 1-2. Results of repeating earthquake search. 8

Figure 1-3. Repeating earthquake plots of time vs. local magnitude. 9

Figure 1-4. Seismic reflection profile 05CM-04 (Figure 1-2) modified from Barker et al., 2018. 11

Figure 1-5. Comparative map of the 2014-2015 and 2018-2019 ocean-bottom seismometer deployments. 16

Figure 1-6. Map of burst-type repeating earthquakes related to the 2019 slow slip event. 18

Figure 1-7. Timing of seismicity and burst-type repeating earthquakes related to the 2019 slow slip event. 19

Figure 1-8. Comparison of seismicity and burst-type repeating earthquake rates related to the 2014 and 2019 slow slip events. 21

Figure 2-1. Seismicity map of the trifurcation area of the San Jacinto fault zone near Anza in southern California. 28

Figure 2-2. Seismicity, near-repeating earthquakes, and borehole strainmeter (BSM) data in the study region from 2010-2016. 38

Figure 2-3. Spatial distribution of the 2010 afterslip. 41

Figure 2-4. Spatial distribution of the 2013 afterslip. 44

Figure 2-5. Timing of the 2016 afterslip ... 47

Figure 2-6. Spatial distribution of the 2016 afterslip. ... 48

Figure 2-7. Timing and spatial distribution of the 2015 shallow, spontaneous aseismic slip transient. ... 50

Figure 2-8. Fault perpendicular cross-section of seismicity and near-repeating earthquakes within 15 km of A-A’ on Figure 2-1 during afterslip or triggered aseismic slip. ... 54

Figure 2-9. Spatial distribution of the 2020 aseismic slip transient. ... 65

Figure 3-1. Map of the study area and schematic of a propagating internal solitary wave in the South China Sea. ... 74

Figure 3-2. Oceanic water temperature and land seismic data from May 13 - June 11, 2019. ... 83

Figure 3-3. Comparison of satellite images and seismic observations as internal waves pass Dongsha Atoll ... 85

Figure 3-4. Detailed comparison of satellite images and seismic observations as internal waves pass Dongsha Atoll. ... 86

Figure 3-5. Comparison of shallow oceanic water temperature data to seismic observations at VDOS during spring tide on May 27 (a), May 25 (b), and May 22 (c). ... 89

Figure 3-6. Comparison of tilt signal across seismic stations on May 15, 2019. ... 91

Figure 3-7. Amplitude of seismic internal wave detections. ... 93

Figure 3-8. Map of Dongsha Atoll with ocean-bottom seismic station BB01 and cartoon of an internal solitary wave of depression. 105

Figure 3-9. Year of ocean-bottom seismic data. 107

Figure 3-10. Spring-neap tidal cycle of internal wave detections on BB01. 108

Figure 3-11. Ocean-bottom seismic observations from May 6 - May 12, 2020. 110

Figure 3-12. Comparison of satellite and ocean bottom seismic observations from passing type-a internal waves on May 10, 2020. 111

Figure 3-13. Comparison of satellite and ocean bottom seismic observations from passing type-a internal waves on May 12, 2020. 112

Figure 3-14. Ocean-bottom seismic observations from June 3 – June 9, 2020. 114

Figure 3-15. Comparison of satellite, ocean bottom, and land seismic observations from a type-b internal wave on June 4, 2020. 115

Figure A-1. Map and cross-section of seismicity (within 25 km of A-A') from May 2014 – June 2015.. 126

Figure A-2. GrowClust location errors. 127

Figure A-3. Comparison of velocity models... 128

Figure A-4. Example burst-type repeating earthquake seismogram, average CC of 0.96. 129

Figure A-5. Example burst-type repeating earthquake seismogram, average CC of 0.95. 130

Figure A-6. Example burst-type repeating earthquake seismogram, average CC of 0.99. 131

Figure A-7. Example burst-type repeating earthquake seismogram, average CC of 0.95. 132

Figure B-1. Histogram of earthquake depths in the study region. 136

Figure B-2. Spectral plot for local earthquakes averaged within local magnitude (ML) bins and averaged noise in 2014 at station BZN component BHZ. 137

Figure B-3. Example near-repeating earthquake. 138

Figure B-4. Timing of the 2010 afterslip. 139

Figure B-5. Timing of the 2013 afterslip. 140

Figure B-6. Strain data for the 2020 afterslip. 141

Figure C-1. Seismic amplitude compared to local tide, water and land temperature, and barometric pressure fluctuations. 161

Figure C-2. Signal-to-noise comparison for internal wave detections on June 6 and June 7, 2019 on VDOS HHN 162

Figure C-3. Signal-to-noise comparison for internal wave detections on June 6 and June 7, 2019 on VDOS HHE. 163

List of Tables

Table A-1. Near-Repeating Earthquakes at Subducted Seamount 133

Table B-1. Details of local moderate-sized ($M_W > 4.5$) earthquakes in the study region and modeled afterslip 142

Table B-2. Near-repeating earthquakes during the 2010-2016 study period 143

Table B-3. Near-repeating earthquakes in March 1 - May 6, 2020 156

Abstract

(Dumpster) Diving from the Land into the Sea with Seismology

Heather R. Shaddox

Seismology is a geophysical tool that can probe the earth and provide insight into processes that are otherwise difficult to observe. I am primarily interested in using seismological methods to detect and study ubiquitous processes that are challenging to observe due to noise sources and other observational limitations. This dissertation encompasses two seemingly distinct areas: aseismic fault slip and oceanic internal waves. These areas of study can ultimately be instrumentally and scientifically connected in offshore regions using ocean-bottom seismometers (OBS) for dual-purpose research goals. In particular, as the title of this dissertation suggests, we make use of the often-discarded portion of seismic signals (i.e., “noise”) to study earth processes.

Slip on faults occurs as a spectrum, ranging from stably sliding (aseismic creep) to rapid ruptures (earthquakes). Within the fault slip spectrum are transient events of slow, aseismic slip known as slow slip events (SSEs). SSEs may precede and even trigger large megathrust earthquakes and are therefore critical to detect and understand. SSEs are too slow to generate seismic waves and are generally detected geodetically. However, the shallow portion (<15 km) of many subduction zones is typically located offshore, out of the range of land geodetic networks. This presents an observational limitation of shallow SSEs that may be improved using related

secondary seismicity, such as tremor and microearthquakes, to infer the location of shallow offshore SSEs.

Chapter 1 and Chapter 2 study a specific form of microseismicity, burst-type or near-repeating earthquakes, that can be used to improve the detection of transient aseismic slip. Near-repeating or burst-type repeating earthquakes are families of closely spaced earthquakes (within 200 m) with highly-correlated waveforms, aperiodic repeat intervals and variable magnitudes. We test the hypothesis that sequences of burst-type or near-repeating earthquake families concentrated in time and space are driven to failure by transient aseismic slip on the surrounding fault and can therefore be used as a proxy for aseismic slip transients. Although not included in this dissertation, I am additionally a coauthor on a study that analyzed a cluster of highly similar earthquakes in the southern Cascadia subduction zone likely related to an aseismic slip transient or changes in plate interface coupling (Alongi et al., 2021).

Chapter 1 analyzes burst-type repeating earthquakes related to a well-recorded shallow SSE offshore of Gisborne, New Zealand in September/October 2014 using OBS data. (Shaddox et al., 2019). These burst-type repeating earthquakes are coincident with tectonic tremor and are located within an upper plate fracture network above a subducted seamount after the 2014 Gisborne SSE. I was additionally a coauthor on a study of the microseismicity during the entire OBS deployment (Yarce et al., 2019). We have also performed a brief follow-up study during a similarly located SSE in 2019, and once again find burst-type repeating earthquakes within the upper plate fracture network after the plate boundary SSE. We propose that the SSEs caused fluid migration from over-pressured sediments down-dip of the seamount into the upper plate fracture network, triggering further slow slip on preexisting faults. This is strong evidence that burst-type repeating earthquakes are a promising proxy for transient aseismic slip. These findings also demonstrate the need for offshore seismic observations to detect microseismicity related to shallow, offshore transient aseismic slip. However, although OBS instrumentation is necessary to detect small offshore earthquakes not detected by land seismometers, they generally have low signal-to-noise ratios below ~3 Hz due to oceanographic processes. This is a current limitation in OBS networks.

In Chapter 2 we further demonstrate the utility of near-repeating earthquakes as a proxy for transient aseismic slip. We investigate the occurrence of near-repeating earthquake families during aseismic transients independently detected by borehole strainmeter data but beneath the noise level of continuous Global Positioning System (cGPS) stations in the trifurcation area of the San Jacinto fault zone near Anza in southern California (Shaddox, Schwartz et al., 2021). We find that all moderate-sized earthquakes occurring in this region during the time studied have afterslip signals on borehole strainmeter data and are accompanied by near-repeating earthquakes and elevated seismicity rates. Afterslip geometries defined by the near-repeating earthquake families are consistent with strain change observations. We conclude that families of near-repeating earthquakes, similar to low-frequency earthquakes within tremor, can be useful indicators of aseismic slip transients and can reveal faulting complexities during aseismic slip.

Oceanic internal gravity waves propagate along density stratification within the water column and are ubiquitous. They can propagate thousands of kilometers before breaking in shoaling bathymetry and the ensuing turbulent mixing affects coastal processes and climate feedbacks. Despite their importance, internal waves are intrinsically difficult to detect as they result in only minor amplitude deflection of the sea surface; the need for global detection and long time series of internal waves motivates a search for geophysical detection methods. The pressure coupling of a propagating internal wave with the sloping seafloor provides a potential mechanism to generate seismically observable signals.

In Chapter 3 we use data from the South China Sea where exceptional oceanographic and satellite time series are available for comparison to identify internal wave signals in an onshore passive seismic dataset for the first time (Shaddox, Brodsky et al., 2021). We analyze potential seismic signals on broadband seismometers in the context of corroborating oceanographic and satellite data available near Dongsha Atoll in May-June 2019 and find a promising correlation between long-period transient seismic tilt signals and internal wave arrivals and collisions in oceanic and satellite data. It appears that we have successfully detected oceanic internal waves using a subaerial seismometer. This initial detection suggests that the onshore seismic detection and amplitude determination of oceanic internal waves is possible and can potentially be used to expand the historical record by capitalizing on existing island and coastal seismic stations.

After the completion of the terrestrial study, we acquired data from a broadband OBS station that was deployed offshore of Dongsha Atoll from November 2019 – December 2020, providing a great opportunity to detect and quantify the signal of internal waves on an OBS. We were able to successfully identify internal waves on this OBS, opening up the possibility of a year-long study of internal wave activity near Dongsha Atoll. Further, this may allow us to ultimately remove the long-period “noise” from internal waves on this OBS to improve the detection of microseismicity.

There is important information within the “noise” of geophysical data that can help identify and characterize processes that are difficult to otherwise observe. We have successfully identified offshore aseismic slip on minor faults using burst-type or near-repeating earthquakes on noisy OBS instruments, identified and modeled small aseismic slip transients beneath the noise threshold of cGPS stations with near-repeating earthquakes and borehole strainmeter data, and have performed the first subaerial seismic detection of oceanic internal waves as well as observed internal waves on an OBS at periods that are generally considered “noise” for microseismic investigations. The following dissertation provides in depth details of the methods and implications of these findings.

Dedication

“Death is just another path, one that we all must take” - J.R.R Tolkien

This dissertation is dedicated to the memory of my grandmother, Barbara “Momo” Lewis. Thank you for teaching me how to use a computer before I even started to lose my baby teeth. Thank you for passing down your determination and love of learning. Your (lack of) height and horrible eyesight were also passed down, but that is forgiven. Thank you for introducing me to riddles, Matlock, and Anna Karenina. Thank you for teaching me how to be tough but caring, to be independent, to always do my best, and to help others when I can. Thank you for teaching me that looks don’t matter, but my hands were beautiful (and that’s what matters right?!). Thank you for putting up with three crazy teenage girls in the house (sorry about that New Year’s Eve party!). Finally, thank you for encouraging me to keep going to school “until they kick you out!” I listened, and, well…here we are! I would not have done this without you. I love you, always.

“But the more mental effort he made the clearer he saw that it was undoubtedly so: that he had really forgotten and overlooked one little circumstance in life - that Death would come and end everything, so that it was useless to begin anything, and that there was no help for it. Yes, it was terrible but true.

‘But I am still alive; what am I to do now? What am I to do?’ he said despairingly.” ― Leo Tolstoy, Anna Karenina

Acknowledgements

The text of this dissertation includes reprints of the following previously published material. The co-authors listed in these publications directed and supervised the research which forms the basis for the dissertation.

Chapter 1: Shaddox, H.R. and Schwartz, S.Y., 2019, Subducted seamount diverts shallow slow slip to the forearc of the northern Hikurangi subduction zone, New Zealand: Geology, doi: 10.1130/G45810.1.

Chapter 2: Shaddox, H.R., Schwartz, S.Y., and Bartlow, N. M., 2021, Afterslip and spontaneous aseismic slip on the Anza segment of the San Jacinto fault zone, southern California: Journal of Geophysical Research: Solid Earth. doi: 10.1029/2020JB020460.

Chapter 3: Shaddox, H.R., Brodsky, E.E., Ramp, S.R., and Davis, K.A., 2021, Seismic detection of oceanic internal gravity waves from subaerial seismometers: AGU Advances.

I would like to acknowledge the support and assistance from numerous people and organizations that made this PhD dissertation possible.

First, I would like to thank my primary advisor, Susan Schwartz, for the opportunity to work on such fun and interesting projects. The combination of guidance and support you provided while still letting me maintain independence has allowed me to grow professionally and develop my own research goals. I also want to thank you for encouraging me to pursue field work, research interests, and a life outside of graduate school. I want to thank my secondary advisor, Emily Brodsky,

for going on the internal waves journey with me. Working together on this project has been a wonderful experience that not many advisors would have pursued all the way through. I've learned how to really be a scientist from this experience. Thank you to my committee member Kristen Davis for answering all of my oceanography questions with endless patience and kindness, and for taking me with you to Dongsha. I will never eat cabbage again, but what an experience! Thank you to my committee member Thorne Lay for providing invaluable input on my work and answering any questions I've had throughout the years. A special thank you to the E&PS department office staff, especially Jennifer Fish and Amy Kornberg, for their help and kindness over the years! Thank you so much to Sabrina Dalbesio for making the seismology lab run!

I am very grateful to Prof. Kuo-Fong Ma at Institute of Earth Sciences, Academia Sinica and National Central University in Taiwan for the VDOS and BB01 seismic data and for hosting me in Taipei. I am further grateful to Prof. Shu-Kun Hsu and Dr. Shiou-Ya Wang at National Central University in Taiwan for the BB01 seismic data. I am grateful for the support of Dongsha Atoll Research Station (DARS) and Dongsha Atoll Marine National Park for the fieldwork on Pratas Island. I am further grateful to Prof. Keryea Soong, Yi-Bei Liang, and Ke-Hsien Fu at National Sun Yat-sen University, Taiwan, and to Greg Sinnett and Sarah Merrigan, for their efforts in making the internal waves research possible. I am very grateful to Profs. Sen Jan, Y. J. Yang, and Ming-Huei Chang at National Taiwan University for the use of their deep mooring data for the internal waves study. Thank you to Daniel Sampson for teaching me how to deploy the seismometers on Pratas Island!

I am grateful to Jefferson Yarce and Erin Todd for making their earthquake catalogs available to me prior to publication for the HOBITSS project, to Jenny Nakai and Anne Sheehan for their contributions to earthquake catalog preparation and data collection, and to Kimihiro Mochizuki for providing the OBS data. I wish to further thank Kimihiro Mochizuki for providing the 2019 OBS data and for the rest of the science crew on this project, Yusuke Yamashita, Martha Savage, Laura Wallace, Emily Warren-Smith, and Daniel Barker. Thank you to Katherine Woods for providing the 2019 slow slip event contours prior to publication.

Thank you to the graduate students and postdocs in the seismology lab for all of the help and support over the years, especially Grace Barcheck, Stephanie Taylor, Erin Todd, Thomas Goebel, Shalev Siman Tov, Nadav Wetzler, Travis Alongi, Ricky Garza-Giron, Kelian Dascher-Cousineau, Em Schnorr, Kristina Okamoto, Alba Rodríguez Padilla, and Esteban Chaves. Special thank you to Travis Alongi for reviewing my talks, papers, figures, abstracts, and anything else I’ve sent your way over the years, and for always being down to talk science or listen to me complain. This PhD would not have been the same without you! Special thank you to my intense 4 a.m. research partner, Ricky Garza-Giron. We’ve really pushed each other throughout this roller coaster of a PhD. Advanced seismology was fun! Special thank you to Erin Todd for being an amazing host during my prospective student visit and a great mentor once I arrived.

I want to thank my older sister Amber for always being so understanding, helpful, encouraging, and my best friend. I do not think there is a better human. In the words of the great Keira Knightly (Pride and Prejudice, 2005), “I never saw such a woman. Surely she would be a fearsome thing to behold.” Thank you to Ryan for sending Mountain Dew themed memes at just the right time and always letting me hitch a ride. Though I cannot imagine anyone deserving Amber, you do a pretty good job my dude, and I think you’re great. Oh, and you produce rad kids. Thanks for that.

Thank you to Michelle and Erica for being so supportive, helpful, and just lovely. I’m looking forward to watching Merlin again now that this is finished! Thank you to my dad for his love and support, and for all the Cheesecake Factory dinners. I am 90% cheesecake at this point, and I owe it all to you. Thank you to Yan for being the sweetest person ever and putting up with my Dad and our crazy family with a smile. Thank you to my cousin Ashlyn for always being there, whether for a drink, a panic laptop, or a spontaneous rescue mission. Thank you to Tonya for being the most supportive (through lots of chainsaws), hilarious, and best problem-solving friend a girl could ask for. I wish everyone had a best friend like you!

Chapter 1 - Subducted Seamount Diverts Shallow Slow Slip to the Forearc of the Northern Hikurangi Subduction Margin, New Zealand

1.1 Introduction

Most observational and theoretical studies of slow slip events (SSEs) suggest that they occur in conditionally stable frictional regimes, often interpreted as the transition between velocity-strengthening (i.e., aseismic slip) and velocity-weakening (i.e., stick-slip) zones (Schwartz and Rokosky, 2007; Bürgmann, 2018). Transitional fault zone stability can be influenced by geometrical complexity (Romanet et al., 2018), high pore fluid pressure/low effective stress (Liu and Rice, 2007), or a combination of mechanisms (Saffer and Wallace, 2015). Continuously operating Global Positional System (cGPS) networks have enabled the detection of SSEs at many subduction margins (Schwartz and Rokosky, 2007; Bürgmann, 2018). However, the shallow portion (<15 km) of many subduction zones is typically located far offshore (>50 km), out of the range of cGPS land networks. This presents an observational limitation of shallow SSEs that may be improved using related secondary seismicity, such as tremor and microearthquakes, to infer the location of shallow offshore SSEs.

Transitional frictional properties that promote shallow SSEs may in some cases be a result of subducted oceanic relief. Wang and Bilek (2014) suggest that creep is the predominant mode of motion in areas of rough subducted seafloor. Further, subducted relief has been correlated with SSEs in Costa Rica (Saffer and Wallace, 2015), Nankai (Kodaira et al., 2004), Ecuador (Collot et al., 2017), and New

Zealand (Bell et al., 2010). Wang and Bilek (2011) suggest that subducted seamounts generate a complex fracture network in the upper plate resulting in a heterogeneous and distributed stress field favorable for aseismic creep and microseismicity.

Tectonic tremor and low-frequency earthquakes (LFE) are considered to be the seismic manifestations of the same process as SSEs and have therefore been used to infer the presence and location of both deep (Wech and Creager, 2011) and shallow SSEs (Walter et al., 2013; Annoura et al., 2017). In this paper, we demonstrate the utility of another form of microseismicity, repeating earthquakes, to identify the occurrence of SSEs.

Repeating earthquakes are sequences of events with nearly identical waveforms thought to involve repeated rupture of the same fault asperity (Nadeau and Johnson, 1998) or short-distance triggering of closely spaced asperities (Uchida and Bürgmann, 2019). “Continual-type” repeating earthquakes rupture small plate interface asperities quasi-periodically due to continuous tectonic loading by the surrounding stably sliding plate and have been used to estimate creep rates on both plate boundary transform faults (Nadeau and McEvilly, 1999) and at subduction zones (Igarashi et al., 2003; Uchida et al., 2004). “Burst-type” repeating earthquakes are concentrated in time, have short and irregular repeat intervals, and are often observed during aftershock sequences or afterslip following large magnitude events (Igarashi et al., 2003; Kimura et al., 2006; Templeton et al., 2008; Igarashi, 2010; Yao et al., 2017; Li et al., 2018). These earthquakes frequently have variable magnitude indicating the failure of distinct asperities. In a few instances, migrating sequences of burst-type repeating earthquakes, generally accompanied by an increase in microseismicity, have been interpreted as evidence for SSEs preceding large earthquakes (Kato et al., 2012; Meng et al., 2015). Some studies have also reported burst-type repeating earthquakes triggered by fluid intrusion (Bourouis and Bernard, 2007; Mesimeri and Karakostas, 2018). Thus, rather than tectonic loading, burst-type repeating earthquakes are often associated with aseismic slip or fluid migration. Therefore, sequences of burst-type repeating earthquakes can be indicators of transient slow slip, similar to tectonic tremor, providing another way to indirectly detect shallow SSEs. To this end, we evaluate the spatiotemporal relationship between burst-type repeating earthquakes and the well-recorded M_W 6.8 shallow SSE that occurred offshore of Gisborne, New Zealand in September/October 2014 (Wallace et al., 2016). We utilize data from the Hikurangi Ocean Bottom Investigation of Tremor and Slow Slip (HOBITSS) experiment and focus on the complex relationship between subducted oceanic relief, shallow SSEs and related microseismicity.

1.2 Hikurangi Subduction Margin

New Zealand is located on the boundary of the Pacific and Australian tectonic plates (Figure 1-1). At the North Island, the Hikurangi Plateau, a large igneous province with numerous seamounts, subducts beneath the Australian Plate at a rate of 2-3 cm/yr at southern Hikurangi, increasing to 5-6 cm/yr at the northern Hikurangi margin (Wallace et al., 2004). Shallow (<15 km) SSEs are well documented at the central and northern Hikurangi margin from land cGPS; however, slow slip is not well resolved offshore. These shallow SSEs usually last 1-3 weeks, have moderate moment release (M_W 6.3-6.8), 18-24 month recurrence intervals (Wallace and Beavan, 2010; Wallace et al., 2012), and are associated with tectonic tremor (Todd et al., 2018).

Bell et al. (2010) find a general correlation between the location of SSEs and zones of high-amplitude reflectivity (HRZ) thought to be subducted sediments entrained in front of subducted seamounts that are located directly updip of the HRZs. These locations on the interface in front of the seamounts are suggested to be a site of fluid overpressure (Ellis et al., 2015). Elevated pore fluid pressures promote SSEs by reducing effective stresses (Kodaira et al., 2004; Liu and Rice, 2007; Saffer and Wallace, 2015). These HRZ are broadly correlated with recorded locations of shallow SSEs from 2002-2008 (Bell et al., 2010).

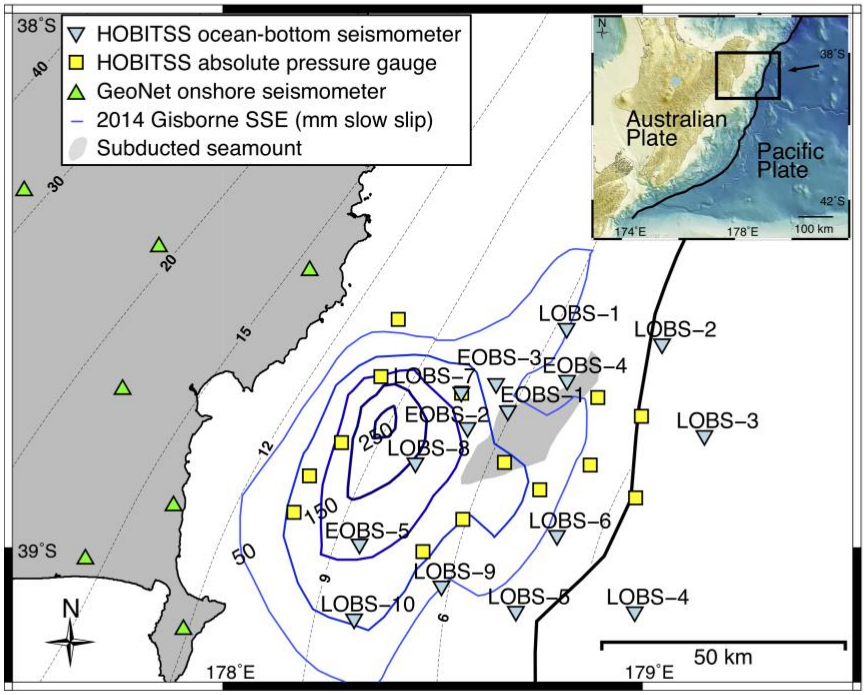

Figure 1-1. Map of Hikurangi Ocean Bottom Investigation of Tremor and Slow Slip (HOBITSS) array. Slow slip contours from Wallace et al., 2016. Slab depth contours (black dashed lines, km) from Williams et al., 2013. SSE, slow slip event.

1.3 Data and methods

The Hikurangi Ocean Bottom Investigation of Tremor and Slow Slip (HOBITSS) experiment deployed 24 absolute pressure gauges (APG) and 15 ocean-bottom seismometers (OBS) offshore of Gisborne, New Zealand from May 2014 - June 2015 above the shallow, episodic, SSEs in the northern Hikurangi subduction margin (Figure 1-1). The HOBITSS network recorded an equivalent M_W 6.8 SSE in September/October 2014 directly beneath the array (Wallace et al., 2016), down-dip of a subducted seamount.

To find repeating earthquakes we perform template matching using EQcorrscan (Chamberlain and Hopp, 2017). We identify suitable templates by starting with two earthquake catalogs (Yarce et al., personal communication, 2018; Todd et al., 2018) compiled using HOBITSS OBS and land GeoNet seismic stations and relocating them where possible using GrowClust, a relative relocation algorithm that uses waveform cross-correlations (Trugman and Shearer, 2017). We use a local 1-D interpretation of the New Zealand 3-D velocity model (Eberhart-Phillips et al., 2010) and relocate 773 out of 2,194 events. We select events (relocated with GrowClust or not) with final locations near the SSE (+/- 5 km of the plate interface) for a total of 123 template events (Figure 1-2, A-1). A cross-correlation coefficient of greater or equal to 0.95 at three or more HOBITSS OBS stations is considered a repeating earthquake candidate. See Appendix A for further method details.

1.4 Results

A total of 29 repeating earthquake families are identified within the SSE area (Figures 1-2, 1-3). Families consist of 2-7 repeating earthquakes. Two families occur before the SSE, north of the main slow slip zone. Two families, one within peak slow slip and one co-located with a subducted seamount, occur during but toward the end of the SSE. The remainder of the families occur days to seven weeks after the reported SSE with a spatial concentration at the subducted seamount (Figures 1-2, 1-3, 1-4, Table A-1) and a weak temporal progression eastward. Although we are unable to determine definitive focal mechanisms, P-wave first motion polarities at several stations for 75% of the events located at the seamount are inconsistent with thrusting on the plate interface. The repeat times within families are short and irregular, ranging from minutes to one month, and events within families have varying magnitudes (Figure 1-3), behaviors consistent with burst-type repeating earthquakes (for now on referred to as repeating earthquakes).

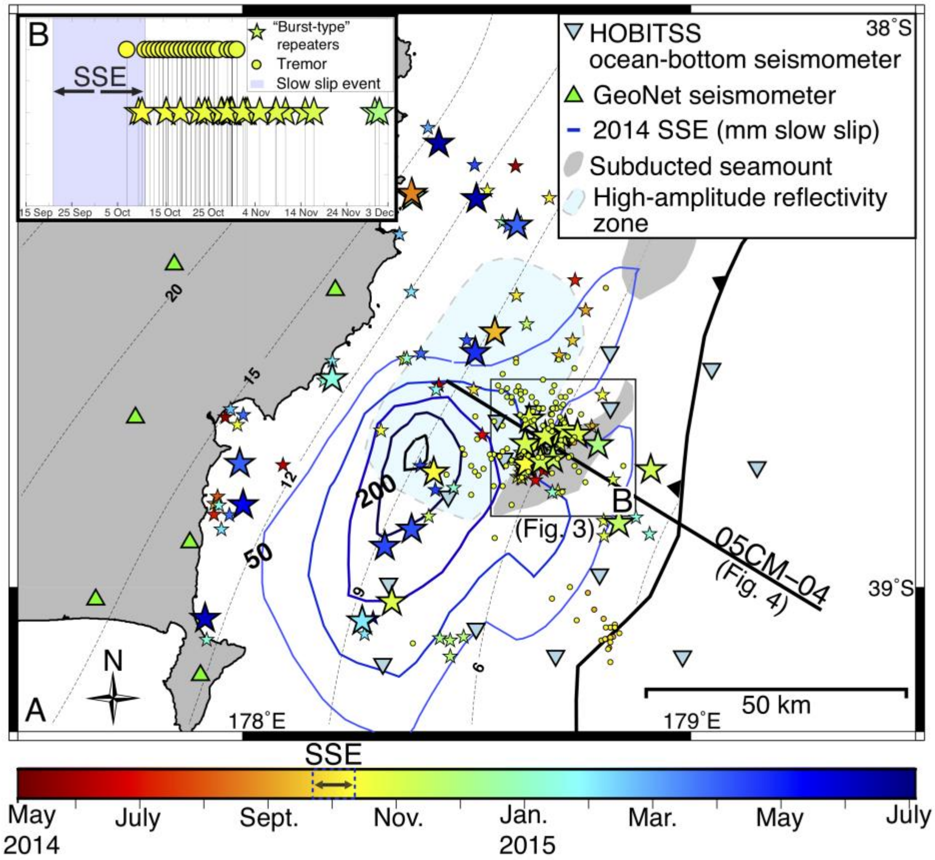

Figure 1-2. Results of repeating earthquake search. A) Map of template events (small stars), repeating earthquake families (large stars), and tectonic tremor (circles, Todd et al., 2018) all colored by time. Slab depth contours (black dashed lines, km) from Williams et al., 2013. B) Tremor and burst-type repeating earthquakes near the subducted seamount plotted for temporal comparison. The September/October 2014 slow slip event (SSE) timing is indicated in both A) and B). 05CM-04—seismic reflection profile of Barker et al. (2018) (see Figure 1-4).

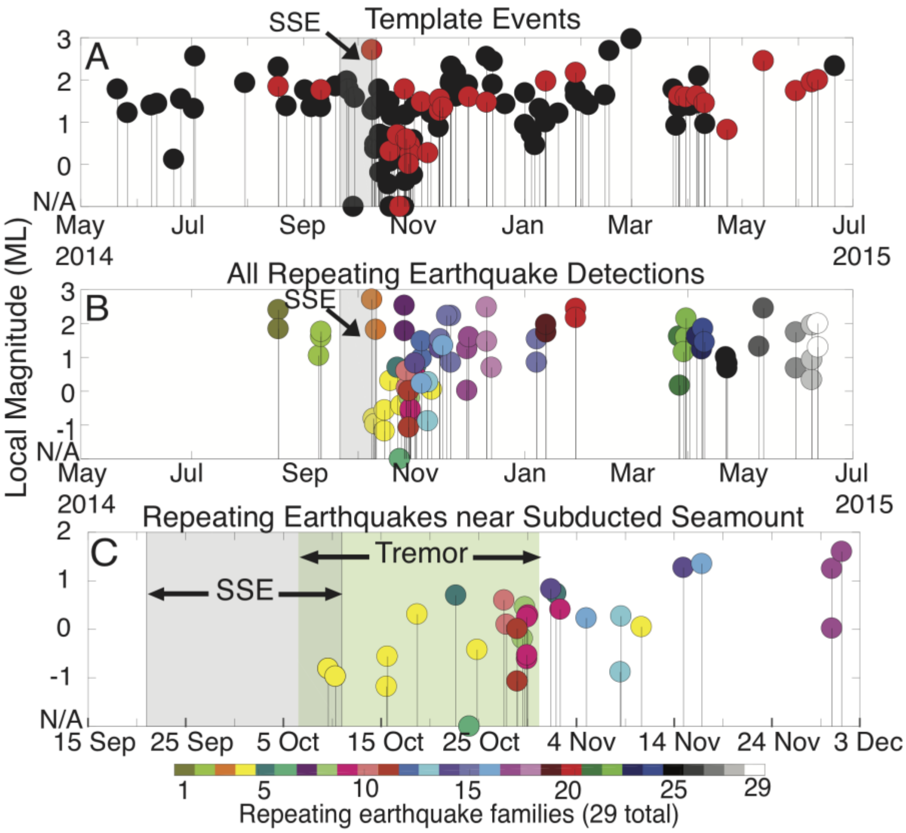

Figure 1-3. Repeating earthquake plots of time vs. local magnitude. A) Template earthquakes (red found a repeating earthquake). B) All repeating earthquake detections. These include the template earthquakes that found repeating earthquakes (shown in red in panel A) and any repeating earthquakes detected by these templates). C) Repeating earthquakes near a subducted seamount (box in Figure 1-2). B) and C) colored by family (see color bar). Slow slip event (SSE) and tremor (within box in Fig 1-2) timing indicated.

1.5 Discussion

Most of the repeating earthquakes co-locate with a subducted seamount, begin at the very end of the SSE, continue for about seven weeks and terminate (Figure 1-3). General background seismicity also increases at the subducted seamount immediately following the SSE (Todd et al., 2018). Todd et al. (2018) detect tectonic tremor at the downdip edge of the subducted seamount that migrates northeastward starting at the very end of the reported SSE and continuing for about 3 weeks following it (Figures 1-2, 1-3, 1-4). These observations of migrating tectonic tremor, an increase in seismicity rate, and burst-type repeating earthquakes have all been associated with strain transients and provide strong evidence of aseismic slip above the subducted seamount.

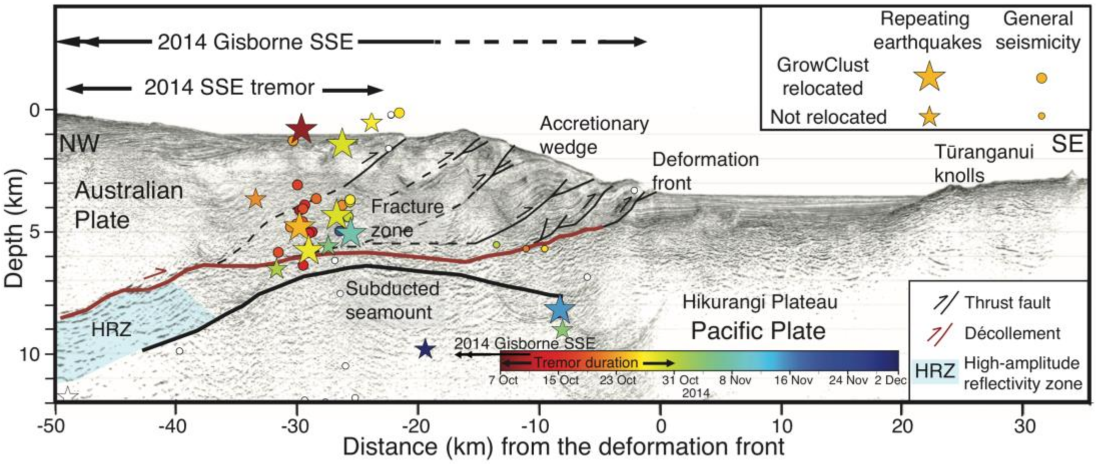

Figure 1-4. Seismic reflection profile 05CM-04 (Figure 1-2) modified from Barker et al., 2018. Repeating earthquakes within 10 km of 05CM-04 shown as stars, colored according to time of first event within the family. All seismicity from May 2014 - June 2015 within 10 km of 05CM-04 shown as circles, also colored by time (events outside of the color bar time period are white). Larger stars and circles have been relocated with GrowClust (Trugman and Shearer, 2017). Slow slip event (SSE) and tremor timing and spatial extent indicated.

Almost all repeating earthquake families at the subducted seamount locate at its downdip edge, within an upper plate fracture network (Figure 1-4) imaged on seismic reflection profile 05CM-04 (Barker et al., 2018), and consistent with the idea that subducted seamounts generate fracture networks and microseismicity (Wang & Bilek, 2011). Repeating earthquake locations on high angle faults in the forearc may explain why most of these events have faulting geometries inconsistent with the shallow décollement. We propose that the repeating earthquakes within the upper plate are driven by aseismic slip on multiple faults within the subducted seamount fracture network, triggered by fluid migration during the main plate interface SSE. Coulomb stress changes following the SSE might also trigger repeating earthquakes on the forearc faults; however, based on the synchronous tremor sequence, the almost two month duration, weak eastward migration and different onset times of repeating earthquake families, we favor fluid migration promoting slow slip on these faults. We propose that during the SSE, the subducted seamount acts as an indenter into the upper plate, breaking low permeability seals in the over-pressurized megathrust (Ellis et al., 2015) and imposing a poro-elastic stress field and pore pressure gradients that drive fluids from sediments entrained with seamount subduction (Bell et al., 2010) through the overlying plate at diffusional timescales (Nakajima and Uchida, 2018). Fluids eventually migrate from the plate interface HRZ into the fracture network and trigger aseismic slip on several faults, resulting in the burst-type repeating earthquakes at seismic asperities on preexisting faults. Slow slip after the main SSE at the subducted seamount is not evident on the APGs - slow slip on multiple faults is likely below the detection threshold (~50 mm) – but coastal cGPS stations possibly detect slow slip in the region through October (Wallace, L., personal communication, 2019).

Repeating earthquakes have previously been associated with deformation zones and fluid intrusion. Kimura et al. (2006) report burst-type repeating earthquakes off the plate interface within a collision zone (possibly similar to the subducted seamount fracture network) to the west of the Kanto District, Japan. Mesimeri and Karakostas (2018) attribute the presence of shallow (5-9 km) burst-type repeating earthquakes in the western Corinth Gulf, Greece to fluid intrusion. Further, aseismic slip triggered by hydraulic stimulation has been observed in multiple induced seismicity experiments, based on families of repeating earthquakes, modeling, laboratory experiments, and direct deformation measurements (Bourouis and Bernard, 2007; Zoback et al., 2012; Guglielmi et al., 2015). These observations indicate that aseismic slip related to fluid pressure perturbations is not only common on large plate interface faults, but on small scale faults such as those found in the fracture network surrounding the subducted seamount.

1.6 Conclusions

The burst-type repeating earthquake families at the subducted seamount after the 2014 Gisborne SSE are likely caused by slow slip on an upper plate fracture network above the subducted seamount. We argue that the 2014 Gisborne SSE caused fluid migration from over-pressured sediments down-dip of the seamount (the HRZ) into the upper plate fracture network, triggering further slow slip on preexisting faults. This resulted in both the observed burst-type repeating earthquakes and tectonic tremor around the subducted seamount.

The complicated interplay of seismic and aseismic slip in this region is likely due to the subducted seamount. The fluid-enriched sediments favorable for quasi-periodic shallow slow slip were entrained with seamount subduction, and the upper plate fracture network above the subducted seamount results in a complicated stress distribution and complex modes of slip. Thus, seamount subduction appears to be a major influence on the mechanics of shallow slow slip and microseismicity at the northern Hikurangi margin. We postulate that burst-type repeating earthquakes may be common seismic indicators of shallow slow sip in other regions of subducted oceanic relief. Since most documented shallow SSEs to date are correlated with rough subducted seafloor, burst-type repeating earthquakes are a promising proxy for shallow SSEs, and for identifying fracture networks that have developed in response to seamount subduction.

1.7 Brief follow-up study during the 2019 slow slip event

1.7.1. Purpose, data, and methods

The same five EOBS stations deployed in the HOBITSS experiment (Figure 1-1) were deployed again from October 2018 – November 2019 near the subducted seamount (Figure 1-5). A SSE occurred offshore of Gisborne, New Zealand in late March – mid April 2019 in a similar location as the 2014 SSE (Woods et al., 2020) (Figure 1-6). This presents an excellent opportunity to perform a follow-up study and evaluate whether the burst-type repeating earthquake activity following the 2014 SSE was anomalous.

To evaluate the potential relationship between burst-type repeating earthquakes and the 2019 SSE we first created a catalog of earthquakes from March 1 – May 31, 2019. Earthquakes were manually detected by picking P-wave and S-wave (where possible) arrivals at the 5 EOBS stations and available land GeoNet seismic stations. Earthquake hypocenters were found using Antelope’s *dbgenloc* algorithm and a local 1-D interpretation of the New Zealand 3-D velocity model (Eberhart-Phillips et al., 2010) centered offshore at -38.8361/178.4672.

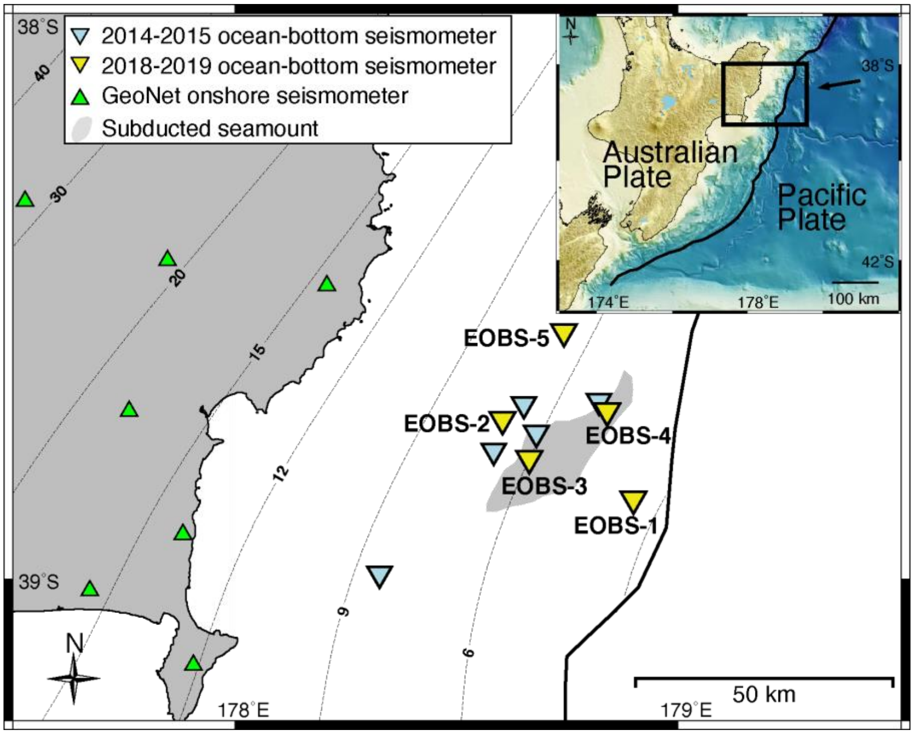

Figure 1-5. Comparative map of the 2014-2015 and 2018-2019 ocean-bottom seismometer deployments. The 2014-2015 and 2018-2019 ocean-bottom seismometers are shown as light blue and yellow inverted triangles, respectively. Slab depth contours (black dashed lines, km) from Williams et al., 2013. The 2018-2019 stations are labeled.

To find burst-type repeating earthquakes potentially related to the 2019 SSE occurring in the upper plate fracture network above the subducted seamount we perform template matching similar to the 2014 study (section 1.3) using EQcorrscan (Chamberlain and Hopp, 2017). Since earthquake depths from the 1-D velocity model are poorly constrained, we selected events near the subducted seamount shallower than 20 km depth as templates, for a total of 1,245 template events (Figure 1-6). Templates are cut to five-second-long windows around the P-phase arrival (0.15 second pre-pick). These templates often include the S-phase arrivals. Template events are then filtered using a 3-10 Hz zero-phase band-pass filter to minimize oceanic noise. Template matching is then performed on the vertical components from March 1 – May 31, 2019. A cross-correlation coefficient of greater or equal to 0.95 at three or more EOBS stations is considered a burst-type repeating earthquake. We compute local magnitudes for template events using the *Mlrichter* Antelope package with a $\log A_0$ attenuation relationship for New Zealand earthquakes derived by Ristau et al. (2016).

1.7.2. Results

We find 84 burst-type repeating earthquakes within 42 families. Most of these families are concentrated at the down-dip edge of the subducted seamount toward the end and after the 2019 SSE (Figures 1-6, 1-7). There is also a clear increase in general seismicity near the subducted seamount after the 2019 SSE (Figure 1-7).

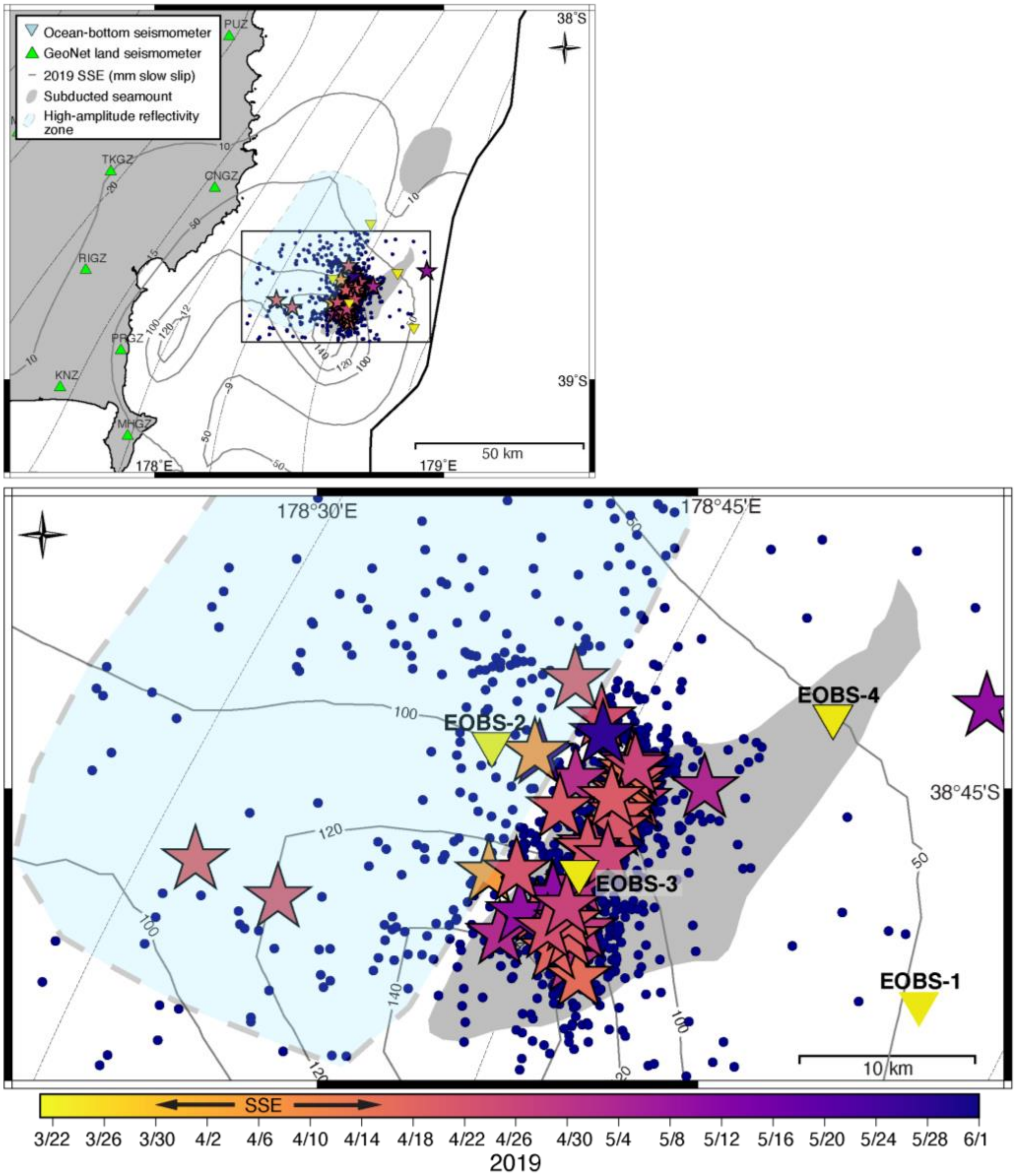

Figure 1-6. Map of burst-type repeating earthquakes related to the 2019 slow slip event. Template earthquakes are shown as dark blue circles and burst-type repeating earthquakes are shown as stars, colored according to time. Slow slip contours (Woods et al., 2020) shown as grey lines. Slab depth contours (black dashed lines, km) from Williams et al., 2013. Bottom: Zoom in of burst-type repeating earthquakes near the subducted seamount in the black box in the top panel.

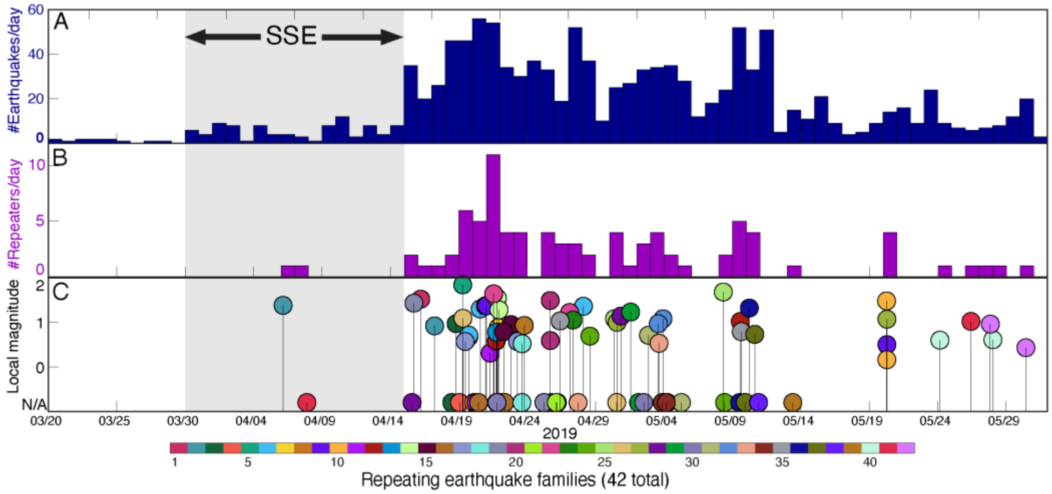

Figure 1-7. Timing of seismicity and burst-type repeating earthquakes related to the 2019 slow slip event. A) Daily seismicity rate at <20 km depth near the subducted seamount (template earthquakes). B) Daily burst-type repeating earthquake rate near the subducted seamount. C) Burst-type repeating earthquake families near the subducted seamount plotted as time vs local magnitude, colored according to family. Timing of the 2019 slow slip event (SSE) shown in grey.

1.7.3. Discussion and conclusions

The distribution of peak slow slip for the 2014 (Figure 1-2; Wallace et al., 2016) and 2019 (Figure 1-7; Woods et al., 2020) SSEs is different. Peak slow slip for the 2014 SSE is located west-southwest of the subducted seamount. For the 2019 SSE, one patch of peak slow slip is located at the southern end of the subducted seamount. Despite these differences, the seismicity and burst-type repeating earthquake patterns are similar. Following both plate boundary SSEs, seismicity and burst-type repeating earthquakes are concentrated at the down-dip edge of the subducted seamount. However, the intensity of seismicity is greater following the 2019 SSE (Figure 1-8). Additional work should be performed to locate the burst-type repeating earthquakes and seismicity with a 3-D velocity model to try to delineate upper plate faults. Still, this initial study demonstrates that the burst-type repeating earthquake activity following the 2014 SSE is not anomalous.

Both the 2014 and 2019 Gisborne SSEs likely caused migration of fluids from over-pressurized fluid-enriched sediments up-dip toward the subducted seamount, triggering further slow slip on minor faults in the upper plate fracture network above the seamount. This is further evidence that seamount subduction is a major influence on the mechanics of shallow slow slip and microseismicity at the northern Hikurangi margin.

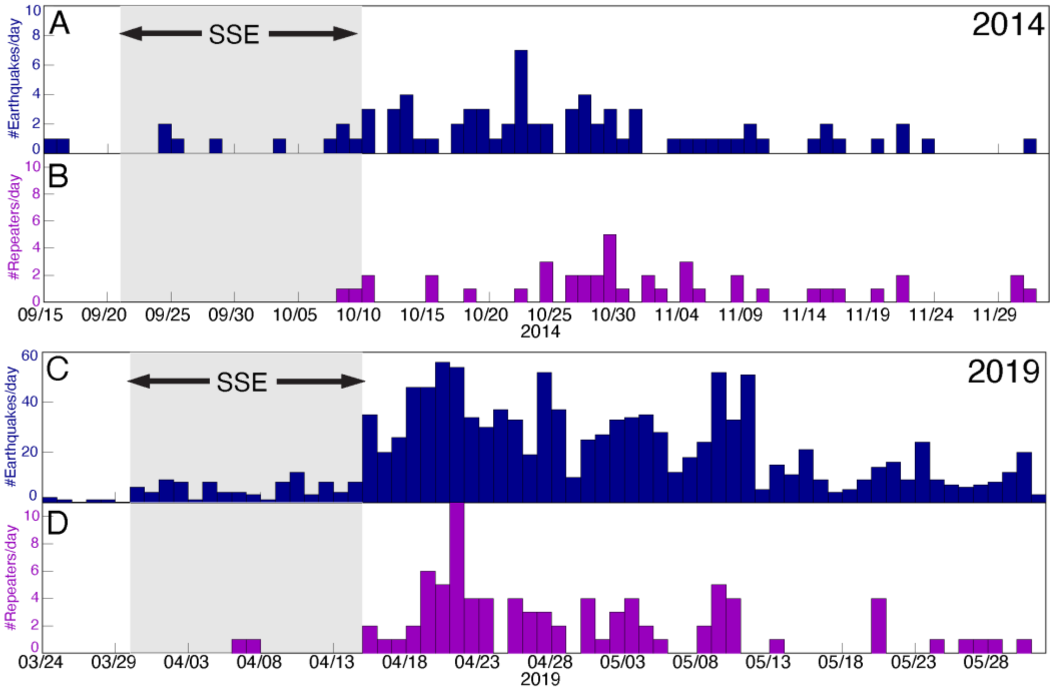

Figure 1-8. Comparison of seismicity and burst-type repeating earthquake rates related to the 2014 and 2019 slow slip events. A) Daily seismicity rate at <20 km depth near the subducted seamount for the 2014 slow slip event (SSE). B) Daily burst-type repeating earthquake rate near the subducted seamount for the 2014 SSE. C) Daily seismicity rate at <20 km depth near the subducted seamount for the 2019 SSE. D) Daily burst-type repeating earthquake rate near the subducted seamount for the 2019 SSE. Timing of the 2014 (A, B) and 2019 (C, D) SSEs shown in grey.

Chapter 2 - Afterslip and Spontaneous Aseismic Slip on the Anza Segment of the San Jacinto Fault Zone, Southern California

2.1 Introduction

Fault slip occurs as a spectrum, ranging from stably sliding (i.e., aseismic creep) to rapid seismic ruptures (i.e., earthquakes/stick-slip events). Within the fault slip spectrum are transient events of slow, aseismic slip that occur in conditionally stable frictional regimes, often interpreted as the transition between velocity-strengthening (aseismic creep) and velocity-weakening (stick-slip) zones (Bürgmann, 2018; Scholz, 1998; Schwartz & Rokosky, 2007). Understanding the interplay of seismic and aseismic slip is key in seismic hazard evaluation since this can determine the largest earthquake a fault can host. Transient aseismic slip can be spontaneous, quasi-periodic events commonly referred to as slow slip events (Beroza & Ide, 2011; Dragert et al., 2001; Peng & Gomberg, 2010; Schwartz & Rokosky, 2007), which may include precursory slow slip leading up to a large earthquake (Ito et al., 2013; Kato et al., 2012; Kato & Nakagawa, 2014; Ruiz et al., 2014). It may also be postseismic afterslip relieving static coseismic stress increases aseismically adjacent to an earthquake rupture (Avouac, 2015 and references therein), or aseismic slip triggered by static or dynamic stress changes from earthquakes not adjacent to ruptures (Araki et al., 2017; Taira et al., 2014; Tymofyeyeva et al., 2019; Wallace et al., 2017; Wei et al., 2015).

Tectonic tremor is considered to be the seismic manifestation of the same process as slow slip and has therefore been used to infer the presence and location of slow slip where it occurs (Annoura et al., 2017; Bartlow et al., 2011; Shelly et al., 2007; Walter et al., 2013; Wech & Creager, 2011). Tectonic tremor is likely made up of repeating low-frequency earthquakes (LFEs) that are driven to failure by slow slip on the surrounding fault (Shelly et al., 2006). LFEs are grouped into families that repeatedly rupture a small patch (~1 km^2)(Sweet et al., 2014), with individual LFEs within a family having variable sizes and likely rupturing multiple (3-10) sub-patches within the larger family patch (Chestler & Creager, 2017b, 2017a). Similarly, repeating "regular" earthquakes, often referred to as "characteristic" (Nadeau & McEvilly, 1999) or "continual-type" (Igarashi et al., 2003), are events with nearly identical waveforms driven to failure quasi-periodically by continuous tectonic loading (i.e., aseismic creep) on the surrounding fault and have therefore been used to estimate creep rates on plate boundary faults (Chen et al., 2008; Igarashi et al., 2003; Nadeau & McEvilly, 1999; Uchida et al., 2004). However, there are important differences; repeating earthquakes have a constant magnitude, regular repeat interval, and are thought to repeatedly rupture the exact same fault asperity (Nadeau & Johnson, 1998; Nadeau & McEvilly, 1999; Uchida & Bürgmann, 2019).

Sequences of nearly identical events have also been observed in short-term (minutes to months), irregularly-repeating bursts (Igarashi, 2010; Igarashi et al., 2003; Kimura et al., 2006; Lengliné & Marsan, 2009; Li et al., 2018; Nadeau et al., 1995; Templeton et al., 2008; Waldhauser & Ellsworth, 2002; Yao et al., 2017). These highly correlated events have been referred to as short-term (Lengliné & Marsan, 2009; Nadeau et al., 1995) or "burst-type" (Igarashi, 2010; Igarashi et al., 2003; Kimura et al., 2006; Shaddox & Schwartz, 2019; Templeton et al., 2008) repeating earthquakes and have been observed during aftershock sequences or afterslip following large magnitude events (Igarashi, 2010; Igarashi et al., 2003; Kimura et al., 2006; Li et al., 2018; Templeton et al., 2008; Yao et al., 2017). These short-term repeating earthquakes have also been observed during migrating slow slip episodes preceding large earthquakes (Kato et al., 2012; Meng et al., 2015).

Nadeau et al. (1995) first identified families or clusters of short-term repeating earthquakes with aperiodic repeat intervals of minutes to days near characteristic repeating earthquake families on the San Andreas fault near Parkfield, California. Based on hypocenter locations they estimated that short-term repeating earthquakes within clusters were located 100-200 m apart. They proposed that these events were occurring on distinct asperities, triggered either by rapid, transient aseismic slip on the surrounding fault or short-distance triggering of closely-spaced asperities. Lengliné & Marsan (2009) also identified short-term repeating earthquakes near Parkfield and found that the locations of events within families were not as tightly clustered as characteristic repeating earthquake families. They proposed that short-term repeating earthquakes could be due to partial rupture of the same asperity after the preceding earthquake did not rupture the entire asperity, or events within clusters rupturing very near but distinct asperities. Shaddox & Schwartz (2019) found these short-term repeating earthquakes at the northern Hikurangi margin coincident with tremor on an upper-plate fracture network above a subducted seamount after a M_W 6.8 offshore slow slip event. Based on the colocation with tremor, they concluded that the short-term repeating earthquake families were driven by transient aseismic slip, possibly triggered by fluids migrating from over-pressured sediments down-dip of the seamount into the upper plate fracture network during the interplate slow slip event.

Short-term repeating earthquakes may rupture closely-spaced or partially overlapping asperities and are different from characteristic repeating earthquakes in source (i.e., repeated rupture of exact same asperity) and therefore mechanism (i.e., loading by steady aseismic creep). Instead of creep, short-term repeating earthquakes have been associated with transient aseismic slip, including afterslip (Igarashi, 2010; Igarashi et al., 2003; Kimura et al., 2006; Li et al., 2018; Templeton et al., 2008; Yao et al., 2017), precursory slow slip (Kato et al., 2012; Meng et al., 2015), and aseismic slip triggered by fluid migration (Shaddox & Schwartz, 2019). In this study, we refer to families of closely spaced earthquakes (within 200 m) as “near-repeating” earthquakes, owing to their highly-correlated waveforms, aperiodic repeat intervals and variable magnitudes, to make the distinction from characteristic repeating earthquakes and previously identified short-term/burst-type repeating earthquakes that likely rupture the same asperity or partially overlapping asperities. We propose that sequences of near-repeating earthquake families concentrated in time and space are more similar in source and mechanism to clusters of LFE families: near-repeating earthquakes likely rupture asperities within family patches and are driven to failure by transient aseismic slip on the surrounding fault. However, unlike LFEs, near-repeating earthquakes are not devoid of high-frequency energy. Some prior studies have successfully used tremor and LFE detections as timing and location indicators to guide the identification of aseismic transient signals in GNSS (Bartlow, 2020; Frank et al., 2015; Rousset et al., 2019) and strainmeter data (Delbridge et al., 2020; Hawthorne et al., 2016a). We propose that similar to LFEs, near-repeating earthquakes can be useful spatiotemporal seismic indicators of transient aseismic slip that can be combined with geodetic observations to model aseismic slip transients.

To demonstrate the utility of near-repeating earthquakes as a proxy for transient aseismic slip, we investigate the occurrence of near-repeating earthquake families during aseismic transients independently detected by borehole strainmeter data that are too small to be robustly detected using GNSS data in the trifurcation area of the San Jacinto fault zone near Anza in southern California (Figure 1-1). We find that all 3 $M_W > 4.5$ earthquakes occurring in this region during the time period studied (2010-2016) have afterslip signals on borehole strainmeter data and are accompanied by near-repeating earthquakes and elevated seismicity rates. We use the location of near-repeating earthquakes to infer the geometry of faults hosting afterslip and find that afterslip occurs at depths between 6-14 km, on all three major strands of the San Jacinto fault zone, and on several different fault segments both on and off the mainshock fault. A local M_W 4.9 earthquake occurred in April 2020, at the conclusion of our study, and we use this event to validate our hypothesis that afterslip accompanied by near-repeating earthquakes follows all moderate magnitude earthquakes in this region. We also identify and locate a spontaneous aseismic slip transient in 2015 using near-repeating earthquakes and a strain signal on the nearest borehole strainmeter station. This demonstrates that aseismic slip in this region is not restricted to afterslip and that near-repeating earthquakes can be generated by spontaneous as well as triggered aseismic slip (i.e., afterslip). We conclude that like LFEs, near-repeating earthquakes can be a useful proxy for aseismic slip transients. This is particularly useful in regions that are not tremorgenic. In addition, detecting and analyzing near-repeating earthquakes following local moderate-sized events can provide insight into whether aseismic slip occurs on main fault strands or on splay faults within damage zones.

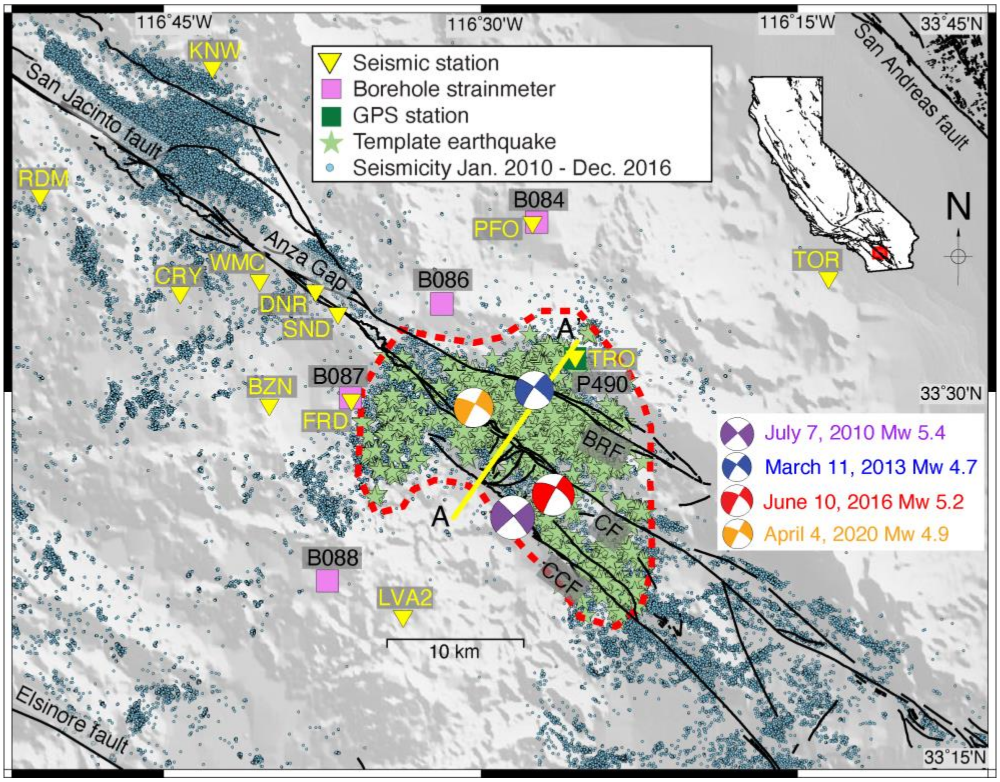

Figure 2-1. Seismicity map of the trifurcation area of the San Jacinto fault zone near Anza in southern California. Seismicity from the Quake Template Matching (QTM) catalog from Ross et al., (2019). Focal mechanisms of the M_W 5.4 July 7, 2010 (purple, M_W 4.7 March 11, 2013 (blue), M_W 5.2 June 10, 2016 (red), and M_W 4.9 April 4, 2020 (orange) earthquakes are shown. The study region is outlined by the red dashed line; late Quaternary faults from the U.S. Geological Survey and California Geological Survey are shown as black lines. CCF – Coyote Creek fault; CF – Clark fault; BRF – Buck Ridge fault. Profile of near-repeating earthquakes and seismicity along cross-section A-A' following the four moderate-sized earthquakes is shown in Figure 2-8.

2.2 Anza Segment of the San Jacinto Fault Zone

The southern San Andreas fault system consists of three main faults: the San Andreas fault (SAF), the San Jacinto fault (SJF), and the Elsinore fault, with a total of 35–40 mm/year of right-lateral strike-slip motion accommodated across these faults (Bennett et al., 1996). The SJF is the most seismically active fault in southern California, with slip of approximately 19 mm/year (Lindsey & Fialko, 2013). The Anza seismic gap is the 20 km locked section of the SJF centered near Anza that is thought to be capable of a large (~M_W 7) earthquake (Sanders & Kanamori, 1984). Determining the locking depth of the SJF in this region is important in constraining the size of a potential large earthquake in the Anza seismic gap, and future earthquake rupture of the Anza seismic gap is likely to start on either end of the gap zone where stress buildup is greatest, thus it is important to understand fault behavior just outside of the Anza seismic gap. Southeast of the Anza seismic gap in the trifurcation area the SJF splays into three semi-parallel strands: the Coyote Creek fault (CCF), the Clark fault (CF), and the Buck Ridge fault (BRF) (Figure 2-1). From 2000-2016 12 $M_W \geq 4$ local earthquakes have occurred in the trifurcation area. Three $M_W > 4.5$ earthquakes occurred in the trifurcation area during our study period (2010-2016): the July 7, 2010 M_W 5.4 Collins Valley earthquake on the Coyote Creek fault, the March 11, 2013 M_W 4.7 earthquake on the Buck Ridge fault, and the June 10, 2016 M_W 5.2 Borrego Springs earthquake on the Clark faut (Figure 2-1). In addition, a M_W 4.9 earthquake occurred toward the conclusion of this study on April 4, 2020 (Figure 2-1).

Seismicity in the trifurcation area of the SJF extends to 17 km depth (Ross et al., 2019), inconsistent with the geodetic locking depth of 10.4 +/- 1.3 km (Lindsey et al., 2014). One possible explanation for the disparity between the seismic and geodetic locking depths is a zone of deep creep driving deep microseismicity beneath the locked upper 10 km (Wdowinski, 2009). However, characteristic repeating earthquakes have not been commonly identified in this region as expected in a primarily velocity strengthening deep creep zone containing distinct velocity weakening seismic asperities (Jiang & Fialko, 2016). Another explanation for the shallow geodetic locking depth is the existence of a transitional region with spatially heterogeneous frictional properties, resulting in ubiquitous but intermittent aseismic slip transients below the locked zone (Jiang & Fialko, 2016; Wei et al., 2013). In this scenario, characteristic repeating earthquakes would not be expected, although near-repeating earthquakes might occur. Anomalously large aftershock zones with logarithmic expansion rates following deep (>12 km) M_W > 4 earthquakes in the study area have been interpreted as deep afterslip (Meng & Peng, 2016) and provide additional evidence for deep, intermittent aseismic slip transients. Further, following the 2010 and 2016 local earthquakes, the magnitudes of the largest aftershocks were smaller than expected; in fact, the largest aftershock of nearly all the magnitude M_W>4.5 earthquakes in this region were ~M 3.5, smaller than expected (Kilb & Vernon, 2020). This is possibly due to the complexity of the fault system limiting the maximum magnitude of the largest aftershock (Kilb & Vernon, 2020). However, smaller than expected aftershocks could also be consistent with seismicity driven by afterslip. Another interpretation for the deep microseismicity that does not require aseismic slip is that it is mostly caused by off-fault activity in broad and deep damage zones between the primary SJF strands (Cheng et al., 2018; Ross, Hauksson, et al., 2017).

Inbal et al. (2017) found deep, triggered aseismic slip in the study region following the remote April 4, 2010 M_W 7.2 El Mayor-Cucapah earthquake and the local July 7, 2010 M_W 5.4 Collins Valley earthquake using Plate Boundary Observatory (PBO) borehole strainmeter (BSM) data and local microseismicity. The triggered aseismic slip transient following the El Mayor-Cucapah earthquake lasted up to 94 days and likely triggered two local earthquakes on June 13, 2010 (M_W 4.45 and M_W 4.2), followed by the M_W 5.4 Collins Valley local earthquake on July 7, 2010. From their joint microseismicity and BSM inversion with rate and state friction they conclude that aseismic slip and seismicity are not coplanar, but deep (>10 km) aseismic slip on the main fault strand drives off-fault seismicity at shallower depth. We find these transients to be associated with both increased seismicity which may be outside of the plane of aseismic slip as concluded by Inbal et al. (2017), and near-repeating earthquakes which are thought to be driven by surrounding aseismic slip. The intermittent and distributed nature of the creep provides strong support for a model with a spatially heterogeneous transition from locked to freely slipping between 6-14 km below the SJF trifurcation region.

2.3 Detecting and locating transient aseismic slip

To demonstrate the utility of near-repeating earthquakes as a proxy for transient aseismic slip, we combine observations of near-repeating earthquake families, seismicity patterns, and strain changes across BSM stations. The instrumentation available near the Anza segment of the SJF enables the combination of these observations. Four BSM stations border the study area to the west, 12 consistently operational seismometers from the Anza Seismic Network and Southern California Seismic Network are within 30 km of the study area, and an excellent seismic catalog covers this region (Figure 2-1; Ross et al., 2019). The 2010-2016 study period was selected to evaluate three moderate-sized (M_W>4.5) local earthquakes that occurred since the BSMs were installed (2006-2007) and had adequate settling time. During this time a high-resolution seismicity catalog was available. The specific study area within the greater region of the SJF was chosen based on the concentration of microseismicity.

2.3.1 Near-repeating earthquakes and general seismicity

We evaluate seismicity patterns using the Quake Template Matching (QTM) catalog (Ross et al., 2019) during our study period: January 1, 2010 – December 31, 2016. The magnitude of completeness of the QTM catalog is around 0.3. Seismicity in the study area during this period is bimodally concentrated around 8 km and 10 km depth, and drops off significantly at 14.6 km but extends down to 17 km depth (Figure B-1, Appendix B).

We perform template matching to identify near-repeating earthquakes. We select template earthquakes from the QTM catalog with a local magnitude ≥1.5 (Figure 2-1) for a total of 1,103 template earthquakes. We chose template earthquakes with local magnitude ≥1.5 based on the average spectral amplitudes for these events generally exceeding noise levels above 3 Hz (Figure B-2). Depths of the template events are concentrated between 6 and 14 km. The template earthquakes are cut to five-second long windows around the P-phase arrival (0.15-second pre-pick) and mostly include the S-phase arrivals. Template events are then filtered using a 3-10 Hz zero-phase band-pass filter. This band-pass is selected due to noise below 3 Hz (Figure B-2), and to detect near-repeating earthquakes that have variable magnitudes (~M0 – M3) and therefore different frequency content. This is particularly important because near-repeating earthquakes are likely closely-spaced (<200 m) or partially overlapping asperities, rather than the exact same asperity. We therefore chose parameters to maximize the detection of closely-spaced events. We performed template matching in higher frequency bands and find fewer near-repeating earthquake families with more uniform magnitudes, as expected. However, the spatiotemporal distribution of near-repeating earthquakes in all frequency bands is similar and does not affect our interpretations (see Appendix B for further discussion of chosen parameters). Template matching is performed from January 1, 2010 through December 31, 2016 using the open-source Python package EQcorrscan (Chamberlain et al., 2017) on the vertical components of the seismometers. The procedure is similar to that outlined in Shaddox and Schwartz (2019). We use 10 seismic stations from the Anza seismic network (AZ) and 2 from the Southern California Seismic Network (SCSN). Templates that yield a cross-correlation coefficient 0.90 at 4-12 stations (average of 9 stations used) are considered near-repeating earthquakes.

A sample near-repeating earthquake detection seismogram is included in Figure B-3, and a list of near-repeating earthquakes found are listed in Tables B-2 and B-3. These are near-repeating earthquakes with high cross-correlation coefficients in the band-pass selected (3-10 Hz). Generally, events with this high level of similarity are located within one-quarter of the dominant wavelength (Geller & Mueller, 1980). The dominant frequency in this band-pass is the 10 Hz cut-off frequency used. Assuming a P-wave velocity potentially ranging from 4-6 km/s, the dominant wavelength is 400-600 m. Thus, any potential near-repeating earthquake pairs detected are likely separated by less than 100-150 m. Further, most of the near-repeating earthquakes within families were located in the QTM catalog and have locations 130 m or less from each other. Based on the local magnitudes of near-repeating earthquakes ranging from 0.09 to 3.18, with an average magnitude of 1.3, near-repeating earthquake pairs within 130 m of each other may be completely overlapping, partially overlapping, or closely spaced seismic asperities. This is consistent with our definition of near-repeating events as potentially closely spaced (<200 m) rather than completely overlapping asperities. Focal mechanisms for most of the near-repeating earthquakes within families were obtained from the Yang et al. (2012) catalog.

2.3.2 Borehole strainmeter data

We use 5-minute level 2 processed strain data calibrated using earth tides (Hodgkinson et al., 2013) from the PBO network for four BSM stations located west of the study region (Figure 2-1) to identify strain transient signals. The strain gauge data is converted to three strain components: differential (pure) shear strain, areal strain, and engineering (simple) shear strain. Then the strain components are corrected for tidal effects, earthquake offsets and other large static offsets, long-term borehole trends from settling, and barometric pressure using the level 2 corrections provided by PBO. The trend from the prior month is first removed, and then strain offsets were manually selected based on best estimates of stable offsets. The expectation of a logarithmic dependence on time as well as the timing from near-repeating earthquake families were used to help guide the time windows of strain offsets.

2.3.3 Afterslip distribution

To determine the slip direction and average magnitude of afterslip following a moderate-sized local earthquake we approximate fault slip using a rectangular Okada dislocation model (Beauducel, 2020; Okada, 1985). We identify the orientation and dimension (strike, dip, center) of the afterslip fault plane using the location of the majority of near-repeating earthquake families, and perform a grid search using the three strain components from the BSM stations (Figure 2-1) and minimum mean squared error to determine the optimal fault length, width (in the dip direction), slip and rake. Since we assume a uniform half-space model, our modeled dislocation depth and slip amplitude may be biased. More compliant shallow layers will generally lead to our estimated depths being too shallow and slip amplitudes being too large (Savage, 1998; Segall, 2010). A near-fault compliant zone could amplify these biases if the BSMs are inside the compliant zone, or have the opposite biases if the BSMs are outside the compliant zone (Segall, 2010). Depth biases are likely in the range of 5 – 20% (Savage, 1998). It should also be noted that since we are modeling afterslip on one fault plane, if afterslip is simultaneously occurring on multiple minor faults that are not oriented similarly to the modeled fault plane, the moment will likely be underestimated.

Figure 2-2. Seismicity, near-repeating earthquakes, and borehole strainmeter (BSM) data in the study region from 2010-2016. (a) Daily seismicity rates from the QTM catalog. (b) Near-repeating earthquakes in 1-week bins. (c) Corrected level 2 5-minute microstrain data from BSM stations B084, B086, B087, and B088 (Figure 2-1) shown in magenta. Two-week running average of corrected strain shown in black. Differential shear strain (εEE-εNN top), areal strain (εEE+εNN; middle) and engineering shear strain (2εNE; bottom) components included. Extension is positive. Triggered (including afterslip) and spontaneous aseismic slip transient times are highlighted in grey and light orange, respectively. Focal mechanisms of the 3 moderate-sized earthquakes from the SCSN are indicated and color coded to match their locations on the map in Figure 2-1.

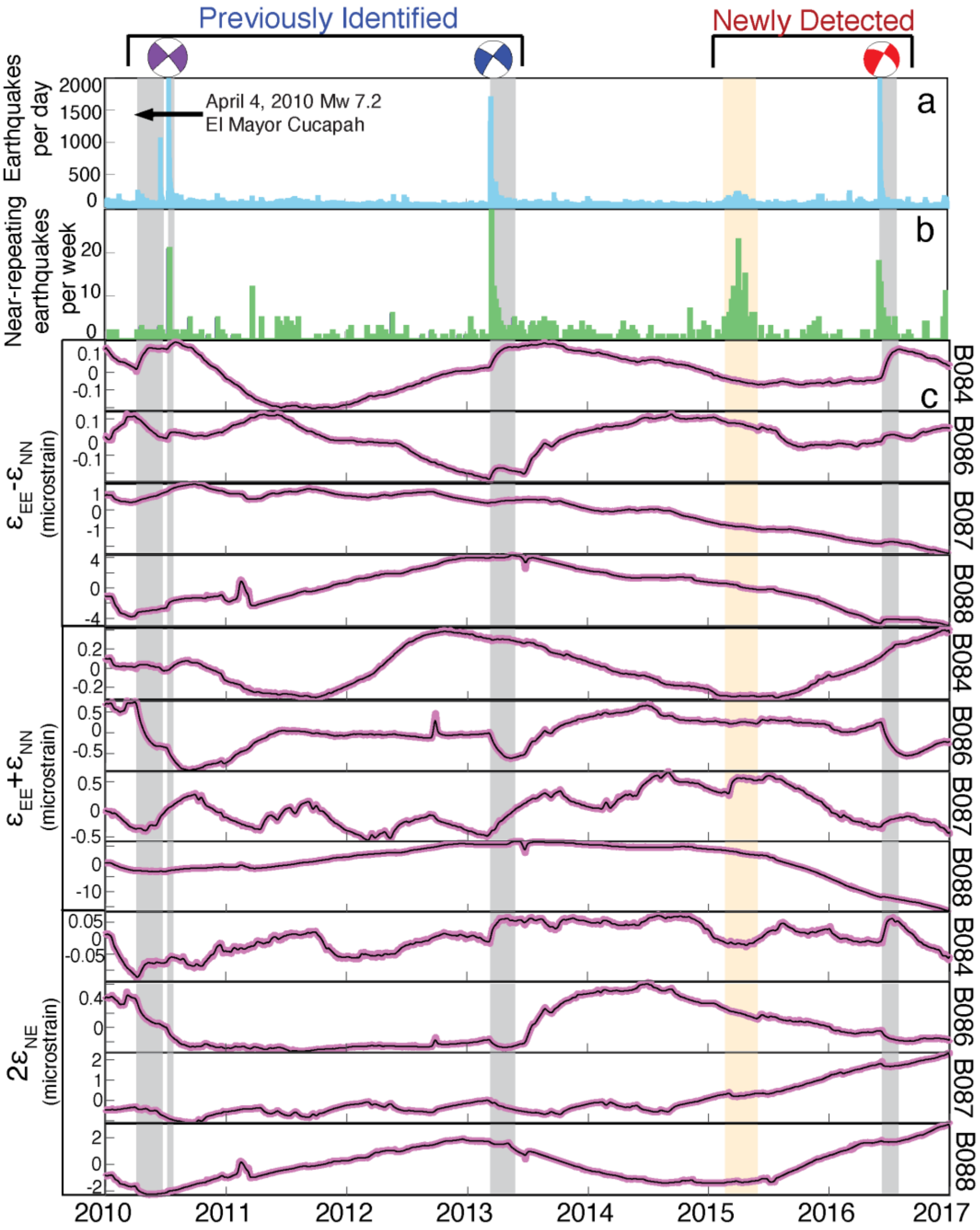
Previously Identified
Newly Detected
Earthquakes per day
2000
1500
1000
500
0
April 4, 2010 Mw 7.2
El Mayor Cucapah
a
Near-repeating earthquakes per week
20
10
0
b
$\varepsilon_{EE}-\varepsilon_{NN}$ (microstrain)
0.1
0
-0.1
c
B084
0.1
0
-0.1
B086
1
0
-1
B087
4
0
-4
B088
$\varepsilon_{EE}+\varepsilon_{NN}$ (microstrain)
0.2
0
-0.2
B084
0.5
0
-0.5
B086
0.5
0
-0.5
B087
0
-10
B088
$2\varepsilon_{NE}$ (microstrain)
0.05
0
-0.05
B084
0.4
0
B086
2
1
0
B087
2
0
-2
B088
2010
2011
2012
2013
2014
2015
2016
2017

2.4 Results

2.4.1 Previously identified afterslip/triggered aseismic slip transients

Following the M_W 5.4 July 7, 2010 Collins Valley (“2010 earthquake”) and M_W 4.7 March 11, 2013 (“2013 earthquake”) local earthquakes (focal mechanism symbols in Figures 2-1, 2-2), there is a sharp increase in seismicity, increase in near-repeating earthquake activity above the background rate (Figure 2-2, Table B-2), and a logarithmic transient signal on the strain data across BSM stations and components (Figures 2-2, B-4, B-5), consistent with previous studies identifying afterslip or aseismic transients following these earthquakes (Agnew, 2017; Hodgkinson, 2013; Inbal et al., 2017; Meng & Peng, 2016). A remotely triggered aseismic slip transient identified in BSM and seismicity data following the 2010 El Mayor-Cucapah earthquake (Figure 2-2; Inbal et al., 2017) is not evident in the near-repeating earthquake time series.

Near-repeating earthquake families following the 2010 and 2013 earthquakes have short and irregular repeat intervals and variable magnitudes (Figures B-4, B-5), consistent with prior observations of short-term/burst-type repeating earthquakes (Igarashi, 2010; Igarashi et al., 2003; Lengliné & Marsan, 2009; Nadeau et al., 1995; Shaddox & Schwartz, 2019; Templeton et al., 2008). We propose that these families of near-repeating earthquakes can be used to infer the location, distribution, and temporal migration of transient afterslip.

Inbal et al. (2017) modeled the triggered aseismic slip transient (or afterslip) following the 2010 earthquake using a joint inversion of strain and seismicity data.

They found a M_W 5.8 event with afterslip distributed along the Coyote Creek fault at depths between 10-14 km, as shown on Figure 2-3b, as well as northwest of the Anza Gap. We find near-repeating earthquakes along strike of the Coyote Creek fault (Figure 2-3b), consistent with the model of Inbal et al. (2017). However, near-repeating earthquakes also locate on what appears to be a dipping structure between the Coyote Creek and Clark faults (Figure 2-3c), suggesting that afterslip may also be occurring on faults between the main SJF strands, likely within deep damage zones.

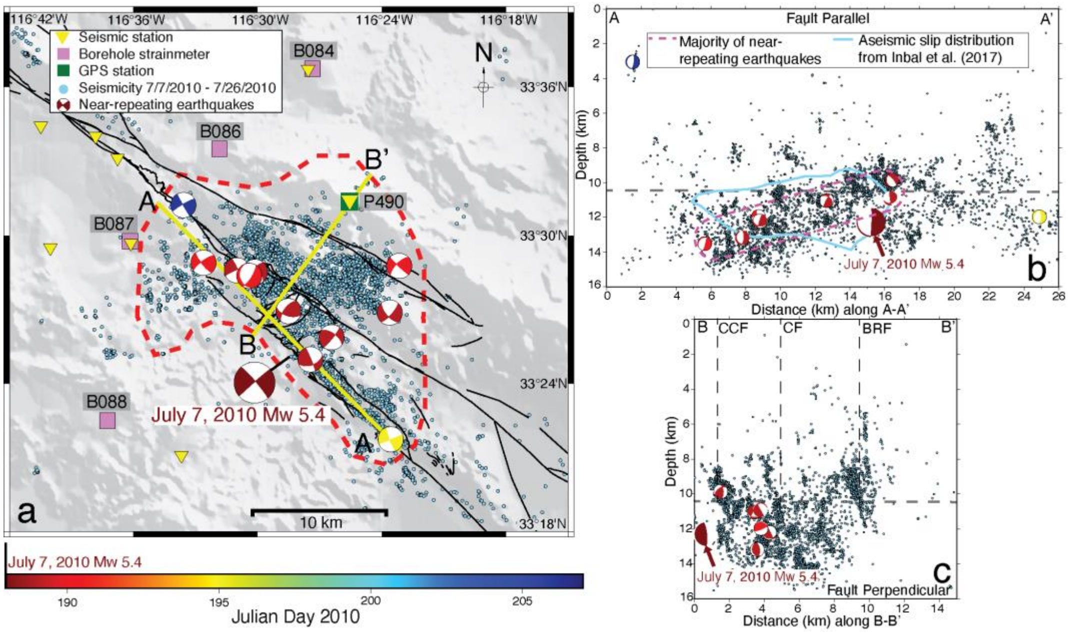

Figure 2-3. Spatial distribution of the 2010 afterslip. (a) Seismicity map during afterslip (7/7/2010-7/26/2010) with focal mechanisms of the M_W 5.4 July 7, 2010 mainshock and repeating earthquake families (colored according to Julian day indicated on color bar [also on b, c]). The study area is outlined by the red dashed line; faults are shown as black lines. (b) Fault parallel cross-section of seismicity and near-repeating earthquake families in the study area within 5 km of A-A’ during afterslip. The majority of near-repeating earthquakes are outlined by the dashed magenta line. (c) Fault perpendicular cross-section of seismicity and near-repeating earthquake families within 5 km of B-B’ during afterslip. Geodetic locking depth (Lindsey et al., 2014) is indicated by the dashed grey line. Faults are indicated as black dashed lines. CCF = Coyote Creek fault; CF = Clark fault; BRF = Buck Ridge fault.

Although a strain transient was previously identified on BSM data following the 2013 earthquake on the Buck Ridge fault (Agnew, 2017; Hodgkinson, 2013), there is no published model for this event. We identified 28 families of near-repeating earthquakes following this event that are mostly shallower (7-11 km depth) than the mainshock earthquake (10.9 km depth) and indicate a shallow temporal migration (Figure 2-4b). We use the location of the majority of near-repeating earthquakes to define a plane (strike, dip, center) hosting afterslip and model the resulting strain changes for comparison to the BSM data for general consistency.

There are several vertical fault planes defined by the locations of near-repeating earthquakes that host afterslip. We use the plane on the steeply dipping Buck Ridge fault (Figure 2-4c), with a strike defined by near-repeating earthquakes, for dislocation modeling. The resulting model and fit to the data is shown in Figure 2-4 and has the following parameters: 301° strike, 90° dip, a rake of 150°, 9.5 km center depth, 5 km fault length, 3 km fault width (8-11 km depth), and slip of 26 cm (Figure 2-4a, Table B-1). These faulting parameters yield afterslip with $M_W = 5.3$ and predicts 3 mm vertical, 0.5 mm north, and 1 mm east displacements at nearby cGPS station P490 (Figure 2-4), which is too small to robustly detect, consistent with a lack of visibly observable signal at this instrument. It is also important to note that our models are far from unique, and other models that fit the BSM data may easily be found which predict even smaller GPS displacements, so the lack of detection by GPS instruments is not considered surprising. Therefore, afterslip with $M_W = 5.3$ following the 2013 earthquake on the mapped Buck Ridge fault with a shallow temporal migration is consistent with both the observations of surface strain changes and the timing and location of the majority of near-repeating earthquake families. However, additional afterslip on minor vertical structures off of the Buck Ridge fault may also be occurring based on the location of additional near-repeating earthquakes. The cumulative seismic moment from seismicity in the study region during the approximate afterslip timing (starting on March 11, 2013 16:56:06 directly following the 2013 earthquake and continuing through May 26, 2013) is less than 1% of the seismic moment of the modeled M_W 5.3 2013 afterslip.

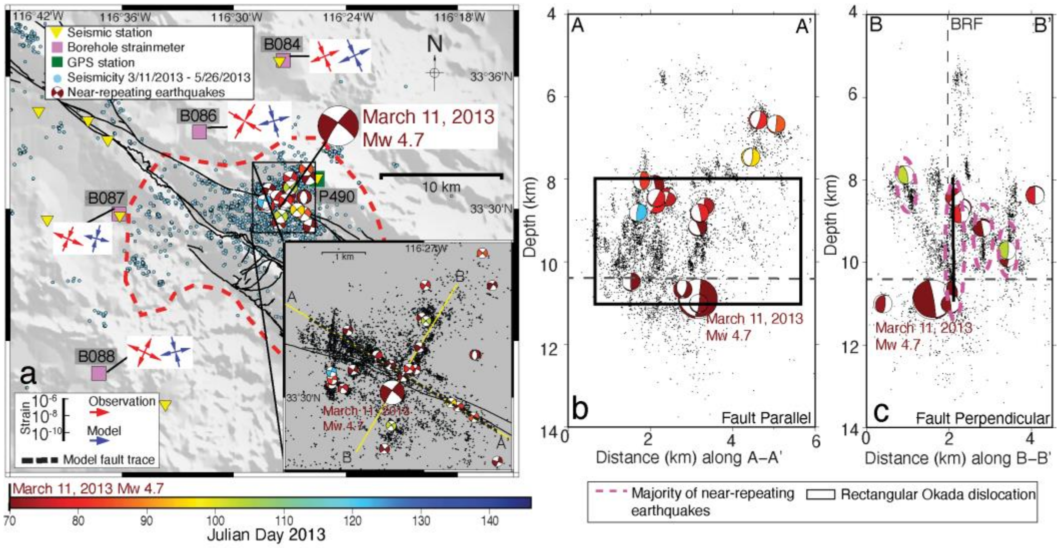

Figure 2-4. Spatial distribution of the 2013 afterslip. (a) Seismicity map during afterslip (3/11/2013 - 5/26/2013) with focal mechanisms of the M_W 4.7 March 11, 2013 mainshock and near-repeating earthquake families (colored according to the Julian day indicated on color bar of the first near-repeating earthquake in the family [also on b, c]), and changes of principal strain at the four BSM stations during afterslip indicated by the red (observed strain changes) and blue (modeled strain changes) arrows. The study area is outlined with the red dashed line; faults are shown as black lines. The inset shows an enlargement of the area in the black box. (b) Fault parallel cross-section of seismicity and near-repeating earthquake families in the study area within 1 km of A-A' during afterslip. The rectangular Okada dislocation plane is included as a black rectangle. (c) Fault perpendicular cross-section of seismicity and near-repeating earthquake families in the study area within 1 km of B-B' during afterslip. The majority of near-repeating earthquakes are outlined by the dashed magenta lines. The location and dip of the rectangular Okada dislocation is shown as the black line. Geodetic locking depth (Lindsey et al., 2014) is indicated by the dashed grey line. The Buck Ridge fault (BRF) is indicated with a black dashed line.

2.4.2 Newly detected afterslip

The M_W 5.2 June 10, 2016 Borrego Springs earthquake ("2016 earthquake") on the Clark fault (focal mechanism symbol in Figures 2-1, 2-2) propagated unilaterally to the northwest (Ross, Kanamori, et al., 2017). Following this earthquake there is a sharp increase in seismicity (Figure 2-2a, 2-5a), increase in near-repeating earthquake activity (Figure 2-2b, 2-5a, Table B-2), and a logarithmic transient signal on the strain data across BSM stations and components (Figure 2-2c, Figure 2-5b – 2-5d) similar to the 2010 and 2013 previously identified transients. This is evidence of newly detected afterslip following a moderate-sized local earthquake. The depth of seismicity following the earthquake ranges from 8-15 km, but is most concentrated at 11-12 km depth (Figure B-1), similar to the 2010 event.

Based on the locations of 23 near-repeating earthquake families following the 2016 earthquake, afterslip extends at least 14 km to the northwest of the hypocenter at a strike of 305° along the Clark fault, from approximately 8 to 14 km depth with a dip of 70° to the northeast (Figure 2-6). There also appears to be a northwest temporal migration of near-repeating earthquake families (Figure 2-6a, 2-6b). Additional afterslip on faults within the damage zone between the Clark and Buck Ridge faults is also likely based on the location of several near-repeating earthquake families on small splay faults (Figure 2-6c).

Using a fault plane defined by the location of the majority of near-repeating earthquake families with the strike constrained to be on the mapped Clark fault (305° strike, 70° northeast dip, centered at 11 km depth; Figure 2-6), we perform a grid search to determine a slip of 11 cm, a fault length of 14 km, a width of 6 km (8.2-13.8 km depth), and a rake of 174° that best fit the observed surface strain changes (Figure 2-6a, Table B-1). These faulting parameters yield afterslip with $M_W = 5.6$. Our model is also consistent with the observation that cGPS station P490 (Figure 2-6a) did not detect postseismic afterslip, as the model predicts vertical (2.5 mm) and horizontal (0.54 mm north; 3.1 mm east) displacements beneath the detection threshold of this single instrument. Therefore, deep, M_W 5.6 afterslip migrating northwest apparently along the Clark fault following the 2016 earthquake is consistent with both the observations of near-repeating earthquake families and surface strain changes. Similar to the 2010 and 2013 earthquakes, the moment of afterslip is larger than for the local mainshock earthquake. The cumulative seismic moment from seismicity in the study region during the approximate afterslip timing (starting on June 10, 2016 08:04:39 directly following the 2016 earthquake and continuing through July 31, 2016) is less than 1% of the seismic moment of the modeled M_W 5.6 2016 afterslip.

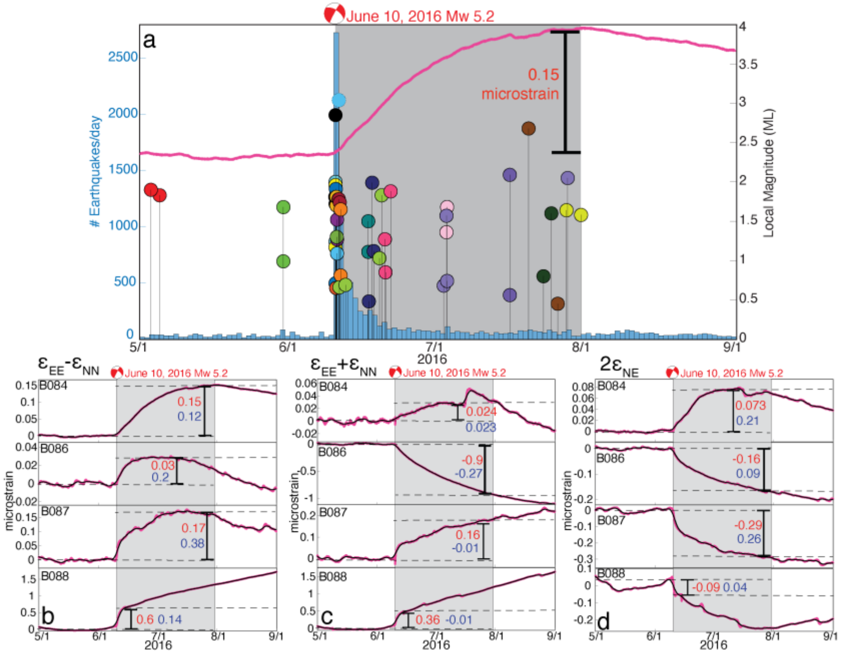

Figure 2-5. Timing of the 2016 afterslip. (a) Seismicity rate (in study area; see Figure 2-1), near-repeating earthquakes, and strain transient timing from BSM data (indicated in grey). Near-repeating earthquakes plotted by local magnitude and colored according to family (25 total families; 22 during afterslip). Differential shear strain from BSM station B084 is plotted as the magenta line. (b)-(d) 5-minute corrected strain data (b: differential shear strain, c: areal strain, d: engineering shear strain) for BSM stations B084, B086, B087, and B088 (see Figure 2-1) with the trend of the month prior to the earthquake removed is shown in magenta, one-week running average shown in black. Observed strain change (microstrain) during afterslip is indicated in red, modeled strain change is indicated in blue. Approximate timing of afterslip from BSM data and near-repeating earthquakes is highlighted in grey. Timing (in UTC) of the Mw 5.2 June 10, 2016 Borrego Springs earthquake is indicated at the top of each panel.

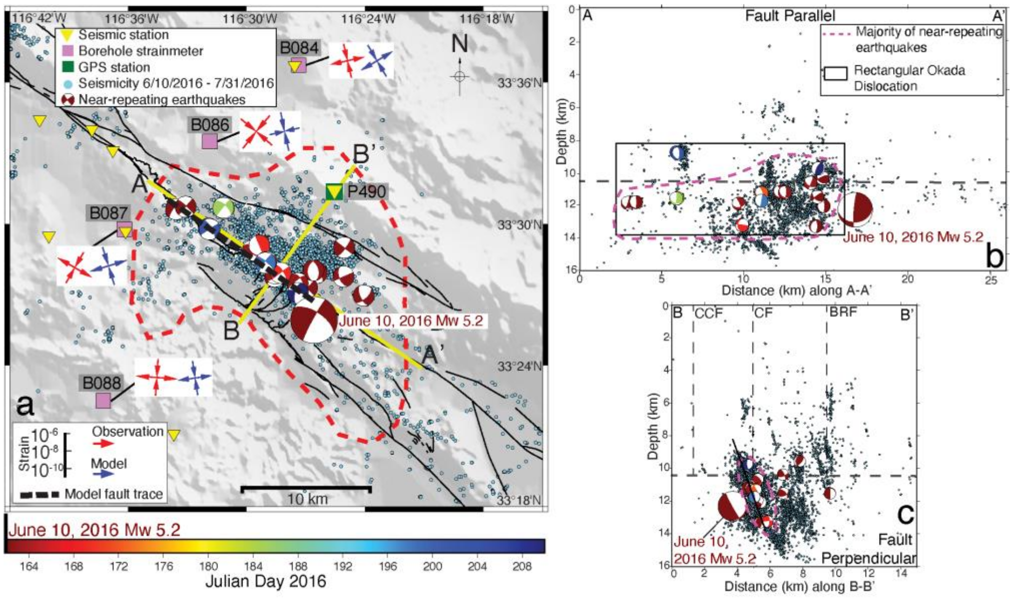

Figure 2-6. Spatial distribution of the 2016 afterslip. (a) Seismicity map during afterslip (6/10/2016-7/31/2016) with focal mechanisms of the M_W 5.2 June 10, 2016 mainshock and near-repeating earthquake families (colored according to Julian day indicated on the color bar of the first near-repeating earthquake in the family [also on b, c]), and changes of principal strain at the four BSM stations during afterslip indicated by the red (observed strain changes) and blue (modeled strain changes) arrows. The study area is outlined with the red dashed line; faults are shown as black lines. (b) Fault parallel cross-section of seismicity and near-repeating earthquake families in the study area within 1.5 km of A-A' during afterslip. The majority of near-repeating earthquakes are outlined by the dashed magenta line. The rectangular Okada dislocation plane is included as a black rectangle. (c) Fault perpendicular cross-section of seismicity and near-repeating earthquake families in the study area within 5 km of B-B' during afterslip. The majority of near-repeating earthquakes are outlined by the dashed magenta line. The location and dip of the rectangular Okada dislocation is shown as the black line. Geodetic locking depth is from Lindsey et al. (2014). Faults are indicated as black dashed lines. CCF = Coyote Creek fault; CF = Clark fault; BRF = Buck Ridge fault.

2.4.3 Newly detected spontaneous aseismic slip transient

From February-May 2015 there is a notable increase in near-repeating earthquake activity above the background rate and a moderate increase in seismicity (Figures 2-2, 2-7c). These increases are much more gradual than what is observed for the 2010, 2013, and 2016 transients, and there is not an obvious regional or local moderate-sized earthquake. The majority of near-repeating earthquake families and microseismicity during this time period are located on two previously unmapped adjacent (0.75 km separation) but unconnected 0.5-1.5 km long faults, trending northeast and approximately orthogonal to the main fault strands, at depths of 7-9 km, which is shallower than most of the seismicity associated with afterslip (Figures 2-7a,b; B-1). A strain transient signal is observed on the areal and engineering shear strain components of the nearest BSM station, B087, located approximately 4 km northwest of these faults. The cumulative slip from microseismicity on the two northeast-trending splay faults from February 25, 2015 - May 31, 2015 (approximate timing of strain transient signal) would result in strain at B087 that is over 1000x less than what is observed. Therefore, the strain transient signal is not due to cumulative strain from microseismicity alone. The near-repeating earthquake families, microseismicity increase, and strain transient signal on B087 are evidence of a spontaneous aseismic slip transient occurring on two separate faults only detected on the nearest BSM station.

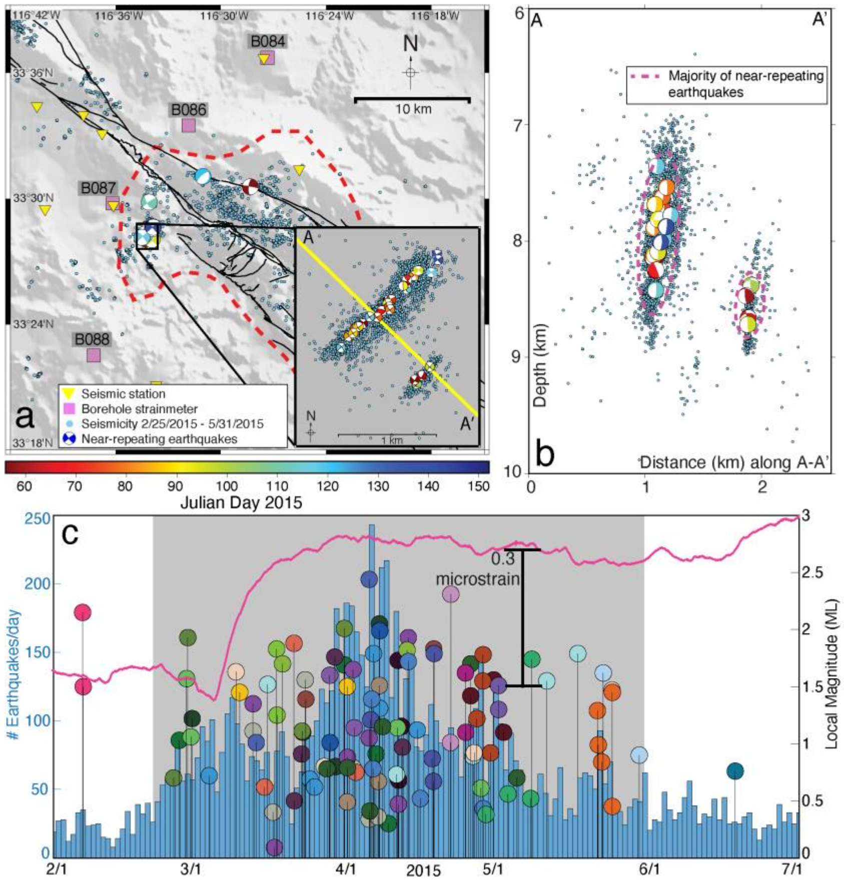

Figure 2-7. Timing and spatial distribution of the 2015 shallow, spontaneous aseismic slip transient. (a) Seismicity map during the aseismic slip transient (2/25/2015-5/31/2015) and focal mechanisms of near-repeating earthquake families (colored according to Julian day indicated on color bar [also on b]). Study area outlined in red dashed line; faults shown as black lines. (b) Fault perpendicular cross-section of seismicity and near-repeating earthquake families in the study area within 5 km of A-A' during the aseismic slip transient. The majority of near-repeating earthquakes are outlined by the dashed magenta line. (c) Seismicity rate in the study region, near-repeating earthquakes, and aseismic slip transient timing from BSM data (indicated in grey). Near-repeating earthquakes are plotted by local magnitude and colored according to family (34 total families). Areal strain from BSM station B087 is plotted as the magenta line.

2.5 Discussion

2.5.1 Afterslip of the 2010, 2013, and 2016 earthquakes

The moment released by afterslip following the 2010, 2013, and 2016 earthquakes was larger than the mainshock moments. The cumulative seismic moment from earthquakes in the study area during afterslip is 1% or less of the afterslip moment of each event. This indicates that the strain transient signals observed across BSM stations are from aseismic rather than seismic slip.

The 2010 and 2016 earthquakes both have hypocentral depths near 12 km (SCSN catalog). Afterslip is mostly deep (> 10 km) on major fault strands beneath the geodetic locking depth of ~10 km (Lindsey et al., 2014). However, near-repeating earthquakes during afterslip of both events locate off-fault, in the damage zone between primary fault strands (Figure 2-8), suggesting that afterslip may also have occurred on minor off-fault structures. The majority of near-repeating earthquakes during the 2016 afterslip define a plane dipping 70° to the northeast, consistent with previous work documenting a change in dip of the main faults in the trifurcation area from near vertical to 70° near a depth of 10 km (Ross, Hauksson, et al., 2017)(Figure 2-8). Near-repeating earthquakes during the 2013 afterslip appear to define a near vertical plane apparently coplanar with and shallower than the mainshock and on the Buck Ridge fault, as well as on multiple minor vertical faults (Figure 2-8). Most of the afterslip is shallower than the geodetic locking depth. Afterslip is likely occurring on several planes, both on and off the major faults from 6-14 km depth (Figure 2-8), providing support for a model with a spatially heterogeneous transition from locked to freely slipping between 6-14 km depth. Our afterslip models for 2013 and 2016 (based on the location of near-repeating earthquakes) are generally not coplanar with the majority of seismicity; indicating that afterslip likely drives off-fault microseismicity.

Although we refer to the transient, aseismic slip observable on local BSMs directly following the 2010, 2013, and 2016 earthquakes as afterslip, it is important to note that afterslip has generally been defined as occurring on the mainshock fault, in regions adjacent to coseismic slip (Avouac, 2015 and references therein). Since we propose that afterslip following these earthquakes occurs on both the mainshock fault and on several other minor faults within the damage zone, it may be appropriate to more broadly characterize these transients as triggered aseismic slip, consistent with terminology adopted by Inbal et al. (2017), Agnew (2017), and Hodgkinson (2013).

Figure 2-8. Fault perpendicular cross-section of seismicity and near-repeating earthquakes within 15 km of A-A’ on Figure 2-1 during afterslip or triggered aseismic slip. Focal mechanisms of the 2010 (Coyote Creek fault; purple), 2013 (Buck Ridge fault; blue), 2016 (Clark fault; red), and 2020 (Clark fault; orange) triggering earthquakes are included as the four large focal mechanisms. Near-repeating earthquakes and seismicity during the 2010 (purple), 2013 (blue), and 2016 (red) triggered aseismic slip transients are shown as smaller focal mechanisms and small filled circles, respectively. Near-repeating earthquakes during the 2020 triggered aseismic slip transient are shown as orange stars. Geodetic locking depth (Lindsey et al., 2014) indicated by the gray dashed line. Fault projections from the surface expressions are shown as black dashed lines. CCF = Coyote Creek fault; CF = Clark fault; BRF = Buck Ridge fault. The dip of the 2013 and 2016 rectangular Okada dislocations are shown as solid black lines.

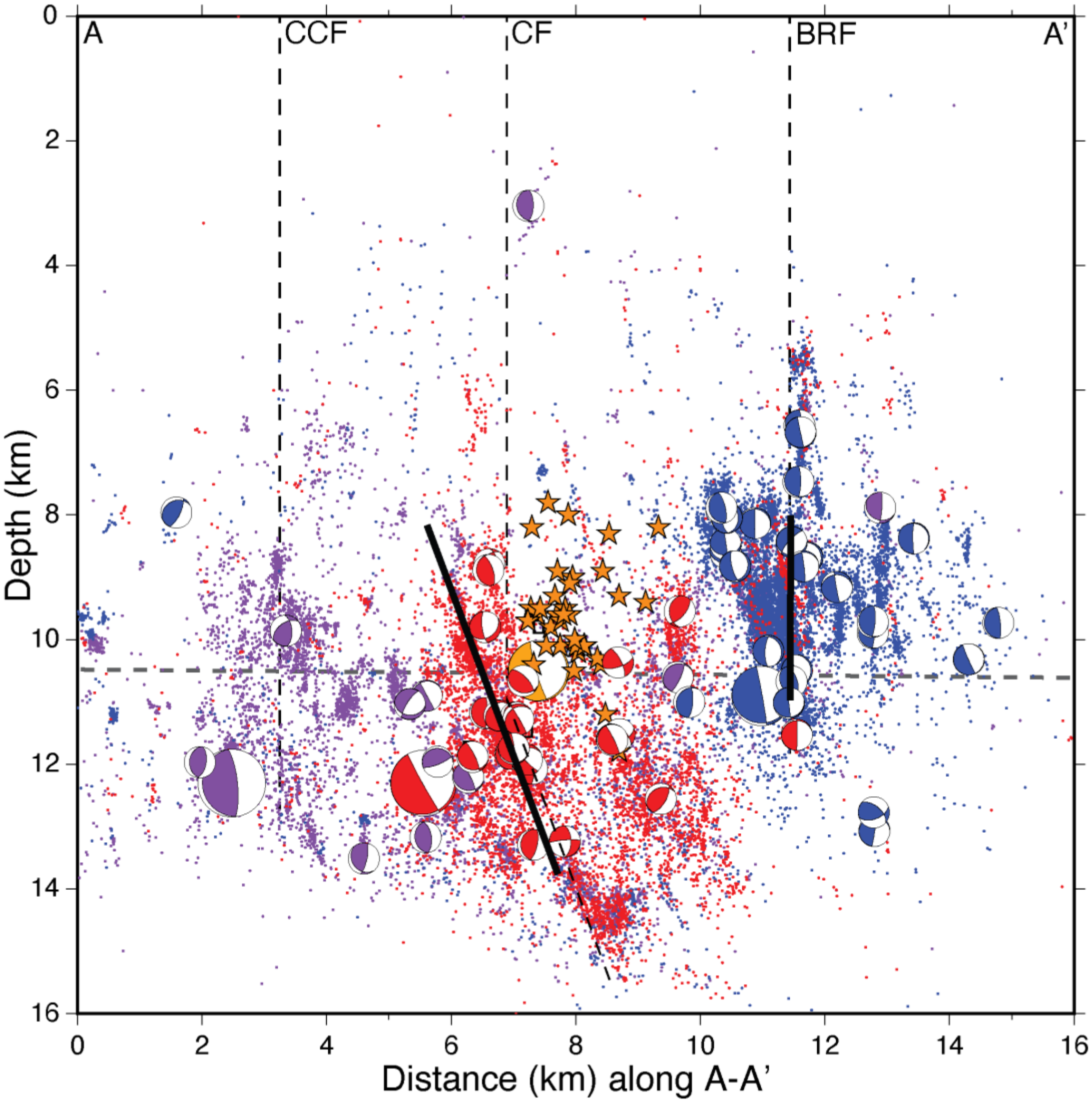
A
CCF
CF
BRF
A’
Depth (km)
Distance (km) along A-A’
0
2
4
6
8
10
12
14
16
0
2
4
6
8
10
12
14
16

2.5.2 Near-repeating earthquakes as a proxy for transient aseismic slip

By defining rectangular afterslip planes based on the locations of the majority of near-repeating earthquake families, we were able to model strain changes largely consistent with observations at the four nearest BSM stations for the 2013 and 2016 afterslip. However, the observed strain changes are likely influenced by unmodeled details including additional afterslip on minor structures, which may account for disparities between the model and observations. Still, the overall general consistency provides confidence that near-repeating earthquakes are coplanar with afterslip and can be used to not only detect aseismic slip transients, but also to reveal aseismic slip geometry. Further, the temporal migration of near-repeating earthquake families can be used in some cases to identify the migration of afterslip. A northwest temporal migration of near-repeating earthquake families during the 2016 afterslip and a shallow temporal migration during the 2013 afterslip are examples of this.

Aftershocks can be driven primarily by afterslip rather than from coseismic stress changes (Avouac, 2015; Hsu et al., 2006; Perfettini et al., 2005; Perfettini & Avouac, 2004; Schaff et al., 1998; Yu et al., 2013). Aftershocks that are loaded by afterslip can be coplanar with afterslip (Yu et al., 2013), occur on adjacent segments of the fault (Hsu et al., 2006; Perfettini et al., 2005), or be located on adjacent faults (Inbal et al., 2017). We believe that the near-repeating earthquakes during the 2010, 2013, and 2016 afterslip are coplanar with afterslip. They may be ruptures of nearby or partially overlapping asperities that are loaded or partially reloaded by transient afterslip. These near-repeating earthquakes are aftershocks, but with unique characteristics, in particular, they occur very close together and are coplanar with afterslip. There are additionally many off-fault aftershocks, consistent with deep transient aseismic slip driving off-fault aftershocks reported by Inbal et al. (2017) following the 2010 earthquake.

We were able to find the first evidence of spontaneous aseismic slip near Anza on two minor faults in 2015 from a notable increase in near-repeating earthquake activity above the background rate. This activity was accompanied by a modest increase in seismicity and a strain transient signal on the closest BSM. The seismicity on these two minor faults is swarm-like, i.e., earthquakes are clustered in both space and time without a clear mainshock (Vidale & Shearer, 2006). The driving mechanisms of swarms are thought to be aseismic, including fluid flow (Chen et al., 2012; Shelly et al., 2015; Shelly, Hill, et al., 2013; Shelly, Moran, et al., 2013; Vidale & Shearer, 2006; Waite & Smith, 2002), transient aseismic slip (Lohman & McGuire, 2007; Ozawa et al., 2007; Roland & McGuire, 2009), or a combination where pore pressure changes from fluid migration trigger aseismic slip that then drives swarm activity (Bourouis & Bernard, 2007; Hainzl, 2004). The strain signal on the closest BSM - 1000x greater than what would be expected from the swarm seismicity alone - is evidence that this swarm was driven by aseismic slip, possibly an episodic event or triggered by fluid migration.

The 2015 transient is evidence that near-repeating earthquakes can be indicative of spontaneous aseismic slip in addition to triggered aseismic slip (i.e., afterslip). These findings are similar to Shaddox & Schwartz (2019) that found near-repeating earthquakes spatiotemporally coincident with tremor and concluded that this seismicity was driven by fluid-included aseismic slip on minor faults. Without the notable increase in near-repeating earthquake activity, the 2015 swarm-like seismicity may not have been noticed. Thus, near-repeating earthquakes can be useful to identify and locate spontaneous transient aseismic slip.

We have demonstrated that near-repeating earthquakes are a useful proxy for triggered and spontaneous transient aseismic slip. This is particularly useful in the absence of tremor and LFEs. Few studies have identified tremor near Anza on the SJF. Triggered tremor composed of 12 LFEs was identified at ~13 km depth northwest of our study region near Anza during the Love-wave arrival of the 2002 M_W 7.8 Denali earthquake (Wang et al., 2013). However, triggered tremor was not identified following 43 other $M_W > 7.4$ teleseismic events analyzed from 2001-2011 (Wang et al., 2013), indicating that a high peak shear stress is required to trigger tremor near Anza. Hutchison & Ghosh (2017) found five discrete short-duration episodes of ambient tremor in June 2011 located near the Wang et al. (2013) triggered tremor at 13-24 km depth. In an attempt to identify LFEs associated with the aseismic slip transients triggered by the remote 2010 M_W 7.2 El Mayor-Cucapah earthquake and the local 2010 earthquake identified by Inbal et al. (2017) we selected the 12 LFEs during the 300 second triggered tremor episode from Wang et al. (2013) as templates and performed template matching for 2010 using 8 seismometers and similar methodology described in Section 3.1. We did not find any LFE detections. Other recent work similarly used these LFEs as templates and performed template matching from 2002-2016 and did not find LFE activity (Bürgmann et al., 2019). This work additionally attempted to identify LFEs within the ambient tremor detected by Hutchison & Ghosh (2017) to use as additional templates but were unsuccessful (Bürgmann et al., 2019). Further, they did not find transient signals above the noise level using a geodetic matched filter analysis on the local GPS network, other than a signal potentially related to the July 2010 aseismic transient identified by Inbal et al. (2017). In general, tremor episodes are infrequent in the Anza region or the anthropogenic noise level is too high for detection of ambient or triggered tremor. Further, the 2013 and 2016 afterslip were not large enough to be detectable with the local GPS network. The combined analysis of near-repeating earthquakes and BSM data allowed for the identification and analysis of these aseismic slip transients.

2.5.3 Deep slip in the trifurcation area

The 2015 aseismic slip transient is the first evidence of any spontaneous aseismic slip in the trifurcation area near Anza. Although we find no direct evidence of other spontaneous or continuous creep events, $M_W > 4.5$ earthquakes have occurred at semi-regular intervals of every 3-5 years between 2001 and 2020. These fairly regular moderate-sized events might be loaded by deep creep that is not detected by BSMs and does not drive characteristic repeating earthquakes. The moderate-sized earthquakes themselves trigger aseismic slip transients near the locking depth that do drive near-repeating earthquakes. It is possible that the loading rate from afterslip is high enough to both drive near-repeating earthquakes and generate a noticeable strain change signal.

The afterslip following the 2010, 2013, and 2016 earthquakes is evidence that deep and moderate-depth transient aseismic slip can occur on each of the main fault strands of the trifurcation area, and on minor structures in the off-fault damage zone. This aseismic slip drives coplanar near-repeating earthquakes and abundant off-fault microseismicity. The 2015 aseismic slip transient is evidence that spontaneous aseismic slip can occur on small faults within the larger damage zone, mostly beneath the detection threshold of nearby BSM stations. It also provides evidence for aseismic slip within the seismogenic zone at a depth of 7-9 km. These observations favor a model where deep microseismicity is located in a transitional region at the bottom of the seismogenic zone with spatially heterogeneous frictional properties. Such an environment could produce frequent and sporadic aseismic slip transients of various sizes, potentially including many too small to drive numerous near-repeating earthquakes and beneath the detection threshold of nearby BSM stations.

2.5.4 Afterslip of moderate-sized earthquakes

In general, afterslip following large earthquakes ($M_W > 7.5$) have moments equal to 10-40% of the coseismic moment (Avouac, 2015; Bürgmann et al., 2002; Lin et al., 2013). The more limited observations of afterslip following small to moderate-sized earthquakes find a larger ratio of postseismic to coseismic moment, often with afterslip moment comparable to the mainshock moment (Alwahedi & Hawthorne, 2019; Bell et al., 2012; Fattahi et al., 2015; Freed, 2007; Furuya & Satyabala, 2008; Hawthorne et al., 2016b; Murray-Moraleda & Simpson, 2009; Taira et al., 2014). The large afterslip moments observed may reflect observational limitations; smaller afterslip is difficult to observe. Further, most of these observations are on terrestrial strike-slip faults with near-field land GPS networks and available InSAR data.

There have been several observations of large afterslip moments following moderate-sized earthquakes on the SAF. Taira et al. (2014) identified a year-long M_W 5.22 triggered slow slip transient following the M_W 5.1 1998 earthquake on the San Juan Bautista segment of the SAF using BSM data, GPS data, and repeating earthquakes. The 2004 M_W 6 Parkfield earthquake triggered afterslip with $M_W = 6.3$ (Freed, 2007) and the 2007 M_W 5.4 Alum Rock earthquake on the Calaveras fault near the junction with the Hayward fault triggered afterslip with a comparable moment to the mainshock (Murray-Moraleda & Simpson, 2009). Using 12 BSMs near the San Juan Bautista and Parkfield segments of the SAF, Alwahedi & Hawthorne (2019) analyzed the coseismic and postseismic (1.5 days following the mainshock) moments of 11 local moderate-sized (M 4-5) earthquakes and found the median postseismic moment is 0.45 times the coseismic moment. Although Alwahei and Hawthorne (2019) are using a much smaller postseismic time frame for analysis than the previously mentioned work, it is still consistent with other observations of larger afterslip following moderate-sized earthquakes than large earthquakes.

During the study period of 2010-2016, we find that all $M_W>4.5$ earthquakes in the trifurcation area southeast of Anza triggered moderate to deep afterslip or aseismic slip transients on different fault strands, each with a larger moment than the mainshock. This is consistent with other observations of moderate-sized earthquakes triggering large afterslip. It is therefore possible that in general, moderate-sized earthquakes trigger afterslip or aseismic slip transients of a comparable or larger moment than the mainshock.

Another possibility is that these observations of moderate-sized earthquakes triggering large afterslip occur in unique locations. The trifurcation area on the Anza segment of the SJF is complex, splaying into three main fault strands with numerous smaller faults within fault-bounded damage zones. Further, the trifurcation area is located in a transitional coupling zone, southeast of the locked Anza seismic gap, and is the most seismically active fault zone in southern California. Similarly, the San Juan Bautista and Parkfield segments of the SAF where large afterslip has been well-documented following moderate-sized earthquakes (Alwahedi & Hawthorne, 2019; Taira et al., 2014), form the transition zones between locked and creeping segments of the SAF. In addition, the 2007 Alum Rock earthquake triggered comparable magnitude afterslip near the junction of the Calaveras and Hayward faults (Murray-Moraleda & Simpson, 2009). The frictional heterogeneity and transitional/partial locking in all of these locations may be the reason for the significant afterslip and strong coupling of seismic and aseismic slip. The interplay of seismic and aseismic slip in these locked to creeping transition zones is of particular interest because they have the greatest fault stressing rates and are likely points for nucleation of future large earthquakes.

2.5.5 April 2020 earthquake and triggered aseismic slip

On April 4, 2020, toward the conclusion of this study, a magnitude 4.9 earthquake occurred on the Clark fault (Figures 2-1, 2-9), northwest of the 2016 earthquake that also ruptured the Clark fault. Although this earthquake occurred after our initial study period (2010-2016) and after creation of the QTM catalog, it is within our study region and provides an opportunity to validate our premise that all moderate-sized earthquakes in this region trigger aseismic slip accompanied by near-repeating earthquakes. We therefore performed a cursory analysis of near-repeating earthquakes, earthquake catalog data, and BSM data approximately four weeks before and after this earthquake to determine whether this moderate-sized earthquake triggered aseismic slip.

We performed template matching similar to 2010-2016 using templates in the study region from March 1 - May 6, 2020 from the SCSN standard catalog (Hutton et al., 2010) with a local magnitude≥1.5 (237 templates) as well as templates with the same magnitude criteria from June 1 - July 31, 2016 (137 templates) from the QTM catalog that occurred during the 2016 slip transient also on the Clark fault. We performed template matching using the 374 template earthquakes (Figure 2-9) from March 1 - May 6, 2020.

We find that following the 2020 earthquake there is a sharp increase in seismicity (Figure 2-9a, 2-9d; SCSN standard catalog), an increase in near-repeating earthquake activity (Figure 9a, 9d, Dataset S2), and a logarithmic transient signal on the strain data across the three nearest BSM stations (B086, B087, and B088; B084 was non-operational) and components (Figure 2-9d, B-6) similar to the 2010, 2013 and 2016 triggered aseismic slip transients. This appears to be a newly detected triggered aseismic slip transient or afterslip following a moderate-sized local earthquake. At the time of writing, it appears that the largest strain changes on BSM stations occurred from April 4 - April 28, 2020 (Figure 2-9d, B-6) and that the triggered aseismic slip transient has finished or has slowed significantly. However, it is too early to know if the aseismic slip transient may continue further in time. Since B084 was non-operational during the aseismic slip transient, and B087 had significant outages before and during the aseismic slip transient, we did not model the triggered aseismic slip transient.

The depth of seismicity following the 2020 earthquake is most concentrated at 8-12 km depth (Figure B-1), with most near-repeating earthquakes at 8.5-11 km depth (Figure 2-9a,b,c). Few of the 2016 templates used detected near-repeating earthquakes, indicating that a different part of the Clark fault was activated following the 2020 earthquake. The 2020 template earthquakes from the SCSN catalog have not been relocated with a 3D velocity model or using waveform similarity and have error estimates of less than 3 km. Further, focal mechanisms are not yet available to help determine plane geometry of near-repeating earthquakes. However, we can still make a general estimate of an aseismic afterslip plane defined by the location of the majority of near-repeating earthquakes (Figures 2-8, 2-9). It appears that aseismic slip occurs parallel to but off of the main Clark fault, dipping at 75° to the northeast, and centered around the geodetic locking depth of 10 km. Overall, this appears to be newly detected moderate-depth triggered aseismic slip transient that drives coplanar near-repeating earthquakes and off-fault microseismicity. Agnew (2017) identified strain transients on the long baseline strainmeter at the Pinon Flat Observatory following the local events in 2010 and 2013 discussed here. He also reported very similar signals following two M 5.0 earthquakes near Anza in 2001and 2005. This provides further support of our contention that all moderate-sized earthquakes in this region trigger aseismic slip transients accompanied by near-repeating earthquakes.

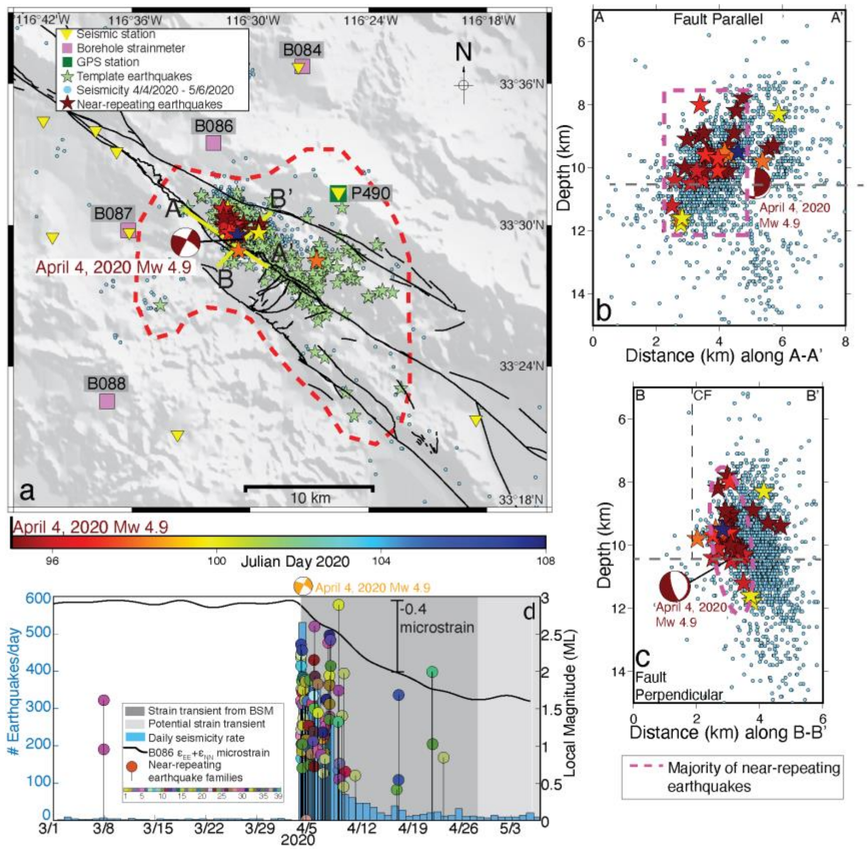

Figure 2-9. Spatial distribution of the 2020 aseismic slip transient. (a) Seismicity map during the aseismic slip transient (4/4/2020 – 5/6/2020), template earthquakes (green stars), near-repeating earthquake families (stars colored according to Julian day indicated on the color bar [also on b, c]), and the focal mechanism of the Mw 4.9 April 4, 2020 local earthquake. The study area is outlined with the red dashed line; faults are shown as black lines. (b) Fault parallel cross-section of seismicity and near-repeating earthquake families in the study area within 5 km of A-A' during the aseismic slip transient. The majority of near-repeating earthquakes are outlined by the dashed magenta line. (c) Fault perpendicular cross-section of seismicity and near-repeating earthquake families in the study area within 5 km of B-B' during the triggered aseismic slip transient. The Clark fault (CF) is indicated by a black dashed line. The geodetic locking depth (Lindsey et al., 2014) is indicated by the dashed grey line. The majority of near-repeating earthquakes are outlined by the dashed magenta line. (d) Seismicity rate (in study area; see Figure 2-1), near-repeating earthquakes, strain transient timing from BSM data (dark grey), potential timing of strain transient continuation (light grey), and one-week running average of BSM station B086 εEE+εNN component (black line). Near-repeating earthquakes are plotted by local magnitude and colored according to family.

2.6 Conclusions

We find that all moderate-sized ($M_W > 4.5$) earthquakes in the Anza region of the SJF between 2010-2016 triggered deep to moderate-depth afterslip with larger moment than the mainshocks. This includes newly identified M_W 5.6 afterslip following the 2016 local earthquake. Following the 2010, 2013, and 2016 earthquakes, families of near-repeating earthquakes defined a dominant afterslip geometry consistent with strain change observations at nearby BSM stations. Their locations revealed that afterslip occurred on each of the main fault strands of the trifurcation area and on minor structures in the off-fault damage zone. We conclude that near-repeating earthquakes, similar to LFEs that make up tremor, are useful indicators of spontaneous and triggered aseismic slip transients and can identify geometric complexities of these events. Further, the Anza region does not appear to be tremorgenic and aseismic slip transients are not consistently detected by the local GPS network; the combined analysis of near-repeating earthquakes and strainmeter data allowed for the identification and analysis of these aseismic slip transients. Serendipity allowed us to successfully use the April 4, 2020 M_W 4.9 local earthquake on the Clark fault, that occurred at the termination of this study, to validate our expectation that all moderate-sized earthquakes in this region trigger afterslip or aseismic slip transients accompanied by near-repeating earthquakes.

The 2010, 2013, and 2016 moderate to deep afterslip add to a growing body of evidence that moderate-sized earthquakes generally trigger large afterslip. However, it is possible that observations of afterslip following moderate-sized earthquakes are biased toward larger signals, and large afterslip has been documented in unique locations. The trifurcation area of the SJF is located in a transitional coupling zone southeast of the Anza seismic gap with complex faulting. Similarly, the San Juan Bautista and Parkfield segments of the SAF and the junction of the Calaveras and Hayward faults where large afterslip has occurred are located in transition zones between locked and creeping segments. The frictional heterogeneity and transitional locking in all of these locations may be the reason for the significant afterslip observed and strong coupling of seismic and aseismic slip.

Finally, we report the first evidence of spontaneous aseismic slip near Anza from near-repeating earthquake families on two minor faults in 2015. This aseismic slip transient is evidence that spontaneous aseismic slip can occur on small faults within the larger damage zone, mostly beneath the detection threshold of nearby BSM stations. Although we find no direct evidence of other spontaneous or continuous creep events, it is possible that the fairly regular moderate-sized events that trigger large aseismic slip transients (i.e., afterslip) are loaded by deep creep. Taken together, our observations favor a model where deep microseismicity is located in a transitional region near the bottom of the seismogenic zone with spatially heterogeneous frictional properties. Such an environment could produce frequent and sporadic aseismic slip transients of various magnitude, some that are beneath the detection threshold of nearby BSM stations.

Chapter 3 - Seismic Detection of Oceanic Internal Gravity Waves from Subaerial Seismometers

3.1 Internal waves and expected seismic signals

Oceanic internal gravity waves propagate along density stratification within the water column (Helfrich and Melville, 2006). These waves are ubiquitous and can propagate thousands of kilometers before breaking on shoaling bathymetry and the ensuing turbulent mixing affects coastal processes, climate feedbacks, and marine ecosystems (Wolanski and Deleersnijder, 1998; Wang et al., 2007; DeCarlo et al., 2015; MacKinnon et al., 2017; Reid et al., 2019). Internal waves are of further importance for submarine navigation, subsurface structures, hydroacoustics, and marine organisms, and their critical role in mixing, energy dissipation, and thermohaline circulation make them one of the most important factors governing oceanic dynamics (Miropol'sky, 2001; Garrett and Kunze, 2007; Ferrari and Wunsch, 2009; Woodson, 2018). Internal waves of tidal frequency, called internal tides or baroclinic tides, are generated in stratified waters when barotropic tidal currents interact with seafloor topography. Internal tides play a particularly important role in oceanic dynamics because they are generated regularly and transfer energy from tides to mixing both in the deep ocean and on continental shelves (Sandstrom and Elliott, 1984; Garrett and Kunze, 2007). Yet, they are not always generated, even in the same ocean basin. Whether internal tides are generated depends on tide-topography interactions and ocean stratification (Garrett and Kunze, 2007). Seasonal and climatological modifications in density stratification can result in dramatic changes in internal tide generation and propagation. Once generated, internal tides can propagate hundreds of kilometers and then break up into shorter, higher-frequency nonlinear internal waves (Ray and Mitchum, 1996; Holloway et al., 1997; Zhao et al., 2004).

Despite their importance, internal waves are intrinsically difficult to detect from remote sensing approaches as they produce only minor amplitude deflection of the sea surface. Detection of internal waves through sea surface roughness variations visible on satellite images is possible (Alpers, 1985; Jackson et al., 2013) but limited by cloud cover and temporal resolution, which is often greater than a tidal period, making it challenging to create a continuous time series of internal waves. Therefore, short-term (weeks-months) field deployments with in-situ oceanographic measurements of temperature, pressure and currents at appropriate depths are used to successfully detect internal waves. However, these deployments only measure deflections at certain depths and can miss some waves. More importantly, they do not provide basin-scale spatial coverage or long time series records. The need for global detection and long time series of internal waves motivates a search for geophysical detection methods.

The pressure coupling of a propagating internal wave with the seafloor provides a potential mechanism to generate seismically observable signals. It is already well-established that oceanic surface waves generate “noise” on seismometers (Orcutt et al., 1993). There is a ubiquitous seismic noise peak at periods of approximately 2.5-25 seconds caused by ocean surface wave energy coupling into the ocean bottom, either from ocean waves in shallow water interacting with coastlines (primary microseisms) or wave-wave interactions (secondary microseisms)

(Bromirski, 2001; Bromirski et al., 2005; Tanimoto, 2007). Infragravity waves, ocean surface waves with periods longer than swell and wind-driven waves, have generated long period (20-400 seconds) signals on ocean-bottom seismometers (OBS) (Dolenc et al., 2008). Internal tides have also been recorded by OBS, including at the ocean bottom from “tremor” signals on OBS geophones (Chang et al., 2016) and infrequent (roughly twice per month) internal tidal bores identified as tilt signals on a broadband OBS (Fukao et al., 2016). Breaking internal waves were also potentially detected on a seafloor distributed acoustic sensing (DAS) cable (Lindsey et al., 2019). It is interesting to note that earthquakes can produce acoustic waves that propagate along the low velocity channel of the ocean (T-waves), and travel times of T-waves are impacted by the internal tide (Munk et al., 1981; Sugioka et al., 2005; Wu et al., 2020). Tsunami waves are a type of infragravity wave that have induced tilt signals due to loading on the seafloor observable on both island (Nishida et al., 2019; Yuan et al., 2005) and coastal (Boudin et al., 2013; Nawa et al., 2007) broadband seismometers; it is therefore possible for seafloor pressure perturbations to generate near-field tilt that is observable onshore.

A typical South China Sea internal solitary wave (i.e., nonlinear dispersive wave) of depression with an amplitude of 100 meters results in a hydrostatic pressure change of approximately 2.5 kPa (Moum and Smyth, 2006), which should generate a near-field tilt on the seafloor around 40 nanoradians (see Appendix C section C-2 for calculation). Broadband seismometers record rotational motion/tilt in addition to translational motion because the gravitational force due to a tilt change results in an acceleration (Wielandt and Forbriger, 1999). A tilt on the order of tens of nanoradians should be observable at long periods (>100 seconds) on a broadband seismometer (Ackerley, 2014), and would be expected as internal waves approach and pass a seismic station (Figure 3-1a). Since the seafloor is elastic, a broadband seismometer can also detect a near-field quasi-static tilt signal from a wave not passing directly over the instrument if the wave is within a distance roughly equal to the finite source length (i.e., the wavelength of the wave), similar to what has been observed on island and coastal seismic stations from passing tsunami waves. This is a simplified view that provides a minimum bound on the potentially observable seismic signals. As will be discussed later in this study, additional pressure sources associated with propagating internal waves would provide additional tilt. For instance, the dynamic pressure change on the seafloor from breaking or interacting internal waves may also result in a seismically observable signal through the same type of elastic interaction illustrated in Figure 3-1a (Moum and Smyth, 2006). In principle, seismology should be able to fill in the observational gap and provide long-term time series of internal waves.

Previous studies detecting internal tides and possibly internal waves using seismology have been based on sparse ocean-bottom instrumentation with little oceanographic context or corroborating data. Here we perform an initial evaluation of the subaerial seismic detectability of internal waves by analyzing potential seismic signals in the context of corroborating data. This pilot project is possible because of exceptional in situ data available from Dongsha Atoll in the South China Sea. On

Pratas Island at the western side of Dongsha Atoll (Figure 3-1c, d) a permanent seismic station (VDOS) and two temporary seismometers (May-June 2019) provide broadband seismic data. A temporary oceanographic deployment (May-June 2019) and available satellite data provide constraints on the arrival times of internal waves at Dongsha Atoll. We find a promising correlation between transient seismic tilt signals and internal wave arrival times in oceanic and satellite data, potentially leading the way to utilizing seismology for both the detection and amplitude determination of internal waves. Further, since there have been roughly 700 operational island stations since the first island station was installed in 1957, the technique applied to global island as well as coastal seismic stations could potentially provide information about the historic record and track the potential reaction of internal waves to climate change.

Figure 3-1. Map of the study area and schematic of a propagating internal solitary wave in the South China Sea. (a) Cartoon of a typical internal solitary wave in the South China Sea and the resulting (exaggerated) transient deformation (dashed brown curve), near-field tilting (dashed green curve) of the underlying seafloor (brown line), sea surface roughness (solid blue line) and radar image intensity (black line). This is a simplified cartoon that does not account for the interaction with the coast or nonlinear wave-wave interactions that would complicate an onshore signal. (b) Bathymetric map of the northern South China Sea. (c) Himawari-8 standard red channel image of sea surface reflections on May 15, 2019 05:30 UTC near Dongsha Atoll. Westward propagating internal waves are indicated by red arrows, including an incoming internal solitary wave from the Luzon Strait 500 km east of Dongsha Atoll, and the northern and southern arms of internal wave trains that are interacting and reforming west of Dongsha Atoll. (d) Zoom in of Dongsha Atoll. Oceanic temperature sensors shown as blue inverted triangles and land broadband seismometers on Pratas Island are shown as green triangles.

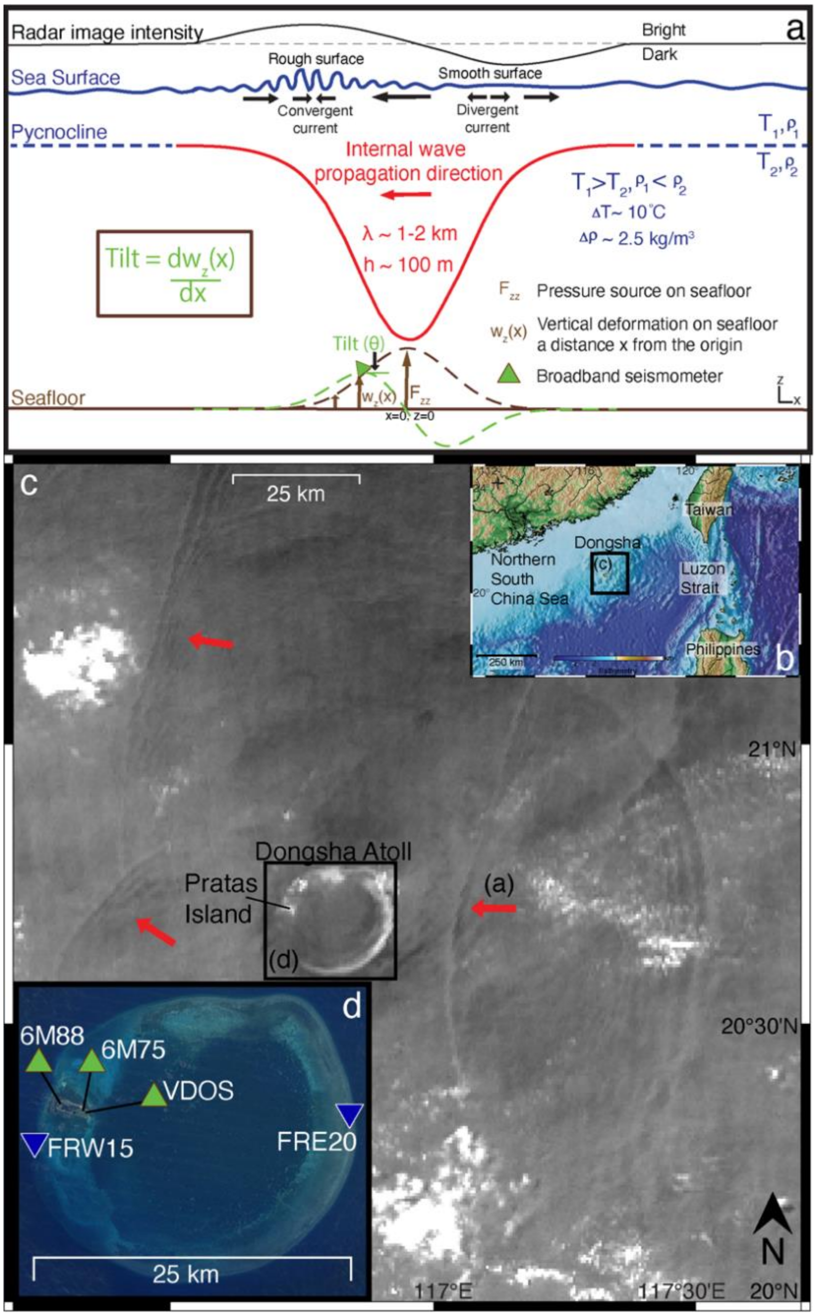
a
Radar image intensity
Bright
Dark
Rough surface
Smooth surface
Sea Surface
Convergent current
Divergent current
Pycnocline
T_1, ρ_1
T_2, ρ_2
Internal wave propagation direction
$T_1 > T_2, \rho_1 < \rho_2$
$\Delta T \sim 10^\circ C$
$\Delta \rho \sim 2.5\ kg/m^3$
$\lambda \sim$ 1-2 km
h ~ 100 m
$Tilt = \frac{dw_z(x)}{dx}$
F_{zz} Pressure source on seafloor
$w_z(x)$ Vertical deformation on seafloor a distance x from the origin
Broadband seismometer
Tilt (θ)
$w_z(x)$
F_{zz}
x=0, z=0
Seafloor
z
x
c
25 km
Taiwan
Dongsha
(c)
Northern South China Sea
Luzon Strait
Philippines
20°
250 km
b
21°N
Dongsha Atoll
Pratas Island
(a)
(d)
20°30'N
d
6M88
6M75
VDOS
FRW15
FRE20
25 km
N
117°E
117°30'E
20°N

3.2 Dongsha Atoll and the South China Sea

The largest amplitude (>100 m) internal solitary waves (i.e., nonlinear dispersive waves) in the world have been observed in the South China Sea. Depending on the stratification, internal solitary waves can propagate as waves of depression or elevation. The pycnocline in the South China Sea is < 100 m, but the basin is deep (up to 5000 m depth). This type of stratification is expected to generate waves of depression as have been observed in the northern South China Sea (Ramp et al., 2010; Simmons et al., 2011; Fu et al., 2012). Large diurnal and semidiurnal barotropic tidal currents flow roughly east-west over two north-south trending ridges in the Luzon Strait (Figure 3-1b), generating strong internal tides that propagate westward into the South China Sea in a narrow beam, steepening into internal solitary waves of depression (Duda et al., 2004; Ramp et al., 2004; Lien et al., 2005; Alford et al., 2015). Internal solitary waves, typically two per day, are generated at peak tidal velocities and their amplitude is modulated on a fortnightly cycle, with the largest amplitude waves generated at peak spring tide when the barotropic tidal forcing is greatest (Duda et al., 2004; Ramp et al., 2004; Lien et al., 2005). Internal waves occur regularly in the South China Sea between March and November and occasionally from December to February (Simmons et al., 2011). Ocean stratification is strongest in autumn and weakest in winter; since the generation of internal tides is dependent on stratification, this is likely the cause for the significant decrease in internal wave generation in the winter.

Dongsha Atoll is a 28 km diameter coral reef at the edge of the continental shelf in the northern South China Sea located approximately 500 km west of the Luzon Strait (Figure 3-1). It takes roughly 50 hours for internal waves generated in the Luzon Strait to arrive at Dongsha Atoll (Davis et al., 2020). Both modeling and observations of internal solitary waves as they propagate upslope at Dongsha Atoll suggests that an incident symmetric depression wave collapses into a packet of elevation waves during shoaling (Fu et al., 2012; Rogers et al., 2019). These wave trains break into northern and southern arms that refract around the atoll, eventually colliding and then reforming west of Dongsha Atoll (Figure 3-1c).

3.3 Data and methods

In order to identify internal wave signals in passive seismic data, we compare seismic observations from one permanent and two temporary seismic stations onshore of Pratas Island to established internal wave signals in satellite and oceanographic data during a temporary deployment in mid-May to mid-June 2019.

3.3.1 Satellite and oceanographic data

Alternating convergence and divergence zones above internal waves result in sea surface roughness changes that are visible from sun glint on satellite images (Alpers, 1985; Jackson et al., 2013). We use the 10-minute temporal and 500-meter spatial resolution standard red channel (0.64 µm wavelength) data of the Himawari-8 geostationary meteorological satellite operated by the Japan Meteorological Agency (JMA) to identify internal waves based on sea surface roughness changes for comparison to seismic observations (Figure 3-1a, c). With these images we can identify internal waves near Dongsha Atoll during daylight hours when there is little cloud cover.

Shoreward of the 100-meter isobath on Dongsha Atoll, internal solitary waves have transformed into packets of elevation waves (Fu et al, 2012; Davis et al, 2020). This is recorded as a sudden drop in water temperature measurements, approximately 4-8°C within several minutes, and is a well-established indicator of the passage of internal waves (Davis et al., 2020). We can therefore use the arrival times of internal waves from in-situ oceanographic temperature measurements to compare to a potential internal wave signal in coastal seismic data. To this end, we use 1-10 second sampling rate oceanic temperature measurements in the water column and on the ocean bottom during a temporary deployment in May/June 2019 around the fore reef of Dongsha Atoll (Figure 3-1d). We utilize a 20-meter mooring on the eastern side of Dongsha Atoll (FRE20) at 19 meters depth from May 13-June 11, 2019 and an ocean bottom temperature sensor at approximately 16.8 meters depth on the western side of Dongsha Atoll (FRW15) roughly 4.5 km southwest of a permanent seismic station onshore of Pratas Island from May 19-June 6, 2019. These shallow temperature sensors are located at depths where the large internal waves have already broken down slope into nonlinear elevation waves or internal bores, but they will still capture an internal wave signal, albeit a more complex and high-frequency one and lagged from the arrival time of the wave in deeper water as the wave decelerates in shallow water (Davis et al., 2020). Further, these point measurements may miss internal wave arrivals depending on stratification and reflection properties of the internal waves.

To help guide the detection of internal waves arriving from the Luzon Strait on these two shallow temperature sensors we rely on the timing of internal wave detections from two deeper (300 m and 500 m depth) moorings 6-9 km east of Dongsha Atoll before internal solitary waves of depression have interacted much with the bottom or transformed into packets of elevation waves. In particular, we use the wave arrival times at the 300 m mooring, wave velocities calculated between the 500 and 300 m moorings, and the distances from the 300 m mooring to the eastern (FRE20; 6.7 km) and western (FRW15; 30.9 km) sensors to estimate the wave arrival times at these shallow sensors. However, these are used as rough time estimates only since they are based on the wave velocity between the 500 m and 300 m moorings, which on average was 1.8 m/s during the deployment, and wave velocities can decrease below 0.5 m/s in shallow water (Fu et al., 2012; Davis et al., 2020). Variations in wave velocity create uncertainty in arrival times at the shallow temperature sensors. For example, a wave with a phase speed of 2 m/s would propagate around the 28 km diameter atoll in approximately 3.9 hours, while a wave with a phase speed of 1 m/s would propagate the same distance in 7.8 hours. It is therefore difficult to predict the exact arrival time of waves at the shallow sensors without measurements of the wave velocities in shallow water.

3.3.2 Seismic data

For seismic data we primarily use the three-component broadband seismometer VDOS operated by the Broadband Array in Taiwan for Seismology (BATS) network located onshore of Pratas Island on the west side of Dongsha Atoll

(Figure 3-1d). This Trillium 120-second posthole instrument is deployed at 2.7 meters depth and has a 100-Hz sampling rate. We additionally deployed two temporary broadband seismometers (6M88 and 6M75 on Figure 3-1d) on Pratas Island from May 11 - June 4, 2019. The signal-to-noise ratio for these two instruments is lower than for VDOS; these stations are primarily used for confirmation of signals observed on VDOS.

Internal solitary waves of depression in the South China Sea propagate with velocities of 2-3.5 m/s (depending on water depth) and wavelengths of 1-2 km. Therefore, in the deep basin, the period of these waves is about 285-1000 seconds. As the waves shoal at Dongsha Atoll, they slow and break up into a packet of shorter period (200-850 s) elevation waves (Fu et al, 2012; Davis et al, 2020). Therefore, it is reasonable to look for a long period tilt signal of passing internal waves on the horizontal components of VDOS. We anticipate a seismically observable tilt signal within roughly 10 km of the source based on the 1-2 km wavelength of these waves. We first decimate the 100-Hz VDOS raw seismic data to 1 Hz by downsampling by a factor of 10 twice, each time applying a low-pass filter. We then apply an acausal (two-pass) 400-second low-pass filter to the decimated seismic data. We do not remove the instrument response when initially identifying small, transient tilt signals in VDOS that are potentially from internal wave activity to prevent identifying deconvolution artifacts as signals. The raw seismic data is in counts, which on VDOS is proportional to velocity at periods below 120 seconds.

There is a diurnal seismic tilt signal on the horizontal components of VDOS (Figure 3-2), 6M75 and 6M88 during daylight hours (22:00 - 10:00 UTC; 6 am - 6 pm local time). This presents a challenge in differentiating between other diurnal tilt-generating signals such as tidally modulated internal waves; the source of this diurnal tilt “noise” is therefore important. Daily temperature fluctuations can cause a change in instrument sensitivity at long periods. Daily temperature fluctuations for the tropical climate on Pratas Island are ~5°C (Figure C-1). For this temperature change, the instrument sensitivity change is about 0.04% (Anthony et al., 2018). The diurnal tilt changes are greater than this sensitivity change. In addition, the Trillium 120-second posthole sensor is buried at 2.7 m depth, below the depth where surface temperature variations are strongest. It is therefore unlikely that the diurnal tilt signal is from instrumental changes in sensitivity with temperature. It is more likely that the diurnal signal is from Pratas Island tilting as a result of diurnal temperature fluctuations as has been observed on other islands (Bilham and Beavan, 1979; Arnoso et al., 2001; Ekström et al., 2006). The amplitude variations of the seismic signal do not correlate with the amplitude of land temperature measurements recorded on the island (Figure C-1). In particular, when daily temperature fluctuations on Pratas Island are largest (May 16 - May 21), the diurnal tilt signal in the seismic recordings is lowest. However, the barometric pressure is larger at these time periods and may result in stronger thermal coupling. The north-south seismic components experience larger diurnal tilt signals than the east-west components; it is possible that Pratas Island preferentially tilts north-south due to its east-west elongation (Figure 3-1d). It is possible that the preferential north-south tilt Pratas Island will bias transient tilt signals in the north-south direction.

3.4 Observations

In order to find tilt signals on VDOS potentially generated by internal waves from the Luzon Strait we need to 1) identify transient tilt signals on VDOS, 2) compare the transient seismic tilt signals to established internal wave signals in satellite and oceanographic data, 3) verify that the tilt signals on VDOS are physical by comparing them to the temporary seismometers 6M75 and 6M88, and 4) determine whether tilt signals of interest are consistent with expected near-field tilt amplitudes generated by internal solitary waves in the South China Sea.

3.4.1 Transient seismic tilt signals

There are transient increases in tilt within the longer period diurnal noise on VDOS HHN and HHE (Figure 3-2). These signals appear to be largest and most frequent during spring tide at the Luzon Strait (Figure 3-2) when the largest amplitude internal waves are generated. Further, transient seismic tilt signals appear to increase at times when the oceanic temperature record at FRE20 has the highest variance, indicative of internal wave activity (Davis et al., 2008) (Figure 3-2). It is therefore possible that some of the observed transient seismic tilt signals are due to internal waves arriving from the Luzon Strait. It should also be noted that the thermal transients on FRE20 are also due to non-tidal currents, the local internal tide, and locally-generated internal waves, which may also generate tilt observable on VDOS.

Figure 3-2. Oceanic water temperature and land seismic data from May 13 - June 11, 2019. Oceanic water temperature measurements at 19 m depth from FRE20 (Figure 3-1d) on the east side of Dongsha Atoll are shown in blue. VDOS HHE (brown) and HHN (green) components are shown with an acausal 400-second low-pass filter applied. Earthquake time periods are highlighted in grey. The Luzon Strait tidal velocities (black lines) were estimated using the Oregon State Tidal Inversion Software (Egbert and Erofeeva, 2002) and plotted with a 50-hour time shift. Spring (yellow) and neap (grey) time periods are indicated. The days that the seismic data is analyzed in more detail in sections 4.2-4.5 are highlighted in red.

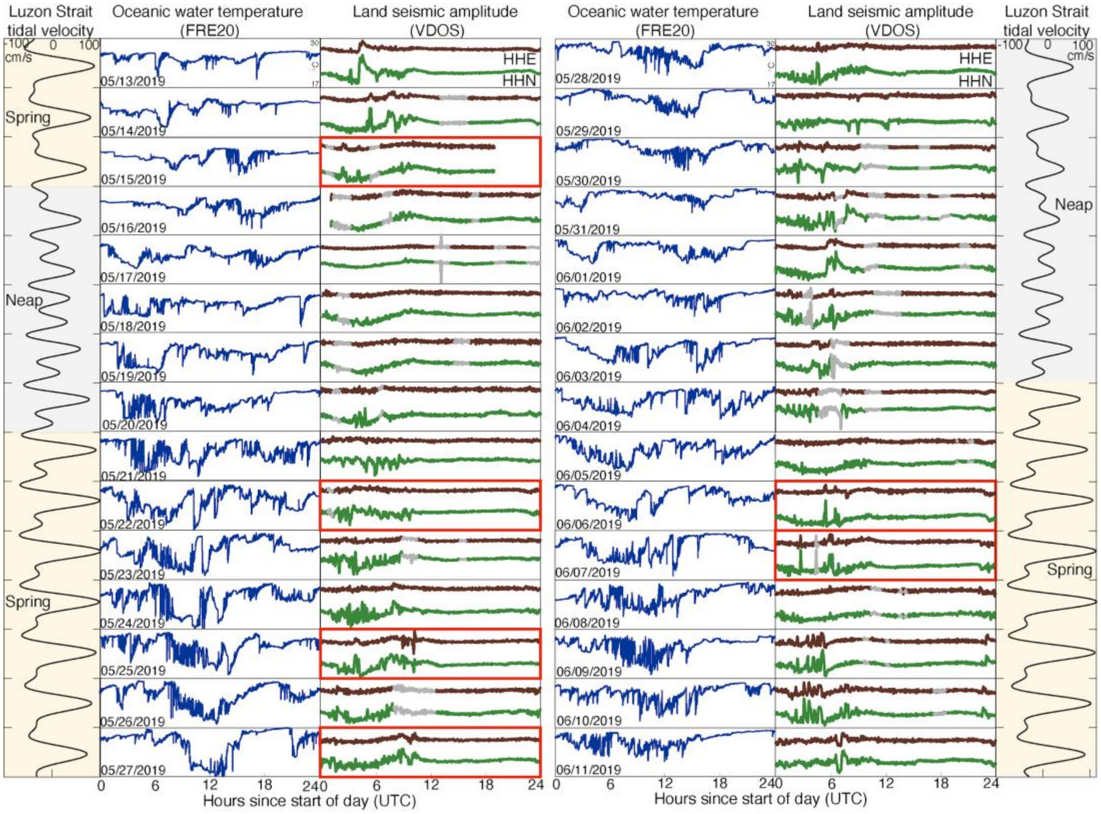
Luzon Strait tidal velocity
Oceanic water temperature (FRE20)
Land seismic amplitude (VDOS)
Oceanic water temperature (FRE20)
Land seismic amplitude (VDOS)
Luzon Strait tidal velocity
-100 0 100
cm/s
30
°C
17
HHE
HHN
Spring
Neap
Spring
Neap
Spring
05/13/2019
05/14/2019
05/15/2019
05/16/2019
05/17/2019
05/18/2019
05/19/2019
05/20/2019
05/21/2019
05/22/2019
05/23/2019
05/24/2019
05/25/2019
05/26/2019
05/27/2019
05/28/2019
05/29/2019
05/30/2019
05/31/2019
06/01/2019
06/02/2019
06/03/2019
06/04/2019
06/05/2019
06/06/2019
06/07/2019
06/08/2019
06/09/2019
06/10/2019
06/11/2019
0 6 12 18 24
Hours since start of day (UTC)
0 6 12 18 24
Hours since start of day (UTC)

3.4.2 Comparison of seismic and satellite observations

We use the Himawari-8 geostationary satellite images on exceptionally clear days from June 6-7, 2019 (Figure 3-3a,b,c; Appendix C Movie C-1) to identify internal waves on the western side of Dongsha Atoll for comparison to transient tilt signals on VDOS. We find that the largest transient increases in tilt on VDOS HHN and HHE are temporally correlated with times when internal waves are clearly visible on satellite images near the western side of Dongsha Atoll near Pratas Island and VDOS (Figures 3-3c, 3-4i; Appendix C Movie C-1). The potential seismic internal wave signals have durations of 30 minutes to 1 hour, are largest on the HHN component (Figures 3-3c, 3-4i), and are roughly 3.5-6 and 2-3 times the background noise on the HHN and HHE components, respectively (Figures C-2, C-3). There appear to be two seismic internal wave signals on June 6 separated by one hour (Figure 3-3c). On June 7, there were two peaks in the transient tilt signal (Figure 3-4i) but there is little separation.

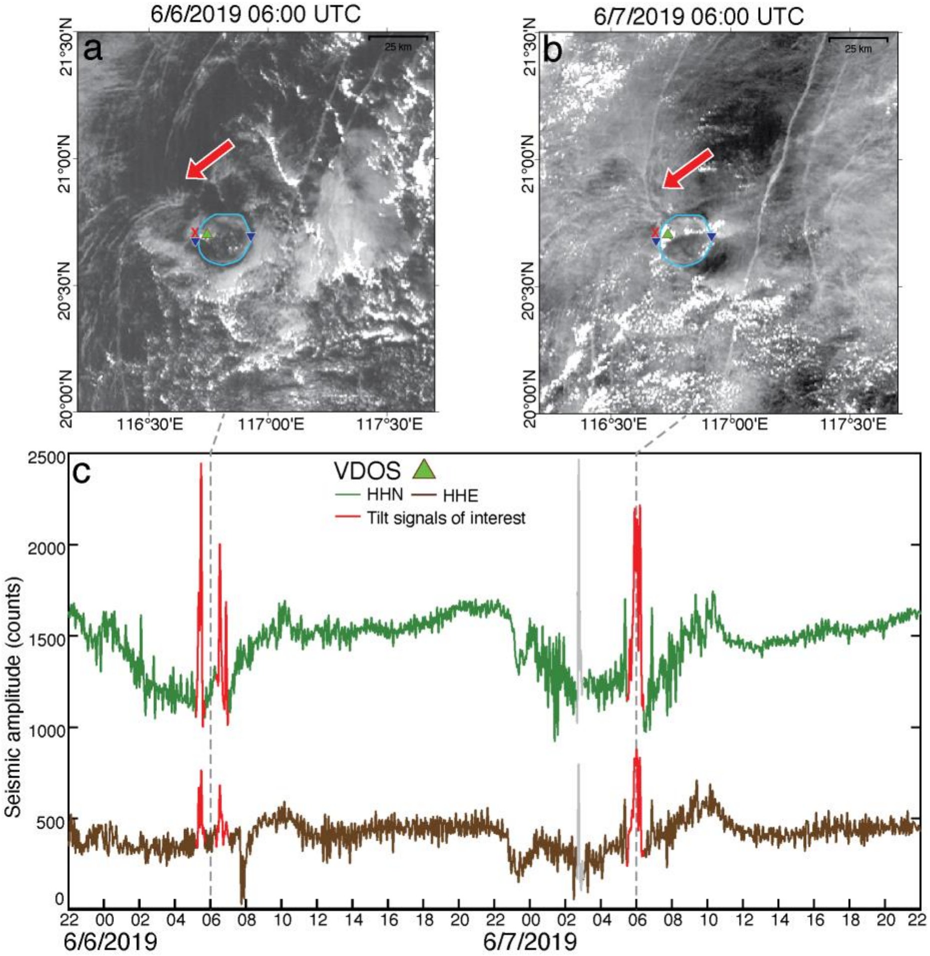

Figure 3-3. Comparison of satellite images and seismic observations as internal waves pass Dongsha Atoll. (a)-(b) Himawari-8 standard red channel images on June 6, 2019 06:00 UTC and June 7, 2019 06:00 UTC. Dongsha Atoll outlined in light blue. Seismic station VDOS on Pratas Island (green triangle) and oceanic temperature sensors (blue inverted triangles) are included. The closest point of internal waves to Pratas Island and VDOS is marked with a red X. Internal waves passing around the western side of Dongsha Atoll are indicated by the red arrows. (c) VDOS components HHE and HHN with an acausal 400-second low-pass filter applied. Tilt signals potentially correlating with timing of internal wave arrivals on the western side of Dongsha Atoll are indicated in red. Earthquake or instrument malfunction times are indicated in grey. The timing of the satellite images are indicated by the dashed grey lines. Time is in UTC. See Appendix C Movie C-1 for a movie of satellite images and seismic data from June 6 - June 7, 2019.

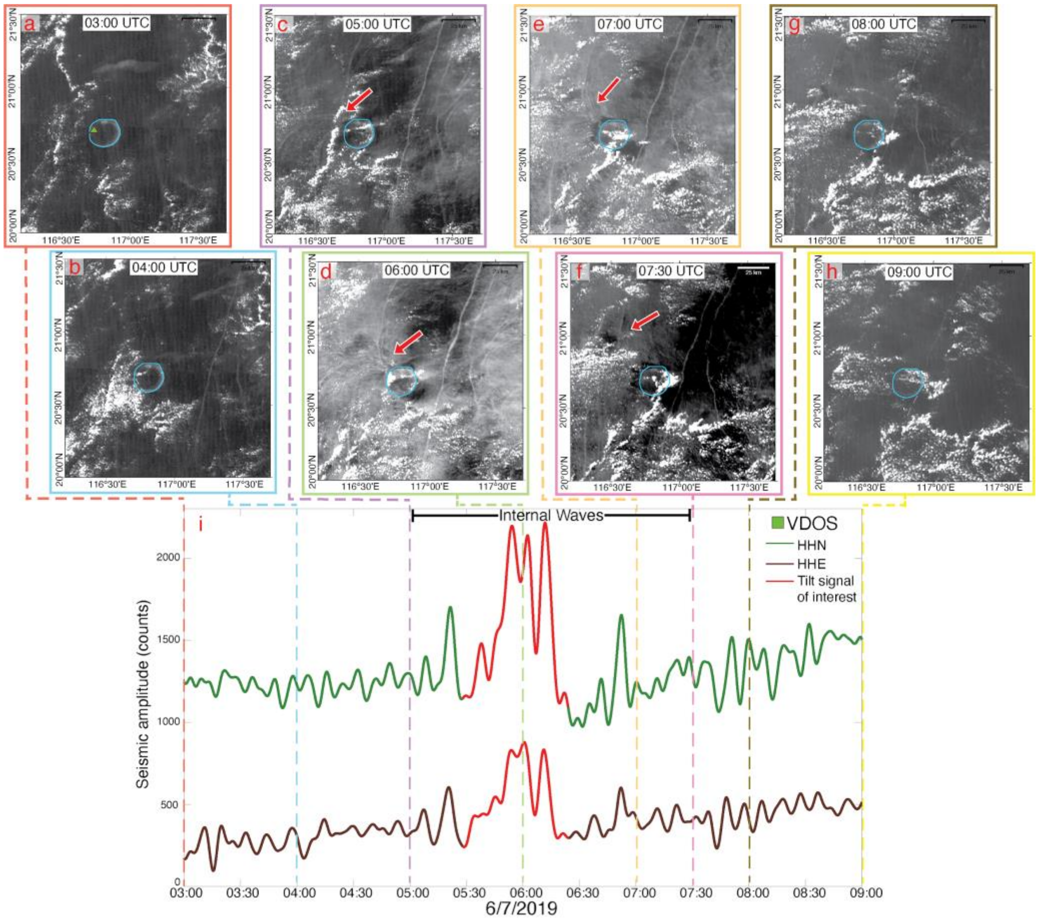

Figure 3-4. Detailed comparison of satellite images and seismic observations as internal waves pass Dongsha Atoll. (a)-(h) Himawari-8 standard red channel images on June 7, 2019 from 03:00 - 09:00 UTC. Dongsha Atoll is outlined in light blue. VDOS seismic station is shown as the green square on panel (a). Internal waves passing around the west side of Dongsha Atoll are indicated by the red arrows. (i) VDOS components HHE and HHN with an acausal 400-second low-pass filter applied. The largest tilt signal is highlighted in red. Timing of the satellite images are indicated with dashed lines corresponding to the border colors of the satellite images. The time period where internal waves are observed on the west side of Dongsha Atoll based on the satellite images is indicated. Time is in UTC. See Appendix C Movie C-1 for a movie of satellite images and seismic data from June 6 - June 7, 2019.

3.4.3 Comparison of seismic and oceanographic observations

There was significant cloud cover from May 18 - June 5, 2019 that prevented the detection of internal waves on satellite images. We can therefore only compare transient seismic tilt signals to thermal transients indicative of internal waves in oceanic water temperature data during this time period. However, differentiating between internal waves arriving from the Luzon Strait, the local internal tide, and locally-generated internal waves at individual shallow oceanic temperature sensors is challenging, and all of these oceanic processes may generate tilt observable at VDOS. Further, depending on the depth of temperature measurements and the pycnocline, internal wave arrivals may be missed by individual shallow oceanic temperature sensors. We therefore rely on the deeper oceanic moorings located 6-9 km east of FRE20 before waves interact strongly with the bottom as a guide of expected arrival times for internal waves generated at the Luzon Strait.

Guided by the deeper moorings we were able to identify internal wave arrivals from the Luzon Strait on May 25 (Figure 3-5b) and May 27, 2019 (Figure 3-5a) during spring tide at both the shallow oceanic water temperature sensors (FRE20 and FRW15), with arrivals at FRW15 lagging 2-4 hours behind FRE20. There are clear transient seismic tilt signals of similar duration on VDOS HHN and HHE that lag 1-1.5 hours behind FRW15 (Figure 3-5a,b). These lags are consistent with a packet of internal waves arriving at Dongsha Atoll from the Luzon Strait, breaking into northern and southern arms as they refract around the atoll, with the southern arm passing FRW15 before reaching the nearest point to VDOS. We were additionally able to identify internal wave arrivals at FRE20 on May 22, 2019 during spring tide (Figure 3-5c). An internal wave signal is not clear on FRW15 at the anticipated arrival time; however, there are transient tilt signals in the seismic data near the expected arrival time (Figure 3-5c).

The thermal transient signals on FRE20 and FRW15 on May 25 and May 27 both related and potentially unrelated to internal wave activity warrant additional discussion. On May 27 the internal wave signal on FRW15 appears to occur during the local steepened internal tide. It is therefore possible that the observed seismic signal is from a combination of the internal wave arrival from the Luzon Strait and the local internal tide. Further, there was a temperature drop on FRW15 two hours prior to the internal wave arrival, which may also be related to the seismic signal (Figure 3-5a). On May 25 there was a large thermal transient propagating from FRE20 to FRW15 (highlighted in orange on Figure 3-5b) approximately 5 hours prior to the internal wave arrival from the Luzon Strait. There is also a transient tilt signal on VDOS that is lagged 3 hours behind FRW15. This lag is longer than the 1-1.5 hour lag observed for VDOS following FRW15 for internal wave arrivals from the Luzon Strait (Figure 3-5a, b). This signal was not observed at the deeper offshore moorings and is therefore unlikely to arrive from the Luzon Strait. This transient may instead be a locally-generated internal wave. However, if this is an internal wave arrival from the Luzon Strait, the increased lag may be due to a collision point farther north of Pratas Island or a slower wave velocity.

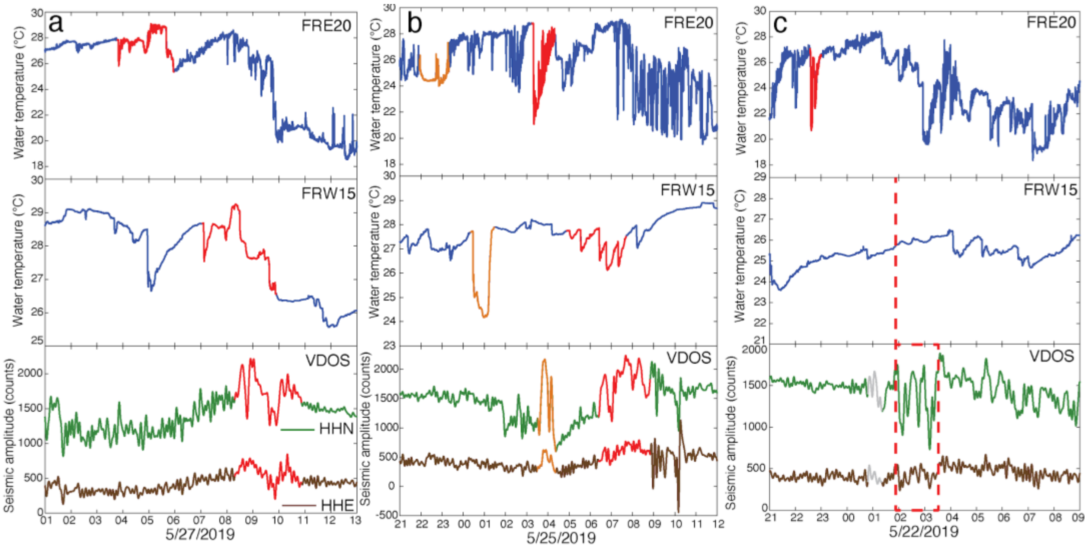

Figure 3-5. Comparison of shallow oceanic water temperature data to seismic observations at VDOS during spring tide on May 27 (a), May 25 (b), and May 22 (c). Top: Shallow water temperature measurements at 19 m depth (FRE20 on Figure 3-1d) on the east side of the Dongsha Atoll shown in blue. Middle: Shallow water temperature measurements on the ocean bottom at 16.8 m depth (FRW15 on Figure 3-1d) on the west side of Dongsha Atoll shown in blue. Bottom: VDOS components HHE (brown) and HHN (green) with an acausal 400-second low-pass filter applied. Internal wave signals arriving from the Luzon Strait on shallow temperature data and corresponding potential internal wave signals on VDOS are highlighted in red on (a) and (b). A potential local internal wave signal is highlighted in orange in (b). The approximate timing of internal wave arrivals on FRE20 is indicated by the red dashed line in (c) and a potential seismic signal is indicated by the red dashed box. Time is in UTC.

3.4.4 Signal across seismic stations

To verify that the transient tilt signals of interest on VDOS are physical, we select a time period (May 15, 2019) when two temporary seismometers (6M75 and 6M88) were operating and at least partial satellite identification of internal waves is available to corroborate the seismic signals. Internal waves are visible on satellite images on the west side of Dongsha Atoll at 05:40 UTC on May 15, 2019 (Figure 3-6b). However, internal waves have passed roughly 20 km west of Pratas Island by the time they can be clearly identified in the satellite image due to cloud cover. It is expected that transient tilt signals observed on broadband seismometers on Pratas Island would occur 3-5.5 hours before this time depending on wave velocity ranging from 1-2 m/s. Two transient tilt signals are visible on VDOS, 6M75, and possibly on 6M88 (Figure 3-6a) starting around 02:00 and 04:00 UTC that are consistent with the satellite time constraints.

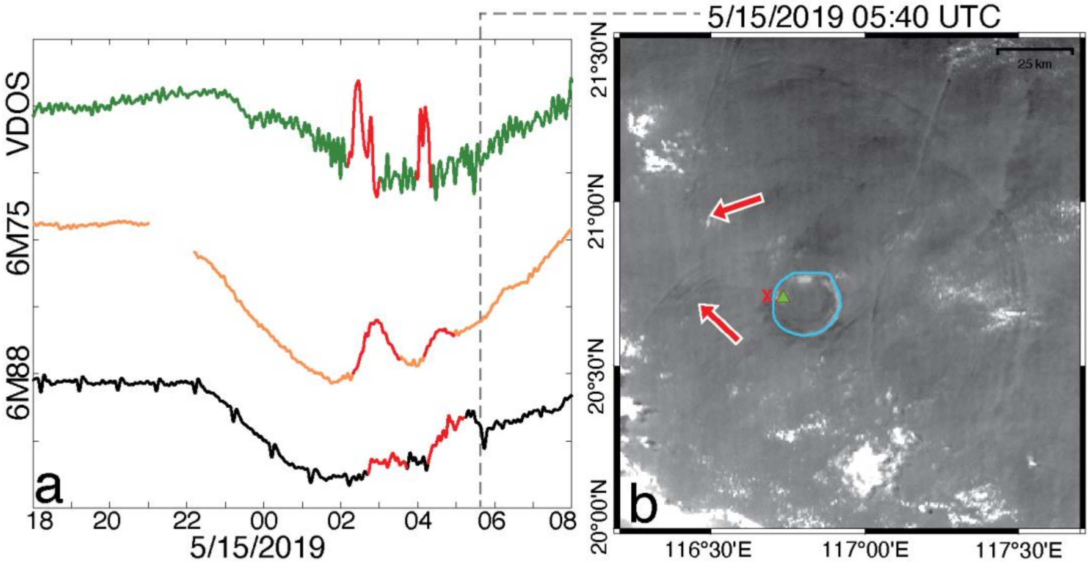

Figure 3-6. Comparison of tilt signal across seismic stations on May 15, 2019. (a) VDOS HHN (green), 6M75 BHN (orange), and 6M88 BHN (black) with acausal 400-second low-pass filters applied. Large transient tilt signals are highlighted in red. Timing of the satellite image in (b) is indicated by the grey dashed line. (b) Himawari-8 standard red channel images on May 15, 2019 at 05:40 UTC. Dongsha Atoll is outlined in blue. Seismic station VDOS on Pratas Island is indicated by the green triangle, the closest point of internal waves to Pratas Island and VDOS is marked with a red X. Internal waves that have recently passed Dongsha Atoll are indicated by the red arrows.

3.4.5 Seismic amplitude

We can estimate the seismic amplitudes during the six days of potential internal wave arrivals detailed in sections 4.1-4.4. We first deconvolve the instrument response to acceleration. We performed a simple linear detrend and then applied a cosine taper band-pass filter with four corner frequencies appropriate for identifying long-period tilt signals expected from internal waves (1/2400 Hz, 1/1200 Hz, 0.5 Hz, and 1 Hz). After the response was deconvolved we decimated the 100-Hz data to 1 Hz by downsampling by a factor of 10 twice, each time applying a low-pass filter. We then applied an acausal 400-second low-pass filter to the seismic data and analyzed the previously identified potential seismic internal wave signals in the raw seismic data (Figure 3-7). It appears that peak seismic tilt signals range from roughly 35 to 80 nanoradians on VDOS HHN (Figure 3-7). Tilt amplitudes are smaller for VDOS HHE, ranging from 15 to 35 nanoradians.

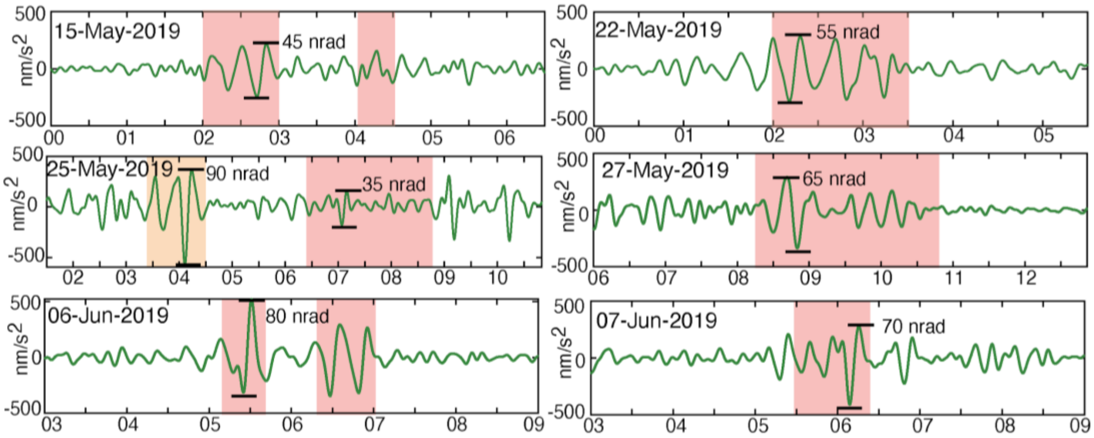

Figure 3-7. Amplitude of seismic internal wave detections. VDOS HHN (green) with the response deconvolved and an acausal 400-second low-pass filter. Approximate timing of internal waves near Pratas Island arriving from the Luzon Strait highlighted in red. A potential local internal wave signal on May 25 highlighted in orange. Rough peak tilt amplitudes in nanoradians (nrad) during internal wave time periods indicated in black. Timing (in hours) is UTC.

3.5 Summary of observations and potential mechanisms

We have found promising evidence of the seismic detection of internal waves. First, there are transient tilt signals on a permanent broadband seismometer onshore of Pratas Island that appear to be larger and occur more frequently during spring tide when the largest amplitude internal waves in the South China Sea are generated at the Luzon Strait (Figure 3-2). These are also the time periods when the oceanographic temperature records have the highest variance, indicative of internal wave activity (Davis et al., 2008). Second, we were able to temporally correlate some of these transient seismic tilt signals with internal wave detections near Pratas Island from satellite and oceanic water temperature measurements (Figures 3-3 – 3-6). Third, some of the transient seismic tilt signals that correlate temporally with satellite and oceanographic measurements are also observed on temporary seismometers on Pratas Island, indicating that these tilt signals are physical (Figure 3-6). Finally, the seismic amplitude of the tilt signals of interest are on the order of tens of nanoradians, consistent with expectations for a near-field elastic tilt signal generated by internal solitary waves in the South China Sea (see Appendic C section C-2 for calculation) (Figure 3-7). These observations taken together are strong evidence of the seismic detection of internal waves.

We now consider two mechanisms to generate seismically observable transient tilt signals through the pressure coupling of internal waves with the underlying seafloor.

3.5.1 Passing of internal waves

The most straightforward mechanism for an internal wave to generate a seismically observable transient tilt signal is simply by passing near a broadband seismometer. As discussed in section 1, the hydrostatic pressure change and resulting elastic deformation of the underlying seafloor from a propagating internal solitary wave typical in the South China Sea would cause a near-field tilt of around 40 nanoradians (Figure 3-1a; Appendix C Section C-2). This is a useful conceptual framework, though it is oversimplified for the geometry of Dongsha Atoll and requires further discussion.

Internal waves arriving from the Luzon Strait refract around Dongsha Atoll. Therefore, the nearest point internal waves reach to VDOS on Pratas Island is at the fore reef approximately 4 km west of VDOS (marked on Figure 3-3a). It is anticipated that the largest hydrostatic pressure change and therefore near-field tilt signal observable by VDOS would occur at this point. This would generate a smaller tilt signal than expected from our calculation (Appendix C Section C-2), which assumes the wave directly passes the seismometer. In addition, the waves are broken into a packet of elevation waves, rather than a single solitary wave of depression, which would further complicate the expected tilt signal.

It is worth noting that the two peaks in transient tilt observed on VDOS on June 6 (Figure 3-3c) are consistent with the deeper mooring observation that this arrived as a two-packet wave. The June 7 wave was a single solitary wave and only one primary peak was observed in the seismic data (Figure 3-3c).

3.5.2 Collision of internal waves

Another mechanism for internal waves to generate near-field tilt signals large enough to be observed seismically is from wave-wave interactions or collisions. This is because breaking or interacting internal waves can produce dynamic pressure changes on the seafloor in addition to hydrostatic pressure changes expected from a passing wave (Moum and Smyth, 2006). The dynamics of nonlinear internal wave interactions are complex and dependent upon the wave amplitudes and interaction angle (Wang & Pawlowicz, 2012). While our measurements do not permit a detailed characterization of the interaction region, satellite imagery of the Dongsha Atoll region clearly shows that as a soliton propagates past the shallow bathymetry of the atoll, it breaks into northern and southern arms that collide after reaching the west side of Dongsha Atoll before eventually reforming (Hsu and Liu, 2000; Li et al., 2013) (Figures 3-1c, 3-3a,b, 3-4c,d,ef, Appendix C Movie C-1). These nonlinear wave-wave interactions would generate both dynamic and hydrostatic pressure changes coupled to the seafloor, causing near-field elastic displacement and tilt that are expected to be larger and thus more observable than for a single propagating wave. We favor this mechanism for several reasons.

First, the observed tilt signals on the north-south component of VDOS range from 35-80 nanoradians (Figure 3-7). This is larger than the 40 nanoradians expected from the hydrostatic pressure change alone, although it is still within the error of this simple calculation. Second, the seismic tilt signals lag 1-2 hours behind internal wave detections on the nearest oceanic temperature sensor (FRW15). The point of nearest approach to VDOS is roughly 3 km north of FRW15; we therefore expect internal waves to first be detected on FRW15. However, considering wave velocities ranging from 0.5-2 m/s, the seismic tilt signals are anticipated to lag 25-100 minutes behind FRW15. The larger observed lag suggests that the peak seismic tilt signals are generated after the waves pass the nearest point to VDOS, potentially when the northern and southern arms interact. The seismic signal from wave-wave interactions may be from the collisions of multiple waves within a packet at the crossover point of the northern and southern arms. Based on satellite images during the study period (Figures 3-3a,b, 3-4c,d,e,f, Appendix C Movie C-1), these collisions occur north-northwest of Pratas Island, within the expected observational limit of VDOS of roughly 10 km.

3.6 Caveats and conundrums

3.6.1 North-south dominant tilt

The likely internal wave signals on VDOS are largest on the north-south component. This may be due to a combination of the preferential tilt of the island as well as the source of the tilt signals. It is likely that the east-west elongated Pratas Island preferentially tilts north-south, as is observed with the diurnal tilt signal (Figures 3-2, C-1). It is unclear at this point if the preferential north-south tilt of Pratas Island would create a north-south bias for other transient tilt sources. In addition, internal waves “wrap” north-south around Dongsha Atoll (Li et al., 2013). When the northern and southern arms meet and collide on the west side of Dongsha Atoll, they are still propagating in a north-south direction (Figures 3-3a,b, 3-4c,d,e,f).

This may produce a dominant north-south tilt. Further, the tilt experienced on Pratas Island may be amplified if this collision point occurs farther north or south, rather than due west of the island.

3.6.2 Detection of only one type of wave

During the study period all the potential internal wave signals identified in the seismic data occur between 02:00 and 11:00 UTC (10:00 and 19:00 local time). This is predominantly during daylight hours and within the large diurnal seismic tilt noise. No potential internal wave detections are made more than once per day. However, internal waves are generated up to twice daily at the Luzon Strait and have been classified as type-a or type-b waves (Duda et al., 2004; Ramp et al., 2004). Type-a waves are generated primarily by the K1 tide, typically have a large amplitude wave followed by smaller amplitude waves, and arrive at the same time each day, 24 hours apart (Duda et al., 2004; Ramp et al., 2004). Type-b waves have a larger contribution from the M2 tidal constituent, propagate as a packet of waves, and arrive approximately one hour later each day (Duda et al., 2004; Ramp et al., 2004). Type-b waves are generated in the northern portion of the Luzon Strait while type-a waves are generated farther south (Du et al., 2008; Ramp et al., 2019). The deeper moorings provide more detailed observations of type-a and type-b waves during the deployment period. In general, type-a waves arrived as two or three-wave packets at an angle more south of east. Type-b waves arrived from almost due east as solitary waves that then broke into multi-wave packets of approximately equal amplitude and spacing between waves.

All of the potential seismic signals we identify are from type-b waves. During the study period, type-b waves arrive on the west side of Dongsha Atoll during daylight hours which allows for identification of these waves and wave-wave interactions on clear days near Pratas Island using satellite imagery. Type-a waves arrive at the east side of Dongsha Atoll around 09:00 UTC (17:00 local time). We can therefore at times identify their arrival but cannot track these waves to the west side for better temporal comparison to onshore seismic data. This makes identifying a seismic signal from type-a waves difficult. Still, there are no clear transient tilt signals on VDOS during expected type-a arrival times on the west side of Dongsha Atoll. Below is a discussion of why type-a waves, and some type-b waves, may not be detected by VDOS.

The collision of the northern and southern arms refracting around Dongsha Atoll is likely a key generator of seismically observable tilt (see section 5.2). Therefore, refraction of waves around Dongsha Atoll and the location of the western collision are important for tilt generation. It is thus potentially significant that in this study only type-b waves have been observed to refract around Dongsha Atoll. This may be due to lack of satellite observations of type-a waves, or lack of satellite signature of type-a waves refracting.

Potential reasons for type-b waves to generate a seismically observable tilt while type-a waves do not include systematic differences in incoming angle, frequency content, depth of the main thermocline upon arrival during local internal tide, or interactions with the bottom. For instance, empirically it is seen that type-b waves refract asymmetrically around Dongsha Atoll resulting in the western collision occurring north-northwest of Pratas Island (Figures 3-3a,b, 3-4c,d,e,f, Appendix C Movie C-1). This may be due to the incoming angle, bathymetry and bathymetry-related velocity differences around the atoll. This asymmetry can generate a larger north-south pressure change and therefore north-south tilt of the underlying seafloor. Since the east-west elongated Pratas Island likely preferentially tilts north-south, this may be a more observable signal. Alternatively, type-a waves arrived with the local tide, creating more disturbances in the thermocline. Last and more speculatively, type-a and type-b waves may interact differently in the near-shore environment due to their frequency content. Type-a and type-b waves are generated in different parts of the Luzon Strait (Du et al., 2008; Ramp et al., 2019). This difference in generation site may affect the frequency content of the waves which may ultimately impact the interactions in the near-shore environment observed in the seismic data.

Not all type-b waves are clearly detected in the seismic data above the noise. The amplitude of waves will also determine the pressure change and near-field tilt signal. The diurnal tilt noise is around 5-10 nanoradians. Therefore, the tilt signal from a relatively small amplitude internal wave, potentially during neap tide, can likely be hidden in the diurnal tilt noise.

3.6.3 Seismic performance compared to existing methods

There are transient tilt signals on VDOS throughout the study period that we have not correlated with internal waves arriving from the Luzon Strait. This is partially due to incomplete satellite and oceanographic measurement coverage;

however, it is likely that some of these signals are not from internal waves generated at the Luzon Strait. The local internal tide and locally-generated internal waves may also cause observable transient tilt signals on VDOS. Caution is therefore warranted at this time when identifying internal wave signals and their origin using seismic data alone.

Satellite imagery can provide remarkable spatial detail and identification of internal waves. However, satellite visible images are limited temporally, are unavailable at night and are highly unreliable during daylight hours. The deeper oceanic temperature moorings reliably detect internal waves of depression before they have interacted with the bottom and transformed, but are limited spatially. The shallow oceanic temperature sensors record internal waves after they have transformed into packets of elevation waves and are shoaling or breaking in the near-shore environment. The shallow temperature sensors are noisy, recording complicated near-shore internal wave interactions as well as non-tidal currents, the local internal tide, and locally-generated internal waves. Other measurements, such as satellite images or deeper moorings, are required to reliably identify internal waves arriving from the Luzon Strait in the shallow temperature data. The seismic data also requires additional verification of internal wave identification at this time, but is currently performing similarly to the shallow temperature sensors. This work is a first proof of concept using onshore seismometers to detect internal waves. Necessarily, the proof of concept is being done where independent data demonstrating the existence of the waves is available. The logical next step would be to utilize the seismic data to identify waves in the absence of such ground truth and we hope to achieve that in future work.

3.6.4 Mechanism

As discussed in section 5, the mechanism for internal waves to generate seismically observable tilt signals on Pratas Island is unclear. However, we favor large (i.e., observable by VDOS) transient tilt signals generated on the west side of Dongsha Atoll near Pratas Island as the northern and southern arms collide and reform, generating both hydrostatic and dynamic pressure changes on the underlying seafloor and therefore near-field displacement and tilt.

3.7 Conclusion

It appears that we have successfully detected oceanic internal waves using a subaerial island seismometer for the first time. We observe dominant north-south transient tilt signals on a broadband seismic station onshore of Pratas Island with amplitudes similar to what is expected from internal solitary waves arriving from the Luzon Strait. These seismic tilt signals appear correlated with internal wave detections in satellite and oceanic data, and apparently occur when waves collide nearshore. The north-south dominance is consistent with internal waves refracting around Dongsha Atoll and the east-west elongated Pratas Island preferentially tilting north-south. This initial detection suggests that the onshore seismic detection and amplitude determination of oceanic internal waves is possible and can potentially be used to expand the historical record by capitalizing on existing island and coastal seismic stations.

3.8 Brief follow-up study from ocean-bottom seismic observations

3.8.1 Purpose and introduction

A broadband OBS with an ocean-bottom pressure sensor was deployed approximately 60 km northeast of the Dongsha Atoll from November 2019 – December 2020 (Figure 3-8a). This data was acquired after the previous analysis was complete, and thus provides a good test of interpretations from the terrestrial seismometer study. This data also presents an excellent opportunity to seismically observe internal waves of depression arriving from the Luzon Strait that have not yet transformed into packets of elevation waves in shallow water. The signal from an internal wave of depression observed on an OBS will be simpler than what was observed on the shallow temperature sensors and land seismic stations (section 3.4), more similar to the cartoon in Figures 3-1a and 3-8b. Here we perform a brief study of ocean-bottom seismic observations of internal waves to demonstrate the detection capability, opening up the potential for a year-long study of internal wave arrivals at Dongsha Atoll. We look first at seasonal and fortnightly tidal signals expected from internal waves in the South China Sea, followed by comparisons of individual internal wave detections to co-located ocean-bottom pressure data and satellite observations.

3.8.2 Data and methods

The broadband OBS (BB01) had three seismic channels (HHZ, HH1, and HH2) and one pressure channel (HDH). We orient the horizontal seismic components of BB01 by analyzing the polarization of seismic waves from the M_W 7.8

July 22, 2020 Simeonof, Alaska earthquake and find HH1 and HH2 are oriented at approximately 36º and 126º, respectively. We analyze long-period, transient tilt signals potentially from internal waves arrivals at BB01 similar to VDOS (section 3.3.2). We first decimate the 100-Hz BB01 raw data to 1 Hz by downsampling by a factor of 10 twice, each time applying a low-pass filter. We then apply an acausal (two-pass) 400-second low-pass filter to the decimated data. We do not remove the instrument response to prevent identifying deconvolution artifacts as the long-period signals of interest.

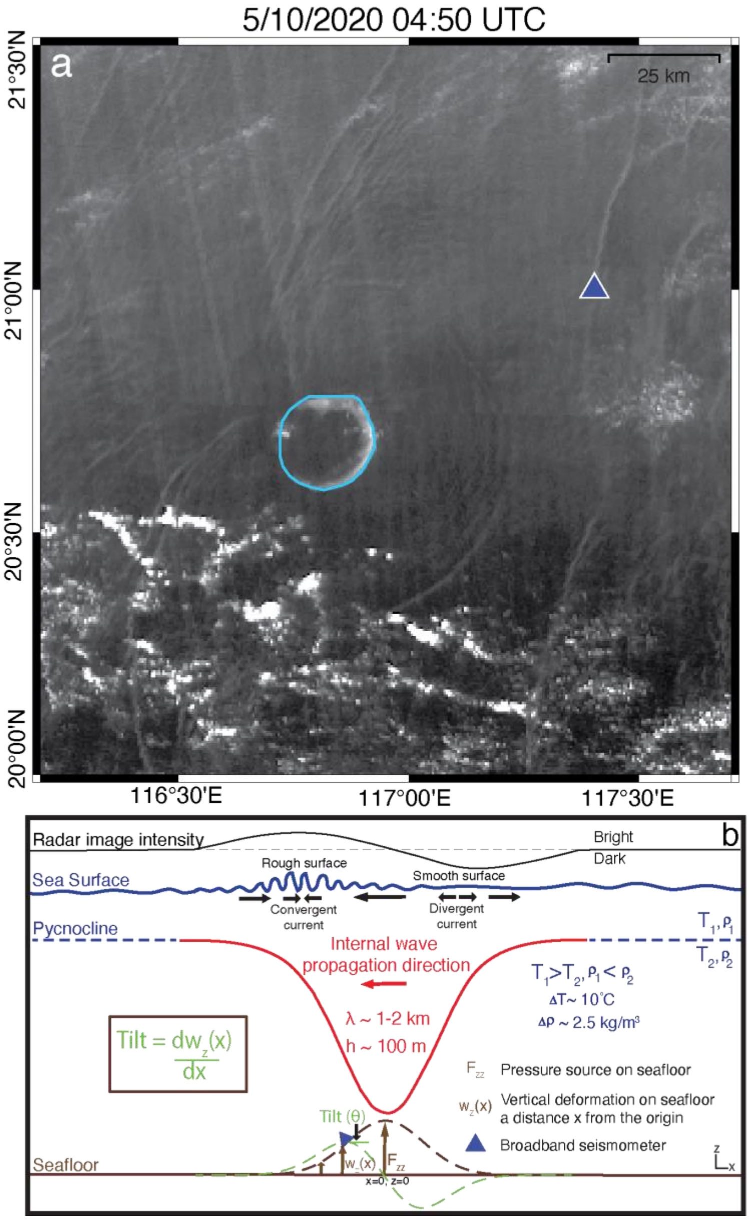

Figure 3-8. Map of Dongsha Atoll with ocean-bottom seismic station BB01 and cartoon of an internal solitary wave of depression. (a) Himawari-8 standard red channel images on May 10, 2020 04:50 UTC. Dongsha Atoll outlined in light blue. Ocean bottom seismic station BB01 is indicated as the dark blue triangle. (b) Cartoon of internal solitary wave of depression from Figure 3-1a.

3.8.3 Observations

There are fewer transient signals on BB01 from December 2019 – February 2020 than the rest of the year (Figure 3-9), consistent with previous observations of internal waves in the South China Sea and the expectation of a significant decrease in internal wave generation in the winter due to weaker ocean stratification (Simmons et al., 2011). During months with strong ocean stratification internal waves are typically generated twice per day at the Luzon Strait at peak tidal velocities with amplitudes modulated on a fortnightly cycle, with the largest amplitude waves generated at peak spring tide (Duda et al., 2004; Ramp et al., 2004; Lien et al., 2005).

We find a clear modulation in transient signals on BB01 in a fortnightly cycle from May 1 – June 30, 2020 (Figure 3-10). This is consistent with the tidally modulated internal waves generated at the Luzon Strait. The transient signals are clearest on components HDH and HHZ and least clear on component HH1. Our observations are consistent with previous work recording internal waves in the South China Sea using ocean-bottom pressure sensors (Lien et al., 2014).

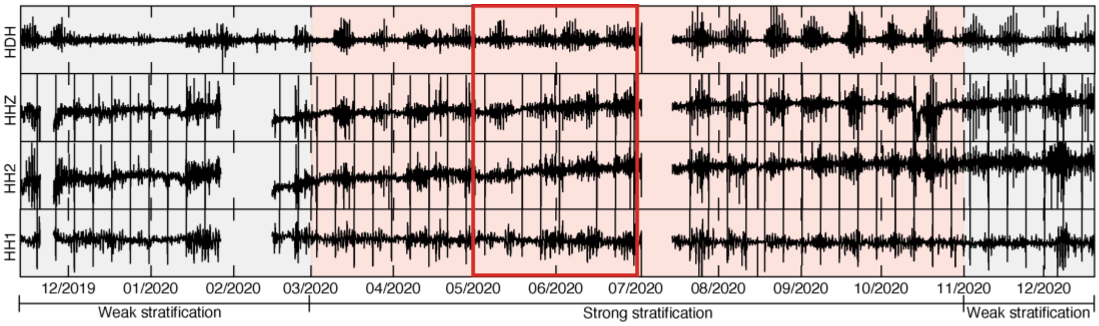

Figure 3-9. Year of ocean-bottom seismic data. BB01 components HDH, HHZ, HH1, and HH2 with an acausal 400-second low-pass filter applied are shown in black. Time periods of typical strong ocean stratification in the South China Sea when internal waves are generated are highlighted in red. Time periods of typical weak ocean stratification in the South China Sea when internal waves are not generated are highlighted in grey. The time of Figure 3-10 is outlined in red. Time is in UTC.

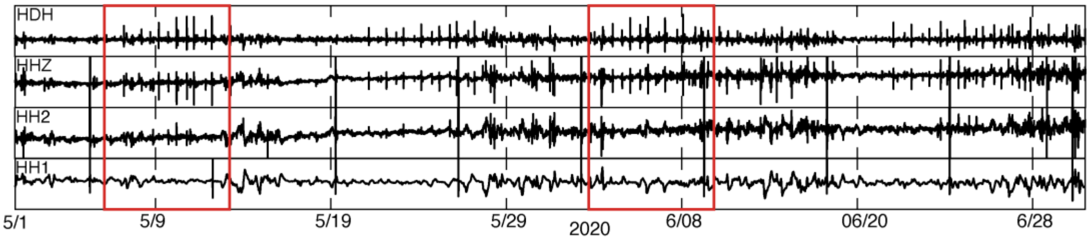

Figure 3-10. Spring-neap tidal cycle of internal wave detections on BB01. BB01 components HDH, HHZ, HH2, and HH1 are shown in black with an acausal 400-second low-pass filter applied. The times of Figures 3-11 and 3-14 are outlined in red. Time is in UTC.

We next analyze in more detail May 6 – May 12, 2020 and find two arrival periods of internal waves on most days (Figure 3-11). At the start of each day around the same time (~05:00 UTC) there is a large transient signal on BB01 HDH, HHZ, and HH2. On three days there is also a second, smaller arrival following the larger one by roughly 2 hours. This is consistent with type-a waves that typically have a large amplitude wave followed by smaller amplitude waves and arrive at the same time each day, 24 hours apart (Duda et al., 2004; Ramp et al., 2004). On at least five of these days, there is a second internal wave packet that arrives roughly one hour later each day. These arrivals are smaller and less impulsive than the type-a waves. This is consistent with type-b waves, which propagate as a packet of waves and arrive approximately one hour later each day (Duda et al., 2004; Ramp et al., 2004).

We use the Himawari-8 geostationary satellite images on clear days on May 10 and May 12, 2020 (Figures 3-12, 3-13) to identify internal waves passing BB01. We find transient signals on BB01 channels HDH, HHZ, and HH2 that are temporally correlated with times when internal waves are clearly visible on satellite images passing over BB01 (Figures 3-12, 3-13). On both days, a large transient signal is followed by a smaller signal 2-2.5 hours later. These signals have durations of 20 to 40 minutes. There is first a pressure decrease, large increase, and then slight decrease visible on BB01 HDH that is anti-correlated with BB01 HHZ. The signals are consistent with what is expected from internal solitary waves generating pressure changes on the underlying seafloor that cause seismically observable near-field deformation and tilt (Figure 3-12a).

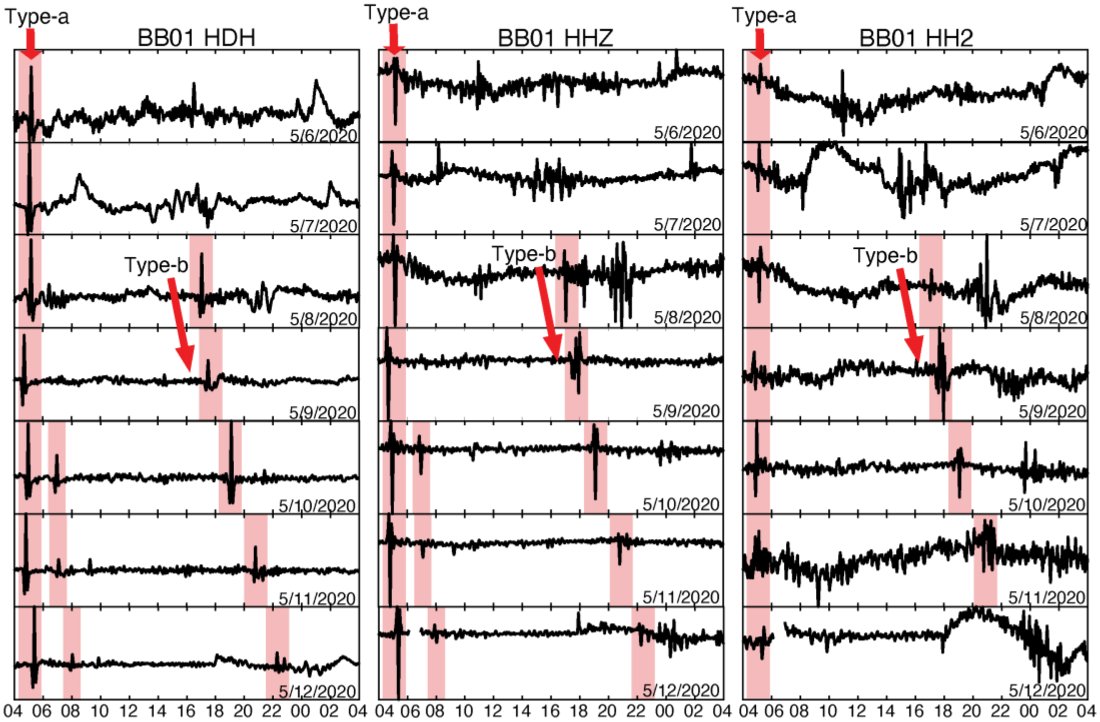

Figure 3-11. Ocean-bottom seismic observations from May 6 - May 12, 2020. Ocean-bottom seismic data from BB01 (Figure 3-8a) with an acausal 400-second low-pass filter applied are shown in black. Internal wave arrival times are highlighted in red. Type-a vs type-b wavs are indicated. Time is in UTC.

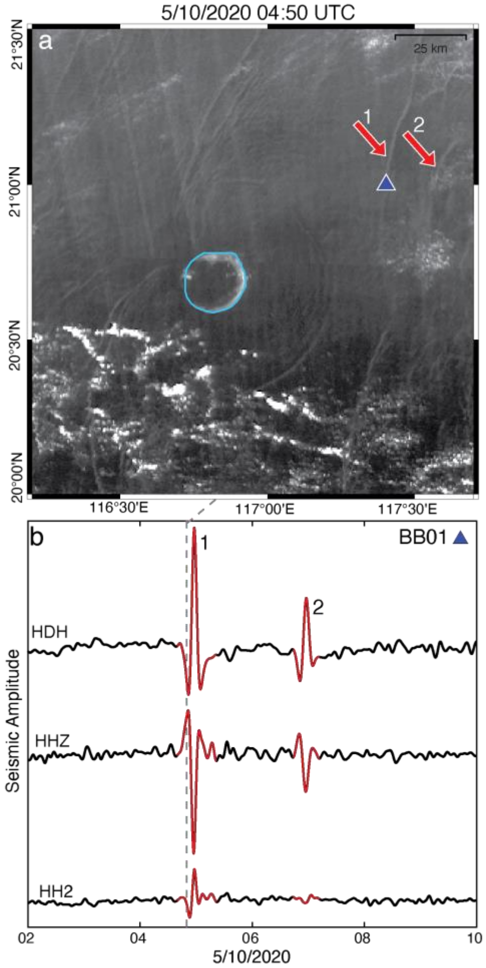

Figure 3-12. Comparison of satellite and ocean bottom seismic observations from passing type-a internal waves on May 10, 2020. (a) Himawari-8 standard red channel images on May 10, 2020 04:50 UTC. Dongsha Atoll outlined in light blue. Ocean bottom seismic station BB01 is indicated as the dark blue triangle. Two incoming internal waves are indicated by the red arrows and labeled as 1 and 2. (b) BB01 components HDH, HHZ, and HH2 with an acausal 400-second low-pass filter applied. Tilt signals from the two passing internal waves labeled as 1 and 2 on panel (a) are highlighted in red. The timing of the satellite image is indicated by the dashed grey line. Time is in UTC.

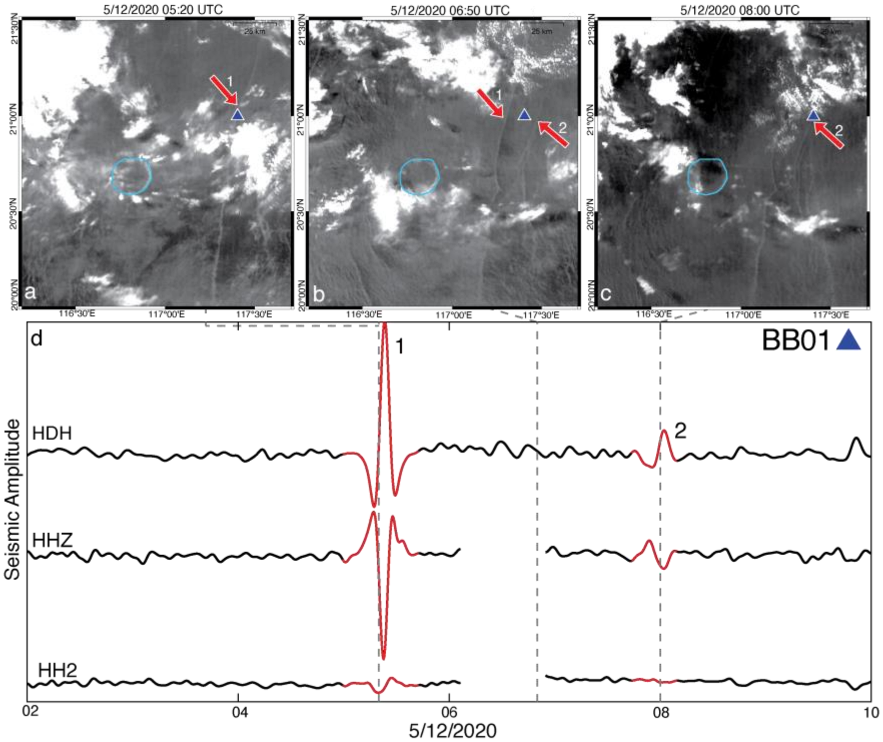

Figure 3-13. Comparison of satellite and ocean bottom seismic observations from passing type-a internal waves on May 12, 2020. (a)-(c) Himawari-8 standard red channel images on May 12, 2020 at 05:20, 06:50, and 08:00 UTC. Dongsha Atoll outlined in light blue. Ocean bottom seismic station BB01 is indicated as the dark blue triangle. Two incoming internal waves are indicated by the red arrows and labeled as 1 and 2. (d) BB01 components HDH, HHZ, and HH2 with an acausal 400-second low-pass filter applied. Tilt signals from the two passing internal waves labeled as 1 and 2 on panel (a) are highlighted in red. The timing of the satellite images are indicated by the dashed grey line. Time is in UTC.

We next analyze in more detail June 3 – June 9, 2020 and find two arrival periods of internal waves on most days (Figure 3-14). Similar to Figure 3-11, at the start of each day around the same time (~01:00 UTC) there is a large transient signal on HDH, HHZ, and HH2. On four days there is also a second, smaller arrival following the large one by roughly two hours. This is consistent with type-a waves. On each of these seven days there is a second internal wave arrival packet that arrives roughly one hour later each day, consistent with type-b waves.

We compare satellite images of internal wave passing BB01 on June 4, 2020 (Figure 3-15) and interacting near VDOS on the west side of Dongsha Atoll. We find that a type-b wave that passed BB01 around 12:00 UTC on 6/3/2020 (Figures 3-14, 3-15b) is interacting on the western side of Dongsha Atoll at 04:40 UTC on 6/4/2020 (Figure 3-15a), and is apparently observed on VDOS starting at 06:00 UTC on 6/4/2020 (Figure 3-15c).

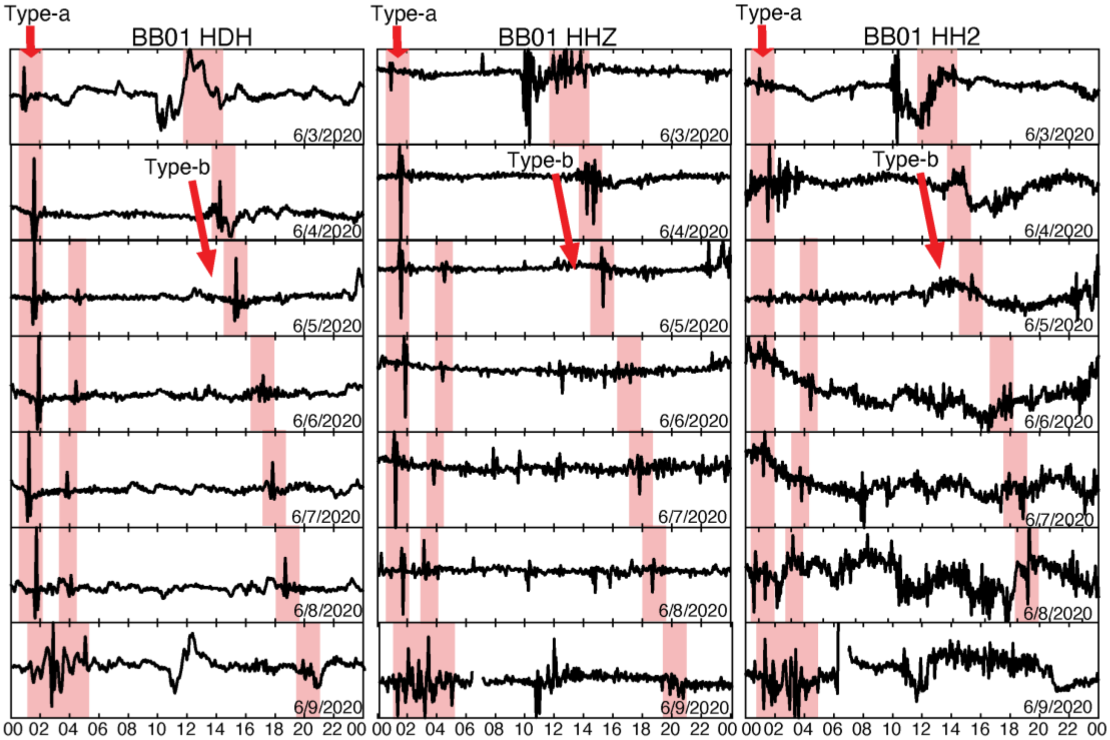

Figure 3-14. Ocean-bottom seismic observations from June 3 – June 9, 2020. Ocean-bottom seismic data from BB01 (Figure 3-8a) with an acausal 400-second low-pass filter applied are shown in black. Internal wave arrival times are highlighted in red. Type-a vs type-b wavs are indicated. Time is in UTC.

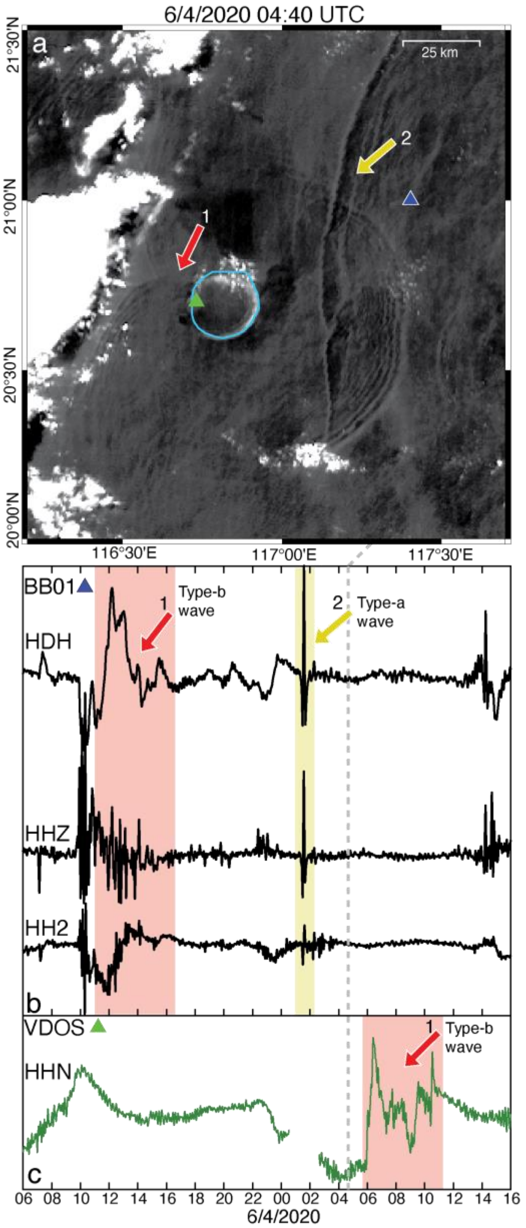

Figure 3-15. Comparison of satellite, ocean bottom, and land seismic observations from a type-b internal wave on June 4, 2020. (a) Himawari-8 standard red channel images on June 4, 2020 04:40 UTC. Dongsha Atoll outlined in light blue. Ocean bottom seismic station BB01 is indicated as the dark blue triangle. Land seismic station is indicated by the green triangle. Internal waves interacting on the west side of Dongsha Atoll near VDOS are indicated by the red arrow. Internal waves arriving from the Luzon Strait that have already passed BB01 are indicated by the yellow arrow. (b) BB01 components HDH, HHZ, and HH2 with an acausal 400-second low-pass filter applied shown in black. The apparent timing of the two internal wave packets labeled as 1 and 2 on panel (a) are indicated and colored according to the corresponding arrows. (b) VDOS HHN with an acausal 400-second low-pass filter applied shown in green. The apparent timing of the internal wave packet labeled as 1 on panel (a) is indicated and colored according to the corresponding arrow. The timing of the satellite image is indicated by the dashed grey line. Time is in UTC.

3.8.4 Discussion and conclusions

Internal tides have been recorded by OBS, including at the ocean bottom from "tremor" signals on OBS geophones (Chang et al., 2016) and sporadic internal tidal bores identified as tilt signals on a broadband OBS (Fukao et al., 2016). Further, internal waves have been recorded on ocean-bottom pressure sensors in the South China Sea (Lien et al., 2014). However, long-period tilt signals from internal solitary waves have not been observed on broadband OBS.

We were able to identify both type-a and type-b internal waves on the seismic components of BB01 that correlate temporally with the pressure component (HDH) and satellite images where available. The vertical component of BB01 is anti-correlated with the pressure, as is expected since a pressure decrease would cause uplift of the seafloor and a pressure increase would cause a depression of the seafloor. This initial detection opens up the possibility of a year-long study of differences in incoming angles of type-a and type-b waves, which would have interesting implications for the different generation locations of these waves.

The transient signals from internal waves are least clear on BB01 component HH1 which is oriented at approximately 36º. It is possible that a tilt signal from passing internal waves arriving mostly from the east would not have a large signal in this direction. It appears that we tracked a type-b wave from BB01 to VDOS on June 4, 2020. No type-a waves from May-June 2020 were clearly detected on VDOS, consistent with our previous observations of only type-b waves detected by VDOS.

This initial detection of internal wave signals on BB01 opens up the possibility of removing internal wave oceanographic “noise” on OBS which could ultimately improve the detection of microseismicity.

Appendices

Appendix A – Supplemental Information for Chapter 1

Data and Methods

A.1 Hikurangi Ocean Bottom Investigation of Tremor and Slow Slip (HOBITSS) Network

The Hikurangi Ocean Bottom Investigation of Tremor and Slow Slip (HOBITSS) experiment deployed 24 absolute pressure gauges (APG) and 15 ocean-bottom seismometers (OBS) offshore of Gisborne, New Zealand from May 2014 - June 2015. Nine of the 15 deployed OBS stations returned data that can be used for time-sensitive analyses (EOBS 1-5, LOBS 1, 2, 6, and 8; Figure 1-1). Two stations (LOBS 4 and 5; Figure 1-1) did not return seismic data during the slow slip event, and four stations (LOBS 3, 7, 9, and 10; Figure 1-1) have timing errors. Stations with timing errors are used in determining first-motion polarities, but do not contribute to the earthquake catalogs or template matching performed in this study.

A.2 Earthquake Locations

We use preliminary earthquake hypocentral locations and origin times from two earthquake catalogs compiled by J. Yarce (personal communication, 2018) and Todd et al. (2018). Both catalog's earthquakes were manually detected by picking P-wave and S-wave (where possible) arrivals at HOBITSS OBS stations and available land GeoNet seismic stations. The J. Yarce catalog includes events during the entire OBS deployment (May 2014 – June 2015). The Todd et al. catalog focuses on events between September and October 2014, around the 2014 Gisborne SSE, and has more events during this time period than the J. Yarce catalog. We use 500 events from the

Todd et al. catalog between September 1, 2014 and October 31, 2014, and 1,694 events from the J. Yarce catalog for the remainder of the study period (May 18, 2014 – August 31, 2014; November 1, 2014 – June 21, 2015), within the study region shown in Figure 1-1. Preliminary hypocenters were found using Antelope's *dbgenloc* and *dblocsat2* algorithms. Hypocentral locations were then improved by relocating events with NonLinLoc v.6.0 (Todd et al., 2018) or BayesLoc (J. Yarce, personal communication, 2018).

To improve relative earthquake locations, we attempt to relocate the total 2,194 events (NonLinLoc and BayesLoc relocations) using GrowClust, a relative relocation algorithm that uses waveform cross-correlations (Trugman and Shearer, 2017). Cross-correlations are used to both determine waveform similarity and improve input differential travel times. GrowClust applies a hybrid, hierarchical clustering algorithm to both group and relocate events within similar clusters. Greater weight is given to event pairs with higher cross-correlations. This algorithm does not require explicit matrix inversion, improving stability, and uses the L1 norm so the results are less sensitive to input time outliers.

We use a local 1-D interpretation of the New Zealand 3-D velocity model (Eberhart-Phillips et al., 2010) centered offshore at -38.8361/178.4672 (Figure A-3). This velocity model is not well constrained offshore. A comparison to the 1-D velocity model developed by Haijima, D. (2015) that uses both land and OBS stations for better offshore constraints is provided in Figure A-3. For our study, the upper 10 km is of most interest because it is the depth range containing the clustered events above the subducted seamount that we interpret as occurring in the upper plate. The Eberhart-Phillips et al. (2010) velocity model has slower offshore seismic velocities above 3 km, then larger offshore seismic velocities until ~10 km compared to the Haijma model. Therefore, use of the Haijima 1-D velocity model in relocation would result in a deepening of the shallowest earthquakes (<3 km) and a shallowing of events in the 3-10 km depth range. These depth changes would move most of the burst-type repeating earthquake families farther from the plate interface and increase our confidence of their location within the upper plate fracture network above the subducted seamount.

Prior to performing waveform cross-correlations, traces are filtered using a 3-10 Hz 1 pass band-pass filter to remove noise on OBS stations below 3 Hz. For all event pairs, we compute cross-correlations for 0.6 seconds around the P-phase (0.2 second pre-pick) on the vertical channels. A maximum station distance of 100 km, a minimum average cross-correlation of 0.2 for each event pair, and a maximum root-mean-square (RMS) differential time residual of 0.3 s to join clusters are used for GrowClust parameterization. With these criteria, 773 of the input 2,194 events are relocated. Events not relocated lack waveform similarity, which is unsurprising given the scattered locations in the study area (Figures A-1 and A-2) and sparse station coverage (even with the HOBITSS array). GrowClust implements a nonparametric resampling approach to estimate location uncertainties, allowing an assessment of the relocation results. Errors are median absolute deviations of the bootstrap distribution of hypocenter locations. Average horizontal and vertical location errors are 790 m and 720 m, respectively (Figure A-2). Few events have final locations on the plate interface offshore. The clustered seismicity shown in Figure A-2b where burst-type repeating earthquakes are found is located within the upper plate even considering the uncertainty in GrowClust locations. All 2,194 events, both GrowClust relocations and non-relocated Bayesloc and NonLinLoc locations, are shown in Figures A-1 and A-2.

A.3 Template Matching

We use template matching to identify repeating earthquakes. We select template earthquakes from the GrowClust relocated earthquake catalog (773) as well the remaining 1,421 events not relocated with GrowClust. We are interested in events potentially related to the SSE. We therefore select events with final locations within 5 km of the plate interface in the general area of the SSE (Figure A-1), for a total of 123 template events. Few of these potential plate boundary events are located within the modeled region of slow slip (slow slip >50 mm). Templates are generated and run two different ways to increase detections and account for emergent P-phase arrivals. The procedure is similar to that outlined in Igarashi et al. (2003).

The first set of templates are cut to five-second long windows around the P-phase arrival (0.15 second pre-pick). These templates often include the S-phase arrivals. Template events are then filtered using a 3-10 Hz zero-phase band-pass filter to minimize oceanic noise on the OBS stations. Template matching is performed on the vertical components. The second set of templates are clipped to two-second long windows around the S-phase (1 second pre-pick) to detect events with emergent P-phase arrivals. These template events are also filtered using a 3-10 Hz zero-phase band-pass filter and horizontal components are used.

Both sets of templates are scanned through continuous data between May 12, 2014 and June 20, 2015 using an open-source Python package, EQcorrscan (Chamberlain and Hopp, 2017). OBS stations are used because events are generally small (<M_L 2) and poorly recorded on land stations. Further, the five EOBS stations (200 Hz sampling rate) have the highest signal-to-noise ratio and are predominantly used. For our study, a cross-correlation coefficient of greater or equal to 0.95 at a minimum of three or more stations is considered a repeating earthquake candidate. Figures A-4 – A-7 give sample repeating earthquake seismograms. These are repeating earthquake candidates with high correlation-coefficients in the bandpass selected (3-10 Hz). Generally, events with this high level of similarity are located within one-quarter of the dominant wavelength (Geller and Mueller, 1980). The dominant frequency is 10 Hz (cut-off frequency used). Assuming a P-wave velocity of 4-5 km/s, the dominant wavelength is 400-500 m. Thus, any potential repeating earthquake pairs detected are likely less than 100-125m from each other.

A.4 Magnitude Estimation

We compute local magnitudes (M_L) for template events using the *Mlrichter* Antelope package, which is a computational class for computing M_L using magnitude and correction functions from Richter (1935). The correction values as a function of distance ($\log A_0$) established by Richter (1935) and applied in *Mlrichter* are based on observed shaking for southern California earthquakes. However, attenuation characteristics differ for New Zealand. We therefore edited the $\log A_0$ attenuation relationship for calculating M_L in the *Mlrichter* program based on the $\log A_0$ function for New Zealand earthquakes derived by Ristau et al. (2016), in which

$$\log A_0(R) = 0.29 - (1.27\times10^{-3})R - 1.49\log(R) \quad (1).$$

The resulting $\log A_0$ curve differs significantly from Richter (1935) at hypocentral distances (R) of less than 100 km and greater than 200 km.

We use the singular value decomposition (SVD) method presented by Rubinstein & Ellsworth (2010) to determine magnitudes of each earthquake within repeating earthquake families. We consider relative amplitudes, rather than moments, to compute the local magnitude of each repeating event based on the local magnitude of the template event, using the following relation:

$$M_L^i = \log_{10}\frac{A^i}{A^t} + M_L^t \quad (2),$$

where A^i/A^t is the relative amplitude for the ith event, and M_L^t is the local magnitude for the template event.

We align the waveforms using cross-correlation prior to performing SVD analysis. To enhance signal to noise ratio (SNR) we apply a 3-10 Hz zero-phase bandpass filter. SVD analysis is computed used windows similar to what was used for template matching (i.e., either 5-second long windows with 0.15 second pre-pick relative to P-phase on vertical EOBS components or 2-second long windows with 1 second prior to S-phase on horizontal EOBS components). We require a cross-correlation of 0.85 at individual stations to compute SVD. Template and repeating earthquake detection magnitudes are included in Figure 1-3 and Table A-1 (families near the subducted seamount).

A.5 Composite Focal Mechanisms

We are interested in the faulting geometry of the repeating earthquake families at the subducted seamount to determine whether these, like the SSE, occur on the plate interface. Since most of the earthquakes within a family are small ($M_L < 2$), first-motion polarities are generally only available at a few nearby stations. Therefore, rather than compute focal mechanisms, we determine whether the repeating earthquake families collocated with the subducted seamount are consistent with the geometry of the megathrust hosting the SSE. We take advantage of the high similarity between repeating earthquakes in a family and stack waveforms at each station within a family to better determine P-wave first-motion polarities. Based on 4-6 available first-motion polarities for each family, nine of the eleven repeating earthquake families collocated with the subducted seamount are not consistent with underthrusting on the plate interface. The other three composite focal mechanisms are potentially consistent with the megathrust geometry.

Figures and Tables

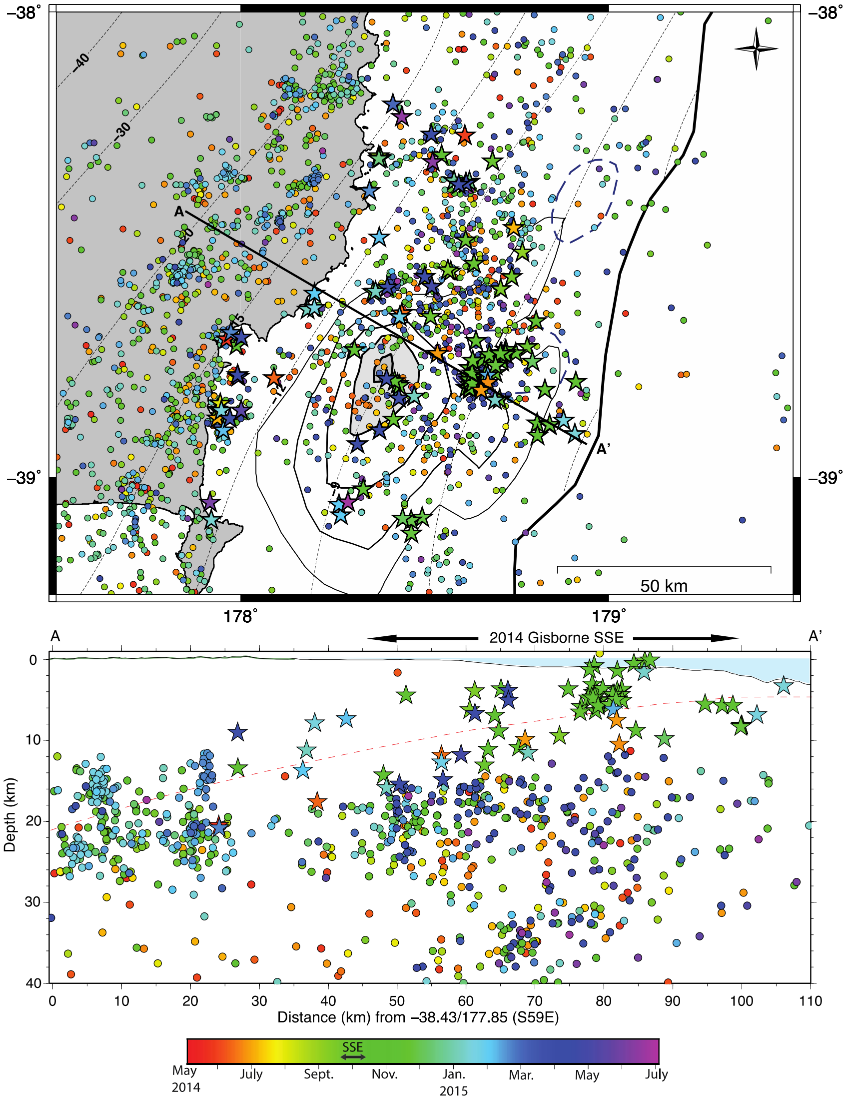

Figure A-1. Map and cross-section of seismicity (within 25 km of A-A') from May 2014 – June 2015. Locations are GrowClust relocations, or J. Yarce (personal communication, 2018) and Todd et al. (2018) initial locations for events that could not be relocated with GrowClust (see Fig. A2 for events relocated with GrowClust). General seismicity shown as circles, colored according to time. Earthquakes used as templates in this study are shown as stars, colored according to time. Plate interface contours (top: black dashed lines; bottom: red dashed line) from Williams et al., 2013. Slow slip event contours (black lines; mm slow slip) from Wallace et al., 2016.

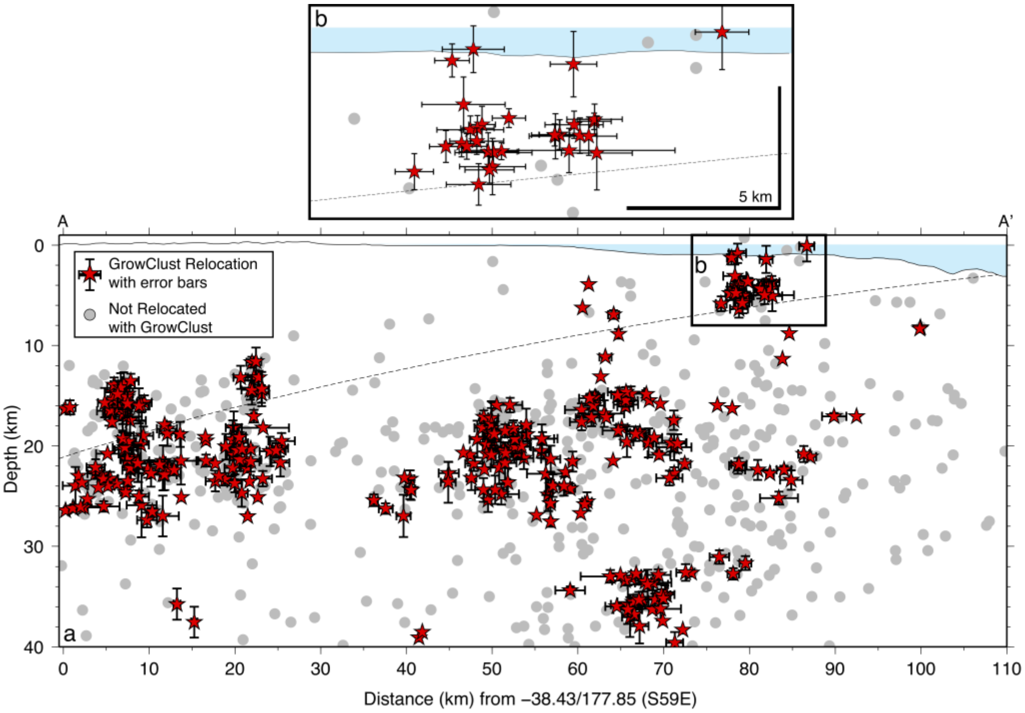

Figure A-2. GrowClust location errors. a) Cross-section of seismicity (within 25 km of A-A' shown on Figure A-1) from May 2014 – June 2015. Red stars: GrowClust relocations with vertical and horizontal error bars. Gray circles: events not relocated with GrowClust, locations are from J. Yarce (personal communication, 2018) or Todd et al. (2018) catalogs. Plate interface (black dashed line) from Williams et al., 2013. b) Zoom-in of upper plate seismicity with GrowClust error bars where burst-type repeating earthquakes are found.

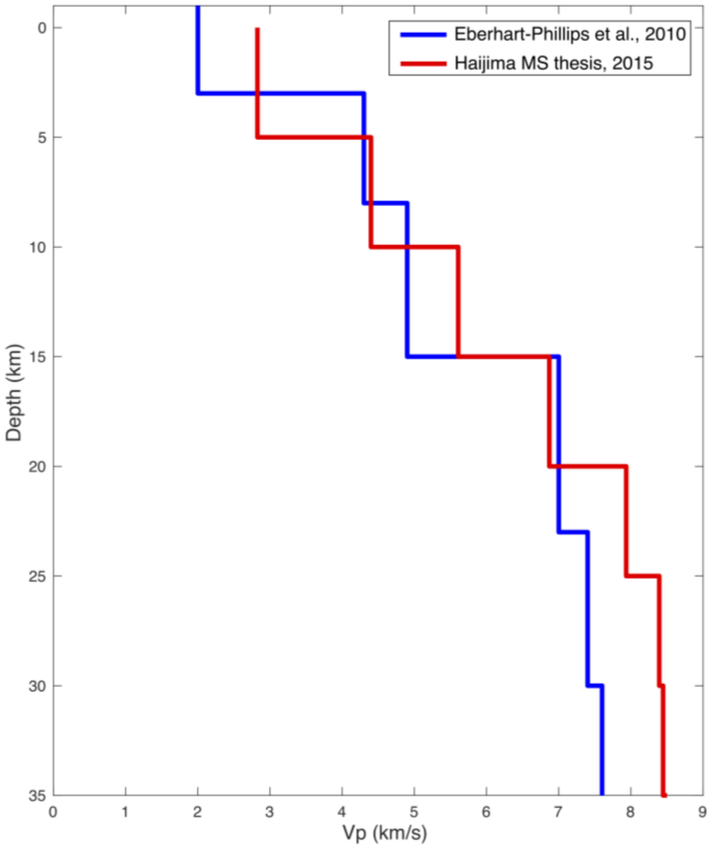

Figure A-3. Comparison of velocity models. Offshore 1-D interpretation of Eberhart-Phillips et al. (2010) 3-D seismic velocity model used in this study for GrowClust relocations, compared to the 1-D seismic velocity model near the subducted seamount from Haijima, D. MS thesis (2015) that used ocean-bottom seismometer data.

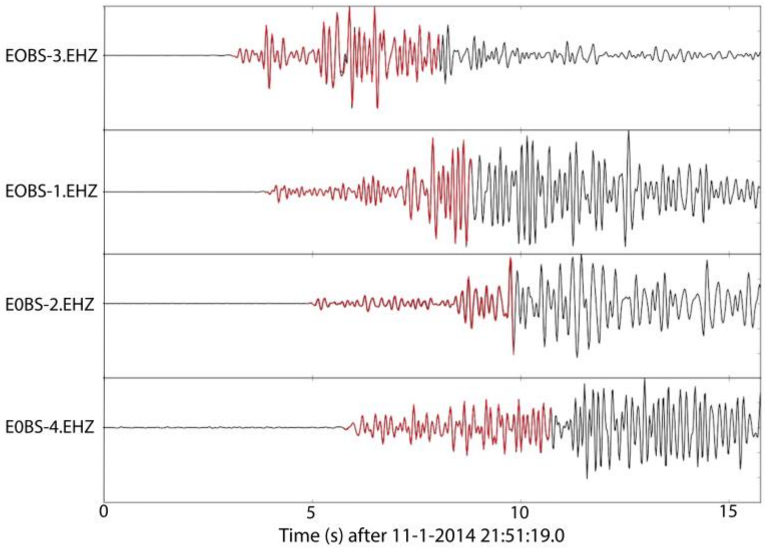

Figure A-4. Example burst-type repeating earthquake seismogram, average CC of 0.96. Template earthquake (Family ID 5, ML 0.70, 2 events in family) shown in red (5s long around P-phase) occurred on 10-22-2014 at 15:54:34.44 UTC (at subducted seamount). Background waveform/detection shown in black. Vertical component, 3-10 Hz bandpass filtered waveforms shown. Traces normalized by maximum amplitude.

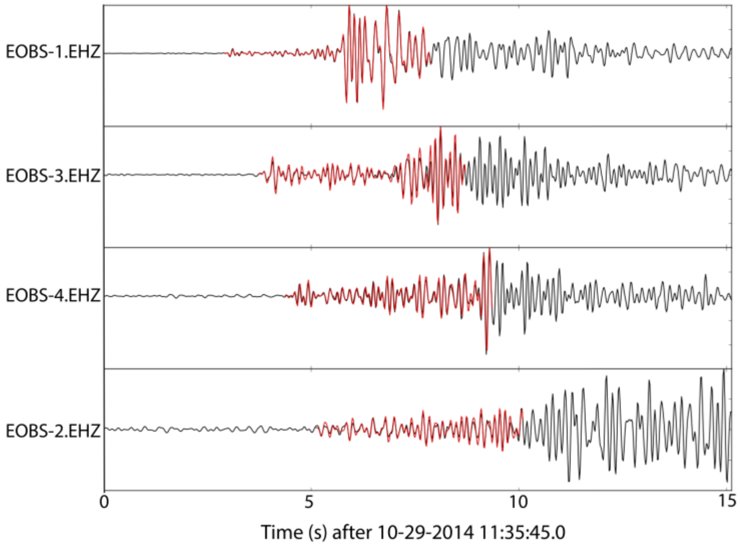

Figure A-5. Example burst-type repeating earthquake seismogram, average CC of 0.95. Template earthquake (Family ID 8, M_L 0.46, 2 events in family) shown in red (5s long around P-phase) occurred on 10-29-2014 at 17:02:15.38 UTC (at subducted seamount). Background waveform/detection shown in black. Vertical component, 3-10 Hz bandpass filtered waveforms shown. Traces normalized by maximum amplitude.

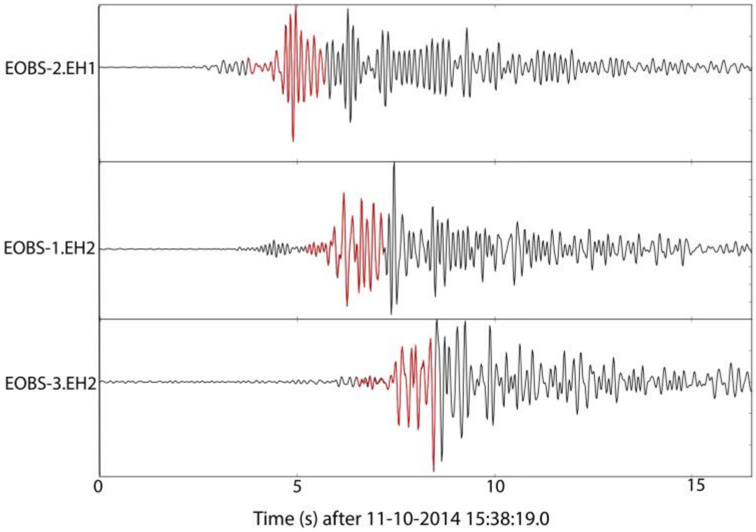

Figure A-6. **Example burst-type repeating earthquake seismogram, average CC of 0.99.** Template earthquake (Family ID 4, M_L 0.31, 7 events in family) shown in red (2s long around S-phase) occurred on 10-18-2014 at 16:44:01.64 UTC (at subducted seamount). Background waveform/detection shown in black. Horizontal components, 3-10 Hz bandpass filtered waveforms shown. Traces normalized by maximum amplitude.

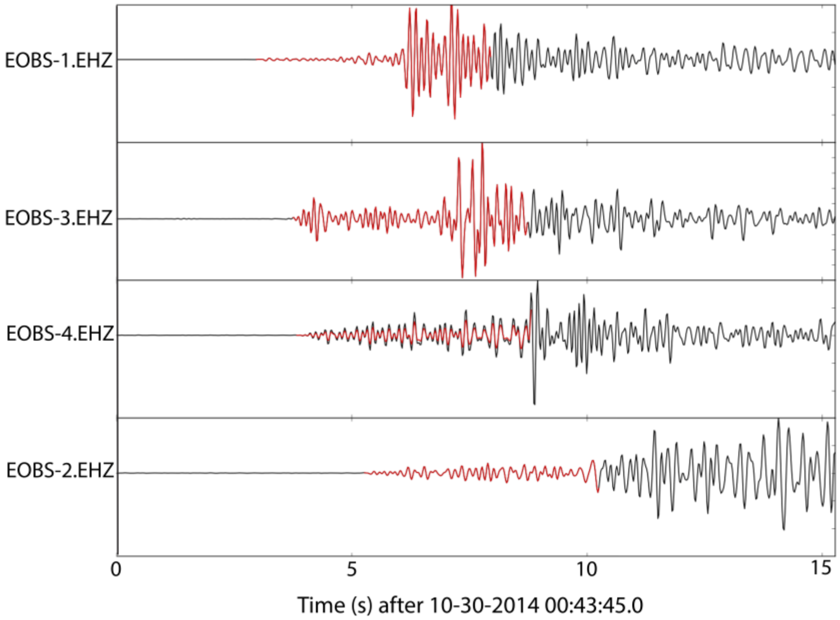

Figure A-7. Example burst-type repeating earthquake seismogram, average CC of 0.95. Template earthquake (Family ID 9, M_L 0.25, 5 events in family) shown in red (5s long around P-phase) occurred on 10-29-2014 at 22:17:49.16 UTC (at subducted seamount). Background waveform/detection shown in black. Vertical component, 3-10 Hz bandpass filtered waveforms shown. Traces normalized by maximum amplitude.

Table A-1. Near-Repeating Earthquakes at Subducted Seamount

Family ID: 4, Template Time: 10-18-2014T16:44:01.64, Latitude: -38.7867, Longitude: 178.6311, Depth (km): 0.809, M_L: 0.31

Detection Time (UTC)	Average CC	# Stations	Template Type	M_L
10-09-2014T14:07:55	0.97	3	S-phase	-0.81
10-10-2014T07:54:49	0.97	3	S-phase	-0.97
10-15 -2014T13:29:47	0.97	3	S-phase	-1.18
10-15-2014T15:25:51	0.97	3	S-phase	-0.56
10-24-2014T20:00:29	0.97	3	S-phase	-0.42
11-10-2014T15:38:22	0.99	3	S-phase	0.05
10-18-2014T16:44:01	1	3	S-phase	0.31

Family ID: 5, Template Time: 10-22-2014T15:54:34.44, Latitude: -38.7088, Longitude: 178.6390, Depth (km): 3.66, M_L: 0.70

Detection Time (UTC)	Average CC	# Stations	Template Type	M_L
11-01-2014T21:51:22	0.96	4	P-phase	0.74
10-22-2014T15:54:34	1	4	P-phase	0.70

Family ID: 6, Template Time: 10-24-2014T00:33:43.98, Latitude: -38.7504, Longitude: 178.6561, Depth (km): 4.80, M_L: N/A

Detection Time (UTC)	Average CC	# Stations	Template Type	M_L
10-24-2014T00:38:53	0.95	4	P-phase	N/A
10-24-2014T00:33:43	1	4	P-phase	N/A

Family ID: 8, Template Time: 10-29-2014T17:02:15.38, Latitude: -38.7355, Longitude: 178.7082, Depth (km): 4.33, M_L: 0.46

Detection Time (UTC)	Average CC	# Stations	Template Type	M_L
10-29-2014T11:35:47	0.95	4	P-phase	0.19
10-29-2014T17:02:15	1	4	P-phase	0.46

Family ID: 9, Template Time: 10-29-2014T22:17:49.16, Latitude: -38.7280, Longitude: 178.7199, Depth (km): 1.42, M_L: 0.25

Detection Time (UTC)	Average CC	# Stations	Template Type	M_L
10-29-2014T22:14:02	0.97	4	P-phase	-0.61
10-29-2014T22:28:27	0.95	4	P-phase	-0.58
10-30-2014T00:43:47	0.95	4	P-phase	0.29
11-02-2014T08:05:22	0.95	4	P-phase	0.41
10-29-2014T22:17:49	1	4	P-phase	0.25

Family ID: 10, Template Time: 10-27-2014T14:03:45.68, Latitude: -38.7349, Longitude: 178.7470, Depth (km): 0.530, M_L: 0.60

Detection Time (UTC)	Average CC	# Stations	Template Type	M_L
10-27-2014T19:52:52	0.95	4	P-phase	0.10
10-27-2014T14:03:45	1	4	P-phase	0.60

Family ID: 11, Template Time: 10-28-2014T22:27:09.54, Latitude: -38.7386, Longitude: 178.6751, Depth (km): 5.76, M_L: 0.01

Detection Time (UTC)	Average CC	# Stations	Template Type	M_L
10-28-2014T22:25:09	0.96	4	P-phase	-1.07
10-28-2014T22:27:09	1	4	P-phase	0.01

Family ID: 13, Template Time: 11-08-2014T13:34:39.90, Latitude: -38.7775, Longitude: 178.6920, Depth (km): 5.07, M_L: 0.27

Detection Time (UTC)	Average CC	# Stations	Template Type	M_L
11-08-2014T11:44:39	0.96	4	S-phase	-0.88
11-08-2014T13:34:39	1	4	S-phase	0.27

Family ID: 14, Template Time: 11-14-2014T22:36:57.92, Latitude: -38.7514, Longitude: 178.6300, Depth (km): 6.52, M_L: 1.27

Detection Time (UTC)	Average CC	# Stations	Template Type	M_L
11-01-2014T09:28:02	0.96	3	S-phase	0.83
11-14-2014T22:36:57	1	3	S-phase	1.27

Family ID: 16, Template Time: 11-16-2014T19:57:17.72, Latitude: -38.7822, Longitude: 178.6640, Depth (km): 5.59, M_L: 1.35

Detection Time (UTC)	Average CC	# Stations	Template Type	M_L
11-05-2014T00:18:46	0.95	4	P-phase	0.23
11-16-2014T19:57:17	1	4	P-phase	1.35

Family ID: 17, Template Time: 12-01-2014T03:33:56.98, Latitude: -38.7532, Longitude: 178.7920, Depth (km): 9.81, M_L: 1.60

Detection Time (UTC)	Average CC	# Stations	Template Type	M_L
11-30-2014T03:29:53	0.99	3	P-phase	1.25
11-30-2014T03:28:32	0.95	3	S-phase	0.02
12-01-2014T03:33:56	1	3	P-phase/S-phase	1.60

P-phase: 5 seconds around P-phase arrival (0.15s pre-pick); S-phase: 2 seconds around S-phase arrival (1s pre-pick)

Template times are in UTC. Average CC = 1 is a template event.

Appendix B – Supplemental Information for Chapter 2

B-1. Template matching parameters

In this study we are analyzing near-repeating earthquakes driven by afterslip (i.e., triggered transient aseismic slip) and spontaneous aseismic slip transients. These events have highly similar waveforms, but have variable magnitudes within families and are therefore likely to be partially overlapping or closely-spaced asperities. Since we are interested in variable magnitudes (~M0 – M3) with different frequency content, and events that are closely spaced (<200 meters), we chose a 3-10 Hz band-pass on waveforms down-sampled to 25 Hz to allow for maximum detection of near-repeating earthquakes. We additionally used 5-second long template waveforms that included the S-phases at most seismometers. To evaluate potential changes in our interpretation using stricter waveform cross-correlation parameters we redid template matching for a subset of data: 22 near-repeating earthquake families identified from June 10 – July 26, 2016 following the 2016 local earthquake.

Template length

We used 5-second long windows for all of our template events. The majority of the stations included the S-phase arrivals. We changed the template lengths to 6-seconds and found negligible changes in the cross-correlation values. The identification of near-repeating earthquake families did not change.

Frequency band

We redid our analysis in June 2016 using a 3-15 Hz band-pass and a 3 Hz high-pass (seismometer sampling rate at 40 Hz). Using a cross-correlation threshold of 0.90, we identified 7 near-repeating earthquake families in the 3-15 Hz band-pass and 5 near-repeating earthquake families with the 3 Hz high-pass filter. Although we find less families, they are along the strike of the Clark fault and consistent with our interpretation of afterslip along the Clark fault with some minor off-fault afterslip. It is also worth noting that the families still detected using higher frequencies have similar magnitudes. We do not detect families with magnitude differences greater than 1 local magnitude.

Cross-correlation threshold

Using our initial 3-10 Hz band-pass filter and a sampling rate of 25 Hz, we find 7 near-repeating earthquake families with a cross-correlation threshold of 0.95 compared to 22 families using 0.90. There are less families, but our interpretation does not change.

Summary

Using stricter waveform cross-correlation parameters and identifying less near-repeating earthquake families does not affect our interpretation of where afterslip is occurring in June 2016. Further, since we are interpreting near-repeating earthquakes as closely spaced asperities, partially overlapping asperities, or repeated partial rupture of a larger asperity, the stricter parameters are not required nor appropriate to identify near-repeating earthquakes.

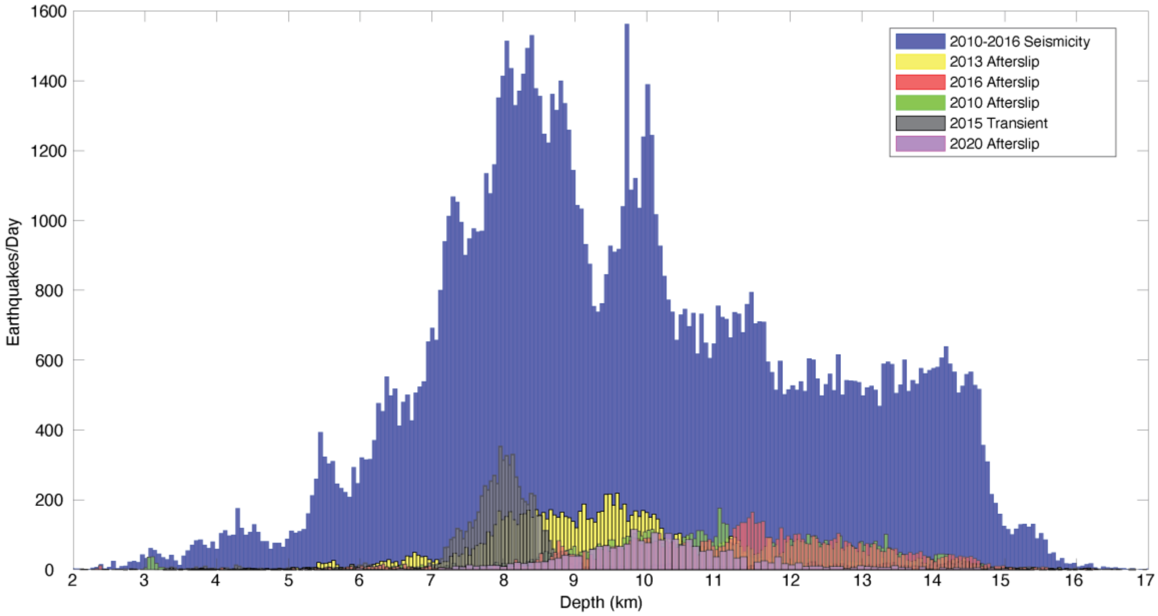

Figure B-1. Histogram of earthquake depths in the study region. All seismicity from 2010-2016 is shown in blue, seismicity during the 2010 afterslip (July 7 - July 26, 2010) is shown in green, seismicity during the 2013 afterslip (March 11 - May 26, 2013) is shown in yellow, seismicity during the 2016 afterslip (June 10 - July 31, 2016) is shown in red, seismicity during the 2015 spontaneous aseismic slip transient (February 25 - May 31, 2015) is shown in dark grey, and seismicity during the 2020 aseismic slip transient (April 4 - May 6, 2020) is shown in lavender.

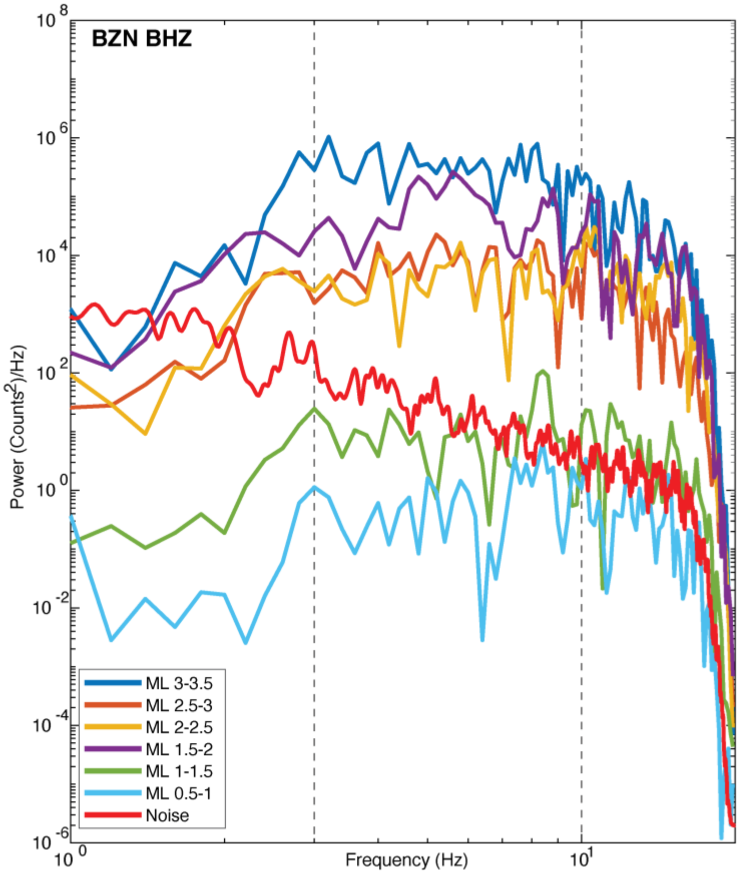

Figure B-2. Spectral plot for local earthquakes averaged within local magnitude (ML) bins and averaged noise in 2014 at station BZN component BHZ. We selected earthquakes from the QTM catalog within the study region (Figure 1) from 2010-2016 and use 5-second long raw waveforms from the P-phase arrival. 7,185 events are used for ML 0.5-1, 3,092 events for ML 1-1.5, 981 events for ML 1.5-2, 271 events for ML 2-2.5, 86 events for ML 2.5-3, and 31 events for ML 3-3.5. The frequency band used for detecting near-repeating earthquakes (3-10 Hz) is indicated with black dashed lines.

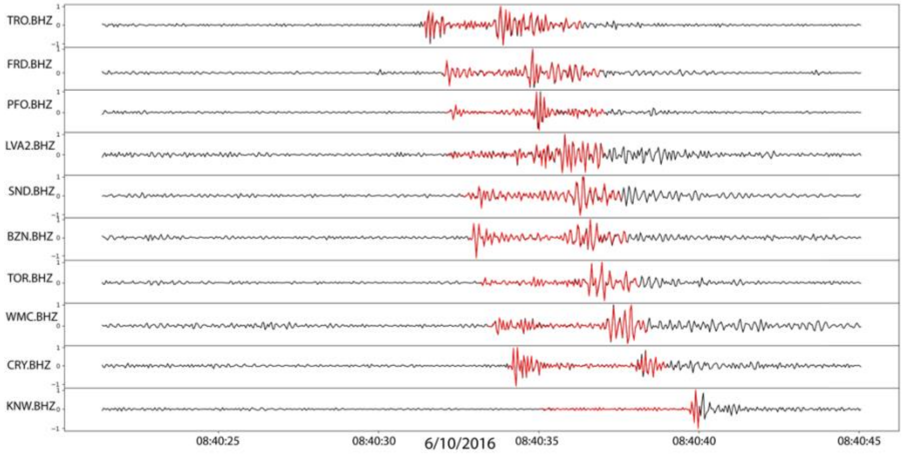

Figure B-3. Example near-repeating earthquake. Station average correlation coefficient of 0.96 using 10 seismic stations. Template time: 6/10/2016 08:39:51. Detection time: 6/10/2016 08:40:31.

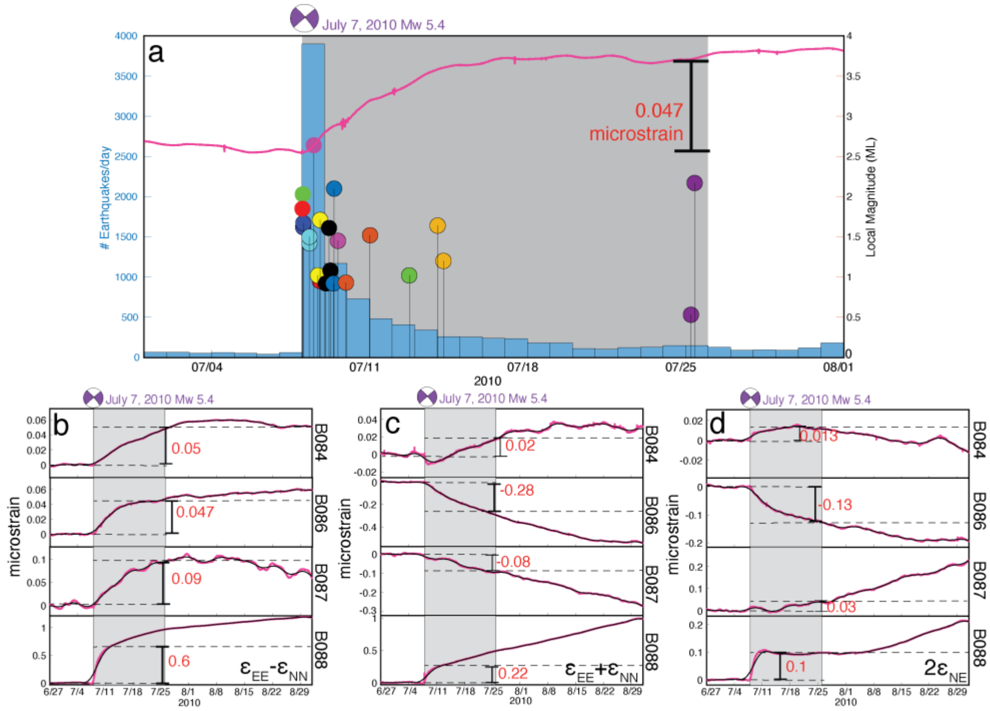

Figure B-4. Timing of the 2010 afterslip. (a) Seismicity rate (in study area; see Figure 1), near-repeating earthquakes, and strain transient timing from BSM data (indicated in grey). Near-repeating earthquakes plotted by local magnitude and colored according to family (11 total families). Differential shear strain from BSM station B086 is plotted as the magenta line. (b)-(d) 5-minute corrected strain data (b: differential shear strain, c: areal strain, d: engineering shear strain) for BSM stations B084, B086, B087, and B088 (see Figure 1) with the trend of the month prior to the earthquake removed is shown in magenta, one-week running average shown in black. Observed strain change (microstrain) during afterslip shown in red. Approximate timing of afterslip highlighted in grey. Timing (in UTC) of the Collins Valley July 7, 2010 M_W 5.4 earthquake indicated at the top of each panel.

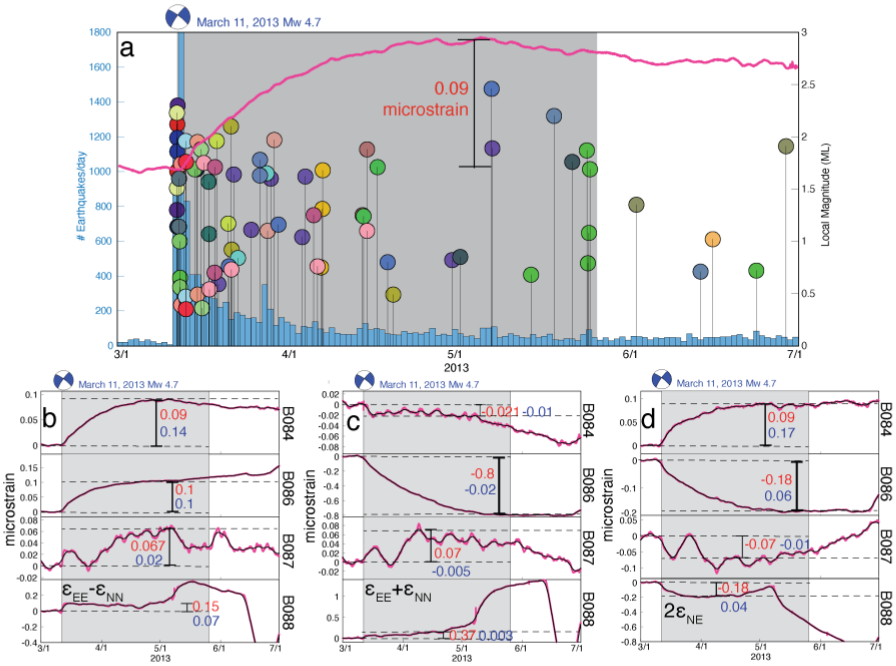

Figure B-5. Timing of the 2013 afterslip. (a) Seismicity rate (in study area; see Figure 1), near-repeating earthquakes, and strain transient timing from BSM data (indicated in grey). Near-repeating earthquakes plotted by local magnitude and colored according to family (31 families total; 28 during timing of afterslip). Differential shear strain from BSM station B084 is plotted as the magenta line. (b)-(d) 5-minute corrected strain data (b: differential shear strain, c: areal strain, d: engineering shear strain) for BSM stations B084, B086, B087, and B088 (see Figure 1) with the trend of the month prior to the earthquake removed is shown in magenta, one-week running average shown in black. Observed strain change (microstrain) during afterslip shown in red, modeled strain change is indicated in blue. Approximate timing of afterslip highlighted in grey. Timing (in UTC) of the March 11, 2013 M_W 4.7 earthquake indicated at the top.

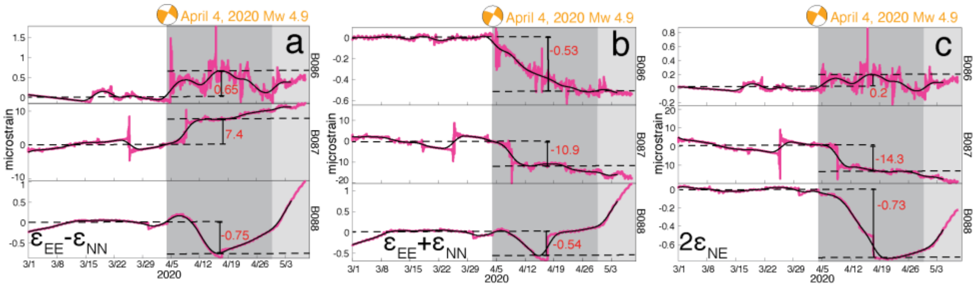

Figure B-6. Strain data for the 2020 afterslip. (a)-(c) 5-minute level 2 corrected strain data (a: differential shear strain, b: areal strain, c: engineering shear strain) for BSM stations B086, B087, and B088 with the trend of the month prior to the earthquake removed is shown in magenta, one-week running average shown in black. Largest strain transient signals shown in dark gray, potential strain transient continuation shown in light gray. Observed strain changes (microstrain) during afterslip shown in red. Approximate timing of afterslip highlighted in grey. Timing (in UTC) of the April 4, 2020 M_W 4.9 earthquake indicated at the top.

Table B-1. Details of local moderate-sized ($M_W > 4.5$) earthquakes in the study region and modeled afterslip.

Local Moderate-Sized Earthquakes				**Afterslip**			
[1]Origin Time (UTC)	**[1]Hypocentral Location**	**[1]M_W**	**[1]Strike Dip Rake**	**[2]Approx. Timing**	**[3]Strike Dip Center**	**[4]Length Width Slip Rake**	**[4]M_W**
7/7/2010 23:53:33	33.417°N 116.475°W 12.3 km depth Coyote Creek fault	5.4	319° 84° -178°				
3/11/2013 16:56:06	33.501°N 116.458°W 10.9 km depth Buck Ridge fault	4.7	307° 80° -171°	3/11/2013 - 5/26/2013	301° 90° 33.504898 -116.455289 9.5 km depth Buck Ridge fault	5 km 3 km (8-11 km depth) 26 cm 150°	5.3
6/10/2016 08:04:38	33.432°N 116.443°W 12.3 km depth Clark fault	5.2	302° 61° -174°	6/10/2016 - 7/31/2016	305° 70° NE 33.480729 -116.504681 11 km depth Clark fault	14 km 6 km (8.2-13.8 km depth) 11 cm 174°	5.6
4/4/2020 01:53:18	33.490°N 116.506°W 10.5 km depth Clark fault	4.9	298° 74° -178°				

[1] Southern California Seismic Network; strike, dip and rake are from the Best-fit Double Couple Solution
[2] Based on borehole strainmeter data and timing of near-repeating earthquakes
[3] Based on locations of near-repeating earthquake families
[4] Rectangular Okada dislocation model

Table B-2: Near-repeating earthquakes during the 2010-2016 study period. Average CC = 1.0 is the template event. Locations and magnitudes of template events and detected events are from the QTM catalog. Near-repeating earthquakes during afterslip time periods are in bold. Times are in UTC.

Family #	Template Origin Time	Detection Time	Average CC	# Stations	ML	Depth(km)	Latitude	Longitude
1	08-Jan-2010 18:50:17	07-Jan-2010 02:28:36	0.9149	10	1.28	3.881	33.46330	-116.43136
1	08-Jan-2010 18:50:17	08-Jan-2010 18:50:22	1.0	10	2.43	3.838	33.46297	-116.43153
2	15-Jan-2010 01:45:16	15-Jan-2010 01:47:03	0.9751	10	1.09	3.649	33.46788	-116.43231
2	15-Jan-2010 01:45:16	15-Jan-2010 01:45:20	1.0	10	1.52	3.45	33.46802	-116.43229
3	22-Jan-2010 06:52:29	22-Jan-2010 06:52:18	0.9469	7	0.75	11.828	33.47875	-116.44546
3	22-Jan-2010 06:52:29	22-Jan-2010 06:52:33	1.0	7	2.4	11.599	33.47868	-116.44594
4	31-Jan-2010 08:49:59	31-Jan-2010 18:17:20	0.9076	11	0.51	10.086	33.45001	-116.58098
4	31-Jan-2010 08:49:59	31-Jan-2010 08:50:01	1.0	11	1.54	10.005	33.44945	-116.57983
5	05-Apr-2010 10:38:51	05-Apr-2010 10:46:45	0.9033	8	2.56	11.713	33.45441	-116.45494
5	05-Apr-2010 10:38:51	05-Apr-2010 10:38:55	1.0	8	1.66	11.765	33.45460	-116.45469
6	18-Jul-2010 21:05:49	19-Apr-2010 20:13:14	0.9038	11	1.31	6.257	33.50353	-116.44938
6	18-Jul-2010 21:05:49	18-Jul-2010 21:05:54	1.0	11	2.79	6.298	33.50374	-116.44909
7	21-Apr-2010 10:18:40	21-Apr-2010 10:22:04	0.9327	8	1.00	9.292	33.49748	-116.48277
7	21-Apr-2010 10:18:40	21-Apr-2010 10:18:44	1.0	8	1.67	9.375	33.49791	-116.48296
8	01-May-2010 20:53:29	01-May-2010 16:08:56	0.9522	9	1.42	9.954	33.45987	-116.58790
8	01-May-2010 20:53:29	01-May-2010 20:53:32	1.0	9	1.54	9.955	33.46016	-116.58832
9	31-May-2010 05:22:48	13-May-2010 20:43:03	0.9099	8	0.91	9.754	33.42952	-116.58245
9	31-May-2010 05:22:48	14-May-2010 20:21:56	0.9352	8	1.46	9.822	33.42931	-116.58257
9	31-May-2010 05:22:48	31-May-2010 05:22:52	1.0	8	1.71	9.39	33.42936	-116.58251
10	05-Jun-2010 19:30:04	21-May-2010 06:26:18	0.9195	8	1.24	9.084	33.47080	-116.40840
10	05-Jun-2010 19:30:04	05-Jun-2010 19:30:09	1.0	8	1.8	8.957	33.47075	-116.40949
11	03-Jun-2010 08:44:13	30-May-2010 16:23:39	0.9443	11	0.89	6.280	33.50303	-116.44817
11	03-Jun-2010 08:44:13	03-Jun-2010 08:44:17	1.0	11	3.18	6.424	33.50333	-116.44811
12	15-Jun-2010 16:23:44	15-Jun-2010 13:13:53	0.9024	12	0.93	8.528	33.39705	-116.40665
12	15-Jun-2010 16:23:44	15-Jun-2010 16:23:49	1.0	12	3.04	8.367	33.39714	-116.40665
13	18-Jun-2010 14:48:27	16-Jun-2010 11:27:19	0.9096	11	1.46	7.340	33.39367	-116.40083
13	18-Jun-2010 14:48:27	18-Jun-2010 14:48:32	1.0	11	2.15	6.857	33.39384	-116.40012
14	18-Jun-2010 16:34:40	30-Jun-2010 05:30:50	0.901	10	0.89	7.101	33.39279	-116.40227
14	18-Jun-2010 16:34:40	18-Jun-2010 16:34:45	1.0	10	2.2	7.044	33.39300	-116.40195
15	**08-Jul-2010 01:30:20**	**08-Jul-2010 01:18:17**	**0.932**	**8**	**1.62**	**13.209**	**33.47598**	**-116.51630**
15	**08-Jul-2010 01:30:20**	**08-Jul-2010 01:30:23**	**1.0**	**8**	**1.67**	**13.17**	**33.47630**	**-116.51671**
16	**08-Jul-2010 07:56:18**	**08-Jul-2010 07:56:50**	**0.933**	**12**	**1.42**	**10.898**	**33.43111**	**-116.44052**
16	**08-Jul-2010 07:56:18**	**08-Jul-2010 07:56:22**	**1.0**	**12**	**1.5**	**10.898**	**33.43111**	**-116.44052**
17	**08-Jul-2010 00:29:46**	**08-Jul-2010 19:09:48**	**0.9105**	**11**	**0.95**	**10.932**	**33.44903**	**-116.47566**
17	**08-Jul-2010 00:29:46**	**08-Jul-2010 00:29:50**	**1.0**	**11**	**1.85**	**11.03**	**33.44884**	**-116.47529**
18	**08-Jul-2010 19:21:36**	**08-Jul-2010 17:01:13**	**0.9244**	**9**	**1.02**	**12.138**	**33.47552**	**-116.50281**
18	**08-Jul-2010 19:21:36**	**08-Jul-2010 19:21:39**	**1.0**	**9**	**1.71**	**12.21**	**33.47522**	**-116.50224**
19	**08-Jul-2010 12:32:52**	**09-Jul-2010 14:20:45**	**0.9604**	**10**	**1.45**	**10.753**	**33.44779**	**-116.39391**
19	**08-Jul-2010 12:32:52**	**08-Jul-2010 12:32:57**	**1.0**	**10**	**2.64**	**10.602**	**33.44780**	**-116.39372**
20	**09-Jul-2010 04:49:39**	**09-Jul-2010 01:34:12**	**0.9162**	**10**	**0.92**	**13.517**	**33.48144**	**-116.54366**
20	**09-Jul-2010 04:49:39**	**09-Jul-2010 06:20:14**	**0.9618**	**10**	**1.08**	**13.510**	**33.48136**	**-116.54362**
20	**09-Jul-2010 04:49:39**	**09-Jul-2010 04:49:42**	**1.0**	**10**	**1.61**	**13.51**	**33.48136**	**-116.54362**
21	**11-Jul-2010 00:28:28**	**09-Jul-2010 22:50:54**	**0.9036**	**4**	**0.93**	**12.015**	**33.47248**	**-116.50677**
21	**11-Jul-2010 00:28:28**	**11-Jul-2010 00:28:31**	**1.0**	**4**	**1.52**	**11.957**	**33.47256**	**-116.50680**
22	**09-Jul-2010 10:14:19**	**09-Jul-2010 09:28:38**	**0.9038**	**10**	**0.92**	**7.827**	**33.47933**	**-116.38616**

22,09-Jul-2010 10:14:19,09-Jul-2010 10:14:24,1.0,10,2.1,7.884,33.47920,-116.38603
23,08-Jul-2010 00:51:39,12-Jul-2010 18:08:25,0.9084,9,1.02,9.892,33.41618,-116.45736
23,08-Jul-2010 00:51:39,08-Jul-2010 00:51:43,1.0,9,2.03,9.854,33.41620,-116.45753
24,14-Jul-2010 00:20:21,14-Jul-2010 06:33:57,0.9228,10,1.20,11.995,33.36284,-116.39317
24,14-Jul-2010 00:20:21,14-Jul-2010 00:20:27,1.0,10,1.64,11.967,33.36233,-116.39288
25,25-Jul-2010 09:44:13,25-Jul-2010 05:51:16,0.9344,11,0.53 ,3.050,33.52019,-116.55982
25,25-Jul-2010 09:44:13,25-Jul-2010 09:44:15,1.0,11,2.17,3.044,33.52026,-116.55988
26,01-Aug-2010 08:42:10,01-Aug-2010 08:44:48,0.9401,12,1.38,11.468,33.50983,-116.50922
26,01-Aug-2010 08:42:10,01-Aug-2010 08:42:13,1.0,12,1.73,11.534,33.51031,-116.50952
27,21-Aug-2010 14:36:14,11-Aug-2010 20:52:32,0.9309,5,2.01,7.103,33.37955,-116.39682
27,21-Aug-2010 14:36:14,21-Aug-2010 14:36:19,1.0,5,1.63,7.248,33.38022,-116.39661
28,03-Sep-2010 09:13:44,24-Aug-2010 04:37:50,0.9129,10,0.63,10.089,33.44892,-116.57941
28,03-Sep-2010 09:13:44,01-Sep-2010 12:15:36,0.911,11,1.7,10.119,33.44876,-116.57933
28,03-Sep-2010 09:13:44,03-Sep-2010 09:13:47,1.0,10,2.39,10.119,33.44876,-116.57933
29,21-Oct-2015 20:01:41,31-Aug-2010 04:46:32,0.901,4,1.19,10.807,33.42089,-116.37544
29,21-Oct-2015 20:01:41,21-Oct-2015 20:01:47,1.0,4,2.03,10.911,33.42090,-116.37464
30,07-Sep-2010 07:01:01,13-Oct-2010 22:26:08,0.9691,10,1.82,5.883,33.50958,-116.46000
30,07-Sep-2010 07:01:01,10-Sep-2010 15:17:32,0.9195,10,0.73,5.975,33.50950,-116.45912
30,07-Sep-2010 07:01:01,07-Sep-2010 07:01:05,1.0,10,1.96,5.848,33.50960,-116.45978
31,12-Sep-2010 04:25:32,12-Sep-2010 04:52:31,0.9487,11,0.89,4.492,33.38806,-116.37591
31,12-Sep-2010 04:25:32,12-Sep-2010 04:25:38,1.0,11,1.87,4.497,33.38801,-116.37589
32,14-Sep-2010 08:08:34,14-Sep-2010 10:37:49,0.9611,10,1.70,6.960,33.43627,-116.45084
32,14-Sep-2010 08:08:34,14-Sep-2010 08:08:38,1.0,10,1.58,6.96,33.46327,-116.45084
33,02-Dec-2010 22:34:26,25-Sep-2010 02:36:43,0.9045,7,0.49,7.303,33.49154,-116.57607
33,02-Dec-2010 22:34:26,02-Dec-2010 22:34:29,1.0,7,1.82,7.286,33.49170,-116.57641
34,19-Sep-2010 21:42:14,30-Sep-2010 12:37:45,0.9211,8,0.63,6.656,33.46609,-116.45854
34,19-Sep-2010 21:42:14,19-Sep-2010 21:42:19,1.0,8,1.83,6.722,33.46571,-116.45799
35,06-May-2014 23:24:56,17-Oct-2010 07:20:43,0.9008,4,0.71,14.016,33.50304,-116.51275
35,06-May-2014 23:24:56,06-May-2014 23:24:59,1.0,4,2.32,14.038,33.50288,-116.51335
36,13-Mar-2015 02:11:48,06-Nov-2010 14:09:09,0.9153,5,1.05,10.085,33.42503,-116.38751
36,13-Mar-2015 02:11:48,13-Mar-2015 02:11:53,1.0,5,1.65,10.124,33.42498,-116.38806
37,03-Dec-2010 08:20:15,03-Dec-2010 08:21:00,0.904,8,0.89,13.580,33.48988,-116.48021
37,03-Dec-2010 08:20:15,03-Dec-2010 08:20:19,1.0,8,1.57,13.559,33.48998,-116.48069
38,03-Dec-2010 04:10:16,03-Dec-2010 05:42:46,0.9079,8,1.26,13.691,33.48937,-116.48061
38,03-Dec-2010 04:10:16,03-Dec-2010 04:10:19,1.0,8,2.27,13.588,33.48981,-116.48046
39,10-Jul-2011 06:19:19,22-Dec-2010 05:33:32,0.9705,3,0.67,7.185,33.49126,-116.57611
39,10-Jul-2011 06:19:19,22-Dec-2010 10:32:47,0.9199,3,0.55,7.266,33.49091,-116.57602
39,10-Jul-2011 06:19:19,10-Jul-2011 06:19:21,1.0,3,1.83,7.208,33.49128,-116.57607
40,15-Apr-2012 23:06:10,26-Jan-2011 04:09:58,0.9113,6,0.91,6.039,33.50586,-116.45307
40,15-Apr-2012 23:06:10,05-Aug-2011 10:14:58,0.945,5,0.71,6.197,33.50598,-116.45307
40,15-Apr-2012 23:06:10,28-Jun-2012 15:26:13,0.9421,7,1.03,6.163,33.50569,-116.45257
40,15-Apr-2012 23:06:10,15-Apr-2012 23:06:13,1.0,7,1.73,6.05,33.50565,-116.45275
41,18-Dec-2010 15:16:37,07-Feb-2011 00:03:24,0.9476,4,1.20,7.528,33.49067,-116.57542
41,18-Dec-2010 15:16:37,09-Nov-2011 19:56:05,0.9064,3,0.66,7.605,33.49065,-116.57501
41,18-Dec-2010 15:16:37,18-Dec-2010 15:16:42,1.0,3,1.57,7.528,33.49067,-116.57542
42,19-Mar-2011 03:17:34,19-Mar-2011 03:21:08,0.9352,6,2.07,7.166,33.46163,-116.42725
42,19-Mar-2011 03:17:34,19-Mar-2011 03:23:46,0.9218,6,1.53,6.817,33.46220,-116.42700
42,19-Mar-2011 03:17:34,19-Mar-2011 03:17:38,1.0,6,1.61,6.788,33.46156,-116.42672
43,19-Mar-2011 08:22:52,19-Mar-2011 00:19:06,0.9599,8,1.10,6.863,33.46267,-116.42559
43,19-Mar-2011 08:22:52,19-Mar-2011 03:30:46,0.9029,8,0.81,6.872,33.46344,-116.42676
43,19-Mar-2011 08:22:52,19-Mar-2011 03:41:58,0.912,8,2.15,6.627,33.46287,-116.42719
43,19-Mar-2011 08:22:52,19-Mar-2011 08:22:56,1.0,8,1.9,6.911,33.46272,-116.42718
44,19-Mar-2011 03:19:42,19-Mar-2011 02:32:46,0.9046,9,1.05,6.797,33.46260,-116.42698

```
44,19-Mar-2011 03:19:42,19-Mar-2011 03:28:26,0.941,9,1.04,6.897,33.46213,-116.42638
44,19-Mar-2011 03:19:42,19-Mar-2011 03:19:47,1.0,9,1.76,6.842,33.46233,-116.42719
45,19-Mar-2011 03:32:35,19-Mar-2011 03:31:38,0.9765,8,1.27,6.793,33.46255,-116.42699
45,19-Mar-2011 03:32:35,19-Mar-2011 03:32:40,1.0,8,1.57,6.705,33.46239,-116.42724
46,18-Apr-2011 21:07:00,18-Apr-2011 21:13:54,0.9615,7,0.90,6.385,33.46478,-116.42910
46,18-Apr-2011 21:07:00,18-Apr-2011 21:07:06,1.0,7,2.08,6.344,33.46471,-116.42923
47,18-Apr-2011 21:23:34,18-Apr-2011 20:57:19,0.9513,7,1.87,6.454,33.46467,-116.42904
47,18-Apr-2011 21:23:34,18-Apr-2011 21:25:42,0.9466,7,1.73,6.253,33.46441,-116.42885
47,18-Apr-2011 21:23:34,18-Apr-2011 21:23:39,1.0,7,2.66,6.245,33.46442,-116.42889
48,03-Jun-2011 17:58:20,03-Jun-2011 21:02:49,0.907,10,0.68,8.997,33.48108,-116.57170
48,03-Jun-2011 17:58:20,03-Jun-2011 03:35:36,0.9693,10,0.85,9.010,33.48141,-116.57137
48,03-Jun-2011 17:58:20,11-Jun-2011 01:37:26,0.9042,9,0.83,9.048,33.48141,-116.57114
48,03-Jun-2011 17:58:20,03-Jun-2011 17:58:22,1.0,9,1.89,8.999,33.48130,-116.57153
49,04-Jun-2011 05:58:01,06-Jun-2011 04:04:13,0.9038,6,0.64,9.042,33.48167,-116.57097
49,04-Jun-2011 05:58:01,09-Jun-2011 21:09:42,0.9568,6,1.03,8.888,33.48101,-116.57184
49,04-Jun-2011 05:58:01,21-Jul-2011 13:56:43,0.9054,6,1.16,8.901,33.48056,-116.57226
49,04-Jun-2011 05:58:01,04-Jun-2011 05:58:04,1.0,6,1.63,8.901,33.48127,-116.57142
50,19-Jul-2011 20:42:25,12-Jun-2011 09:37:53,0.9323,3,0.87,9.099,33.48123,-116.57206
50,19-Jul-2011 20:42:25,19-Jul-2011 20:42:27,1.0,3,1.63,9.092,33.48105,-116.57227
51,22-Jun-2011 13:12:06,22-Jun-2011 10:55:20,0.9339,8,1.14,6.836,33.46323,-116.45309
51,22-Jun-2011 13:12:06,22-Jun-2011 13:12:12,1.0,8,2.16,6.824,33.46366,-116.45377
52,05-Jul-2011 04:40:56,05-Jul-2011 03:50:22,0.9051,10,0.90,7.314,33.46639,-116.45117
52,05-Jul-2011 04:40:56,05-Jul-2011 04:41:00,1.0,10,2.2,7.237,33.46636,-116.45151
53,05-Jul-2011 04:39:32,05-Jul-2011 03:44:00,0.924,9,0.78,7.314,33.46639,-116.45117
53,05-Jul-2011 04:39:32,05-Jul-2011 04:39:35,1.0,9,1.55,7.355,33.46629,-116.45089
54,09-Jul-2011 22:34:40,15-Jul-2011 11:32:01,0.9032,7,1.19,7.959,33.40806,-116.39287
54,09-Jul-2011 22:34:40,09-Jul-2011 22:34:47,1.0,7,1.97,7.898,33.40774,-116.39293
55,03-Jul-2011 23:25:53,15-Jul-2011 07:02:08,0.9244,5,0.92,8.847,33.47949,-116.57399
55,03-Jul-2011 23:25:53,03-Jul-2011 23:25:57,1.0,5,2.01,8.754,33.47979,-116.57319
56,10-Jun-2011 17:24:52,17-Jul-2011 22:17:23,0.9416,8,0.87,8.919,33.48091,-116.57215
56,10-Jun-2011 17:24:52,25-Jul-2011 05:34:57,0.9251,7,0.67,8.850,33.48064,-116.57208
56,10-Jun-2011 17:24:52,10-Jun-2011 17:24:55,1.0,8,1.67,8.978,33.48089,-116.57217
57,26-Jun-2011 08:12:37,17-Jul-2011 09:29:07,0.9449,8,0.55,8.480,33.48164,-116.57048
57,26-Jun-2011 08:12:37,26-Jun-2011 08:12:40,1.0,8,2.36,8.546,33.48193,-116.57030
58,05-Aug-2011 04:24:00,05-Aug-2011 01:09:16,0.9049,8,1.65,6.119,33.50613,-116.45377
58,05-Aug-2011 04:24:00,05-Aug-2011 11:49:55,0.9016,8,1.00,6.227,33.50611,-116.45355
58,05-Aug-2011 01:09:14,04-Aug-2011 09:16:31,0.9083,4,1.83,6.116,33.50651,-116.45395
58,05-Aug-2011 04:24:00,05-Aug-2011 04:24:05,1.0,8,1.56,6.285,33.50639,-116.45404
59,30-Jul-2013 01:54:58,29-Sep-2011 10:28:03,0.9062,4,0.22,5.534,33.50461,-116.45243
59,30-Jul-2013 01:54:58,30-Jul-2013 01:55:03,1.0,4,1.83,5.4,33.50442,-116.45203
60,31-Oct-2011 19:00:54,15-Nov-2011 14:21:21,0.923,4,0.81,11.408,33.47305,-116.56334
60,31-Oct-2011 19:00:54,31-Oct-2011 19:00:58,1.0,4,1.98,11.459,33.47361,-116.56303
61,05-Dec-2011 09:52:26,18-Nov-2011 07:40:39,0.9534,4,0.85,11.546,33.47216,-116.56341
61,05-Dec-2011 09:52:26,05-Dec-2011 09:52:28,1.0,4,1.7,11.527,33.47197,-116.56368
62,05-Jan-2012 00:21:35,05-Jan-2012 00:21:09,0.9171,9,0.62,12.512,33.48823,-116.47114
62,05-Jan-2012 00:21:35,05-Jan-2012 00:21:39,1.0,9,1.18,12.507,33.48804,-116.47122
63,11-Jan-2012 07:58:50,11-Jan-2012 07:58:31,0.9583,3,1.03,13.379,33.46868,-116.49353
63,11-Jan-2012 07:58:50,11-Jan-2012 07:59:14,0.9277,3,1.47,13.383,33.46829,-116.49268
63,11-Jan-2012 07:58:50,11-Jan-2012 07:58:54,1.0,3,1.27,13.316,33.46828,-116.49309
64,29-Feb-2012 16:35:59,29-Feb-2012 17:50:20,0.9172,8,0.46,10.294,33.49171,-116.55478
64,29-Feb-2012 16:35:59,01-Mar-2012 02:44:20,0.9531,7,1.26,10.572,33.48949,-116.55569
64,29-Feb-2012 16:35:59,29-Feb-2012 16:36:02,1.0,8,1.67,10.572,33.48988,-116.55574
65,23-Mar-2012 16:20:36,17-Mar-2012 04:41:37,0.9381,8,1.33,6.915,33.47382,-116.55705
```

65,23-Mar-2012 16:20:36,23-Mar-2012 16:20:38,1.0,8,2.13,6.933,33.47390,-116.55715
66,06-Apr-2012 04:03:48,05-Apr-2012 16:20:29,0.906,8,0.83,8.288,33.36641,-116.40498
66,06-Apr-2012 04:03:48,06-Apr-2012 04:03:54,1.0,8,1.65,8.34,33.36653,-116.40464
67,14-Nov-2012 04:27:46,14-Jun-2015 08:39:35,0.9226,4,0.24,11.065,33.42021,-116.37264
67,14-Nov-2012 04:27:46,23-Oct-2015 12:53:53,0.9227,6,1.04,10.895,33.41949,-116.37266
67,14-Nov-2012 04:27:46,26-Dec-2014 10:53:43,0.9819,6,1.67,10.907,33.41975,-116.37247
67,14-Nov-2012 04:27:46,26-Dec-2014 10:54:02,0.9145,6,1.91,11.005,33.41979,-116.37237
67,14-Nov-2012 04:27:46,26-Dec-2014 10:56:44,0.9156,6,1.35,10.837,33.41933,-116.37251
67,29-Oct-2016 00:01:23,08-Apr-2012 12:00:38,0.914,6,0.58,10.987,33.41931,-116.37170
67,26-Dec-2014 10:53:38,29-Oct-2016 00:01:27,0.926,6,1.86,10.945,33.41937,-116.37190
67,14-Nov-2012 04:27:46,14-Nov-2012 04:27:53,1.0,4,1.85,10.998,33.42014,-116.37278
68,13-Apr-2012 06:25:43,13-Apr-2012 09:29:40,0.9441,9,2.09,8.252,33.36677,-116.40476
68,13-Apr-2012 06:25:43,13-Apr-2012 06:25:47,1.0,9,1.67,8.367,33.36650,-116.40425
69,01-May-2012 07:54:12,18-Apr-2012 22:48:38,0.9314,6,0.59,11.204,33.48017,-116.59165
69,01-May-2012 07:54:12,04-Jun-2012 23:23:19,0.9008,4,1.85,11.256,33.47943,-116.59227
69,01-May-2012 07:54:12,15-Jun-2015 09:43:07,0.9263,6,0.81,11.232,33.48011,-116.59143
69,01-May-2012 07:54:12,01-May-2012 07:54:14,1.0,6,1.54,11.244,33.48001,-116.59179
70,30-Apr-2012 19:51:03,29-Apr-2012 22:53:59,0.9047,6,2.79 ,7.168,33.46351,-116.45258
70,30-Apr-2012 19:51:03,30-Apr-2012 19:51:07,1.0,6,1.81,7.106,33.46303,-116.45241
71,21-May-2012 06:19:16,17-May-2012 16:50:25,0.9396,7,1.06,13.553,33.48088,-116.48301
71,21-May-2012 06:19:16,20-May-2012 10:07:44,0.9455,7,1.18,13.719,33.48130,-116.48284
71,21-May-2012 06:19:16,20-May-2012 16:27:40,0.9407,7,1.36,13.666,33.48156,-116.48348
71,21-May-2012 06:19:16,21-May-2012 06:19:20,1.0,7,1.88,13.617,33.48130,-116.48297
72,19-May-2012 03:32:25,19-May-2012 03:32:53,0.9052,11,1.0,13.596,33.48688,-116.49155
72,19-May-2012 03:32:25,19-May-2012 03:32:29,1.0,11,1.6,13.564,33.48715,-116.49177
73,19-May-2013 04:31:42,23-Jun-2012 01:27:29,0.9465,5,0.85,11.233,33.42037,-116.37288
73,19-May-2013 04:31:42,19-May-2013 04:31:49,1.0,5,1.67,11.356,33.42037,-116.37216
74,30-Jun-2012 03:20:41,30-Jun-2012 03:19:55,0.9062,8,1.77,14.197,33.50230,-116.49510
74,30-Jun-2012 03:20:41,30-Jun-2012 03:20:45,1.0,8,2.77,14.063,33.50283,-116.49522
75,28-Dec-2012 04:22:33,15-Aug-2012 09:41:52,0.9169,5,1.12,10.799,33.42164,-116.37696
75,28-Dec-2012 04:22:33,28-Dec-2012 04:22:40,1.0,5,2.28,10.7,33.42115,-116.37646
76,20-Sep-2012 12:13:12,14-Sep-2012 12:08:24,0.9347,7,1.93,7.537,33.46263,-116.43396
76,20-Sep-2012 12:13:12,14-Sep-2012 12:17:09,0.959,7,1.50,7.438,33.46270,-116.43435
76,20-Sep-2012 12:13:12,20-Sep-2012 12:13:16,1.0,7,2.39,7.289,33.46286,-116.43475
77,26-Oct-2012 23:23:33,19-Oct-2012 14:42:48,0.9218,7,1.75,14.239,33.49082,-116.48414
77,26-Oct-2012 23:23:33,26-Oct-2012 23:23:37,1.0,7,1.73,14.246,33.49130,-116.48376
78,11-Jan-2013 12:24:10,11-Jan-2013 12:23:36,0.9462,8,0.96,12.697,33.46956,-116.49817
78,11-Jan-2013 12:24:10,11-Jan-2013 12:24:21,0.9064,8,1.85,11.954,33.46879,-116.49671
78,11-Jan-2013 12:24:10,11-Jan-2013 12:24:15,1.0,8,1.63,12.697,33.46956,-116.49817
79,11-Jan-2013 20:33:44,11-Jan-2013 20:25:26,0.9317,10,0.96,13.988,33.50860,-116.51119
79,11-Jan-2013 20:33:44,11-Jan-2013 20:33:48,1.0,10,1.51,13.988,33.50860,-116.51119
80,20-Jan-2013 01:31:15,20-Jan-2013 01:31:07,0.9168,7,0.96,8.581,33.51951,-116.42024
80,20-Jan-2013 01:31:15,20-Jan-2013 01:31:19,1.0,7,1.56,8.606,33.51955,-116.42020
81,17-Mar-2013 09:41:09,22-Jan-2013 06:38:36,0.9253,6,1.13,9.498,33.44294,-116.56595
81,17-Mar-2013 09:41:09,17-Mar-2013 09:41:12,1.0,6,1.59,9.665,33.44370,-116.56567
82,03-Mar-2013 17:20:55,13-Feb-2013 13:22:16,0.9306,7,1.22,5.150,33.50605,-116.45379
82,03-Mar-2013 17:20:55,15-Feb-2013 05:44:39,0.9567,8,1.64,5.200,33.50563,-116.45344
82,03-Mar-2013 17:20:55,03-Mar-2013 17:20:59,1.0,8,2.25,5.136,33.50594,-116.45387
83,11-Mar-2013 18:13:40,11-Mar-2013 18:14:28,0.9805,9,2.12,12.987,33.50869,-116.43731
83,11-Mar-2013 18:13:40,11-Mar-2013 18:13:45,1.0,9,1.67,13.069,33.50869,-116.43725
84,15-Mar-2013 06:23:25,11-Mar-2013 18:38:34,0.9037,8,1.14,9.969,33.50985,-116.44989
84,15-Mar-2013 06:23:25,15-Mar-2013 06:23:29,1.0,8,1.69,9.156,33.51036,-116.45127
85,11-Mar-2013 19:08:31,11-Mar-2013 17:12:55,0.9186,8,1.3,10.519,33.52347,-116.43350

```
85,11-Mar-2013 19:08:31,11-Mar-2013 19:08:35,1.0,8,2.3,10.317,33.52311,-116.43325
86,11-Mar-2013 17:23:51,11-Mar-2013 17:35:31,0.9306,7,1.99,10.495,33.51384,-116.46899
86,11-Mar-2013 17:23:51,11-Mar-2013 17:23:55,1.0,7,1.86,10.429,33.51325,-116.46904
87,11-Mar-2013 16:51:09,11-Mar-2013 16:50:55,0.945,9,1.51,10.820,33.50684,-116.45839
87,11-Mar-2013 16:51:09,11-Mar-2013 16:51:13,1.0,9,2.23,10.671,33.50664,-116.45849
88,12-Mar-2013 10:28:03,12-Mar-2013 10:12:55,0.9079,6,0.39,10.951,33.50426,-116.45531
88,12-Mar-2013 10:28:03,12-Mar-2013 10:28:08,1.0,6,1.74,11.013,33.50426,-116.45536
89,12-Mar-2013 01:29:39,12-Mar-2013 01:20:51,0.9369,7,1.14,10.104,33.48663,-116.43235
89,12-Mar-2013 01:29:39,12-Mar-2013 01:29:44,1.0,7,1.6,10.178,33.48673,-116.43201
90,24-May-2013 02:54:06,12-Mar-2013 06:18:22,0.907,6,0.65,10.016,33.51684,-116.45116
90,24-May-2013 02:54:06,23-Jun-2013 12:35:13,0.9014,7,0.72,9.793,33.51689,-116.45110
90,24-May-2013 02:54:06,17-Jul-2013 21:58:05,0.9696,8,1.86,10.053,33.51652,-116.45098
90,24-May-2013 02:54:06,17-Jul-2013 23:05:52,0.9127,8,0.92,10.081,33.51668,-116.45084
90,24-May-2013 02:54:06,17-Jul-2013 23:46:27,0.9183,8,1.13,10.036,33.51647,-116.45075
90,24-May-2013 02:54:06,08-Aug-2013 18:34:16,0.9053,7,1.64,10.039,33.51636,-116.45057
90,08-Aug-2013 18:34:14,14-May-2013 02:40:42,0.9269,4,0.68,9.932,33.51615,-116.45017
90,08-Aug-2013 18:34:14,24-May-2013 07:13:03,0.9365,7,0.79,10.099,33.51620,-116.45009
90,08-Aug-2013 18:34:14,24-May-2013 15:45:52,0.9462,7,1.69,9.992,33.51608,-116.45013
90,17-Jul-2013 21:58:02,24-May-2013 12:07:02,0.9257,9,1.08,10.058,33.51646,-116.45045
90,24-May-2013 15:45:50,09-Aug-2013 18:18:43,0.9207,8,0.90,9.989,33.51590,-116.45000
90,24-May-2013 15:45:50,14-Aug-2013 13:27:20,0.9201,9,0.71,9.947,33.51625,-116.45021
90,24-May-2013 02:54:06,24-May-2013 02:54:10,1.0,8,1.87,9.889,33.51642,-116.45070
91,14-Mar-2013 20:50:15,12-Mar-2013 04:52:00,0.9782,6,1.00,8.110,33.50565,-116.46783
91,14-Mar-2013 20:50:15,12-Mar-2013 06:02:29,0.9116,6,0.56,8.118,33.50581,-116.46780
91,14-Mar-2013 20:50:15,14-Mar-2013 20:50:19,1.0,6,1.69,8.129,33.50568,-116.46775
92,13-Mar-2013 06:34:58,13-Mar-2013 06:36:40,0.9199,8,0.47,11.162,33.48933,-116.45990
92,13-Mar-2013 06:34:58,13-Mar-2013 06:35:03,1.0,8,1.96,11,33.48934,-116.45993
93,13-Mar-2013 07:12:05,13-Mar-2013 07:11:53,0.9527,7,0.35,13.288,33.50918,-116.43760
93,13-Mar-2013 07:12:05,13-Mar-2013 07:12:10,1.0,7,1.76,12.768,33.50879,-116.43759
94,15-Mar-2013 08:39:21,15-Mar-2013 08:41:44,0.9247,10,0.49,8.806,33.50593,-116.45206
94,15-Mar-2013 08:39:21,15-Mar-2013 08:39:25,1.0,10,1.95,8.681,33.50575,-116.45223
95,15-Mar-2013 23:19:16,16-Mar-2013 04:13:12,0.9,5,0.36,7.996,33.36457,-116.40335
95,15-Mar-2013 23:19:16,15-Mar-2013 23:19:21,1.0,5,1.88,7.961,33.36429,-116.40318
96,17-Mar-2013 09:43:59,17-Mar-2013 09:45:07,0.9502,10,1.07,8.371,33.52320,-116.44983
96,17-Mar-2013 09:43:59,17-Mar-2013 09:44:03,1.0,10,1.57,8.371,33.52320,-116.44983
97,14-Jun-2012 07:05:07,17-Mar-2013 03:24:25,0.9053,7,0.53,6.393,33.46251,-116.45557
97,14-Jun-2012 07:05:07,14-Jun-2012 07:05:11,1.0,7,1.82,6.363,33.46254,-116.45563
98,16-Mar-2013 11:37:07,17-Mar-2013 11:39:57,0.9101,8,0.54,8.486,33.50900,-116.46145
98,16-Mar-2013 11:37:07,21-Mar-2013 10:28:12,0.9169,8,0.73,8.495,33.50886,-116.46130
98,16-Mar-2013 11:37:07,05-Apr-2013 20:47:41,0.9039,5,0.76,8.538,33.50849,-116.46157
98,16-Mar-2013 11:37:07,14-Apr-2013 17:22:22,0.9201,7,1.10,8.361,33.50847,-116.46112
98,16-Mar-2013 11:37:07,16-Mar-2013 11:37:10,1.0,8,1.75,8.434,33.50863,-116.46178
99,18-Mar-2013 11:15:26,18-Mar-2013 09:56:23,0.9365,9,0.70,8.597,33.50212,-116.47025
99,18-Mar-2013 11:15:26,05-Apr-2013 04:28:10,0.9145,7,1.25,8.824,33.50214,-116.47032
99,18-Mar-2013 11:15:26,18-Mar-2013 11:15:29,1.0,9,1.71,8.599,33.50183,-116.47015
100,03-Apr-2013 17:10:47,19-Mar-2013 03:26:08,0.9147,7,0.59,8.706,33.50227,-116.47069
100,03-Apr-2013 17:10:47,21-Mar-2013 20:51:34,0.9368,8,1.64,8.624,33.50238,-116.47107
100,03-Apr-2013 17:10:47,03-Apr-2013 02:44:29,0.9646,9,1.04,8.741,33.50250,-116.47093
100,03-Apr-2013 17:10:47,03-Apr-2013 17:10:50,1.0,9,1.62,8.602,33.50184,-116.47016
101,18-Mar-2013 19:22:34,20-Mar-2013 20:37:24,0.913,7,1.17,8.380,33.50159,-116.46991
101,18-Mar-2013 19:22:34,18-Mar-2013 19:22:38,1.0,7,1.96,8.464,33.50183,-116.47015
102,21-Mar-2013 09:40:58,21-Mar-2013 11:42:25,0.9215,9,0.92,8.019,33.50336,-116.47318
102,21-Mar-2013 09:40:58,19-Apr-2013 10:31:57,0.9014,8,0.49,8.015,33.50327,-116.47305
```

102,21-Mar-2013 09:40:58,21-Mar-2013 09:41:01,1.0,9,2.1,7.919,33.50287,-116.47309
103,07-May-2013 04:50:00,24-Mar-2013 23:35:03,0.9825,7,1.11,8.131,33.50387,-116.47328
103,07-May-2013 04:50:00,28-Mar-2013 12:27:35,0.9158,7,1.60,8.205,33.50430,-116.47345
103,07-May-2013 04:50:00,30-Apr-2013 00:36:48,0.9488,3,0.82,8.199,33.50486,-116.47314
103,07-May-2013 04:50:00,07-May-2013 04:50:04,1.0,7,1.89,8.041,33.50372,-116.47287
104,27-Mar-2013 17:29:08,22-Mar-2013 14:38:32,0.9302,7,0.84,6.368,33.49807,-116.44160
104,27-Mar-2013 17:29:08,27-Mar-2013 17:29:12,1.0,7,1.65,6.565,33.49808,-116.44173
105,21-May-2014 01:03:05,23-Mar-2013 06:54:23,0.9054,5,0.66,8.906,33.51592,-116.44716
105,21-May-2014 01:03:05,28-May-2014 21:38:01,0.9507,5,0.56,9.068,33.51589,-116.44667
105,21-May-2014 01:03:05,21-May-2014 01:03:09,1.0,5,1.7,8.986,33.51594,-116.44675
106,26-Mar-2013 13:33:54,26-Mar-2013 13:33:32,0.9089,8,1.78,9.586,33.52940,-116.43582
106,26-Mar-2013 13:33:54,26-Mar-2013 13:33:59,1.0,8,1.63,9.729,33.52980,-116.43574
107,29-Mar-2013 02:41:04,27-Mar-2013 22:07:07,0.9211,8,1.10,6.752,33.49614,-116.43802
107,29-Mar-2013 02:41:04,29-Mar-2013 02:41:08,1.0,8,1.97,6.676,33.49590,-116.43779
108,13-Dec-2013 04:11:05,27-Mar-2013 17:59:21,0.9607,8,1.16,7.039,33.49776,-116.44125
108,13-Dec-2013 04:11:05,13-Dec-2013 04:11:09,1.0,8,1.75,7.046,33.49782,-116.44103
109,07-May-2013 02:09:56,21-Mar-2013 00:38:26,0.9316,8,0.76,8.854,33.50621,-116.45392
109,07-May-2013 02:09:56,29-Mar-2013 21:15:18,0.922,6,1.16,8.918,33.50601,-116.45378
109,07-May-2013 02:09:56,18-Apr-2013 10:44:59,0.9433,7,0.80,8.860,33.50638,-116.45364
109,07-May-2013 02:09:56,07-May-2013 02:10:01,1.0,8,2.46,8.823,33.50598,-116.45388
110,06-Apr-2013 19:24:02,06-Apr-2013 12:01:32,0.9641,9,0.75,7.460,33.49882,-116.44349
110,06-Apr-2013 19:24:02,06-Apr-2013 18:42:16,0.9826,9,1.31,7.480,33.49889,-116.44333
110,06-Apr-2013 19:24:02,06-Apr-2013 19:24:06,1.0,9,1.68,7.471,33.49884,-116.44342
111,14-Apr-2013 18:33:54,13-Apr-2013 22:14:56,0.9059,8,1.25,7.983,33.49420,-116.45783
111,14-Apr-2013 18:33:54,14-Apr-2013 18:33:58,1.0,8,1.88,7.881,33.49411,-116.45831
112,16-Apr-2013 15:10:16,14-Apr-2013 03:40:42,0.9258,7,1.24,9.802,33.51569,-116.44952
112,16-Apr-2013 15:10:16,16-Apr-2013 15:10:20,1.0,7,1.71,9.712,33.51576,-116.44961
113,14-Jul-2013 05:49:12,27-Apr-2013 01:24:28,0.9002,5,0.91,8.137,33.50750,-116.47238
113,14-Jul-2013 05:49:12,14-Jul-2013 05:49:17,1.0,5,1.68,8.065,33.50777,-116.47103
114,06-Sep-2013 03:12:33,01-May-2013 10:11:36,0.9274,8,0.85,8.736,33.50496,-116.47342
114,06-Sep-2013 03:12:33,21-May-2013 11:38:57,0.9175,5,1.76,8.507,33.50484,-116.47345
114,06-Sep-2013 03:12:33,22-Jul-2013 08:43:33,0.9247,6,0.46,8.743,33.50482,-116.47317
114,21-May-2013 11:38:53,02-Aug-2013 10:12:24,0.9382,6,1.45,8.507,33.50484,-116.47345
114,06-Sep-2013 03:12:33,06-Sep-2013 03:12:38,1.0,8,1.74,8.82,33.50525,-116.47305
115,18-Nov-2013 19:50:23,11-May-2013 17:24:43,0.9199,7,1.29,8.561,33.52852,-116.44335
115,18-Nov-2013 19:50:23,18-Nov-2013 19:52:19,0.9681,10,0.73,8.654,33.52883,-116.44394
115,18-Nov-2013 19:50:23,18-Nov-2013 19:50:27,1.0,10,1.88,8.605,33.52882,-116.44371
116,28-Jun-2013 19:52:31,01-Jun-2013 23:15:40,0.9974,6,1.35,7.789,33.50615,-116.47193
116,28-Jun-2013 19:52:31,02-Jun-2013 15:48:59,0.908,7,1.31,7.811,33.50627,-116.47173
116,28-Jun-2013 19:52:31,12-Aug-2013 18:49:45,0.9052,6,2.07,7.886,33.50667,-116.47220
116,28-Jun-2013 19:52:31,28-Jun-2013 19:52:35,1.0,7,1.91,7.821,33.50614,-116.47176
117,15-Nov-2013 02:01:50,21-Sep-2013 22:52:27,0.9381,10,0.81,7.988,33.50605,-116.47254
117,15-Nov-2013 02:01:50,05-Mar-2014 07:57:41,0.9205,9,0.66,7.907,33.50605,-116.47211
117,15-Nov-2013 02:01:50,15-Nov-2013 02:01:54,1.0,10,1.65,8.129,33.50613,-116.47230
118,18-May-2013 05:28:05,13-Jun-2013 12:00:24,0.9015,7,0.71,11.059,33.51604,-116.44828
118,18-May-2013 05:28:05,18-May-2013 05:28:09,1.0,7,2.2,10.929,33.51622,-116.44779
119,15-Jun-2013 15:39:13,15-Jun-2013 16:13:36,0.9306,8,1.02,8.238,33.50436,-116.47328
119,15-Jun-2013 15:39:13,16-Jun-2013 07:11:44,0.9078,8,0.78,8.293,33.50490,-116.47319
119,15-Jun-2013 15:39:13,15-Jun-2013 15:39:19,1.0,8,1.9,8.475,33.50449,-116.47319
120,27-Aug-2013 08:09:41,19-Jun-2013 16:49:16,0.9359,4,1.66,8.593,33.50685,-116.47290
120,27-Aug-2013 08:09:41,19-Jul-2013 04:54:05,0.9346,4,1.14,8.326,33.50719,-116.47276
120,27-Aug-2013 08:09:41,27-Aug-2013 08:09:44,1.0,4,1.97,8.481,33.50719,-116.47289
121,21-Sep-2013 17:54:09,02-Jul-2013 10:55:18,0.9715,7,0.91,8.085,33.50651,-116.47278

```
121,21-Sep-2013 17:54:09,21-Sep-2013 18:20:11,0.9467,9,1.30,8.156,33.50654,-116.47259
121,21-Sep-2013 17:54:09,21-Sep-2013 17:54:12,1.0,9,1.58,8.034,33.50663,-116.47222
122,08-Aug-2013 18:32:48,10-Jul-2013 13:37:10,0.9473,3,0.63 ,10.027,33.51626,-116.45018
122,08-Aug-2013 18:32:48,08-Aug-2013 18:32:53,1.0,3,2.65,9.889,33.51642,-116.45070
123,22-Nov-2015 21:11:03,14-Jul-2013 12:28:42,0.9086,7,0.29,5.214,33.51098,-116.46125
123,22-Nov-2015 21:11:03,22-Nov-2015 19:07:11,0.9909,9,1.09,4.715,33.50791,-116.45960
123,22-Nov-2015 21:11:03,22-Nov-2015 21:11:07,1.0,9,1.83,4.715,33.50791,-116.45960
124,01-Apr-2013 03:00:01,30-Jul-2013 15:51:02,0.9067,5,1.22,5.292,33.50451,-116.45210
124,01-Apr-2013 03:00:01,01-Apr-2013 03:00:05,1.0,5,1.63,5.292,33.50425,-116.45151
125,12-Mar-2013 10:26:11,05-Aug-2013 12:52:35,0.9021,5,1.74,9.870,33.51762,-116.45250
125,12-Mar-2013 10:26:11,12-Mar-2013 10:26:16,1.0,5,1.65,10.075,33.51729,-116.45238
126,19-Aug-2013 01:36:20,18-Aug-2013 18:54:56,0.9196,7,0.95,10.169,33.48507,-116.43059
126,19-Aug-2013 01:36:20,19-Aug-2013 01:36:25,1.0,7,1.63,9.949,33.48417,-116.42943
127,11-Mar-2013 16:58:50,24-Aug-2013 04:58:04,0.9197,3,1.17,10.106,33.51016,-116.45357
127,11-Mar-2013 16:58:50,11-Mar-2013 16:58:54,1.0,3,2.16,10.135,33.51055,-116.45323
128,25-Aug-2013 06:08:21,25-Aug-2013 05:59:01,0.9582,7,0.83,11.190,33.48154,-116.48344
128,25-Aug-2013 06:08:21,25-Aug-2013 06:52:30,0.9558,7,1.12,11.142,33.48185,-116.48437
128,25-Aug-2013 06:08:21,25-Aug-2013 06:08:26,1.0,7,1.76,11.144,33.48135,-116.48360
129,14-Apr-2014 16:07:03,03-Sep-2013 10:14:33,0.9675,6,1.06,5.512,33.50396,-116.45107
129,14-Apr-2014 16:07:03,04-Sep-2013 11:00:49,0.9146,6,0.58,5.626,33.50421,-116.45134
129,14-Apr-2014 16:07:03,14-Apr-2014 16:07:07,1.0,6,1.67,5.521,33.50395,-116.45098
130,22-Sep-2013 04:26:09,05-Sep-2013 06:12:22,0.9092,7,0.62,9.741,33.44451,-116.56783
130,22-Sep-2013 04:26:09,13-Sep-2013 10:19:31,0.9605,6,1.46,9.629,33.44444,-116.56816
130,22-Sep-2013 04:26:09,22-Sep-2013 04:26:13,1.0,7,1.83,9.707,33.44434,-116.56769
131,23-Sep-2013 19:40:03,25-Sep-2013 05:41:29,0.9465,6,1.00,8.710,33.47364,-116.56857
131,23-Sep-2013 19:40:03,23-Sep-2013 19:40:06,1.0,6,1.66,8.71,33.47362,-116.56846
132,25-Jan-2014 23:45:05,26-Sep-2013 16:38:40,0.9389,4,2.41,7.133,33.44004,-116.44491
132,25-Jan-2014 23:45:05,25-Jan-2014 23:45:09,1.0,4,1.94,7.133,33.44004,-116.44491
133,31-Oct-2013 13:33:50,23-Oct-2013 06:29:41,0.9586,7,1.11,12.229,33.35238,-116.38737
133,31-Oct-2013 13:33:50,31-Oct-2013 13:33:56,1.0,7,1.57,12.184,33.35248,-116.38785
134,21-Jan-2014 14:12:59,27-Oct-2013 19:30:26,0.9034,8,0.84,7.323,33.50290,-116.47232
134,21-Jan-2014 14:12:59,04-Jan-2014 06:38:58,0.9042,9,0.53,7.331,33.50352,-116.47200
134,21-Jan-2014 14:12:59,21-Jan-2014 14:13:02,1.0,9,1.62,7.276,33.50298,-116.47215
135,16-Nov-2013 05:12:47,16-Nov-2013 00:28:20,0.9377,10,1.15,8.949,33.51230,-116.46793
135,16-Nov-2013 05:12:47,16-Nov-2013 05:12:52,1.0,10,1.79,8.979,33.51217,-116.46800
136,02-Dec-2013 16:54:56,02-Dec-2013 16:54:05,0.9221,9,0.79,14.030,33.49516,-116.50326
136,02-Dec-2013 16:54:56,02-Dec-2013 16:54:59,1.0,9,1.7,14.053,33.49503,-116.50359
137,19-Dec-2013 17:46:06,19-Dec-2013 18:19:40,0.9665,8,1.21,7.238,33.50561,-116.44947
137,19-Dec-2013 17:46:06,19-Dec-2013 19:58:40,0.9375,8,0.93,7.391,33.50589,-116.44960
137,19-Dec-2013 17:46:06,21-Dec-2013 14:08:33,0.9056,6,1.20,7.466,33.50561,-116.44947
137,19-Dec-2013 17:46:06,19-Dec-2013 17:46:10,1.0,8,1.86,7.238,33.50561,-116.44947
138,05-Jan-2014 23:11:38,03-Jan-2014 17:23:56,0.9583,8,0.86,7.794,33.50391,-116.47257
138,05-Jan-2014 23:11:38,05-Jan-2014 23:11:42,1.0,8,2.54,7.757,33.50365,-116.47288
139,28-May-2015 10:39:34,07-Jan-2014 09:51:29,0.9068,10,1.62,7.757,33.50513,-116.47231
139,28-May-2015 10:39:34,30-Jul-2015 04:16:17,0.9128,7,0.59,7.653,33.50488,-116.47211
139,28-May-2015 10:39:34,28-May-2015 10:39:38,1.0,10,2.12,7.474,33.50513,-116.47243
140,07-Feb-2014 06:12:47,19-Feb-2014 05:16:50,0.9354,7,0.85,7.169,33.50389,-116.47178
140,07-Feb-2014 06:12:47,07-Feb-2014 06:12:51,1.0,7,1.5,7.265,33.50382,-116.47201
141,12-Jan-2014 01:29:02,26-Feb-2014 04:14:47,0.9564,6,1.18,7.489,33.50473,-116.47240
141,12-Jan-2014 01:29:02,12-Jan-2014 01:29:07,1.0,6,1.54,7.464,33.50438,-116.47237
142,24-Jan-2016 20:15:42,10-Mar-2014 09:16:00,0.9112,3,0.56,10.753,33.42100,-116.37611
142,24-Jan-2016 20:15:42,24-Jan-2016 20:15:47,1.0,3,1.84,10.744,33.42055,-116.37533
143,29-Sep-2014 21:49:46,10-Apr-2014 10:39:52,0.9112,5,0.93,14.859,33.48961,-116.47749
```

143,29-Sep-2014 21:49:46,29-Sep-2014 21:49:50,1.0,5,1.91,14.857,33.48954,-116.47761
144,25-Apr-2014 12:50:40,25-Apr-2014 05:41:12,0.9265,9,0.74,8.711,33.46545,-116.42286
144,25-Apr-2014 12:50:40,25-Apr-2014 09:59:55,0.9168,9,0.35,8.682,33.46594,-116.42319
144,25-Apr-2014 12:50:40,25-Apr-2014 13:02:53,0.9689,9,1.66,8.662,33.46593,-116.42328
144,25-Apr-2014 12:50:40,25-Apr-2014 12:50:44,1.0,9,1.94,8.887,33.46600,-116.42272
145,14-Apr-2014 14:58:30,07-May-2014 20:48:10,0.9498,4,0.95,5.663,33.50363,-116.45023
145,14-Apr-2014 14:58:30,15-Sep-2014 06:42:41,0.9263,7,0.70,5.699,33.50313,-116.44956
145,14-Apr-2014 14:58:30,14-Apr-2014 14:58:33,1.0,7,1.92,5.619,33.50352,-116.45018
146,23-May-2014 22:15:16,23-May-2014 00:36:21,0.9107,10,0.84,8.925,33.51583,-116.44908
146,23-May-2014 22:15:16,23-May-2014 22:15:21,1.0,10,1.99,8.858,33.51623,-116.44899
147,02-Jun-2014 01:35:14,01-Jun-2014 00:52:33,0.9225,5,1.50,6.968,33.37246,-116.38918
147,02-Jun-2014 01:35:14,02-Jun-2014 01:35:19,1.0,5,1.81,7.008,33.37250,-116.38912
148,13-Jul-2014 21:47:25,13-Jul-2014 21:47:22,0.9508,8,1.38,13.244,33.49989,-116.49812
148,13-Jul-2014 21:47:25,13-Jul-2014 21:53:29,0.9111,8,1.07,13.320,33.50042,-116.49838
148,13-Jul-2014 21:47:25,13-Jul-2014 21:47:29,1.0,8,2.82,13.345,33.49994,-116.49809
149,16-Aug-2014 10:54:22,06-Aug-2014 17:26:43,0.941,3,1.28,7.364,33.50766,-116.47153
149,16-Aug-2014 10:54:22,16-Aug-2014 10:54:27,1.0,3,1.52,7.368,33.50761,-116.47157
150,06-Oct-2011 17:53:25,19-Aug-2014 10:38:54,0.9243,3,1.54,10.297,33.42505,-116.38660
150,06-Oct-2011 17:53:25,06-Oct-2011 17:53:32,1.0,3,1.68,10.308,33.42489,-116.38609
151,17-Aug-2013 20:11:10,07-Sep-2014 05:38:46,0.9135,6,0.85,14.564,33.48233,-116.47743
151,17-Aug-2013 20:11:10,17-Aug-2013 20:11:14,1.0,6,1.53,14.621,33.48225,-116.47715
152,11-Apr-2015 09:25:57,11-Nov-2014 03:41:18,0.913,6,1.01,8.376,33.46569,-116.56673
152,11-Apr-2015 09:25:57,14-Nov-2014 10:21:14,0.9602,3,0.30,8.370,33.46562,-116.56687
152,11-Apr-2015 09:25:57,15-Nov-2014 18:33:03,0.9184,5,1.06,8.590,33.46606,-116.56763
152,11-Apr-2015 09:25:57,15-Nov-2014 18:33:30,0.9388,5,1.59,8.365,33.46562,-116.56690
152,11-Apr-2015 09:25:57,11-Apr-2015 11:34:16,0.9012,8,0.68,8.400,33.46535,-116.56695
152,11-Apr-2015 09:25:57,12-Apr-2015 02:47:36,0.9489,8,1.15,8.344,33.46557,-116.56689
152,15-Nov-2014 18:33:27,14-Nov-2014 10:34:31,0.9186,3,0.11,8.354,33.46532,-116.56697
152,11-Apr-2015 09:25:57,11-Apr-2015 09:25:59,1.0,8,1.73,8.38,33.46565,-116.56679
153,07-Jul-2014 13:53:03,13-Nov-2014 02:43:40,0.9757,5,0.97,10.211,33.45829,-116.58881
153,07-Jul-2014 13:53:03,07-Jul-2014 13:53:07,1.0,5,1.61,10.211,33.45827,-116.58871
154,07-Apr-2015 14:32:36,14-Nov-2014 21:49:19,0.9404,3,0.44,8.623,33.46662,-116.56548
154,07-Apr-2015 14:32:36,28-Feb-2015 22:48:59,0.9184,6,1.22,8.591,33.46595,-116.56648
154,07-Apr-2015 14:32:36,23-Mar-2015 05:02:43,0.9051,6,1.10,8.506,33.46659,-116.56626
154,07-Apr-2015 14:32:36,29-Mar-2015 21:33:46,0.9064,8,0.80,8.538,33.46627,-116.56631
154,07-Apr-2015 14:32:36,07-Apr-2015 14:32:39,1.0,8,2.05,8.47,33.46604,-116.56699
155,20-Nov-2014 01:18:45,20-Nov-2014 01:14:39,0.9541,10,1.62,11.809,33.50858,-116.51606
155,20-Nov-2014 01:18:45,20-Nov-2014 01:18:48,1.0,10,1.97,11.646,33.50848,-116.51606
156,06-Apr-2015 10:20:25,07-Dec-2014 07:31:04,0.9134,7,0.19,8.575,33.46657,-116.56614
156,06-Apr-2015 10:20:25,04-Mar-2015 09:35:34,0.9057,8,0.72,8.618,33.46609,-116.56628
156,06-Apr-2015 10:20:25,24-Mar-2015 14:25:29,0.9337,7,0.69,8.651,33.46644,-116.56641
156,06-Apr-2015 10:20:25,25-Mar-2015 13:44:02,0.9188,7,0.62,8.616,33.46636,-116.56638
156,06-Apr-2015 10:20:25,07-Apr-2015 16:43:46,0.9575,7,1.31,8.611,33.46606,-116.56655
156,06-Apr-2015 10:20:25,15-Apr-2015 05:22:33,0.9553,9,1.12,8.570,33.46634,-116.56636
156,06-Apr-2015 10:20:25,06-Apr-2015 10:20:29,1.0,9,1.79,8.661,33.46643,-116.56625
157,27-Mar-2015 08:49:10,09-Dec-2014 14:34:48,0.9569,8,0.37,8.665,33.46683,-116.56608
157,27-Mar-2015 08:49:10,27-Mar-2015 08:49:13,1.0,8,1.74,8.619,33.46672,-116.56603
158,13-Nov-2012 22:09:24,26-Dec-2014 15:36:26,0.9014,3,0.68,11.127,33.42073,-116.37296
158,13-Nov-2012 22:09:24,13-Nov-2012 22:09:28,1.0,3,1.87,10.971,33.42073,-116.37373
159,25-Oct-2014 09:36:41,02-Jan-2015 09:49:36,0.9119,3,0.38,9.359,33.44660,-116.56868
159,25-Oct-2014 09:36:41,22-Nov-2015 11:24:24,0.9903,4,0.75,9.375,33.44603,-116.56879
159,25-Oct-2014 09:36:41,25-Oct-2014 09:36:44,1.0,4,1.83,9.373,33.44644,-116.56889
160,08-Jan-2015 15:26:10,08-Jan-2015 15:06:03,0.9051,8,1.25,14.685,33.50675,-116.49571

160,08-Jan-2015 15:26:10,08-Jan-2015 15:26:14,1.0,8,1.5,14.772,33.50720,-116.49531
161,08-Dec-2012 19:56:43,09-Jan-2015 16:30:01,0.907,3,1.02,14.869,33.48309,-116.47681
161,08-Dec-2012 19:56:43,08-Dec-2012 19:56:48,1.0,3,1.5,14.641,33.48155,-116.47563
162,06-Feb-2015 20:28:35,06-Feb-2015 23:50:59,0.9027,6,1.50,9.596,33.45706,-116.40970
162,06-Feb-2015 20:28:35,06-Feb-2015 20:28:40,1.0,6,2.15,9.473,33.45727,-116.41073
163,19-Dec-2014 00:48:04,18-Feb-2015 03:09:12,0.9146,3,1.16,7.557,33.39717,-116.38260
163,19-Dec-2014 00:48:04,19-Dec-2014 00:48:11,1.0,3,1.68,7.581,33.39619,-116.38165
164,28-Feb-2015 01:18:57,25-Feb-2015 04:39:56,0.9283,6,0.70,7.787,33.50940,-116.47199
164,28-Feb-2015 01:18:57,28-Feb-2015 01:18:59,1.0,6,1.93,7.825,33.50935,-116.47220
165,31-Mar-2015 14:33:07,26-Feb-2015 08:07:01,0.9919,9,1.03,8.127,33.47334,-116.56996
165,31-Mar-2015 14:33:07,06-Apr-2015 23:05:30,0.9589,6,0.91,8.153,33.47323,-116.56996
165,31-Mar-2015 14:33:07,09-Apr-2015 09:51:43,0.92,8,0.30,8.175,33.47357,-116.56956
165,31-Mar-2015 14:33:07,31-Mar-2015 14:33:09,1.0,9,1.69,8.117,33.47337,-116.56983
166,27-Feb-2015 20:07:50,28-Feb-2015 16:14:22,0.9126,5,1.06,8.278,33.47165,-116.57221
166,27-Feb-2015 20:07:50,11-Apr-2015 06:27:32,0.9382,6,1.14,8.228,33.47082,-116.57304
166,27-Feb-2015 20:07:50,28-Apr-2015 01:47:36,0.9449,5,0.61,8.166,33.47095,-116.57297
166,27-Feb-2015 20:07:50,27-Feb-2015 20:07:52,1.0,6,1.57,8.251,33.47122,-116.57271
167,01-Dec-2013 19:22:25,01-Mar-2015 14:24:41,0.9175,8,1.07,13.448,33.42983,-116.43142
167,01-Dec-2013 19:22:25,01-Dec-2013 19:22:30,1.0,8,1.52,13.448,33.42983,-116.43142
168,01-Apr-2015 03:02:51,10-Mar-2015 11:32:44,0.9952,6,1.45,7.793,33.47246,-116.57074
168,01-Apr-2015 03:02:51,01-Apr-2015 03:02:54,1.0,6,1.5,7.819,33.47242,-116.57060
169,23-Mar-2015 16:37:09,13-Mar-2015 04:56:39,0.9689,4,1.11,7.904,33.47327,-116.56972
169,23-Mar-2015 16:37:09,17-Mar-2015 04:45:24,0.9613,5,0.40,7.987,33.47364,-116.56948
169,23-Mar-2015 16:37:09,02-Apr-2015 07:53:48,0.9133,5,0.79,7.885,33.47298,-116.57011
169,23-Mar-2015 16:37:09,05-Apr-2015 13:03:25,0.9408,5,0.34,7.934,33.47345,-116.56947
169,23-Mar-2015 16:37:09,07-Apr-2015 07:48:59,0.9482,5,0.36,7.940,33.47337,-116.56923
169,23-Mar-2015 16:37:09,23-Mar-2015 16:37:12,1.0,5,1.56,7.916,33.47343,-116.56958
170,02-Apr-2015 08:11:56,17-Mar-2015 12:42:06,0.9298,7,0.09,7.938,33.47332,-116.56951
170,02-Apr-2015 08:11:56,13-Mar-2015 04:56:12,0.9356,6,1.35,7.882,33.47319,-116.56993
170,02-Apr-2015 08:11:56,05-Apr-2015 12:58:58,0.985,7,1.05,7.889,33.47332,-116.56965
170,02-Apr-2015 08:11:56,11-Apr-2015 09:49:48,0.9787,6,0.47,7.866,33.47315,-116.56976
170,02-Apr-2015 08:11:56,13-Apr-2015 10:27:00,0.9404,4,1.93,7.880,33.47309,-116.56997
170,02-Apr-2015 08:11:56,02-Apr-2015 08:11:58,1.0,7,1.65,7.88,33.47309,-116.56997
170,13-Apr-2015 10:26:57,01-Apr-2015 04:21:21,0.9004,7,0.88,7.801,33.47254,-116.57051
171,05-Apr-2015 12:56:54,13-Mar-2015 20:02:51,0.9046,11,1.01,7.883,33.47295,-116.57021
171,05-Apr-2015 12:56:54,05-Apr-2015 12:56:57,1.0,11,2.44,7.88,33.47309,-116.56997
172,21-Mar-2015 10:39:42,15-Mar-2015 12:18:15,0.9661,9,0.62,7.803,33.47292,-116.56989
172,21-Mar-2015 10:39:42,02-Apr-2015 20:42:44,0.9245,7,0.75,7.739,33.47270,-116.56988
172,21-Mar-2015 10:39:42,21-Mar-2015 10:39:44,1.0,9,1.88,7.738,33.47277,-116.56985
173,11-May-2015 07:21:27,16-Mar-2015 02:53:54,0.9049,10,1.52,8.063,33.47088,-116.57325
173,11-May-2015 07:21:27,11-Apr-2015 01:54:44,0.9252,9,0.73,8.092,33.47091,-116.57328
173,11-May-2015 07:21:27,26-Apr-2015 10:52:01,0.9264,9,0.89,8.101,33.47056,-116.57399
173,16-Mar-2015 02:53:53,17-May-2015 13:56:54,0.9511,5,1.79,8.063,33.47089,-116.57316
173,11-May-2015 07:21:27,11-May-2015 07:21:29,1.0,10,1.55,8.137,33.47072,-116.57360
174,28-Mar-2015 14:42:09,02-Apr-2015 13:43:50,0.9137,7,1.14,8.110,33.47065,-116.57373
174,28-Mar-2015 14:42:09,28-Mar-2015 14:42:11,1.0,7,1.6,8.12,33.47094,-116.57318
175,17-Mar-2015 22:28:03,17-Mar-2015 23:41:07,0.9368,12,1.25,14.213,33.50056,-116.50231
175,17-Mar-2015 22:28:03,17-Mar-2015 22:28:07,1.0,12,1.83,14.131,33.50045,-116.50243
176,19-Mar-2015 03:32:12,13-Apr-2015 03:48:53,0.9701,6,1.82,7.633,33.47169,-116.57110
176,19-Mar-2015 03:32:12,19-Mar-2015 03:32:15,1.0,6,1.7,7.62,33.47181,-116.57111
177,29-Mar-2015 15:38:09,21-Mar-2015 11:39:55,0.9474,7,0.50,7.596,33.47253,-116.56973
177,29-Mar-2015 15:38:09,22-Mar-2015 23:14:40,0.9025,6,0.91,7.547,33.47206,-116.57010
177,29-Mar-2015 15:38:09,12-Apr-2015 05:52:41,0.9065,8,0.97,7.565,33.47250,-116.57004

177,29-Mar-2015 15:38:09,29-Mar-2015 15:38:11,1.0,8,1.76,7.536,33.47252,-116.56970
178,31-Mar-2015 12:53:04,23-Mar-2015 01:17:56,0.906,7,1.11,7.888,33.47005,-116.57425
178,31-Mar-2015 12:53:04,31-Mar-2015 12:53:06,1.0,7,2.01,7.922,33.46976,-116.57484
179,18-Apr-2015 14:13:04,23-Mar-2015 19:02:43,0.9342,5,1.39,8.174,33.47566,-116.56716
179,18-Apr-2015 14:13:04,18-Apr-2015 14:13:08,1.0,5,1.83,8.095,33.47562,-116.56713
180,18-Apr-2015 14:39:55,05-Apr-2015 21:42:48,0.968,8,1.21,8.118,33.47592,-116.56654
180,18-Apr-2015 14:39:55,18-Apr-2015 06:39:51,0.9542,8,0.87,8.063,33.47575,-116.56687
180,18-Apr-2015 14:39:55,18-Apr-2015 12:23:41,0.9158,8,0.67,8.013,33.47612,-116.56639
180,18-Apr-2015 14:39:55,18-Apr-2015 14:39:59,1.0,8,1.79,8.095,33.47611,-116.56662
181,09-Mar-2015 18:03:19,27-Mar-2015 11:25:58,0.9473,7,0.80,8.078,33.47446,-116.56793
181,09-Mar-2015 18:03:19,26-Apr-2015 17:00:15,0.9023,5,0.92,8.099,33.47473,-116.56772
181,09-Mar-2015 18:03:19,24-May-2015 10:42:33,0.9469,7,1.47,8.118,33.47483,-116.56785
181,09-Mar-2015 18:03:19,09-Mar-2015 18:03:23,1.0,7,1.63,8.248,33.47527,-116.56785
182,26-Apr-2015 00:37:31,28-Mar-2015 01:48:14,0.9195,5,0.78,8.083,33.47476,-116.56760
182,26-Apr-2015 00:37:31,01-Apr-2015 04:37:37,0.9251,6,0.79,8.020,33.47445,-116.56788
182,26-Apr-2015 00:37:31,05-Apr-2015 15:59:55,0.9105,6,0.41,8.051,33.47466,-116.56789
182,26-Apr-2015 00:37:31,08-Apr-2015 06:25:04,0.9041,4,1.15,8.103,33.47485,-116.56769
182,26-Apr-2015 00:37:31,05-May-2015 07:01:34,0.9256,4,0.70,7.923,33.47410,-116.56821
182,26-Apr-2015 00:37:31,26-Apr-2015 00:37:33,1.0,6,1.7,7.985,33.47440,-116.56787
183,07-Apr-2015 17:05:01,28-Mar-2015 17:04:43,0.9294,7,1.01,7.682,33.47025,-116.57390
183,07-Apr-2015 17:05:01,07-Apr-2015 17:05:03,1.0,7,1.99,7.685,33.47034,-116.57376
184,07-Apr-2015 15:44:02,01-Apr-2015 02:47:25,0.924,6,0.49,7.982,33.47454,-116.56799
184,07-Apr-2015 15:44:02,07-Apr-2015 10:29:17,0.9446,7,0.67,7.813,33.47471,-116.56825
184,07-Apr-2015 15:44:02,07-Apr-2015 15:44:04,1.0,7,1.51,8.016,33.47447,-116.56782
185,21-Nov-2015 21:39:44,06-Apr-2015 09:43:41,0.9024,6,0.34,8.121,33.46938,-116.57581
185,21-Nov-2015 21:39:44,20-Nov-2015 19:34:07,0.9013,8,0.81,8.355,33.46995,-116.57477
185,21-Nov-2015 21:39:44,21-Nov-2015 21:39:46,1.0,8,1.71,8.306,33.46979,-116.57463
186,13-Apr-2015 11:10:15,06-Apr-2015 02:13:12,0.9784,4,1.39,8.651,33.46710,-116.56604
186,13-Apr-2015 11:10:15,06-Apr-2015 07:16:17,0.9694,4,0.78,8.708,33.46759,-116.56512
186,13-Apr-2015 11:10:15,15-Apr-2015 21:28:16,0.9078,6,0.52,8.861,33.46722,-116.56535
186,13-Apr-2015 11:10:15,28-Apr-2015 12:07:00,0.9414,4,0.43,8.836,33.46742,-116.56524
186,13-Apr-2015 11:10:15,13-Apr-2015 11:10:19,1.0,6,1.72,8.717,33.46725,-116.56534
187,21-Apr-2015 23:41:53,21-Apr-2015 22:05:58,0.9008,7,1.01,12.322,33.49707,-116.56832
187,21-Apr-2015 23:41:53,21-Apr-2015 23:41:55,1.0,7,2.31,12.338,33.49707,-116.56826
188,24-Apr-2015 23:09:45,24-Apr-2015 23:20:44,0.9237,8,1.10,8.436,33.47176,-116.57214
188,24-Apr-2015 23:09:45,14-Nov-2015 23:14:09,0.9032,6,0.38,8.353,33.47202,-116.57174
188,24-Apr-2015 23:09:45,24-Apr-2015 23:09:47,1.0,8,1.62,8.422,33.47185,-116.57193
189,30-Apr-2015 15:32:16,26-Apr-2015 00:03:15,0.9598,4,1.42,7.797,33.47593,-116.56538
189,30-Apr-2015 15:32:16,02-May-2015 15:35:42,0.9402,4,1.10,7.804,33.47627,-116.56483
189,30-Apr-2015 15:32:16,30-Apr-2015 15:32:20,1.0,4,1.56,7.779,33.47592,-116.56518
190,08-May-2015 07:22:48,29-Apr-2015 01:32:54,0.9284,6,0.38,7.411,33.46914,-116.57480
190,08-May-2015 07:22:48,30-Apr-2015 00:31:59,0.9629,6,0.92,7.305,33.46919,-116.57470
190,08-May-2015 07:22:48,03-May-2015 11:21:35,0.9346,5,0.56,7.320,33.46886,-116.57461
190,08-May-2015 07:22:48,08-May-2015 02:04:14,0.9036,7,0.52,7.299,33.46887,-116.57415
190,08-May-2015 07:22:48,08-May-2015 07:22:51,1.0,7,1.74,7.355,33.46901,-116.57510
191,28-Apr-2015 10:46:16,27-Apr-2015 06:12:11,0.9806,5,1.22,7.355,33.46901,-116.57510
191,28-Apr-2015 10:46:16,30-Apr-2015 00:31:59,0.9161,7,0.92,7.305,33.46919,-116.57470
191,28-Apr-2015 10:46:16,28-Apr-2015 11:49:29,0.9428,8,1.78,7.355,33.46901,-116.57510
191,28-Apr-2015 10:46:16,28-Apr-2015 10:46:18,1.0,8,1.55,7.355,33.46901,-116.57510
192,01-May-2015 14:50:51,01-May-2015 14:51:31,0.9348,5,1.30,13.827,33.51749,-116.51724
192,01-May-2015 14:50:51,01-May-2015 14:50:56,1.0,5,1.51,13.827,33.51749,-116.51724
193,27-May-2013 09:54:02,20-May-2015 07:14:13,0.9056,7,1.16,10.838,33.37265,-116.40018
193,27-May-2013 09:54:02,27-May-2013 09:54:07,1.0,7,1.91,10.927,33.37265,-116.39944

194,21-Jul-2015 09:45:12,21-May-2015 12:26:07,0.902,4,1.29,8.021,33.47750,-116.56470
194,21-Jul-2015 09:45:12,21-May-2015 16:02:49,0.9107,4,0.99,8.024,33.47759,-116.56461
194,21-Jul-2015 09:45:12,22-May-2015 09:09:01,0.951,3,0.84,8.044,33.47771,-116.56415
194,21-Jul-2015 09:45:12,24-May-2015 11:58:19,0.9342,4,1.45,8.012,33.47755,-116.56460
194,21-Jul-2015 09:45:12,24-May-2015 12:08:47,0.9067,4,0.45,8.010,33.47753,-116.56455
194,21-Jul-2015 09:45:12,02-Aug-2015 19:02:37,0.9323,4,0.86,7.934,33.47710,-116.56454
194,21-Jul-2015 09:45:12,21-Jul-2015 09:45:14,1.0,4,1.53,8.009,33.47759,-116.56457
195,22-May-2015 16:26:29,29-May-2015 22:37:41,0.9613,4,0.90,8.017,33.47759,-116.56456
195,22-May-2015 16:26:29,22-May-2015 16:26:35,1.0,4,1.62,7.876,33.47710,-116.56441
196,07-Nov-2015 23:36:33,26-May-2015 09:23:08,0.9175,7,0.13,8.401,33.47132,-116.57342
196,07-Nov-2015 23:36:33,07-Nov-2015 23:36:35,1.0,7,1.91,8.348,33.47110,-116.57314
197,07-Jul-2015 01:17:10,18-Jun-2015 06:05:26,0.9062,7,0.76,8.127,33.53578,-116.41212
197,07-Jul-2015 01:17:10,07-Jul-2015 01:17:15,1.0,7,1.82,8.055,33.53625,-116.41283
198,17-Jul-2015 02:39:36,17-Jul-2015 02:43:23,0.9654,10,1.24,12.043,33.50389,-116.50561
198,17-Jul-2015 02:39:36,17-Jul-2015 02:54:24,0.9046,10,0.44,12.043,33.50389,-116.50561
198,17-Jul-2015 02:39:36,17-Jul-2015 02:39:40,1.0,10,1.73,12.043,33.50389,-116.50561
199,30-Aug-2015 02:01:14,30-Aug-2015 02:59:16,0.9362,10,2.67,11.580,33.44732,-116.57838
199,30-Aug-2015 02:01:14,30-Aug-2015 02:01:16,1.0,10,2.41,11.609,33.44742,-116.57779
200,19-Jan-2016 08:40:08,01-Nov-2015 12:27:04,0.9258,9,0.79,8.665,33.51867,-116.47152
200,19-Jan-2016 08:40:08,19-Jan-2016 08:40:12,1.0,9,1.76,8.693,33.51874,-116.47170
201,11-Nov-2015 10:17:05,11-Nov-2015 10:15:56,0.9234,8,0.86,10.85,33.52051,-116.43864
201,11-Nov-2015 10:17:05,11-Nov-2015 10:17:09,1.0,8,1.54,10.85,33.52051,-116.43864
202,10-Dec-2015 20:49:43,07-Dec-2015 10:51:30,0.9163,5,0.65,10.397,33.47072,-116.48621
202,10-Dec-2015 20:49:43,09-Dec-2015 19:35:27,0.9382,3,0.49,10.261,33.46986,-116.48642
202,10-Dec-2015 20:49:43,10-Dec-2015 20:49:47,1.0,5,1.82,10.211,33.46948,-116.48622
203,10-Dec-2015 18:22:53,10-Dec-2015 17:25:03,0.9462,8,0.83,10.000,33.46816,-116.48706
203,10-Dec-2015 18:22:53,10-Dec-2015 18:22:56,1.0,8,1.89,10.017,33.46830,-116.48733
204,28-Dec-2015 22:06:10,12-Dec-2015 02:52:45,0.9488,6,0.53,8.411,33.52212,-116.47071
204,28-Dec-2015 22:06:10,28-Dec-2015 22:06:14,1.0,6,1.66,8.664,33.52246,-116.47052
205,08-Feb-2016 12:47:45,07-Feb-2016 23:08:04,0.9569,6,1.18,8.948,33.52100,-116.47125
205,08-Feb-2016 12:47:45,08-Feb-2016 12:47:49,1.0,6,2.5,8.886,33.52088,-116.47120
206,22-Apr-2016 12:35:13,22-Apr-2016 14:26:49,0.9353,9,1.15,7.952,33.47178,-116.44610
206,22-Apr-2016 12:35:13,22-Apr-2016 12:35:17,1.0,9,2.51,7.952,33.47178,-116.44610
207,03-May-2016 07:18:37,05-May-2016 02:27:24,0.917,9,1.83,8.060,33.47565,-116.48943
207,03-May-2016 07:18:37,03-May-2016 07:18:41,1.0,9,1.9,8.09,33.47597,-116.48981
208,30-May-2016 15:10:36,30-May-2016 14:55:49,0.9547,9,0.99,6.358,33.46235,-116.47894
208,30-May-2016 15:10:36,30-May-2016 15:10:40,1.0,9,1.68,6.369,33.46202,-116.47912
209,10-Jun-2016 23:46:11,10-Jun-2016 14:39:36,0.9367,9,1.30,9.545,33.46272,-116.41812
209,10-Jun-2016 23:46:11,10-Jun-2016 23:46:16,1.0,9,1.78,9.545,33.46272,-116.41812
210,10-Jun-2016 09:19:23,10-Jun-2016 09:18:42,0.913,10,1.72,11.525,33.48315,-116.41760
210,10-Jun-2016 09:19:23,10-Jun-2016 09:19:28,1.0,10,2.85,11.525,33.48315,-116.41760
211,10-Jun-2016 10:39:21,10-Jun-2016 09:36:38,0.9487,10,0.71,12.656,33.44918,-116.40065
211,10-Jun-2016 10:39:21,10-Jun-2016 10:39:26,1.0,10,1.91,12.554,33.44923,-116.40118
212,10-Jun-2016 09:04:41,10-Jun-2016 09:04:23,0.9778,9,1.17,11.881,33.51027,-116.55975
212,10-Jun-2016 09:04:41,10-Jun-2016 09:04:44,1.0,9,1.81,11.881,33.51027,-116.55975
213,10-Jun-2016 13:37:40,10-Jun-2016 13:37:23,0.9376,7,1.70,10.368,33.46525,-116.44085
213,10-Jun-2016 13:37:40,10-Jun-2016 13:37:44,1.0,7,1.81,10.368,33.46525,-116.44085
214,10-Jun-2016 11:21:52,10-Jun-2016 11:51:32,0.9093,6,0.65,9.443,33.46416,-116.41853
214,10-Jun-2016 11:21:52,10-Jun-2016 11:21:57,1.0,6,1.81,9.394,33.46508,-116.41896
215,10-Jun-2016 09:12:58,10-Jun-2016 09:12:37,0.9329,10,1.17,11.881,33.51169,-116.55126
215,10-Jun-2016 09:12:58,10-Jun-2016 09:13:01,1.0,10,1.96,11.834,33.51202,-116.55147
216,10-Jun-2016 08:11:27,10-Jun-2016 10:28:03,0.9021,4,1.24,13.291,33.45747,-116.45302
216,10-Jun-2016 08:11:27,10-Jun-2016 08:11:32,1.0,4,1.81,13.124,33.45650,-116.45204

```
217,10-Jun-2016 08:39:47,10-Jun-2016 08:40:31,0.9664,10,1.24,12.072,33.45486,-116.44893
217,10-Jun-2016 08:39:47,10-Jun-2016 08:39:51,1.0,10,2,12.072,33.45486,-116.44893
218,10-Jun-2016 16:54:36,10-Jun-2016 15:57:55,0.9726,9,1.27,11.515,33.46712,-116.44350
218,10-Jun-2016 16:54:36,10-Jun-2016 16:54:40,1.0,9,1.52,11.515,33.46712,-116.44350
219,11-Jun-2016 01:40:30,10-Jun-2016 16:49:58,0.9223,7,1.09,11.311,33.46237,-116.47605
219,11-Jun-2016 01:40:30,11-Jun-2016 01:40:35,1.0,7,3.04,11.177,33.46272,-116.47616
220,11-Jun-2016 05:34:57,11-Jun-2016 01:39:55,0.9783,10,1.78,10.659,33.45794,-116.45687
220,11-Jun-2016 05:34:57,11-Jun-2016 05:35:03,1.0,10,1.74,10.659,33.45794,-116.45687
221,11-Jun-2016 10:02:26,11-Jun-2016 10:15:04,0.9214,10,0.81,11.883,33.48156,-116.49457
221,11-Jun-2016 10:02:26,11-Jun-2016 10:02:31,1.0,10,1.65,11.928,33.48125,-116.49478
222,19-Jun-2016 21:08:57,11-Jun-2016 03:45:03,0.9322,7,0.66,11.329,33.46477,-116.47558
222,19-Jun-2016 21:08:57,12-Jun-2016 10:38:12,0.9751,7,0.69,11.336,33.46463,-116.47554
222,19-Jun-2016 21:08:57,19-Jun-2016 09:58:24,0.9303,8,1.03,11.213,33.46477,-116.47588
222,19-Jun-2016 21:08:57,19-Jun-2016 21:09:01,1.0,8,1.83,11.216,33.46488,-116.47558
223,17-Jun-2016 02:35:11,17-Jun-2016 02:34:49,0.9303,5,1.11,13.207,33.48423,-116.48920
223,17-Jun-2016 02:35:11,17-Jun-2016 02:35:15,1.0,5,1.5,13.236,33.48464,-116.48917
224,17-Jun-2016 23:03:16,17-Jun-2016 06:24:28,0.9232,6,0.48,11.464,33.46530,-116.47131
224,17-Jun-2016 23:03:16,18-Jun-2016 06:39:44,0.9049,5,1.12,11.248,33.46528,-116.47127
224,17-Jun-2016 23:03:16,17-Jun-2016 23:03:20,1.0,6,1.99,11.373,33.46532,-116.47108
225,21-Jun-2016 18:42:14,20-Jun-2016 13:59:11,0.939,5,1.27,11.28,33.47297,-116.48339
225,21-Jun-2016 18:42:14,20-Jun-2016 16:36:21,0.9319,5,0.85,11.252,33.47281,-116.48334
225,21-Jun-2016 18:42:14,21-Jun-2016 18:42:20,1.0,5,1.88,11.28,33.47297,-116.48339
226,28-Jul-2016 05:46:29,02-Jul-2016 17:01:12,0.9061,8,0.68,11.631,33.51112,-116.51963
226,28-Jul-2016 05:46:29,03-Jul-2016 06:28:22,0.9126,8,1.57,11.788,33.51137,-116.51922
226,28-Jul-2016 05:46:29,03-Jul-2016 08:20:14,0.974,8,0.74,11.608,33.51074,-116.51924
226,28-Jul-2016 05:46:29,28-Jul-2016 05:46:32,1.0,8,2.05,11.599,33.51080,-116.51910
227,03-Jul-2016 09:35:14,03-Jul-2016 06:29:37,0.9108,9,1.36,11.733,33.51135,-116.51953
227,03-Jul-2016 09:35:14,03-Jul-2016 09:35:16,1.0,9,1.68,11.607,33.51125,-116.51966
228,16-Jul-2016 07:19:31,16-Jul-2016 07:19:27,0.9026,11,0.56,11.639,33.47228,-116.48411
228,16-Jul-2016 07:19:31,16-Jul-2016 07:19:35,1.0,11,2.09,11.748,33.47246,-116.48403
229,24-Jul-2016 20:32:57,23-Jul-2016 06:39:06,0.9232,6,0.80,8.697,33.49745,-116.53180
229,24-Jul-2016 20:32:57,24-Jul-2016 20:33:01,1.0,6,1.6,8.789,33.49669,-116.53189
230,20-Jul-2016 04:12:48,26-Jul-2016 04:25:54,0.9018,6,0.45,8.781,33.49555,-116.53102
230,20-Jul-2016 04:12:48,20-Jul-2016 04:12:51,1.0,6,2.68,8.886,33.49614,-116.53127
231,28-Jul-2016 00:05:17,30-Jul-2016 23:59:06,0.9657,9,1.58,9.794,33.45107,-116.45661
231,28-Jul-2016 00:05:17,28-Jul-2016 00:05:22,1.0,9,1.64,9.794,33.45107,-116.45661
232,04-Sep-2016 05:13:53,02-Sep-2016 06:44:42,0.9799,7,1.12,9.682,33.50084,-116.52891
232,04-Sep-2016 05:13:53,02-Sep-2016 15:59:48,0.9925,7,1.22,9.728,33.50108,-116.52893
232,04-Sep-2016 05:13:53,04-Sep-2016 05:13:56,1.0,7,1.77,9.728,33.50108,-116.52893
233,24-Aug-2016 19:57:03,10-Sep-2016 17:20:01,0.9254,5,1.16,6.332,33.48795,-116.42151
233,24-Aug-2016 19:57:03,24-Aug-2016 19:57:09,1.0,5,1.88,6.332,33.48795,-116.42151
234,25-Oct-2016 22:42:42,25-Oct-2016 11:53:47,0.9414,11,0.41,9.888,33.50178,-116.53083
234,25-Oct-2016 22:42:42,26-Oct-2016 04:19:15,0.9868,7,1.97,9.848,33.50170,-116.53095
234,25-Oct-2016 22:42:42,26-Oct-2016 04:23:30,0.9063,7,1.73,9.945,33.50202,-116.53122
234,25-Oct-2016 22:42:42,29-Oct-2016 21:51:11,0.9011,11,1.10,9.955,33.50153,-116.53063
234,25-Oct-2016 22:42:42,25-Oct-2016 22:42:44,1.0,11,1.75,9.848,33.50170,-116.53095
235,29-Oct-2016 04:49:23,29-Oct-2016 07:50:17,0.9304,11,0.79,14.092,33.47495,-116.42950
235,29-Oct-2016 04:49:23,29-Oct-2016 04:49:27,1.0,11,2,13.981,33.47483,-116.43018
236,23-Dec-2016 00:12:51,21-Dec-2016 22:38:28,0.9376,7,2.69,8.680,33.50563,-116.54669
236,21-Dec-2016 22:38:27,18-Dec-2016 06:21:24,0.9228,9,0.55,8.787,33.50596,-116.54654
236,23-Dec-2016 00:12:51,23-Dec-2016 07:58:14,0.9052,8,0.24,8.589,33.50566,-116.54666
236,23-Dec-2016 00:12:51,30-Dec-2016 05:33:15,0.9739,7,2.81,8.622,33.50517,-116.54647
236,23-Dec-2016 00:12:51,23-Dec-2016 00:12:55,1.0,8,2.16,8.622,33.50517,-116.54647
```

```
237,23-Dec-2016 07:05:12,22-Dec-2016 09:33:19,0.9007,9,1.18,8.798,33.50415,-116.54546
237,23-Dec-2016 07:05:12,30-Dec-2016 05:35:28,0.9219,8,0.87,8.716,33.50450,-116.54593
237,23-Dec-2016 07:05:12,23-Dec-2016 07:05:16,1.0,9,1.51,8.756,33.50461,-116.54586
238,23-Dec-2016 06:59:32,23-Dec-2016 01:01:24,0.9367,9,0.59,8.652,33.50455,-116.54591
238,23-Dec-2016 06:59:32,23-Dec-2016 06:59:35,1.0,9,1.57,8.641,33.50456,-116.54592
239,24-Dec-2016 06:40:35,23-Dec-2016 14:08:14,0.9293,6,1.06,8.732,33.49154,-116.47852
239,24-Dec-2016 06:40:35,24-Dec-2016 06:40:39,1.0,6,1.67,8.73,33.49176,-116.47909
240,25-Dec-2016 23:18:05,27-Dec-2016 10:32:01,0.9161,10,0.43,9.016,33.49098,-116.47637
240,25-Dec-2016 23:18:05,25-Dec-2016 23:18:09,1.0,10,1.57,8.828,33.49095,-116.47694
241,29-Dec-2016 20:33:27,29-Dec-2016 21:13:08,0.9168,7,0.83,8.715,33.50411,-116.54571
241,29-Dec-2016 20:33:27,29-Dec-2016 20:33:29,1.0,7,1.69,8.569,33.50406,-116.54591
```

Table B-3: Near-repeating earthquakes in March 1 - May 6, 2020. Average CC = 1.0 is the template event. Locations and magnitudes of template events and detected events are from the SCSN catalog. Near-repeating earthquakes during afterslip time periods are in bold. Times are in UTC.

Family #, Template Origin Time, Detection Time, Average CC, # Stations, ML, Depth(km), Latitude, Longitude
242,03-Jul-2016 06:28:20,09-Apr-2020 07:15:39,0.92,6,2.89,11.1,33.5077,-116.5298
227,03-Jul-2016 09:35:14,07-Apr-2020 01:28:09,0.91,7,1.09,10.6,33.5140,-116.5171
226,28-Jul-2016 05:46:29,09-Apr-2020 07:30:18,0.9,8,0.67,11.4,33.5150,-116.5155
244,07-Mar-2020 22:29:58,07-Mar-2020 22:31:20,0.92,11,0.95,8.2,33.4745,-116.4442
244,07-Mar-2020 22:29:58,07-Mar-2020 22:30:01,1.0,11,1.61,8.2,33.4745,-116.4442
245,04-Apr-2020 02:11:26,04-Apr-2020 02:18:46,0.9,4,1.14,10.4,33.5003,-116.5037
245,04-Apr-2020 02:11:26,04-Apr-2020 06:46:55,0.96,4,1.28,9.8,33.5037,-116.5098
245,04-Apr-2020 02:11:26,04-Apr-2020 02:11:29,1.0,4,1.6,10.1,33.501,-116.5118
246,04-Apr-2020 02:21:28,05-Apr-2020 02:09:38,0.92,4,1.73,10.4,33.5007,-116.5103
246,04-Apr-2020 02:21:28,04-Apr-2020 02:21:31,1.0,4,2.21,9.6,33.499,-116.5168
247,04-Apr-2020 02:46:16,04-Apr-2020 01:57:34,0.93,3,2.19,8.9,33.5007,-116.5058
247,04-Apr-2020 02:46:16,04-Apr-2020 10:50:40,0.94,3,1.37,9.9,33.5020,-116.5097
247,04-Apr-2020 02:46:16,07-Apr-2020 04:16:31,0.91,3,0.63,11.5,33.5067,-116.5003
247,04-Apr-2020 02:46:16,04-Apr-2020 02:46:21,1.0,3,2.22,9.9,33.5,-116.5123
248,04-Apr-2020 02:55:05,04-Apr-2020 04:06:03,0.91,4,0.83,7.7,33.4935,-116.5060
248,04-Apr-2020 02:55:05,04-Apr-2020 02:55:08,1.0,4,2.07,8.2,33.492,-116.5123
249,04-Apr-2020 03:58:37,04-Apr-2020 04:14:45,0.97,4,1.22,9.5,33.5043,-116.5155
249,04-Apr-2020 03:58:37,04-Apr-2020 16:50:26,0.95,4,0.81,10.5,33.5055,-116.5108
249,04-Apr-2020 03:58:37,04-Apr-2020 19:05:02,0.9,4,0.74,11,33.5032,-116.5143
249,04-Apr-2020 03:58:37,04-Apr-2020 03:58:40,1.0,4,1.76,9,33.5028,-116.5185
250,04-Apr-2020 05:34:44,17-Apr-2020 07:19:00,0.92,4,0.41,10.7,33.5008,-116.4975
250,04-Apr-2020 05:34:44,04-Apr-2020 05:34:47,1.0,4,1.87,9.4,33.5002,-116.492
251,04-Apr-2020 06:03:58,10-Apr-2020 05:08:57,0.94,4,0.65,9.5,33.5033,-116.5075
251,04-Apr-2020 06:03:58,04-Apr-2020 06:04:01,1.0,4,1.72,9.3,33.496,-116.5122
252,04-Apr-2020 06:13:42,04-Apr-2020 02:31:39,0.9,4,2.36,9.8,33.5002,-116.5157
252,04-Apr-2020 06:13:42,04-Apr-2020 06:13:45,1.0,4,2.28,9.8,33.4973,-116.5157
253,04-Apr-2020 07:29:24,04-Apr-2020 18:30:07,0.94,4,0.90,9.7,33.4987,-116.5117
253,04-Apr-2020 07:29:24,04-Apr-2020 07:29:27,1.0,4,1.56,10.1,33.4987,-116.51
254,04-Apr-2020 09:12:17,04-Apr-2020 04:18:25,0.9,4,1.02,10,33.5017,-116.5083
254,04-Apr-2020 09:12:17,04-Apr-2020 09:12:20,1.0,4,1.92,10.7,33.5005,-116.5078
255,04-Apr-2020 09:19:24,04-Apr-2020 09:39:46,0.92,3,1.27,9.8,33.5058,-116.5158
255,04-Apr-2020 09:19:24,04-Apr-2020 09:19:27,1.0,3,1.75,9.1,33.5045,-116.5223
256,04-Apr-2020 15:45:46,09-Apr-2020 09:47:08,0.93,3,0.76,9.2,33.4978,-116.4982
256,04-Apr-2020 15:45:46,04-Apr-2020 15:45:48,1.0,3,1.88,7.8,33.4928,-116.5088
257,04-Apr-2020 15:52:06,07-Apr-2020 08:07:50,0.92,4,0.9,10.4,33.5053,-116.5057
257,04-Apr-2020 15:52:06,04-Apr-2020 15:52:09,1.0,4,1.61,9.5,33.5008,-116.5173
258,04-Apr-2020 15:52:06,04-Apr-2020 15:52:09,1.0,4,1.61,9.5,33.5008,-116.5173
258,04-Apr-2020 17:31:49,04-Apr-2020 05:04:02,0.96,4,0.93,9.3,33.5032,-116.5127
258,04-Apr-2020 17:31:49,04-Apr-2020 17:31:52,1.0,4,1.86,8.9,33.5003,-116.5188
259,05-Apr-2020 00:11:03,04-Apr-2020 23:46:18,0.97,3,0.99,10,33.5047,-116.5107
259,05-Apr-2020 00:11:03,05-Apr-2020 00:11:05,1.0,7,1.6,9.6,33.501,-116.5163
260,05-Apr-2020 07:08:55,04-Apr-2020 07:08:00,0.9,6,0.70,8.8,33.5020,-116.5138
260,05-Apr-2020 07:08:55,05-Apr-2020 07:10:13,0.9,11,0.74,10.2,33.5053,-116.5075
260,05-Apr-2020 07:08:55,22-Apr-2020 05:46:31,0.92,10,1.02,9.8,33.5032,-116.5112
260,05-Apr-2020 07:08:55,05-Apr-2020 07:08:57,1.0,11,1.88,10.1,33.4975,-116.5132
261,05-Apr-2020 14:41:05,07-Apr-2020 08:31:30,0.9,9,1.15,10.3,33.5098,-116.5167

```
261,05-Apr-2020 14:41:05,05-Apr-2020 14:41:08,1.0,9,1.57,10.4,33.5102,-116.5227
262,05-Apr-2020 21:19:18,05-Apr-2020 21:16:30,0.91,11,1.07,9.7,33.5098,-116.5137
262,05-Apr-2020 21:19:18,05-Apr-2020 21:19:21,1.0,11,1.67,10.3,33.506,-116.5165
263,05-Apr-2020 21:35:08,05-Apr-2020 03:09:49,0.91,11,1.27,10.9,33.5070,-116.5143
263,05-Apr-2020 21:35:08,05-Apr-2020 21:37:50,0.91,11,0.72,11.1,33.5102,-116.5098
263,05-Apr-2020 21:35:08,05-Apr-2020 21:35:10,1.0,11,2.15,10.5,33.5045,-116.521
264,05-Apr-2020 21:46:26,05-Apr-2020 22:43:38,0.9,10,1.12,9.5,33.5095,-116.5150
264,05-Apr-2020 21:46:26,05-Apr-2020 21:46:29,1.0,10,1.5,10.2,33.5032,-116.5175
265,05-Apr-2020 23:11:58,08-Apr-2020 01:16:21,0.92,10,1.39,10.3,33.5008,-116.5147
265,05-Apr-2020 23:11:58,05-Apr-2020 23:12:01,1.0,11,2.6,10.4,33.4977,-116.5215
266,06-Apr-2020 00:33:13,05-Apr-2020 20:45:26,0.94,11,1.19,10.2,33.5025,-116.5100
266,06-Apr-2020 00:33:13,06-Apr-2020 00:33:15,1.0,11,1.93,10.1,33.5003,-116.5132
267,06-Apr-2020 10:22:12,05-Apr-2020 12:33:13,0.9,11,0.89,11.0,33.5145,-116.5168
267,06-Apr-2020 10:22:12,06-Apr-2020 10:22:15,1.0,11,1.83,11.2,33.5112,-116.523
268,07-Apr-2020 14:37:09,04-Apr-2020 19:44:50,0.93,5,0,9.3,33.4962,-116.4932
268,07-Apr-2020 14:37:09,07-Apr-2020 14:37:11,1.0,11,1.6,9.3,33.4962,-116.4932
269,07-Apr-2020 21:07:29,07-Apr-2020 11:50:13,0.98,12,1.33,8.8,33.4947,-116.5058
269,07-Apr-2020 21:07:29,07-Apr-2020 11:50:33,0.92,12,1.26,8.5,33.4968,-116.5020
269,07-Apr-2020 21:07:29,07-Apr-2020 21:07:32,1.0,12,2.38,9.6,33.4938,-116.5138
270,08-Apr-2020 00:27:21,06-Apr-2020 10:03:37,0.95,10,0.94,9.7,33.5053,-116.5147
270,08-Apr-2020 00:27:21,08-Apr-2020 00:27:23,1.0,11,1.83,8,33.5022,-116.5188
271,08-Apr-2020 00:36:56,07-Apr-2020 03:03:04,0.92,11,1.18,9.7,33.4985,-116.5068
271,08-Apr-2020 00:36:56,07-Apr-2020 14:16:13,0.96,11,1.62,8.5,33.4962,-116.5097
271,08-Apr-2020 00:36:56,08-Apr-2020 00:36:59,1.0,11,2.48,9.5,33.4938,-116.5157
272,08-Apr-2020 00:38:57,06-Apr-2020 11:01:57,0.91,10,1.44,9.8,33.5037,-116.5177
272,08-Apr-2020 00:38:57,08-Apr-2020 00:39:00,1.0,11,1.94,9.6,33.5008,-116.5178
273,08-Apr-2020 01:19:37,04-Apr-2020 19:51:22,0.91,6,1.08,10.1,33.5048,-116.5120
273,08-Apr-2020 01:19:37,08-Apr-2020 01:18:49,0.94,10,1.81,9.9,33.5033,-116.5175
273,08-Apr-2020 01:19:37,08-Apr-2020 01:19:40,1.0,10,1.56,10.1,33.5035,-116.5163
274,08-Apr-2020 04:01:09,05-Apr-2020 18:44:27,0.93,10,1.06,10.3,33.5057,-116.5093
274,08-Apr-2020 04:01:09,08-Apr-2020 04:01:11,1.0,11,2.42,10.1,33.5002,-116.522
275,08-Apr-2020 04:49:22,04-Apr-2020 06:51:45,0.9,4,1.02,9.4,33.5032,-116.5160
275,08-Apr-2020 04:49:22,08-Apr-2020 00:40:05,0.94,9,1.35,10.3,33.5058,-116.5162
275,08-Apr-2020 04:49:22,08-Apr-2020 04:49:24,1.0,9,2.07,10,33.5055,-116.5225
276,09-Apr-2020 06:48:51,06-Apr-2020 21:09:47,0.92,11,0.88,9.5,33.4990,-116.5065
276,09-Apr-2020 06:48:51,09-Apr-2020 08:33:34,0.92,12,0.55,9.4,33.4988,-116.5123
276,09-Apr-2020 06:48:51,09-Apr-2020 06:48:53,1.0,12,1.74,9.7,33.4945,-116.5178
277,10-Apr-2020 00:32:07,07-Apr-2020 09:21:10,0.9,12,0.82,10.2,33.4868,-116.4955
277,10-Apr-2020 00:32:07,09-Apr-2020 18:31:16,0.9,12,1.4,8.8,33.4822,-116.5007
277,10-Apr-2020 00:32:07,09-Apr-2020 23:53:04,0.91,12,0.45,11.9,33.4852,-116.4973
277,10-Apr-2020 00:32:07,11-Apr-2020 13:54:41,0.94,10,0.6,8.8,33.4862,-116.4937
277,10-Apr-2020 00:32:07,23-Apr-2020 18:12:37,0.94,9,0.84,10,33.4848,-116.4997
277,10-Apr-2020 00:32:07,10-Apr-2020 00:32:09,1.0,12,1.97,9.8,33.4817,-116.51
278,17-Apr-2020 13:37:55,17-Apr-2020 13:10:41,0.94,11,0.54,8.3,33.4967,-116.5057
278,17-Apr-2020 13:37:55,17-Apr-2020 13:37:57,1.0,11,1.68,9.5,33.4927,-116.511
279,22-Apr-2020 04:39:19,09-Apr-2020 05:13:41,0.92,11,1.32,8.1,33.4948,-116.4892
279,22-Apr-2020 04:39:19,22-Apr-2020 04:39:21,1.0,11,1.99,8.3,33.4942,-116.4928
```

Appendix C – Supplemental Information for Chapter 3

C-1. Estimating tilt on a broadband seismometer

The horizontal acceleration detected by a seismometer is

$$a_x(t) = \ddot{u}_x(t) - g\theta \qquad \text{(C1)},$$

where g is the gravitational acceleration (9.81 m/s^2), $\ddot{u}_x(t)$ is the true horizontal acceleration due to translational motion, and θ is the angle of horizontal tilt in radians (Wielandt & Forbriger, 1999). If we assume that all of the observed acceleration in a seismic signal is due to tilt, we can solve for the tilt angle as

$$a_x(t) = -g\theta \rightarrow \theta = \frac{a_x(t)}{g} \qquad \text{(C2)}.$$

To estimate the tilt from the horizontal component of a seismometer in this study, we first deconvolve the instrument response to acceleration and then divide by g.

C-2. Tilt expected from an internal solitary wave in the South China Sea

To estimate the tilt expected from a propagating internal solitary wave in the South China Sea we approximate the wave as a point source on the seafloor due to a pressure perturbation. In general, a pressure change (ΔP) can be separated into a hydrostatic component (due, in large part, to the wave-induced changes in the density field, but also to a small internal-wave induced change to the sea surface height) and a non-hydrostatic component, due to wave-induced vertical accelerations (Moum and Smyth, 2006). Here we will estimate the hydrostatic pressure change due to wave-induced changes to the density field only as:

$$\Delta P = \Delta\rho g h \quad \text{(C3)}.$$

Here, $\Delta\rho$ is the change in density and h is the amplitude of the internal solitary wave (~100 m). In the South China Sea the density change is mostly dependent on the temperature change (ΔT). If the temperature change is ~10°C, typical at 190 m depth during the passage of an internal wave (Ramp et al., 2019), this gives a density change of roughly 2.5 $\frac{kg}{m^3}$ (Fofonoff & Millard, 1983). The pressure change ΔP on the seafloor from a propagating internal solitary wave is then 2.5 kPa. Using a typical basalt elastic modulus (E) of 6x10^{10} Pa, this gives an order of magnitude approximation the normal strain (ε_{zz}) as

$$\varepsilon_{zz} \approx \frac{\Delta P}{E} = 4x10^{-8} \quad \text{(C4).}$$

Now, to determine the tilt resulting from this normal strain, we can consider the solution for the deformation from a force (F) applied on the free surface of an elastic halfspace, i.e.,

$$w_z(x) = \frac{F(1-\nu^2)}{\pi E x} \quad \text{(C5),}$$

where $w_z(x)$ is the vertical deformation on the free surface (seafloor) at a distance x from the applied force, ν is Poisson's ratio, and E is Young's modulus (Timoshenko & Goodier, 1970). In general, tilt (θ) is the horizontal derivative of the vertical displacement (Figure 3-1a). Therefore, the derivative of $w_z(x)$ with respect to x is the tilt (θ), which is

$$\frac{dw_z(x)}{dx} = \theta \sim \frac{-F}{\pi E x^2} \qquad \text{(C6).}$$

If we assume the pressure change ΔP (Equation C3) is applied to a disk of radius R, and the observation is in the nearfield where $x \sim R$, then

$$\theta \sim \frac{-P\pi R^2}{\pi E x^2} \sim \frac{-P}{E} \sim \varepsilon_{zz} \qquad \text{(C7).}$$

Therefore, for a near-field source, the tilt is approximately equal to the normal strain. The calculated normal strain (Equation C4) is approximately 4x10^{-8} or a tilt of 40 nanoradians. This value is consistent with the observed range of 15-80 nanoradians.

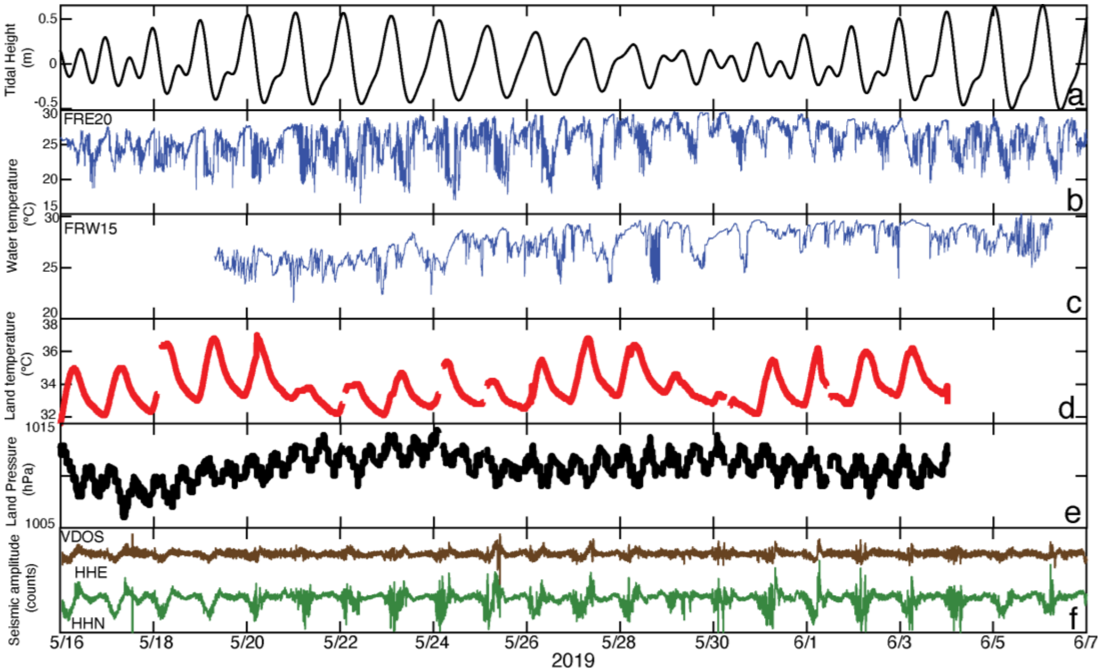

Figure C-1. Seismic amplitude compared to local tide, water and land temperature, and barometric pressure fluctuations. (a) Local predicted tidal height near Dongsha Atoll (Egbert & Erofeeva, 2002). (b) Oceanic water temperature measurements from FRE20 (Figure 1d). (c) Oceanic water temperature measurements from FRW15 (Figure 1d). (d) Temperature measurements on land at Pratas Island, co-located with 6M88 on Figure 1d. e) Barometric pressure on land at Pratas Island, co-located with 6M88 on Figure 1d. f) Seismic station VDOS HHN (green) and HHE (brown) components with a 400 second acausal low-pass filter applied. Time is in UTC.

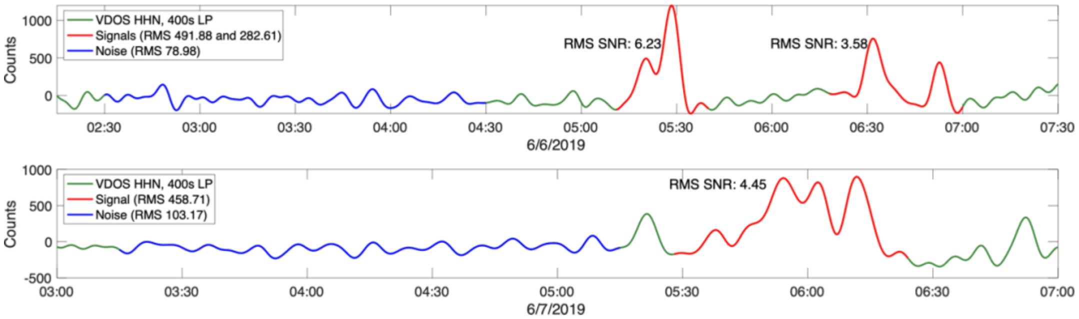

Figure C-2. Signal-to-noise comparison for internal wave detections on June 6 and June 7, 2019 on VDOS HHN. Seismic station VDOS HHN with an acausal 400-second low-pass filter applied is shown in green. Potential internal wave signals are indicated in red. The two-hour windows used to compute the root-mean-square (RMS) amplitude of the noise prior to the internal wave detections are shown in blue. The RMS signal-to-noise ratios (SNR) computed for each internal wave detection are indicated next to each detection. Time is in UTC.

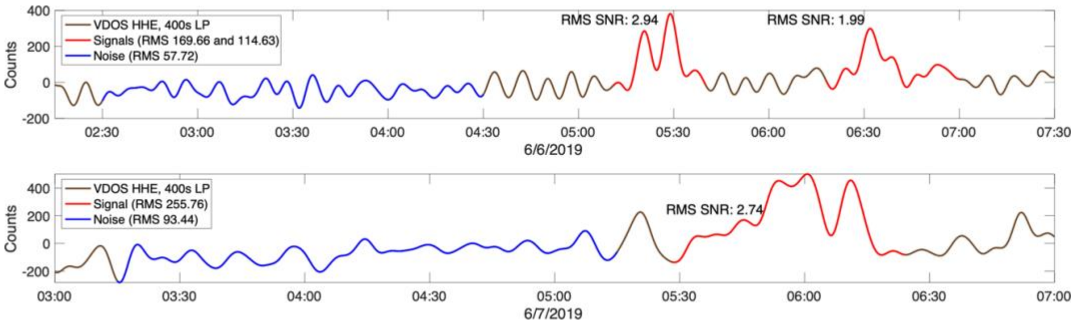

Figure C-3. Signal-to-noise comparison for internal wave detections on June 6 and June 7, 2019 on VDOS HHE. Seismic station VDOS HHE with an acausal 400-second low-pass filter applied is shown in brown. Potential internal wave signals are indicated in red. The two-hour windows used to compute the root-mean-square (RMS) amplitude of the noise prior to the internal wave detections are shown in blue. The RMS signal-to-noise ratios (SNR) computed for each internal wave detection are indicated next to each detection. Time is in UTC.

Movie C-1. **Movie of satellite images and seismic signals from June 6 - June 7, 2019.** Top: Himawari-8 standard red channel images near Dongsha Atoll. Seismic station VDOS on Pratas Island is included as the green triangle. Bottom: VDOS components HHN (green) and HHE (brown) with an acausal 400-second low-pass filter applied. Tilt signals potentially correlating with timing of internal wave arrivals on the western side of Dongsha Atoll are indicated in red. Earthquake or instrument malfunction times are indicated in grey. The timing (UTC) of the satellite image is indicated by the dashed black line.

References

Ackerley, N. (2014). Principles of Broadband Seismometry, *in* Beer, M., Kougioumtzoglou, I.A., Patelli, E., and Au, I.S.-K. eds., Encyclopedia of Earthquake Engineering, Berlin, Heidelberg, Springer Berlin Heidelberg, p. 1–35, doi:10.1007/978-3-642-36197-5_172-1.

Agnew, D., C. (2017). *Understanding triggering of repeated aseismic strain changes in the Anza Gap* (Final Technical Report No. G14AP00071). USGS.

Alford, M.H. et al. (2015). The formation and fate of internal waves in the South China Sea: Nature, v. 521, p. 65, doi:10.1038/nature14399.

Alongi, T., Schwartz, S. Y., Shaddox, H. R., Small, D. T. (2021). Probing the Southern Cascadia Plate Interface With the Dense Amphibious Cascadia Initiative Seismic Array: Journal of Geophysical Research: Solid Earth, 126, doi: 10.1029/2021JB022180.

Alpers, W. (1985). Theory of radar imaging of internal waves: Nature, v. 314, p. 245–247.

Alwahedi, M. A., & Hawthorne, J. C. (2019). Intermediate-Magnitude Postseismic Slip Follows Intermediate-Magnitude (M 4 to 5) Earthquakes in California. *Geophysical Research Letters*, *46*(7), 3676–3687. https://doi.org/10.1029/2018GL081001

Annoura, S., Hashimoto, T., Kamaya, N., & Katsumata, A. (2017). Shallow episodic tremor near the Nankai Trough axis off southeast Mie prefecture, Japan. *Geophysical Research Letters*, *44*(8), 3564–3571. https://doi.org/10.1002/2017GL073006

Anthony, R.E., Ringler, A.T., and Wilson, D.C. (2018). Improvements in Absolute Seismometer Sensitivity Calibration Using Local Earth Gravity Measurements Short Note: Bulletin of the Seismological Society of America, v. 108, p. 503–510, doi:10.1785/0120170218.

Araki, E., Saffer, D. M., Kopf, A. J., Wallace, L. M., Kimura, T., Machida, Y., et al. (2017). Recurring and triggered slow-slip events near the trench at the Nankai Trough subduction megathrust. *Science*, *356*(6343), 1157–1160. https://doi.org/10.1126/science.aan3120

Arnoso, J., Viera, R., Velez, E., Weixin, C., Shiling, T., Jun, J., and Venedikov, A. (2001). Monitoring Tidal and Non-tidal Tilt Variations in Lanzarote Island (Spain): Journal of the Geodetic Society of Japan, v. 47, p. 456–462.

Avouac, J.-P. (2015). From Geodetic Imaging of Seismic and Aseismic Fault Slip to Dynamic Modeling of the Seismic Cycle. *Annual Review of Earth and Planetary Sciences*, *43*(1), 233–271. https://doi.org/10.1146/annurev-earth-060614-105302

Barker, D.H.N., Henrys, S., Tontini, F.C., Barnes, P.M., Bassett, D., Todd, E., and Wallace, L. (2018). Geophysical Constraints on the Relationship Between Seamount Subduction, Slow Slip, and Tremor at the North Hikurangi Subduction Zone, New Zealand: Geophysical Research Letters, v. 45, p. 12,804-12,813, doi:10.1029/2018GL080259.

Bartlow, N. M. (2020). A Long-Term View of Episodic Tremor and Slip in Cascadia. Geophysical Research Letters, 47(3), e2019GL085303. https://doi.org/10.1029/2019GL085303

Bartlow, N. M., Miyazaki, S., Bradley, A. M., & Segall, P. (2011). Space-time correlation of slip and tremor during the 2009 Cascadia slow slip event. *Geophysical Research Letters*, *38*(18), L18309. https://doi.org/10.1029/2011GL048714

Beauducel, F. (2020). Okada: Surface deformation due to a finite rectangular source. Retrieved March 4, 2020, from https://www.mathworks.com/matlabcentral/fileexchange/25982-okada-surface-deformation-due-to-a-finite-rectangular-source

Bell, J. W., Amelung, F., & Henry, C. D. (2012). InSAR analysis of the 2008 Reno-Mogul earthquake swarm: Evidence for westward migration of Walker Lane style dextral faulting. *Geophysical Research Letters*, *39*(18). https://doi.org/10.1029/2012GL052795

Bell, R., Sutherland, R., Barker, D.H.N., Henrys, S., Bannister, S., Wallace, L., and Beavan, J. (2010). Seismic reflection character of the Hikurangi subduction interface, New Zealand, in the region of repeated Gisborne slow slip events: Geophysical Journal International, v. 180, p. 34–48, doi:10.1111/j.1365-246X.2009.04401.x.

Bennett, R., A., Rodi, W., & Rellinger, R. E. (1996). Global Positioning System constraints on fault slip rates in southern California and northern Baja, Mexico. *Journal of Geophysical Research: Solid Earth*, *101*(B10), 21943–21960.

Beroza, G. C., & Ide, S. (2011). Slow Earthquakes and Nonvolcanic Tremor. *Annual Review of Earth and Planetary Sciences*, *39*(1), 271–296. https://doi.org/10.1146/annurev-earth-040809-152531

Bilham, R., and Beavan, J. (1979). Surface Deformation and Elasticity Studies in the Virgin Islands: National Aeronaautics and Space Administration NSG 5072.

Boudin, F., Allgeyer, S., Bernard, P., Hébert, H., Olcay, M., Madariaga, R., et al. (2013). Analysis and modelling of tsunami-induced tilt for the 2007, M = 7.6, Tocopilla and the 2010, M = 8.8 Maule earthquakes, Chile, from long-base tiltmeter and broadband seismometer records. Geophysical Journal International, 194(1), 269–288. https://doi.org/10.1093/gji/ggt123

Bourouis, S., & Bernard, P. (2007). Evidence for coupled seismic and aseismic fault slip during water injection in the geothermal site of Soultz (France), and implications for seismogenic transients. Geophysical Journal International, 169(2), 723–732. https://doi.org/10.1111/j.1365-246X.2006.03325.x

Bromirski, P. D. (2001). Vibrations from the “Perfect Storm.” Geochemistry, Geophysics, Geosystems, 2(7). https://doi.org/10.1029/2000GC000119

Bromirski, P. D., Duennebier, F. K., & Stephen, R. A. (2005). Mid-ocean microseisms. Geochemistry, Geophysics, Geosystems, 6(4). https://doi.org/10.1029/2004GC000768

Bürgmann, R. (2018). The geophysics, geology and mechanics of slow fault slip. *Earth and Planetary Science Letters*, *495*, 112–134. https://doi.org/10.1016/j.epsl.2018.04.062

Bürgmann, R., Ergintav, S., Segall, P., Hearn, E. H., McClusky, S., Reilinger, R. E., et al. (2002). Time-Dependent Distributed Afterslip on and Deep below the İzmit Earthquake Rupture. Bulletin of the Seismological Society of America, 92(1), 126–137. https://doi.org/10.1785/0120000833

Bürgmann, R., Frank, W., & Rousset, B. (2019). *Multidisciplinary exploration for slow aseismic slip and low-frequency earthquakes in the Anza Gap (San Jacinto fault zone)* (Report for SCEC Award #18014). SCEC.

Chamberlain, C. J., Hopp, C. J., Boese, C. M., Warren-Smith, E., Chambers, D., Chu, S. X., et al. (2017). EQcorrscan: Repeating and Near-Repeating Earthquake Detection and Analysis in Python. *Seismological Research Letters*, *89*(1), 173–181. https://doi.org/10.1785/0220170151

Chang, E. T. Y., Chao, B. F., Chen, G.-Y., & Liau, J.-M. (2016). Internal tides recorded at ocean bottom off the coast of Southeast Taiwan. Journal of Geophysical Research: Oceans, 121(5), 3381–3394. https://doi.org/10.1002/2015JC011370

Chen, K. H., Nadeau, R. M., & Rau, R.-J. (2008). Characteristic repeating earthquakes in an arc-continent collision boundary zone: The Chihshang fault of eastern Taiwan. Earth and Planetary Science Letters, 276(3), 262–272. https://doi.org/10.1016/j.epsl.2008.09.021

Chen, X., Shearer, P. M., & Abercrombie, R. E. (2012). Spatial migration of earthquakes within seismic clusters in Southern California: Evidence for fluid diffusion. Journal of Geophysical Research: Solid Earth, 117(B4). https://doi.org/10.1029/2011JB008973

Cheng, Y., Ross, Z. E., & Ben-Zion, Y. (2018). Diverse Volumetric Faulting Patterns in the San Jacinto Fault Zone. *Journal of Geophysical Research: Solid Earth*, *123*(6), 5068–5081. https://doi.org/10.1029/2017JB015408

Chestler, S. R., & Creager, K. C. (2017a). A Model for Low-Frequency Earthquake Slip. Geochemistry, Geophysics, Geosystems, 18(12), 4690–4708. https://doi.org/10.1002/2017GC007253

Chestler, S. R., & Creager, K. C. (2017b). Evidence for a scale-limited low-frequency earthquake source process. Journal of Geophysical Research: Solid Earth, 122(4), 3099–3114. https://doi.org/10.1002/2016JB013717

Collot, J.-Y., Sanclemente, E., Nocquet, J.-M., Leprêtre, A., Ribodetti, A., Jarrin, P., Chlieh, M., Graindorge, D., and Charvis, P. (2017). Subducted oceanic relief locks the shallow megathrust in central Ecuador: Journal of Geophysical Research: Solid Earth, v. 122, p. 2016JB013849, doi:10.1002/2016JB013849.

Davis, K.A., Arthur, R.S., Reid, E.C., Rogers, J.S., Fringer, O.B., DeCarlo, T.M., and Cohen, A.L., 2020, Fate of Internal Waves on a Shallow Shelf: Journal of Geophysical Research: Oceans, v. 125, p. e2019JC015377, doi:10.1029/2019JC015377.

Davis, K.A., Leichter, J.J., Hench, J.L., and Monismith, S.G., 2008, Effects of western boundary current dynamics on the internal wave field of the Southeast Florida shelf: Journal of Geophysical Research: Oceans, v. 113, doi:https://doi.org/10.1029/2007JC004699.

DeCarlo, T.M., Karnauskas, K.B., Davis, K.A., and Wong, G.T.F., 2015, Climate modulates internal wave activity in the Northern South China Sea:

Geophysical Research Letters, v. 42, p. 2014GL062522, doi:10.1002/2014GL062522.

Delbridge, B. G., Carmichael, J. D., Nadeau, R. M., Shelly, D. R., & Bürgmann, R. (2020). Geodetic Measurements of Slow-Slip Events Southeast of Parkfield, CA. Journal of Geophysical Research: Solid Earth, 125(5), e2019JB019059. https://doi.org/10.1029/2019JB019059

Dolenc, D., Romanowicz, B., McGill, P., & Wilcock, W. (2008). Observations of infragravity waves at the ocean-bottom broadband seismic stations Endeavour (KEBB) and Explorer (KXBB). Geochemistry, Geophysics, Geosystems, 9(5). https://doi.org/10.1029/2008GC001942

Dragert, H., Wang, K., & James, T. S. (2001). A Silent Slip Event on the Deeper Cascadia Subduction Interface. *Science*, *292*(5521), 1525–1528. https://doi.org/10.1126/science.1060152

Du, T., Tseng, Y.-H., and Yan, X.-H., 2008, Impacts of tidal currents and Kuroshio intrusion on the generation of nonlinear internal waves in Luzon Strait: Journal of Geophysical Research: Oceans, v. 113, doi:https://doi.org/10.1029/2007JC004294.

Duda, T.F., Lynch, J.F., Irish, J.D., Beardsley, R.C., Ramp, S.R., Chiu, C.-S., Tang, T.Y., and Yang, Y.-, 2004, Internal tide and nonlinear internal wave behavior at the continental slope in the northern south China Sea: IEEE Journal of Oceanic Engineering, v. 29, p. 1105–1130, doi:10.1109/JOE.2004.836998.

Eberhart-Phillips, D., Reyners, M., Bannister, S., Chadwick, M., and Ellis, S. (2010). Establishing a Versatile 3-D Seismic Velocity Model for New Zealand: Seismological Research Letters, v. 81, p. 992–1000, doi:10.1785/gssrl.81.6.992.

Egbert, G.D., and Erofeeva, S.Y., 2002, Efficient Inverse Modeling of Barotropic Ocean Tides: Journal of Atmospheric and Oceanic Technology, v. 19, p. 183–204, doi:10.1175/1520-0426(2002)019<0183:EIMOBO>2.0.CO;2.

Ekström, G., Dalton, C.A., and Nettles, M., 2006, Observations of Time-dependent Errors in Long-period Instrument Gain at Global Seismic Stations: Seismological Research Letters, v. 77, p. 12–22, doi:10.1785/gssrl.77.1.12.

Ellis, S., Fagereng, Å., Barker, D., Henrys, S., Saffer, D., Wallace, L., Williams, C., and Harris, R. (2015). Fluid budgets along the northern Hikurangi subduction margin, New Zealand: the effect of a subducting seamount on fluid pressure: Geophysical Journal International, v. 202, p. 277–297, doi:10.1093/gji/ggv127.

Fattahi, H., Amelung, F., Chaussard, E., & Wdowinski, S. (2015). Coseismic and postseismic deformation due to the 2007 M5.5 Ghazaband fault earthquake, Balochistan, Pakistan. *Geophysical Research Letters*, *42*(9), 3305–3312. https://doi.org/10.1002/2015GL063686

Ferrari, R., and Wunsch, C., 2009, Ocean Circulation Kinetic Energy: Reservoirs, Sources, and Sinks: Annual Review of Fluid Mechanics, v. 41, p. 253–282, doi:10.1146/annurev.fluid.40.111406.102139.

Fofonoff, N., Pand Millard, R.C., 1983, Algorithms for computation of fundamental properties of seawater. Unesco Technical Papers in Marine Science, 44, 53 pp.

Frank, W. B., Radiguet, M., Rousset, B., Shapiro, N. M., Husker, A. L., Kostoglodov, V., et al. (2015). Uncovering the geodetic signature of silent slip through repeating earthquakes. Geophysical Research Letters, 42(8), 2015GL063685. https://doi.org/10.1002/2015GL063685

Freed, A. M. (2007). Afterslip (and only afterslip) following the 2004 Parkfield, California, earthquake. *Geophysical Research Letters*, *34*(6). https://doi.org/10.1029/2006GL029155

Fu, K.-H., Wang, Y.-H., St. Laurent, L., Simmons, H., and Wang, D.-P., 2012, Shoaling of large-amplitude nonlinear internal waves at Dongsha Atoll in the northern South China Sea: Continental Shelf Research, v. 37, p. 1–7, doi:10.1016/j.csr.2012.01.010.

Fukao, Y., Sugioka, H., Ito, A., Shiobara, H., Paros, J. M., & Furue, R. (2016). Sensing of upslope passages of frontal bores across the trench slope break of the Japan Trench. Journal of Geophysical Research: Oceans, 121(5), 3422–3434. https://doi.org/10.1002/2015JC011432

Furuya, M., & Satyabala, S. P. (2008). Slow earthquake in Afghanistan detected by InSAR. *Geophysical Research Letters*, *35*(6). https://doi.org/10.1029/2007GL033049

Garrett, C., and Kunze, E., 2007, Internal Tide Generation in the Deep Ocean: Annual Review of Fluid Mechanics, v. 39, p. 57–87, doi:10.1146/annurev.fluid.39.050905.110227.

Geller, R. J., & Mueller, C. S. (1980). Four similar earthquakes in central California. *Geophysical Research Letters*, *7*(10), 821–824. https://doi.org/10.1029/GL007i010p00821

Guglielmi, Y., Cappa, F., Avouac, J.-P., Henry, P., and Elsworth, D. (2015). Seismicity triggered by fluid injection–induced aseismic slip: Science, v. 348, p. 1224–1226, doi:10.1126/science.aab0476.

Haijima, D. (2015). Seismic Activity and Velocity Structure in the Northern Hikurangi Subduction Zone offshore the North Island of New Zealand [M.S. thesis]: University of Tokyo.

Hainzl, S. (2004). Seismicity patterns of earthquake swarms due to fluid intrusion and stress triggering. Geophysical Journal International, 159(3), 1090–1096. https://doi.org/10.1111/j.1365-246X.2004.02463.x

Hawthorne, J. C., Bostock, M. G., Royer, A. A., & Thomas, A. M. (2016a). Variations in slow slip moment rate associated with rapid tremor reversals in Cascadia. Geochemistry, Geophysics, Geosystems, 17(12), 4899–4919. https://doi.org/10.1002/2016GC006489

Hawthorne, J. C., Simons, M., & Ampuero, J.-P. (2016b). Estimates of aseismic slip associated with small earthquakes near San Juan Bautista, CA: *Journal of Geophysical Research: Solid Earth*, *121*(11), 8254–8275. https://doi.org/10.1002/2016JB013120

Helfrich, K.R., and Melville, W.K., 2006, Long Nonlinear Internal Waves: Annual Review of Fluid Mechanics, v. 38, p. 395–425, doi:10.1146/annurev.fluid.38.050304.092129.

Hodgkinson, K. (2013). Strainmeters capture strain transients following the M4.7 March 2013 Anza Earthquake. Retrieved February 24, 2020, from https://www.unavco.org/highlights/2013/anza.html

Hodgkinson, K., Langbein, J., Henderson, B., Mencin, D., & Borsa, A. (2013). Tidal calibration of plate boundary observatory borehole strainmeters. *Journal of Geophysical Research: Solid Earth*, *118*(1), 447–458. https://doi.org/10.1029/2012JB009651

Holloway, P.E., Pelinovsky, E., Talipova, T., and Barnes, B., 1997, A Nonlinear Model of Internal Tide Transformation on the Australian North West Shelf: JOURNAL OF PHYSICAL OCEANOGRAPHY, v. 27, p. 26.

Hsu, M.-K., & Liu, A. K. (2000). Nonlinear Internal Waves in the South China Sea. Canadian Journal of Remote Sensing, 26(2), 72–81. https://doi.org/10.1080/07038992.2000.10874757

Hsu, Y.-J., Simons, M., Avouac, J.-P., Galetzka, J., Sieh, K., Chlieh, M., et al. (2006). Frictional Afterslip Following the 2005 Nias-Simeulue Earthquake, Sumatra. Science, 312(5782), 1921–1926. https://doi.org/10.1126/science.1126960

Hutchison, A. A., & Ghosh, A. (2017). Ambient Tectonic Tremor in the San Jacinto Fault, near the Anza Gap, Detected by Multiple Mini Seismic ArraysAmbient Tectonic Tremor in the San Jacinto Fault, near the Anza Gap, Detected by Multiple Mini Seismic Arrays. *Bulletin of the Seismological Society of America*, *107*(5), 1985–1993. https://doi.org/10.1785/0120160385

Hutton, K., Woessner, J., & Hauksson, E. (2010). Earthquake Monitoring in Southern California for Seventy-Seven Years (1932-2008). *Bulletin of the Seismological Society of America*, *100*(2), 423–446. https://doi.org/10.1785/0120090130

Igarashi, T. (2010). Spatial changes of inter-plate coupling inferred from sequences of small repeating earthquakes in Japan. *Geophysical Research Letters*, *37*(20). https://doi.org/10.1029/2010GL044609

Igarashi, T., Matsuzawa, T., & Hasegawa, A. (2003). Repeating earthquakes and interplate aseismic slip in the northeastern Japan subduction zone. *Journal of Geophysical Research: Solid Earth*, *108*(B5). https://doi.org/10.1029/2002JB001920

Inbal, A., Ampuero, J.-P., & Avouac, J.-P. (2017). Locally and remotely triggered aseismic slip on the central San Jacinto Fault near Anza, CA, from joint inversion of seismicity and strainmeter data: *Journal of Geophysical Research: Solid Earth*, *122*(4), 3033–3061. https://doi.org/10.1002/2016JB013499

Ito, Y., Hino, R., Kido, M., Fujimoto, H., Osada, Y., Inazu, D., et al. (2013). Episodic slow slip events in the Japan subduction zone before the 2011 Tohoku-Oki earthquake. *Tectonophysics*, *600*(Supplement C), 14–26. https://doi.org/10.1016/j.tecto.2012.08.022

Jackson, C., da Silva, J., Jeans, G., Alpers, W., and Caruso, M., 2013, Nonlinear Internal Waves in Synthetic Aperture Radar Imagery: Oceanography, v. 26, doi:10.5670/oceanog.2013.32.

Jiang, J., & Fialko, Y. (2016). Reconciling seismicity and geodetic locking depths on the Anza section of the San Jacinto fault. *Geophysical Research Letters*, *43*(20), 10,663-10,671. https://doi.org/10.1002/2016GL071113

Kato, A., & Nakagawa, S. (2014). Multiple slow-slip events during a foreshock sequence of the 2014 Iquique, Chile Mw 8.1 earthquake. *Geophysical*

Research Letters, *41*(15), 2014GL061138. https://doi.org/10.1002/2014GL061138

Kato, A., Obara, K., Igarashi, T., Tsuruoka, H., Nakagawa, S., & Hirata, N. (2012). Propagation of Slow Slip Leading Up to the 2011 Mw 9.0 Tohoku-Oki Earthquake. *Science*, *335*(6069), 705–708. https://doi.org/10.1126/science.1215141

Kilb, D., & Vernon, F. (2020). Southern California jolted by moderate but intense quake. Retrieved May 30, 2020, from http://doi.org/10.32858/temblor.084

Kimura, H., Kasahara, K., Igarashi, T., & Hirata, N. (2006). Repeating earthquake activities associated with the Philippine Sea plate subduction in the Kanto district, central Japan: A new plate configuration revealed by interplate aseismic slips. *Tectonophysics*, *417*(1–2), 101–118. https://doi.org/10.1016/j.tecto.2005.06.013

Kodaira, S., Iidaka, T., Kato, A., Park, J.-O., Iwasaki, T., and Kaneda, Y. (2004). High Pore Fluid Pressure May Cause Silent Slip in the Nankai Trough: Science, v. 304, p. 1295–1298, doi:10.1126/science.1096535.

Lengliné, O., & Marsan, D. (2009). Inferring the coseismic and postseismic stress changes caused by the 2004 Mw = 6 Parkfield earthquake from variations of recurrence times of microearthquakes. Journal of Geophysical Research: Solid Earth, 114(B10). https://doi.org/10.1029/2008JB006118

Li, X., Jackson, C.R., and Pichel, W.G. (2013). Internal solitary wave refraction at Dongsha Atoll, South China Sea: Geophysical Research Letters, v. 40, p. 3128–3132, doi:10.1002/grl.50614.

Li, C., Peng, Z., Yao, D., Guo, H., Zhan, Z., & Zhang, H. (2018). Abundant aftershock sequence of the 2015 Mw7.5 Hindu Kush intermediate-depth earthquake. *Geophysical Journal International*, *213*(2), 1121–1134. https://doi.org/10.1093/gji/ggy016

Lien, R.-C., Henyey, F., Ma, B., Yang, Y.J. (2014). Large-Amplitude Internal Solitary Waves Observed in the Northern South China Sea: Properties and Energetics: American Meteorological Society, v. 44, p. 1095-1115, doi:10.1175/JPO-D-13-088.1.

Lien, R.-C., Tang, T.Y., Chang, M.H., and D’Asaro, E.A., 2005, Energy of nonlinear internal waves in the South China Sea: Geophysical Research Letters, v. 32, doi:10.1029/2004GL022012.

Liu, Y., and Rice, J.R. (2007). Spontaneous and triggered aseismic deformation transients in a subduction fault model: Journal of Geophysical Research: Solid Earth, v. 112, p. B09404, doi:10.1029/2007JB004930.

Lin, Y. N., Sladen, A., Ortega-Culaciati, F., Simons, M., Avouac, J.-P., Fielding, E. J., et al. (2013). Coseismic and postseismic slip associated with the 2010 Maule Earthquake, Chile: Characterizing the Arauco Peninsula barrier effect. Journal of Geophysical Research: Solid Earth, 118(6), 3142–3159. https://doi.org/10.1002/jgrb.50207

Lindsey, N. J., Dawe, T. C., & Ajo-Franklin, J. B. (2019). Illuminating seafloor faults and ocean dynamics with dark fiber distributed acoustic sensing. Science, 366(6469), 1103–1107. https://doi.org/10.1126/science.aay5881

Lindsey, E. O., & Fialko, Y. (2013). Geodetic slip rates in the southern San Andreas Fault system: Effects of elastic heterogeneity and fault geometry. *Journal of Geophysical Research: Solid Earth*, *118*(2), 689–697. https://doi.org/10.1029/2012JB009358

Lindsey, E. O., Sahakian, V. J., Fialko, Y., Bock, Y., Barbot, S., & Rockwell, T. K. (2014). Interseismic Strain Localization in the San Jacinto Fault Zone. *Pure and Applied Geophysics*, *171*(11), 2937–2954. https://doi.org/10.1007/s00024-013-0753-z

Lohman, R. B., & McGuire, J. J. (2007). Earthquake swarms driven by aseismic creep in the Salton Trough, California. Journal of Geophysical Research: Solid Earth, 112(B4). https://doi.org/10.1029/2006JB004596

MacKinnon, J.A. et al., 2017, Climate Process Team on Internal Wave–Driven Ocean Mixing: Bulletin of the American Meteorological Society, v. 98, p. 2429–2454, doi:10.1175/BAMS-D-16-0030.1.

Meng, L., Huang, H., Bürgmann, R., Ampuero, J. P., & Strader, A. (2015). Dual megathrust slip behaviors of the 2014 Iquique earthquake sequence. *Earth and Planetary Science Letters*, *411*, 177–187. https://doi.org/10.1016/j.epsl.2014.11.041

Meng, X., & Peng, Z. (2016). Increasing lengths of aftershock zones with depths of moderate-size earthquakes on the San Jacinto Fault suggests triggering of deep creep in the middle crust. *Geophysical Journal International*, *204*(1), 250–261. https://doi.org/10.1093/gji/ggv445

Mesimeri, M., and Karakostas, V. (2018). Repeating earthquakes in western Corinth Gulf (Greece): implications for aseismic slip near locked faults: Geophysical Journal International, v. 215, p. 659–676, doi:10.1093/gji/ggy301.

Miropol'sky, Y.Z., 2001, Dynamics of Internal Gravity Waves in the Ocean (O. D. Shishkina, Ed.): Springer Netherlands, Atmospheric and Oceanographic Sciences Library, https://www.springer.com/us/book/9780792369356 (accessed February 2019).

Moum, J.N., and Smyth, W.D., 2006, The pressure disturbance of a nonlinear internal wave train: Journal of Fluid Mechanics, v. 558, p. 153, doi:10.1017/S0022112006000036.

Munk, W., Zetler, B., Clark, J., Glll, S., Porter, D., Spiesberger, J., & Spindel, R. (1981). Tidal effects on long-range sound transmission. Journal of Geophysical Research: Oceans, 86(C7), 6399–6410. https://doi.org/10.1029/JC086iC07p06399

Murray-Moraleda, J. R., & Simpson, R. W. (2009). Geodetically Inferred Coseismic and Postseismic Slip due to the M 5.4 31 October 2007 Alum Rock EarthquakeGeodetically Inferred Coseismic and Postseismic Slip due to the M 5.4 Alum Rock Earthquake. *Bulletin of the Seismological Society of America*, *99*(5), 2784–2800. https://doi.org/10.1785/0120090017

Nadeau, R. M., Foxall, W., & McEvilly, T. V. (1995). Clustering and Periodic Recurrence of Microearthquakes on the San Andreas Fault at Parkfield, California. Science, 267(5197), 503–507. https://doi.org/10.2307/2886200

Nadeau, R. M., & Johnson, L. R. (1998). Seismological studies at Parkfield VI: Moment release rates and estimates of source parameters for small repeating earthquakes. *Bulletin of the Seismological Society of America*, *88*(3), 790–814.

Nadeau, R. M., & McEvilly, T. V. (1999). Fault Slip Rates at Depth from Recurrence Intervals of Repeating Microearthquakes. *Science*, *285*(5428), 718–721. https://doi.org/10.1126/science.285.5428.718

Nakajima, J., and Uchida, N. (2018). Repeated drainage from megathrusts during episodic slow slip: Nature Geoscience, v. 11, p. 351–356, doi:10.1038/s41561-018-0090-z.

Nawa, K., Suda, N., Satake, K., Fujii, Y., Sato, T., Doi, K., et al. (2007). Loading and Gravitational Effects of the 2004 Indian Ocean Tsunami at Syowa Station, Antarctica. Bulletin of the Seismological Society of America, 97(1A), S271–S278. https://doi.org/10.1785/0120050625

Nishida, K., Maeda, T., & Fukao, Y. (2019). Seismic Observation of Tsunami at Island Broadband Stations. Journal of Geophysical Research: Solid Earth, 124(2), 1910–1928. https://doi.org/10.1029/2018JB016833

Okada, Y. (1985). Surface deformation due to shear and tensile faults in a half-space. *Bulletin of the Seismological Society of America*, *75*(4), 1135–1154.

Orcutt, J. A., Cox, C. S., Kibblewhite, A. C., Kuperman, W. A., & Schmidt, H. (1993). Observations and Causes of Ocean and Seafloor Noise at Ultra-Low and Very-Low Frequencies. In B. R. Kerman (Ed.), Natural Physical Sources of Underwater Sound: Sea Surface Sound (2) (pp. 203–232). Dordrecht: Springer Netherlands. https://doi.org/10.1007/978-94-011-1626-8_17

Ozawa, S., Suito, H., & Tobita, M. (2007). Occurrence of quasi-periodic slow-slip off the east coast of the Boso peninsula, Central Japan. Earth, Planets and Space, 59(12), 1241–1245. https://doi.org/10.1186/BF03352072

Peng, Z., & Gomberg, J. (2010). An integrated perspective of the continuum between earthquakes and slow-slip phenomena. *Nature Geoscience*, *3*(9), 599–607. https://doi.org/10.1038/ngeo940

Perfettini, H., & Avouac, J.-P. (2004). Postseismic relaxation driven by brittle creep: A possible mechanism to reconcile geodetic measurements and the decay rate of aftershocks, application to the Chi-Chi earthquake, Taiwan. Journal of Geophysical Research: Solid Earth, 109(B2). https://doi.org/10.1029/2003JB002488

Perfettini, H., Avouac, J.-P., & Ruegg, J.-C. (2005). Geodetic displacements and aftershocks following the 2001 Mw = 8.4 Peru earthquake: Implications for the mechanics of the earthquake cycle along subduction zones. Journal of Geophysical Research: Solid Earth, 110(B9). https://doi.org/10.1029/2004JB003522

Ramp, S.R., Park, J.-H., Yang, Y.J., Bahr, F.L., and Jeon, C., 2019, Latitudinal Structure of Solitons in the South China Sea: Journal of Physical Oceanography, v. 49, p. 1747–1767, doi:10.1175/JPO-D-18-0071.1.

Ramp, S.R., Tang, T.Y., Duda, T.F., Lynch, J.F., Liu, A.K., Chiu, C.-S., Bahr, F.L., Kim, H.-R., and Yang, Y.-, 2004, Internal solitons in the northeastern south China Sea. Part I: sources and deep water propagation: IEEE Journal of Oceanic Engineering, v. 29, p. 1157–1181, doi:10.1109/JOE.2004.840839.

Ramp, S.R., Yang, Y.J., and Bahr, F.L., 2010, Characterizing the nonlinear internal wave climate in the northeastern South China Sea: Nonlinear Processes in Geophysics, v. 17, p. 481–498, doi:10.5194/npg-17-481-2010.

Ray, R.D., and Mitchum, G.T., 1996, Surface manifestation of internal tides generated near Hawaii: Geophysical Research Letters, v. 23, p. 2101–2104, doi:10.1029/96GL02050.

Reid, E.C., DeCarlo, T.M., Cohen, A.L., Wong, G.T.F., Lentz, S.J., Safaie, A., Hall, A., and Davis, K.A., 2019, Internal waves influence the thermal and nutrient environment on a shallow coral reef: Limnology and Oceanography, v. 64, p. 1949–1965, doi:https://doi.org/10.1002/lno.11162.

Richter, C.F. (1935). An instrumental earthquake magnitude scale: Bulletin of the Seismological Society of America, v. 25, p. 1–32.

Ristau, J., Harte, D., and Salichon, J. (2016). A Revised Local Magnitude (ML) Scale for New Zealand Earthquakes: Bulletin of the Seismological Society of America, v. 106, p. 398–407, doi:10.1785/0120150293.

Rogers, J.S., Rayson, M.D., Ko, D.S., Winters, K.B., and Fringer, O.B., 2019, A framework for seamless one-way nesting of internal wave-resolving ocean models: Ocean Modelling, v. 143, p. 101462, doi:10.1016/j.ocemod.2019.101462.

Roland, E., & McGuire, J. J. (2009). Earthquake swarms on transform faults. Geophysical Journal International, 178(3), 1677–1690. https://doi.org/10.1111/j.1365-246X.2009.04214.x

Romanet, P., Bhat, H.S., Jolivet, R., and Madariaga, R., 2018, Fast and Slow Slip Events Emerge Due to Fault Geometrical Complexity: Geophysical Research Letters, v. 45, p. 4809–4819, doi:10.1029/2018GL077579.

Ross, Z. E., Kanamori, H., & Hauksson, E. (2017). Anomalously large complete stress drop during the 2016 Mw 5.2 Borrego Springs earthquake inferred by waveform modeling and near-source aftershock deficit. *Geophysical Research Letters*, *44*(12), 5994–6001. https://doi.org/10.1002/2017GL073338

Ross, Z. E., Hauksson, E., & Ben-Zion, Y. (2017). Abundant off-fault seismicity and orthogonal structures in the San Jacinto fault zone. *Science Advances*, *3*(3), e1601946. https://doi.org/10.1126/sciadv.1601946

Ross, Z. E., Trugman, D. T., Hauksson, E., & Shearer, P. M. (2019). Searching for hidden earthquakes in Southern California. *Science*, *364*(6442), 767–771. https://doi.org/10.1126/science.aaw6888

Rousset, B., Bürgmann, R., & Campillo, M. (2019). Slow slip events in the roots of the San Andreas fault. Science Advances, 5(2), eaav3274. https://doi.org/10.1126/sciadv.aav3274

Rubinstein, J.L., and Ellsworth, W.L. (2010). Precise Estimation of Repeating Earthquake Moment: Example from Parkfield, California: Bulletin of the

Seismological Society of America, v. 100, p. 1952–1961, doi:10.1785/0120100007.

Ruiz, S., Metois, M., Fuenzalida, A., Ruiz, J., Leyton, F., Grandin, R., et al. (2014). Intense foreshocks and a slow slip event preceded the 2014 Iquique Mw 8.1 earthquake. *Science*, *345*(6201), 1165–1169. https://doi.org/10.1126/science.1256074

Saffer, D.M., and Wallace, L.M. (2015). The frictional, hydrologic, metamorphic and thermal habitat of shallow slow earthquakes: Nature Geoscience, v. 8, p. 594–600, doi:10.1038/ngeo2490.

Sanders, C. O., & Kanamori, H. (1984). A seismotectonic analysis of the Anza Seismic Gap, San Jacinto Fault Zone, southern California. *Journal of Geophysical Research: Solid Earth*, *89*(B7), 5873–5890. https://doi.org/10.1029/JB089iB07p05873

Sandstrom, H., and Elliott, J.A., 1984, Internal tide and solitons on the Scotian Shelf: A nutrient pump at work: Journal of Geophysical Research: Oceans, v. 89, p. 6415–6426, doi:10.1029/JC089iC04p06415.

Savage, J. C. (1998). Displacement field for an edge dislocation in a layered half-space. *Journal of Geophysical Research: Solid Earth*, *103*(B2), 2439–2446. https://doi.org/10.1029/97JB02562

Schaff, D. P., Beroza, G. C., & Shaw, B. E. (1998). Postseismic response of repeating aftershocks. Geophysical Research Letters, 25(24), 4549–4552. https://doi.org/10.1029/1998GL900192

Scholz, C. H. (1998). Earthquakes and friction laws. *Nature*, *391*, 37–42. https://doi.org/10.1038/34097

Schwartz, S. Y., & Rokosky, J. M. (2007). Slow slip events and seismic tremor at circum-Pacific subduction zones. *Reviews of Geophysics*, *45*(3), RG3004. https://doi.org/10.1029/2006RG000208

Segall, P. (2010). *Earthquake and Volcano Deformation*. Princeton University Press.

Shaddox, H. R., & Schwartz, S. Y. (2019). Subducted seamount diverts shallow slow slip to the forearc of the northern Hikurangi subduction zone, New Zealand. *Geology*, *47*(5), 415–418. https://doi.org/10.1130/G45810.1

Shaddox, H.R., Schwartz, S.Y., and Bartlow, N. M., 2021, Afterslip and spontaneous aseismic slip on the Anza segment of the San Jacinto fault zone, southern

California: Journal of Geophysical Research: Solid Earth. doi: 10.1029/2020JB020460.

Shaddox, H.R., Brodsky, E.E., Ramp, S.R., and Davis, K.A., 2021, Seismic detection of oceanic internal gravity waves from subaerial seismometers: AGU Advances.

Shelly, D. R., Beroza, G. C., & Ide, S. (2007). Non-volcanic tremor and low-frequency earthquake swarms. Nature, 446(7133), 305–307. https://doi.org/10.1038/nature05666

Shelly, D. R., Beroza, G. C., Ide, S., & Nakamula, S. (2006). Low-frequency earthquakes in Shikoku, Japan, and their relationship to episodic tremor and slip. Nature, 442(7099), 188–191. https://doi.org/10.1038/nature04931

Shelly, D. R., Hill, D. P., Massin, F., Farrell, J., Smith, R. B., & Taira, T. (2013). A fluid-driven earthquake swarm on the margin of the Yellowstone caldera. Journal of Geophysical Research: Solid Earth, 118(9), 4872–4886. https://doi.org/10.1002/jgrb.50362

Shelly, D. R., Moran, S. C., & Thelen, W. A. (2013). Evidence for fluid-triggered slip in the 2009 Mount Rainier, Washington earthquake swarm. Geophysical Research Letters, 40(8), 1506–1512. https://doi.org/10.1002/grl.50354

Shelly, D. R., Taira, T., Prejean, S. G., Hill, D. P., & Dreger, D. S. (2015). Fluid-faulting interactions: Fracture-mesh and fault-valve behavior in the February 2014 Mammoth Mountain, California, earthquake swarm. Geophysical Research Letters, 42(14), 2015GL064325. https://doi.org/10.1002/2015GL064325

Simmons, H., Chang, M.-H., Chang, Y.-T., Chao, S.-Y., Fringer, O., Jackson, C., and Ko, D.S., 2011, Modeling and Prediction of Internal Waves in the South China Sea: Oceanography, v. 24, p. 88–99, doi:10.5670/oceanog.2011.97.

Sugioka, H., Fukao, Y., & Hibiya, T. (2005). Submarine volcanic activity, ocean-acoustic waves and internal ocean tides. Geophysical Research Letters, 32(24). https://doi.org/10.1029/2005GL024001

Sweet, J. R., Creager, K. C., & Houston, H. (2014). A family of repeating low-frequency earthquakes at the downdip edge of tremor and slip. Geochemistry, Geophysics, Geosystems, 15(9), 3713–3721. https://doi.org/10.1002/2014GC005449

Taira, T., Bürgmann, R., Nadeau, R. M., & Dreger, D. S. (2014). Variability of fault slip behavior along the San Andreas Fault in the San Juan Bautista Region.

Journal of Geophysical Research: Solid Earth, *119*(12), 8827–8844. https://doi.org/10.1002/2014JB011427

Tanimoto, T. (2007). Excitation of microseisms. Geophysical Research Letters, 34(5). https://doi.org/10.1029/2006GL029046

Templeton, D. C., Nadeau, R. M., & Bürgmann, R. (2008). Behavior of Repeating Earthquake Sequences in Central California and the Implications for Subsurface Fault Creep. *Bulletin of the Seismological Society of America*, *98*(1), 52–65. https://doi.org/10.1785/0120070026

Timoshenko, S. and J. N. Goodier (1951). Theory of Elasticity, 2nd Edition, New York, McGraw-Hill Book Company, Inc., 506 p.

Todd, E.K. et al. (2018). Earthquakes and Tremor Linked to Seamount Subduction During Shallow Slow Slip at the Hikurangi Margin, New Zealand: Journal of Geophysical Research: Solid Earth, v. 123, p. 6769–6783, doi:10.1029/2018JB016136.

Trugman, D.T., and Shearer, P.M. (2017). GrowClust: A Hierarchical Clustering Algorithm for Relative Earthquake Relocation, with Application to the Spanish Springs and Sheldon, Nevada, Earthquake Sequences: Seismological Research Letters, doi:10.1785/0220160188.

Tymofyeyeva, E., Fialko, Y., Jiang, J., Xu, X., Sandwell, D., Bilham, R., et al. (2019). Slow Slip Event On the Southern San Andreas Fault Triggered by the 2017 Mw8.2 Chiapas (Mexico) Earthquake. *Journal of Geophysical Research: Solid Earth*, *124*(9), 9956–9975. https://doi.org/10.1029/2018JB016765

Uchida, N., & Bürgmann, R. (2019). Repeating Earthquakes. *Annual Review of Earth and Planetary Sciences*, *47*(1), null. https://doi.org/10.1146/annurev-earth-053018-060119

Uchida, N., Hasegawa, A., Matsuzawa, T., & Igarashi, T. (2004). Pre- and post-seismic slow slip on the plate boundary off Sanriku, NE Japan associated with three interplate earthquakes as estimated from small repeating earthquake data. *Tectonophysics*, *385*(1), 1–15. https://doi.org/10.1016/j.tecto.2004.04.015

Vidale, J. E., & Shearer, P. M. (2006). A survey of 71 earthquake bursts across southern California: Exploring the role of pore fluid pressure fluctuations and aseismic slip as drivers. Journal of Geophysical Research: Solid Earth, 111(B5). https://doi.org/10.1029/2005JB004034

Waite, G. P., & Smith, R. B. (2002). Seismic evidence for fluid migration accompanying subsidence of the Yellowstone caldera. Journal of Geophysical Research: Solid Earth, 107(B9), ESE 1-1-ESE 1-15. https://doi.org/10.1029/2001JB000586

Waldhauser, F., & Ellsworth, W. L. (2002). Fault structure and mechanics of the Hayward Fault, California, from double-difference earthquake locations. Journal of Geophysical Research: Solid Earth, 107(B3), ESE 3-1-ESE 3-15. https://doi.org/10.1029/2000JB000084

Wallace, L.M., and Beavan, J. (2010). Diverse slow slip behavior at the Hikurangi subduction margin, New Zealand: Journal of Geophysical Research: Solid Earth, v. 115, p. B12402, doi:10.1029/2010JB007717.

Wallace, L.M., Beavan, J., Bannister, S., and Williams, C. (2012). Simultaneous long-term and short-term slow slip events at the Hikurangi subduction margin, New Zealand: Implications for processes that control slow slip event occurrence, duration, and migration: Journal of Geophysical Research: Solid Earth, v. 117, p. B11402, doi:10.1029/2012JB009489.

Wallace, L.M., Beavan, J., McCaffrey, R., and Darby, D. (2004). Subduction zone coupling and tectonic block rotations in the North Island, New Zealand: Journal of Geophysical Research: Solid Earth, v. 109, p. B12406, doi:10.1029/2004JB003241.

Wallace, L. M., Kaneko, Y., Hreinsdóttir, S., Hamling, I., Peng, Z., Bartlow, N., et al. (2017). Large-scale dynamic triggering of shallow slow slip enhanced by overlying sedimentary wedge. *Nature Geoscience*, *10*(10), 765–770. https://doi.org/10.1038/ngeo3021

Wallace, L.M., Webb, S.C., Ito, Y., Mochizuki, K., Hino, R., Henrys, S., Schwartz, S.Y., and Sheehan, A.F. (2016). Slow slip near the trench at the Hikurangi subduction zone, New Zealand: Science, v. 352, p. 701–704, doi:10.1126/science.aaf2349.

Walter, J. I., Schwartz, S. Y., Protti, M., & Gonzalez, V. (2013). The synchronous occurrence of shallow tremor and very low frequency earthquakes offshore of the Nicoya Peninsula, Costa Rica. *Geophysical Research Letters*, *40*(8), 1517–1522. https://doi.org/10.1002/grl.50213

Wang, K., and Bilek, S.L., 2011, Do subducting seamounts generate or stop large earthquakes? Geology, v. 39, p. 819–822, doi:10.1130/G31856.1.

Wang, K., and Bilek, S.L., 2014, Invited review paper: Fault creep caused by subduction of rough seafloor relief: Tectonophysics, v. 610, p. 1–24, doi:10.1016/j.tecto.2013.11.024.

Wang, T.-H., Cochran, E. S., Agnew, D., & Oglesby, D. D. (2013). Infrequent Triggering of Tremor along the San Jacinto Fault near Anza, California. *Bulletin of the Seismological Society of America*, *103*(4), 2482–2497. https://doi.org/10.1785/0120120284

Wang, Y.-H., Dai, C.-F., and Chen, Y.-Y. (2007). Physical and ecological processes of internal waves on an isolated reef ecosystem in the South China Sea: Geophysical Research Letters, v. 34, doi: https://doi.org/10.1029/2007GL030658.

Wang, C., & Pawlowicz, R. (2012). Oblique wave-wave interactions of nonlinear near-surface internal waves in the Strait of Georgia. Journal of Geophysical Research: Oceans, 117(C6). https://doi.org/10.1029/2012JC008022

Wdowinski, S. (2009). Deep creep as a cause for the excess seismicity along the San Jacinto fault. *Nature Geoscience*, *2*(12), 882–885. https://doi.org/10.1038/ngeo684

Wech, A. G., & Creager, K. C. (2011). A continuum of stress, strength and slip in the Cascadia subduction zone. *Nature Geoscience*, *4*(9), 624–628. https://doi.org/10.1038/ngeo1215

Wei, M., Kaneko, Y., Liu, Y., & McGuire, J. J. (2013). Episodic fault creep events in California controlled by shallow frictional heterogeneity. *Nature Geoscience*, *6*(7), 566–570. https://doi.org/10.1038/ngeo1835

Wei, M., Liu, Y., Kaneko, Y., McGuire, J. J., & Bilham, R. (2015). Dynamic triggering of creep events in the Salton Trough, Southern California by regional M≥5.4 earthquakes constrained by geodetic observations and numerical simulations. *Earth and Planetary Science Letters*, *427*, 1–10. https://doi.org/10.1016/j.epsl.2015.06.044

Wielandt, E., and Forbriger, T., 1999, Near-field seismic displacement and tilt associated with the explosive activity of Stromboli: Annals of Geophysics, v. 42, doi:10.4401/ag-3723.

Williams, C.A., Eberhart-Phillips, D., Bannister, S., Barker, D.H.N., Henrys, S., Reyners, M., and Sutherland, R. (2013). Revised Interface Geometry for the Hikurangi Subduction Zone, New Zealand: Seismological Research Letters, v. 84, p. 1066–1073, doi:10.1785/0220130035.

Wolanski, E., and Deleersnijder, E., 1998, Island-generated internal waves at Scott Reef, Western Australia: Continental Shelf Research, v. 18, p. 1649–1666, doi:10.1016/S0278-4343(98)00069-7.

Woods, K., Wallace, L.M., Webb, S.C., Ito, Y., Savage, M.K., Chadwell, C.D., Williams, C.A., Jr., Hino, R., Mochizuki, K., Warren-Smith, E., Barker, D.H.N. (2020). Updip Migration of Slow Slip Revealed Through Seafloor Geodesy during 2019 East Coast Slow Slip at the Hikurangi Margin, New Zealand, American Geophysical union, Fall Meeting 2020, Abstract #T022-04.

Woodson, C.B., 2018, The Fate and Impact of Internal Waves in Nearshore Ecosystems: Annual Review of Marine Science, v. 10, p. 421–441, doi:10.1146/annurev-marine-121916-063619.

Wu, W., Zhan, Z., Peng, S., Ni, S., & Callies, J. (2020). Seismic ocean thermometry. Science, 369(6510), 1510–1515. https://doi.org/10.1126/science.abb9519

Yao, D., Walter, J. I., Meng, X., Hobbs, T. E., Peng, Z., Newman, A. V., et al. (2017). Detailed spatiotemporal evolution of microseismicity and repeating earthquakes following the 2012 Mw 7.6 Nicoya earthquake. *Journal of Geophysical Research: Solid Earth*, *122*(1), 2016JB013632. https://doi.org/10.1002/2016JB013632

Yang, W., Hauksson, E., & Shearer, P. M. (2012). Computing a Large Refined Catalog of Focal Mechanisms for Southern California (1981-2010): Temporal Stability of the Style of Faulting. *Bulletin of the Seismological Society of America*, *102*(3), 1179–1194. https://doi.org/10.1785/0120110311

Yarce, J., Sheehan, A. F., Nakai, J. S., Schwartz, S. Y., Mochizuki, K., Savage, M. K., Wallace, L.M., Henrys, S.A., Webb, S.C., Ito, Y., Abercrombie, R. E., Fry, B., Shaddox, H., Todd, E.K. (2019). Seismicity at the northern Hikurangi Margin, New Zealand, and investigation of the potential spatial and temporal relationships with a shallow slow slip event. Journal of Geophysical Research: Solid Earth, 124, 4751–4766. https://doi.org/10.1029/2018JB017211

Yu, W., Song, T.-R. A., & Silver, P. G. (2013). Repeating aftershocks of the great 2004 Sumatra and 2005 Nias earthquakes. Journal of Asian Earth Sciences, 67–68, 153–170. https://doi.org/10.1016/j.jseaes.2013.02.018

Yuan, X., Kind, R., & Pedersen, H. A. (2005). Seismic monitoring of the Indian Ocean tsunami. Geophysical Research Letters, 32(15). https://doi.org/10.1029/2005GL023464

Zhao, Z., Klemas, V., Zheng, Q., and Yan, X.-H., 2004, Remote sensing evidence for baroclinic tide origin of internal solitary waves in the northeastern South China Sea: Geophysical Research Letters, v. 31, doi:10.1029/2003GL019077.

Zoback, M.D., Kohli, A., Das, I., and Mcclure, M.W. (2012). The Importance of Slow Slip on Faults During Hydraulic Fracturing Stimulation of Shale Gas Reservoirs, *in* Society of Petroleum Engineers, doi:10.2118/155476-MS.